Fall 12-18-2015

Developing and Testing an Anguilliform Robot Swimming with Theoretically High Hydrodynamic Efficiency

John B. Potts III
University of New Orleans, jbpotts@uno.edu

Recommended Citation

Developing and Testing an Anguilliform Robot Swimming with Theoretically High Hydrodynamic
Efficiency

A Dissertation

Submitted to the Graduate Faculty of the
University of New Orleans
in partial fulfillment of the
requirements for the degree of

Doctor of Philosophy
in
Engineering and Applied Science
Naval Architecture and Marine Engineering

by

J. Baker Potts, III
jbpotts@uno.edu
baker.potts@gmail.com

B.S. Tufts University, 2009
M.S. University of New Orleans, 2012

December, 2015

For my beautiful and lovely wife, Kaity, who never ceased to be patient with me over the past four and a half years yet still motivating me to complete this body of work. Thanks.

"The best time to plant a tree was 20 years ago. The second best time is now."

— Chinese Proverb

"To know, is to know that you know nothing. That is the meaning of true knowledge."

— Socrates

ACKNOWLEDGEMENTS

I am extremely grateful for this. He is very creative and full of talent. He is the best at bouncing off product development ideas, such as during the development and fabrication of the anguilliform robot prototypes. He is also extremely knowledgeable with electrical engineering, aiding with all the aspects associated with this field, such as the mechatronics and programming. He wrote the LabVIEW program to remotely control the robot prototypes, and this was a difficult and time-consuming undertaking. Ryan helped me countless other times throughout the project on tasks such as experimental testing equipment setup or whenever I encountered a mental stumbling block.

UNO NAME Facilities Manager George Morrisey has been very helpful with anything related to equipment in the UNO Towing Tank and Model Shop. If a testing apparatus needed fabrication or help was needed during some testing, he was the person to talk to. At times, George was a good motivator with his can-do attitude. Where I was very thoughtful and planned the project to the smallest details, George would tell me "stop thinking, just do!"

Several undergraduate and graduate students have helped me over the years. Chase Rogers worked on the computational fluid dynamics part of the project and helped me intermittently during tank testing. Chase was also a good person to bounce mathematical and programming ideas off of, as well as being an entertaining person to be around, bringing levity to the graduate student offices. Jacob Todd began the CFD part of the project for Chase and also helped me with various setting up of tests in the tank. Cory Collongues helped with ordering parts from various companies and vendors. Jan Felix, the UNO NAME Department Administrator, also helped with ordering parts from vendors and helped me with submitting the correct paperwork at the right times. Jake Kindred helped me set up the testing of the robot for load cell measurements and PIV testing. Jackson Wilson helped the most out of the research assistants, mostly because of his specialty experience in SCUBA diving. With this capability, he was able to set up the PIV calibration plate underwater, which is a time-consuming process that required more than just breaths of air. Jackson also helped with the fabrication of the tether, creating the CAM toolpath generation and setting up the tooling in the CNC mill.

Matt Stegmeir, of TSI, Inc., helped with the installation, setup, and usage of the PIV equipment. The measuring technique of this equipment is relatively new in the experimental world, particularly the type of PIV system obtained, and thus there were some stumbling blocks. However, Matt was just a phone call or email away and was always very patient and willing to provide assistance. His

During the lowest moments, she reminded me why I was working on this tiring work and motivated me to return to my path of one step at a time. During the highs, she kept me humble and made me not forget what work was still left to be done.

Thanks to all of you,

Baker

FOREWORD

I first met Baker Potts when he was a graduate student in pursuit of a Master's degree in Naval Architecture and Marine Engineering. He was working on a propeller dynamometer for use in the UNO towing tank. As the staff electrical engineer, I got to work closely with Baker on that project. I learned quickly that Baker was an excellent engineer, so I was delighted when he decided to continue his education in the pursuit of a Ph.D. with us at UNO.

I again got to work with Baker in support of the Anguilliform project, which is the subject of this dissertation. The project goal was to build an eel-like robot to reproduce Bill Vorus' theoretical "wakeless" swimming motion. We would then measure the results to see if they match the predictions. The project quickly turned into a multidisciplinary affair. An incomplete list of fields includes hydrodynamics, mechanics, mechatronics, structures, manufacturing, electronics, embedded computing, communications, electric machinery, controls, optimization, instrumentation, data acquisition, optics, and image processing. Bakers engineering versatility allowed him to shift expertly from one field to another, which was vital to the completion of this dissertation.

Just as any engineering or academic endeavor can be, this project was frustrating at times, such as when the eel would flood with water or batteries would die unexpectedly or a communication error would cause the robot to curl up like a dying animal. In spite of the frustrations we had many gratifying times as well, like when NEELBOT-1.0 swam on the surface for the first time and when the project was recognized on the local news and in the UNO Magazine. But the most rewarding experience for me is to see the completed work documented in Bakers dissertation. I feel fortunate and proud to have been part of this project. I learned a great deal working with Baker Potts over the past few years, and I hope you will learn something from his dissertation.

Ryan Douglas Thiel, Research Engineer

University of New Orleans

TABLE OF CONTENTS

CHAPTER

LIST OF FIGURES

Figure

LIST OF TABLES

ABSTRACT

An anguilliform swimming robot replicating an idealized motion is a complex marine vehicle necessitating both a theoretical and experimental analysis to completely understand its propulsion characteristics. The ideal anguilliform motion within is theorized to produce "wakeless" swimming (Vorus and Taravella (2011)), a reactive swimming technique that produces thrust by accelerations of the added mass in the vicinity of the body. The net circulation for the unsteady motion is theorized to be eliminated.

The robot was designed to replicate the desired, theoretical motion by applying control theory methods. Independent joint control was used due to hardware limitations.

The fluid velocity vectors in the propulsive wake downstream of the tethered, swimming robot were measured using Stereoscopic Particle Image Velocimetry (SPIV) equipment. Simultaneously, a load cell measured the thrust (or drag) forces of the robot via a hydrodynamic tether. The measured field velocities and thrust forces were compared to the theoretical predictions for each.

The desired, ideal motion was not replicated consistently during SPIV testing, producing off-design scenarios. The thrust-computing method for the ideal motion was applied to the actual, recorded motion and compared to the load cell results. The theoretical field velocities were computed differently by accounting for shed vortices due to a different shape than ideal. The theoretical thrust shows trends similar to the measured thrust over time. Similarly promising comparisons are found between the theoretical and measured flow-field velocities with respect to qualitative trends and velocity magnitudes. The initial thrust coefficient prediction was deemed insufficient, and a new one was determined from an iterative process.

The off-design cases shed flow structures into the downstream wake of the robot. The first is a residual disturbance of the shed boundary layer, which is to be expected for the ideal case, and dissipates within one motion cycle. The second are larger-order vortices that are being shed at two

distinct times during a half-cycle.

These qualitative and quantitative comparisons were used to confirm the possibility of the original hypothesis of "wakeless" swimming. While the ideal motion could not be tested consistently, the results of the off-design cases agree significantly with the adjusted theoretical computations. This shows that the boundary conditions derived from slender-body constraints and the assumptions of ideal flow theory are sufficient enough to predict the propulsion characteristics of an anguilliform robot undergoing this specific motion.

Keywords: anguilliform; robotics; particle image velocimetry (PIV); control theory; fluid dynamics; ideal flow

CHAPTER I

Introduction

The field of robotics has been growing steadily for the last couple of decades and then more significantly in the last 10 years alone due to several factors from grass-roots efforts all the way up to a push by the US government. The federal administration has been advocating for more learning in the STEM (Science, Technology, Engineering, and Math) fields, which invariably are associated with the robotics field, and thus more attention and funding has been pushed in this direction. Additionally, DARPA (Defense Advanced Research Projects Agency), a Department of Defense research program, has initiated some rather popular robotic competitions in the last decade with the autonomous car race and the humanoid search-and-rescue robot more recently. Both of these competitions have been marketed very well to the general public and have incited a feverish excitement to the field. (The Office of Naval Research, the main supporter of this research, is very similar to the DARPA program but for US Navy activities.) On the other end of the spectrum of getting things done, there has been a huge grass-roots movement across the country (and the world) due to the tools for developing robotics being more accessible. Software programming, needed for controlling the robotic hardware, has grown due to various reasons, including computers being absolutely ubiquitous, increase of easy-to-learn high-level languages, and the open-source culture, allowing for easy accessibility to the hundreds of algorithms needed for arm (and/or leg) manipulation, computer vision, path generation, etc. Hardware has also become incredibly accessible and usable with the decrease in cost and size of microcontrollers and the availability of rapid prototyping due to patents expiring on 3-D printing processes. These last few developments have been a major factor in allowing the robot for the current project to be more easily and affordably developed. Just 20 years ago, a similar project was attempted but failed due

to the inability to develop the robot with the proper actuators and rapid prototyping. In addition to the aspects stated above, this research is cutting into the relatively unknown field of underwater robotics, with the critical feature of needing to be waterproof. Most importantly, this robot can accomplish jobs that would otherwise place naval or scientific personnel at serious risk.

During the past few years of working on this research, one of the first questions I get asked is "what are the practical uses of a swimming anguilliform robot?" Unbelievably, there are an unlimited number of specific practical uses for an underwater robot imitating a biological anguilliform eel. More generally, there are three types of use considered at the moment. There is the ultimate use of it being a tool in the defense repertoire of the United States Navy in terms of searching for mines or adverse weapons in the littoral and riverine environments, which is explained in more detail in the next section. Secondly, this robot could be used by environmental scientists to monitor the world's oceans, estuaries, and other bodies of water by carrying a suite of measurement tools such as salinometers, thermometers, raw video footage, etc., all while minimally affecting the natural surroundings. The third practical use is an academic one, of which this dissertation expounds on: the robot's propulsive wake is being investigated in order to determine whether the theoretical hydrodynamics compare to the experimentally measured results. More specifically, the theory consists of slender body theory describing the fluid flow about the robot and proper shifting, in time and in space, of hydrodynamic added mass to generate forward thrust, as opposed to typical first-order lift methods (see Vorus and Taravella (2011) for more details). The experimentally measured results are obtained by cameras imaging the downstream flow which is illuminated and recorded by lasers reflecting off neutrally-buoyant seed particles. Successive images are cross-correlated in order to compute velocity vectors over the entire flow field for each instance in time. Practically, the proving (or disproving) of this theory will provide for a better design of a swimming anguilliform robot for the next prototype. This dissertation elucidates the theory involved in specifying the swimming motion, the development of the swimming prototypes, the experimental measurements of the wake field's velocities, and finally the conclusions found from the comparison of the theoretical and experimental results.

This chapter explains the motivation for the project and then provides a brief overview of previous research on similar work involving anguilliform swimming theory and testing. The chapter concludes with where this dissertation's research fits into the field of anguilliform swimming and

how this project contributes to that part of the field. Chapter 2 provides an explanation of the two- and three-dimensional derivations of this highly efficient anguilliform swimming motion using the assumptions of ideal flow theory applied to slender bodies. Extensions are made to the original derivation in order to apply the theory to a non-ideal shape, or off-design recorded motion of the actual robot. Chapter 3 illustrates the design-build development of the prototypes by explaining the physics-based model used to predict joint loads and also the product development of the actual robots, which included in-house fabrication. Precise development was critical to ensure the robot can attain the desired motion. Chapter 4 details the experimental testing required to measure the wake velocities using Particle Image Velocimetry (PIV) equipment and the propulsive forces generated by the swimming motion. Supporting factors such as the experimental hardware setup and the post-processing software that analyzes the recorded data to compute the velocity vectors are explained. Chapter 5 states the conclusions determined from all the facts gathered throughout the entire research process. These conclusions tie in all aspects of the theory and the experiment and provide a comparison to the overall field of associated research. A call to future work and improvements and additions beyond the current research is made.

1.1 Mission Objectives and Motivation

The primary objective of the research explained within is to contribute academically to the field by comparing experimental results to that of an improved development of the swimming motion. A secondary objective that is beyond the scope of this dissertation's objectives is that this research will aid in producing a functional, practical prototype that can be further developed and refined for use in a Naval Intelligence, Surveillance, and Reconnaissance (ISR) mission, an inspection or search-and-rescue (SAR) mission, or aid in scientific research of the world's oceans by measuring and monitoring key variables such as acidity, salinity, and temperature.

Recent changes in Naval warfare have produced increased emphasis on operations in littoral shallow-water areas and in riverine environments. One important mission is ISR, which sometimes involves monitoring and data collection under harsh conditions where Naval personnel can be at risk. To reduce risk and to expand collection opportunities, new methods and sensors are constantly undergoing research and development. There is strong interest in developing Autonomous

Underwater Vehicles (AUVs), with low acoustic, radar, and optical signatures, to carry sensors into dangerous areas, like harbors and streams, in support of ISR missions. This project contributes to the investigation of the science and engineering aspects of a new type of AUV that could eventually meet some special Naval maritime sensing and stealth objectives. It is believed that a small, nearly undetectable vehicle capable of autonomous, long-range sub-surface missions would be capable of accomplishing these tasks.

The types of sensors that can be placed on the head of the robot are only limited by their size and power requirements allowed by the robot. The robot can be used for search-and-rescue missions to scan the seafloor using SONAR (Sound Navigation and Ranging) for sunken vessels or missing airplanes such as the recently lost Malaysian Airline Flight MH370 (Wikipedia (2015b)). With an ultrasonic sensor or even video camera for immediate human-readable feedback, this robot could also be used to inspect the hundreds of miles of undersea oil and gas pipelines over the world, which are a threat to the wildlife if unchecked as shown by the recent pipeline failure off the coast of California (Wikipedia (2015a)). With its bio-mimicry, the robot would be minimally invasive to the surrounding environment during any of its missions. From a scientific research standpoint, the robot could contain a suite of sensors related to monitoring the world's oceans, especially considering the need to measure variables that may be harbingers of climate change, such as ocean acidity or temperature.

Most unbelievably, this robot could theoretically propel itself for unlimited periods of time, in addition to it already predicted to be highly efficient due to no induced vortices being shed. Once its batteries begin to run low, it could attach itself to the seafloor, vertical pile, or catenary chain and then let the ambient ocean currents run past it inducing an oscillating motion along the length of the robot, forcing the actuators to act as generators and recharge its batteries. The only limits would be its ability to attach to an object in time and the number of times the batteries can be recharged.

It is amazing to think that the idea for this possible AUV stems from a fishing trip by Dr. Vorus, on which he noticed a "water snake slithering through the surfactant field of spring pollen covering the surface of a farm pond." According to him, "the animal left a very clean and distinct serpentine track of its progression through the pollen, barely wider than the width of its body."

It has been established theoretically that self-propulsion of deformable bodies in ideal fluid can

occur with a careful specification of the deformation mode shape (Saffman (1967) and Miloh and Galper (1993)). With the fluid assumed ideal, vortex shedding, rotational wake, and induced drag would not occur. The implication is that for a real fluid, provided the existence of a thin boundary layer, similarly configured bodies with the same deformation mode shape self-propel without vortex shedding, rotational wake, and induced drag (Vorus (2005)). Only viscous drag effects, due to the existence of the thin boundary layer, are present and unavoidable. The motion mode examined by Vorus (2005) is the little-exploited anguilliform mode exhibited in some aquatic animal swimming; the Anguilla includes the snake, eel, lamprey, and leach, among others. The anguilliform swimming differs from the high-speed carangiform and tunniform fish swimming in that the thrust is produced by more global body motions, rather than by the flapping of the lunate tail of the latter high-speed group.

Researchers have been studying the anguilliform swimming motion for quite some time. Some notable works include that of Wu (1961) and Lighthill (1970), with the "elongated body theory" in the Appendix of Lighthill (1960) being the basis for several recent analyses. Besides the recent works of Vorus (2005) and Vorus and Taravella (2011) directly related to this project, there have been other recent works expanding on the theoretical hydrodynamic analysis of the anguilliform motion such as Carling et al. (1998), Pedley and Hill (1999), and Cheng and Chahine (2001). Key points and results of these analyses are described in more detail in the Literature Survey section to follow.

This theoretical concept of the anguilliform motion is driving the designed and expected capabilities of the experimental robotic eel. Using the assumption of high Reynolds number and a thin boundary layer, Vorus (2005) developed a two-dimensional solution using ideal flow theory for the displacement wave-form which develops zero circulation around the body length over time. This zero circulation results in the absence of shedding a vortex wake and its associated drag. Vorus and Taravella (2011) further developed this theory for three dimensions utilizing slender body theory with this latter work being of interest and expanded upon within.
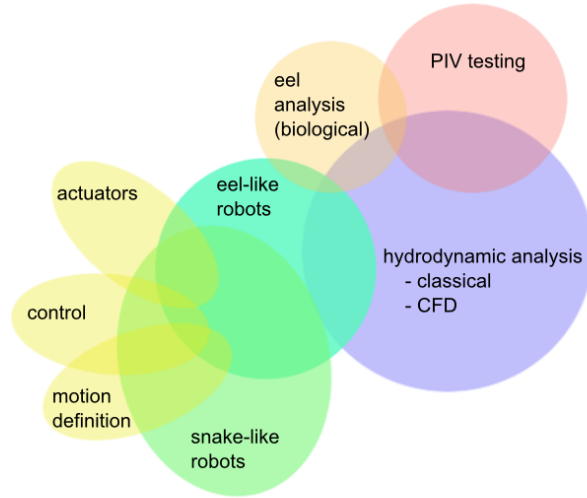
Figure 1.1: Venn diagram showing the different areas of concentration within or related to the field of anguilliform swimming.
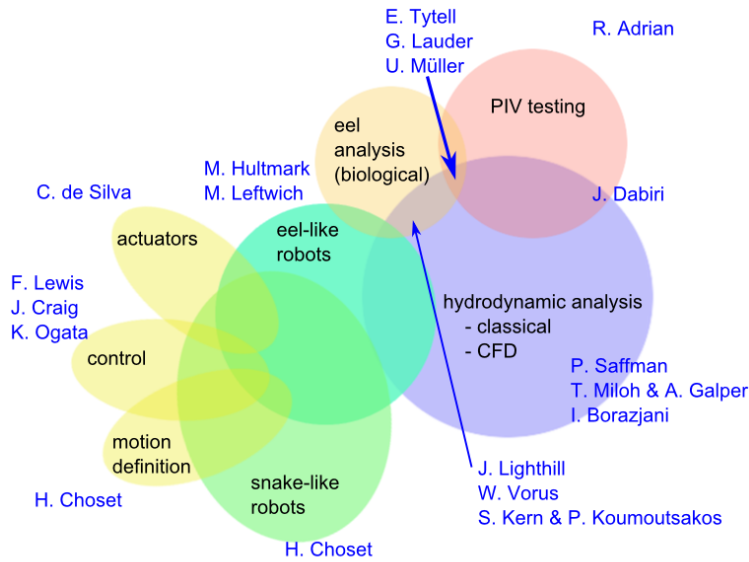
Figure 1.2: Venn diagram showing the different areas of concentration with their associated outstanding researchers. The names shown are by no means exhaustive nor constricting them to their associated area of concentration, i.e. they might (and most likely are to) be working in other areas too.

1.2 Literature Survey

Going back close to a century, several similar and dissimilar studies have preceded this one, shedding light on both carangiform and anguilliform swimming motions ranging from ideal flow theories to PIV testing of live lamprey and anguilla eels to novel numerical techniques that solve the Navier-Stokes equations as applied to these motions. (Carangiform motions will be mentioned briefly throughout the text for comparison, but anguilliform swimming is the sole focus.)

The modern names of anguilliform and carangiform date back to Breder, 1926 (cited in Tytell and Lauder (2004)), but the kinematic distinction between the two have been known for years before that (Marey, 1895 and Alexander, 1983 (cited in Tytell and Lauder (2004)). Distinguishing the kinematic differences between the two was relatively easy; understanding the hydrodynamics of either has been much less understood but studied thoroughly. Some of the first to propose theories on how anguilliform swimming motions can produce thrust include Gray (1933a), Gray (1933b), Taylor (1952), and Lighthill (1960).

With several photographs of eels over a short period of time, Gray (Gray (1933a) and Gray (1933b)) was the first to quantitatively study the body movement of eels and their propulsive mechanism by showing that the body undulations have the form of a backward traveling wave. He determined the now obvious intuition that the longitudinal component of the pressure normal to the eel body is equal to its resistance. Among other things, he determined that the magnitude of the thrust is based on the velocity of the transverse movement of the body and the angle that the mean path of motion makes with the surface of the body while it crosses this line over time. While observing swimming dolphins, Gray is most known for the formulation of his paradox which states that a dolphin swimming at 20 knots cannot have enough muscle to propel itself forward at that speed (Gray (1936)). This paradox has prompted several succeeding researchers to take up the cause and investigate the thrusts of swimming animals, particularly anguilliform eels.

By idealizing an eel as a cylinder immersed in water with waves of constant bending amplitude travelling down it at constant speed, Taylor (1952) found the wave parameters that produce the greatest forward speed for an eel, which are very close to the results of Gray (1933a). He computes the normal component of force on the cylinder using experimentally obtained drag coefficients on a cylinder in an airflow. Using the kinetic theory of gases to account for the viscosity and the 2-D

heat conduction equation as an analog for the tangential stresses, Taylor computes the longitudinal component of force on the cylinder. He then computes the power done on the fluid by the eel for varying parameters to compute the speed at which the eel propels itself at the least energy output.

I am skipping several decades for now and focusing on the last 20 years where more PIV analysis has been done on swimming eels and other fishes; also force estimates from wake measurements.

In the last two decades, several studies have been performed on the wake measurements of swimming fishes (or similarly dynamic, flying animals) using PIV or numerical CFD techniques (Anderson (1996); Müller et al. (1997); Müller et al. (2001); Drucker and Lauder (1999); Nauen and Lauder (2002); Nauen and Lauder, 2002b; Tytell and Lauder (2004); Tytell (2004), (previous articles all cited by Tytell (2004); Borazjani and Sotiropoulos (2009); to name a few). An even fewer number have focused on anguilliform motions: Müller et al. (2001), Borazjani and Sotiropoulos (2009), Kern and Koumoutsakos (2006), Tytell and Lauder (2004), Tytell (2004), Hultmark et al. (2007), Leftwich and Smits (2011), Pedley and Hill (1999), Carling et al. (1998)

Carling et al. (1998) does not predict complex vortical structures and lateral jets. They used a 2-D CFD model to estimate the flow fields behind a self-propelled anguilliform swimmer. Their calculations indicated a single, large vortex ring wrapping around the eel, with the eel in the center, producing upstream flow behind the eel, which has not been verified by any experimental measurements on live eels.

Pedley and Hill (1999) state that the load against which the swimming muscles contract, during the undulatory swmming of a fish, is composed principally of hydrodynamic pressure forces and body inertia. In the past, this has been analyzed through an equation for bending moments for small-amplitude swimming, using Lighthill's elongated-body theory and a vortex-ring panel method to compute the hydrodynamic forces (). They do find that the wake morphology resembles that of a reverse von Karman vortex street, which is not the 2P wake structure found by the majority of other authors.

Müller et al. (2001) found that the anguilliform wake structure is 2P and was the first to experimentally measure the wake structure of eels using PIV techniques.

As the title states, Müller et al. (2001) hypothesize that undulatory swimmers generate thrust by passing a transverse wave down the body. This thrust is generated not just at the tail, but also to a varying degree by the body, depending on the fish's morphology and swimming movements.

They investigate the interaction between body movements and the flow around swimming eels using 2-D PIV. The wake behind eels swimming at 1.5 L/s consisted of a double row of vortices with little backward momentum (NEELBOT-1.1 swims at 0.185 L/s for the nominal design speed, for comparison). The eel sheds two vortices per half tail-beat, which can be identified by their shedding dynamics as a start-stop vortex of the tail and a vortex shed when the body-generated flows reach the 'trailing edge' and cause separation. Two consecutively shed ipsilateral body and tail vortices combine to form a vortex pair that moves away from the mean path of motion. This wake shape resembles flow patterns described previously for a propulsive mode in which neither swimming efficiency nor thrust is maximized but sideways forces are high. The described wake shape is illustrated in B of Fig **??**. It has since been found by later researchers that most of the thrust occurs near the end of the tail, correcting these findings that the entire body produces some form of thrust.

Tytell and Lauder (2004) performed PIV measurement techniques on live American eels swimming steadily at 1.4 L/s to quantify the wake structure, measure the swimming efficiency, and force and power output. They also provide the first quantitative comparison of the predictions of EBT (Lighthill (1971)) to empirical forces estimated using the PIV and demonstrate a partial correlation. Tytell and Lauder (2004) found that the anguilliform wake structure is 2P. Tytell and Lauder (2004) suggest that when the tail starts to move after changing direction, a low pressure region is created that sucks fluid laterally. When this fluid is shed from the tail, it stretches the 1st vortex and creates a new, same-sign vortex. They found that the lateral jets are noticeably large and in an absence of overall downstream flow. The authors infer that the lack of downstream flow results from a spatial and temporal balance of momentum removal (drag) and thrust generated along the body, due to the relatively uniform shape of eels. Previously, the wake of swimming eels was hypothesized to consist of unlinked vortex rings, resulting from a phase offset between vorticity distributed along the body and vorticity shed at the tail (Müller et al. (2001)). The impulse of the assumed small-core vortex ring was estimated using the formula of Faber, 1995 (compare this formula to Spedding et al. (1984), Birch and Dickinson, and others). The mean force that produced the ring was also estimated by dividing the impulse by half the tail beat period. Force, impulse, and power were all normalized to produce coefficients as suggested by Schultz and Webb (2002). The authors did notice a positive momentum flux downstream of the eels which contradicts the

idea that the thrust and drag cancel out for steady-state swimming, producing a control volume of zero momentum. They attribute the increase to the movement of the eel's snout. They go on to state that while thrust cannot be measured directly from the wake of swimming eels, it is still useful, conceptually to separate it from drag. By using a mathematical model, such as EBT or more complex CFD models (Carling et al. (1998); Wolfgang et al. (1999); Zhu et al., 2002), thrust can be estimated and used to calculate a Froude propulsive efficiency. They estimate the efficiency using their measured wake power to be between 0.43 and 0.54. Using EBT, they estimate the efficiency to be 0.87.

As a follow-up to his previous paper, Tytell and Lauder (2004) again investigates the hydrodynamics of eel swimming using PIV but this time applied to the effect of swimming speed. After investigating American eels, *Anguilla rostrata*, at swimming speeds ranging from 0.5 to 2.0 Ls^{-1} (compared to a nominal speed of 0.19 Ls^{-1} for NEELBOT-1.1. He estimates the lateral impulse in the wake assuming that the flow field represents a slice through small core vortex rings and is shown to be significantly larger than forces estimated from the kinematics via elongated body theory and via quasi-steady resistive drag forces. These simple kinematic models predict only 50% of the measured wake impulse, indicating that unsteady effects are important in undulatory force production. EBT does, however, corectly predict both the magnitude and time course of the power shed into the wake. At all speeds, the wake contains almost entirely of lateral jets of fluid in a 2P wake structure (as described in the previous paper, Tytell and Lauder (2004) and first found by Müller et al. (2001), using the nomenclature of Williamson and Roshko (1988)), separated by an unstable shear layer that rapidly breaks down into two vortices. The vortices on either side of the lateral jet appear to be part of a small core vortex ring (also found in Müller et al. (2001). The cost of producing the wake, one component of the total cost of transport, was found to increase with swimming speed to the 1.48 power. Tytell (2004) states that the Strouhal number has been shown to be strongly indicative of the force production and efficiency of flapping foils (Read et al., 2003) and may have a similar importance for undulatory locomotion (this is later confirmed by Borazjani and Sotiropoulos (2009), stating that thrust production is mostly a function of Strouhal number). The author estimated force, power, and impulse from both the kinematics and the flow field. Large amplitude EBT (Lighthill (1971)) was used to estimate thrust and lateral forces and power required to produce the wake from the kinematics. Resistive forces were calculated by summing the quasi-

steady drag forces normal and tangential to the body midline using the kinematics, in a similar way to Jordan, 1992. The normal and tangential drag coefficients were estimated according to empirical descriptions of turbulent flow normal to a cylinder (Taylor (1952); Hoerner, 1965) and parallel to a flat plate (Hoerner, 1965). Wake power was not calculated from the resistive model because it does not explicitly account for how power is shed into the wake. Vortex ring impulse and force were estimated (compare his method here to that of others such as Spedding et al. (1984) and Dabiri (2005)?). Impulse generated at the tail tip was also estimated from the first moment of vorticity (Birch and Dickinson, 2003), averaged over half a tail beat, with the force being estimated by taking the time derivative. The power required to produce the wake was determined by integrating the kinetic energy flux through a CV strip downstream of the eel. Additionally, a lateral power was estimated by assuming the small and relatively noisy axial component of velocity was zero and integrating only the lateral velocity contribution to the kinetic energy flux. The cost of producing the wake was estimated by dividing the wake power by the swimming speed. This cost is one component of the total mechanical cost of transport, which also includes the thrust power and the inertial power required to undulate the body. Tytell (2004) found the Strouhal number to stay approximately constant at 0.324 ± 0.003, and that the amplitude grows slightly with higher swimming speed (as contrasted with Borazjani and Sotiropoulos (2009) and Vorus and Taravella (2011)). However, he does state that tail tip velocity seems to be the kinematic parameter that most affects the flow in the wake. He did find that eels maintain a constant Strouhal number within a single swimming speed by varying tail beat frequency inversely with amplitude. While Froude propulsive efficiency would be useful to estimate, it requires a measurement of thrust, which cannot be estimated due to the lack of axial flow in the wake. However, changes in the cost of producing the wake, one component of the total cost of transport, may indicate trends in propulsive efficiency. At all speeds except the highest, an eel's tail functions like a vortex ring generator (Shariff and Leonard, 1992), adding circulation to the fluid at a rate proportional to its velocity squared.

Kern and Koumoutsakos (2006) investigated the hydrodynamics of anguilliform swimming motions using three-dimensional simulations of the fluid flow past a self-propelled body. In their analysis, they did not specify the motion of the motion *a priori* but obtained it through an evolutionary algorithm used to optimize swimming efficiency and the burst swimming speed. They found for efficient swimming that the whole body undulates laterally with a slightly increasing am-

plitude towards the tail. Most of the thrust production was found to occur at the tail, countering Müller et al. (2001)'s findings. The wake was found to consist of a double row of vortex rings with an axis aligned with the swimming direction and that these vortex rings were responsible for producing lateral jets of fluid, which has also been documented in Tytell and Lauder (2004) and Tytell (2004).

Similarly found by Tytell and Lauder (2004) and Müller et al. (2001), Hultmark et al. (2007) shows that the wake is characterized by a 2P wake structure (according to the nomenclature of Williamson and Roshko (1988)) with 2 same sign vortices being shed each tail beat cycle. The motion of the robot is based on the motion equation empirically found by Tytell and Lauder (2004) and is programmed into a robot very similar to that of NEELBOT-1.1 with the wake being measured by a PIV system. Compared to a lamprey's typical Strouhal number range of 0.3-0.35, the authors' robotic lamprey undulates at a range of 0.6-0.65. The authors attribute this larger range to a higher drag on the robot, so that the robot tail beat frequency needs to be higher to develop a larger thrust required to balance the increased drag. They also note that the wake spreads more quickly relative to the results of Tytell and Lauder (2004), probably because of the higher Strouhal number. Their robot operated at a Reynolds number of approximately 1.15×10^5. To estimate the direction of the resultant force on the robot as a function of St, the authors integrated the momentum flux over a control volume bound by the half wake of the robot, with out of plane motions neglected. The results were summed for an entire cycle to find the time-averaged force direction. At higher Strouhal numbers (coinciding with a slower swimming speed), the wake was found to be wider than in steady swimming because the convective velocity of the vortices were lower while their induced velocity is not as reduced as much, which is the same behavior found in Buchholz and Smits (2006). The authors concluded that when thrust exceeded drag, the induced jet has a streamwise component and that the velocity and vorticity fields along the body suggest that net thrust production occurs primarily at the tail (also confirmed by Leftwich and Smits (2011)), which was supported by estimates of the resultant force using a CV approach. However, the authors go on to say that this CV approach showed that some thrust is produced by the posterior of the body, it is almost balanced by the local drag contribution (which then makes it a momentum-less wake, which is hard to calculate the resultant force from using CV approached as noted by Tytell (2007) and Sirviente and Patel (2000).

Similar to the 2P wakes found in Hultmark et al. (2007), Tytell and Lauder (2004), and Müller et al. (2001), Borazjani and Sotiropoulos (2009) used a customized numerical scheme to compute the hydrodynamics of anguilliform swimming in the transitional and inertial flow regimes. They call their CFD method an "immersed boundary method" and vary the St and Re numbers, but kinematically, their motion is slightly different than that of the NEELBOT-1.1's in that they allow the head to move laterally. They found that the net mean force to be mainly dependent on the tail-beat frequency rather than the tail-beat amplitude, which is also the case for the theory developed by Vorus and Taravella (2011) in that the higher speeds require a smaller tail amplitude. The critical Strouhal number, $St*$, at which the net mean force becomes zero is a decreasing function of Re and approaches the range of St numbers at which most anguilliform swimmers swim in nature ($St = 0.45$ according to these authors, contrasted with $St = 0.3 - 0.35$ according to others such as Leftwich and Smits (2011), Hultmark et al. (2007), Tytell and Lauder (2004)). They find that the propulsive efficiency of anguilliform swimmers at $St*$ is not an increasing function of Re but instead is maximized in the transitional turbulence regime. They show that the form drag decreases while viscous drag increases as St increases. Their simulations reinforce their previous studies (Borazjani and Sotiropoulos (2008)) that the 3-D wake structure depends primarily on the Strouhal number. They separate the hydrodynamic thrust and drag contributions according to a force decomposition approach proposed by Borazjani and Sotiropoulos (2008). For all simulated St, the axial force coefficient in each cycle exhibits two peaks corresponding to the forward and backward tail strokes, which is also seen in Müller et al. (2001) and Vorus and Taravella (2011). For a specific Reynolds number and for the Strouhal number in the range from 0.3 until the critical Strouhal number, the undulations of the body cause a net force also of drag type but of lower magnitude than the corresponding rigid body net force. The authors determine that the anguilliform swimming efficiency is maximized in the transitional regime (i.e. for $Re = 4000$). They attribute the decrease in Froude efficiency for the anguilliform swimmer in the inviscid environment since they say that angulliform swimmers propel themselves as an undulatory pump, i.e. each part of the body generates thrust by accelerating the adjacent fluid. In the inviscid environment, accelerating the adjacent fluid by viscous forces is not possible, and as such the net thrust force is reduced. The authors determine that the observed reduction in form drag for anguilliform swimming is that separation along the body is effectively eliminated due to the undulatory motion.

The authors show illustrations of four wake cases for varying Re and St numbers, pointing out that three are drag-type and the fourth is thrust-like. For two of the drag-type cases, the net flux of the 3-D wake rebuts the original claim and proves that they are in fact thrust-type. Along with the claim by Dabiri (2005), this underscores the difficulty in assessing the wake type from velocity measurements at 2-D planes. Their results confirm that for a fixed Reynolds number, both single- and double-row wake structures can emerge depending on the St number, which is to be expected since the Strouhal number can be viewed as the ratio of the mean lateral tail velocity to the axial swimming velocity. The authors visualize the 3-D structure of anguilliform wakes by plotting instantaneous iso-surfaces of the q-criterion (Hunt et al., 1988). For low St, a single row pattern emerges while at higher St, the double-row structure is observed. For the $Re = 4000$ case, the structure observed is very similar to that obtained in the pitching panel experiments by Buchholz and Smits (2006).

Leftwich and Smits (2011) uses PIV results from Hultmark et al. (2007) and a robot very similar to NEELBOT-1.1 but with a passive tail to investigate the formation of the wake structure, the shedding vorticity from the body, and the relationship between thrust production and pressure on the surface of the robot. Their results indicate that thrust is produced mainly at the tail and that the phase relationship between pressure signal and vortex shedding show a clear connection between the location of vortex structures and the fluctuations of the pressure signal. The authors contradict the results of Müller et al. (2001) by saying that Hultmark et al. (2007) observed that body undulations are not contributing to the thrust production. Another study contradicts Müller et al. (2001)'s finding of body undulation creating thrust. This shows that the understanding of propulsive forces from anguilliform swimming wake morphology is still very much in progress. Leftwich and Smits (2011) shows that the pressure along the robot decreases considerably faster than the lateral velocity squared, indicating that a lift/drag method of calculating the forces on the swimming body would not accurately capture the thrust production. The authors state there is no large concentration of vorticity passing the pressure port when the pressure is high; however, they say there is a strong vorticity concentration passing over the port when the pressure is low. It is unclear where exactly the pressure port is on the robot, except for their longitudinal location (if they are on top, the results of this location would not coincide with the results from the PIV because the PIV is in the medial plane of the robot). These low pressure/strong vorticity situations
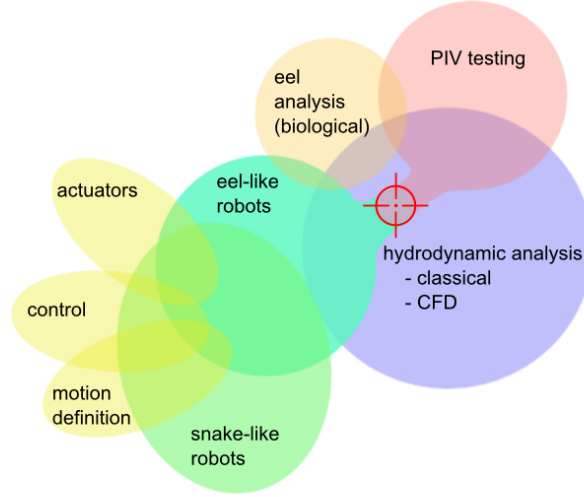
Figure 1.3: Venn diagram showing the different areas of concentration within or related to the field of anguilliform swimming, with the additional overlap amongst the PIV testing, eel-like robots, and hydrodynamic analysis. The red crosshair denotes the additional overlap which is the target contribution of this dissertation research.

may be attributed to separation as noted by Sarpkaya (). The authors compute the instantaneous momentum flux in the streamwise direction over an entire cycle using the integral form of the momentum equation . The authors find that there is a 27% difference in their mean thrust compared to the slender body theory of Lighthill (1960), noting that their method is only 2-D and that of Lighthill is 3-D. The authors concluded that pressure increased rapidly closer to the tail, indicating thrust production occurs closer to the tail. They show that the pressure signal correlates to the fluid structures passing the port, indicating that the organization of the vorticity in the boundary layer is directly linked to the unsteady thrust force produced by an anguilliform swimmer.

1.3   Current Research and Contributions to the Field

As explained in the previous section on the Literature Survey (Section 1.2, the past research can be organized into a couple of different but overlapping areas of concentration. This current research falls into an area of overlap that hasn't been investigated before, to the best of our knowledge. Figure 1.3 shows a Venn diagram similar to the previous one but with an added intersection, denoted by the red crosshair, showing where and how the current research contributes to the field,
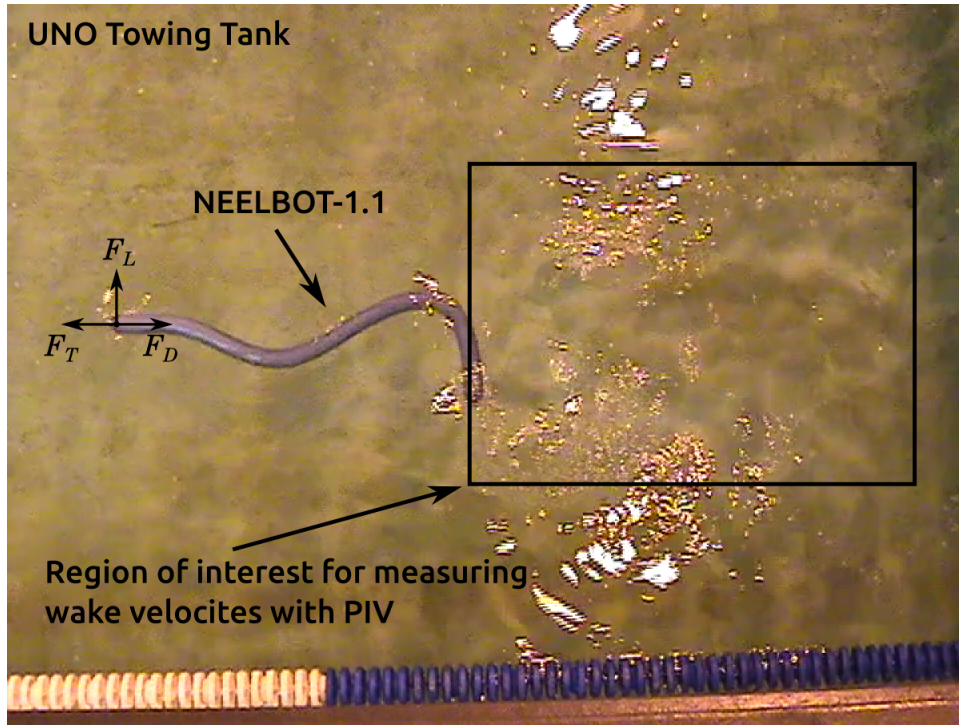
Figure 1.4: Region of interest for measuring fluid flow velocities using PIV techniques.

by combining the PIV testing of an anguilliform robot and a classical hydrodynamic analysis to compare and contrast the experimental and theoretical results. With that being said, the work of Hultmark et al. (2007) and Leftwich and Smits (2011) is very similar in that it investigates a robot with downstream PIV measurements, but it does not contribute a theoretical hydrodynamic analysis to support or disprove their measurements.

This research encompasses developing and building an anguilliform swimming robot to replicate the desired motion predicted by a classical hydrodynamic analysis. Particle Image Velocimetry (PIV) equipment then measured the wake field velocities produced by the robot, and these results were compared to the predicted hydrodynamics. Figure 1.4 shows the final robot prototype, NEELBOT-1.1, swimming on the free surface of the Towing Tank of UNO (University of New Orleans) and a schematic showing the interested wake region behind it. Several assumptions are taken with both the theory and the experiment, but the evidence is still conclusive enough to draw comparisons between the two. Simply, slender-body theory is a very good tool used to predict the propulsion and hydrodynamics of this type of marine vehicle.

Additionally, most of the other similar research encompasses swimming animals that produce

16

thrust by first-order lifting processes. The motion explained within is theorized to produce thrust via the reactive forces of accelerated added mass along the length of the robot. This process results in zero induced drag and zero shedding of vortices. The testing results presented within show that this type of propulsion is still possible, despite very few previous research affirming the same.

While the research explained in detail within is very comprehensive and exhaustive, there are still some aspects of the project that need additional consideration due to more time or funding needed. Additionally, there were several lessons learned over the course of the project, especially in areas that were relatively unfamiliar to the researchers at the onset of the project. All three aspects of the research can be investigated or improved upon in more detail, and ideas for this additional work are listed in Section 5.1 of the Conclusions chapter.

CHAPTER II

Theoretical Development

This chapter provides an explanation of the two- (Section 2.1.1) and three-dimensional (Section 2.1.2) derivations of the highly efficient anguilliform swimming motion using the assumptions of ideal flow theory applied to slender bodies, which produce the so-called ideal anguilliform swimming theory. Extensions are made to the original 3-D derivation in order to apply the theory to a non-ideal shape, or rather, an off-design recorded motion of the actual robot (Section 2.2.2).

2.1 Ideal Anguilliform Swimming Theory

The dominant feature of the ideal swimming theory is the constraint that the circulation is continuously zero about the shape for all time, which produces the resulting condition of no shed vortices and no induced drag — "wakeless swimming." The 2-D and 3-D formulations differ in how the physical shape of the anguilliform eel is modeled in the flow. The 2-D one is represented by vortices, whereas the 3-D uses doublets. The singularities for each case are constrained to the x-axis.

2.1.1 2-D Formulation

The following gives a brief overview of the two-dimensional theory derived in Vorus (2005) that predicts a displacement wave-form for continuously zero circulation over the body length with time, thereby avoiding the shedding of a vortex wake and its induced drag. The thrust is reactive, via acceleration processes, rather than inductive via relative velocity and lift. The analysis assumes high Reynolds number and a thin boundary layer, which allows for the use of ideal-flow theory.

18
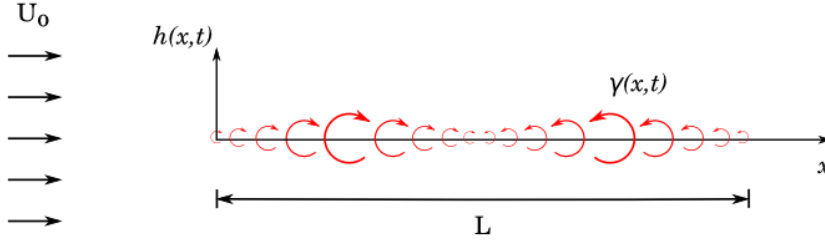
Figure 2.1: Simplified schematic showing how the vortex distribution models the anguilliform shape in a uniform flow for one instance in time. The centers of the 2-D vortices are constrained to the x-axis with the flow past vortex distribution (vortices are not to scale). The net circulation of this distribution is specified as 0 for all time t, while the magnitude and direction of the vortex distribution changes over time and space. The displacement distribution, $h(x,t)$, is to be solved for based on these initial and boundary conditions.

The general oscillatory displacement form of the anguilliform motion is specified as

$$h(x,t) = \Re\{H(x)e^{-i\omega t}\} \tag{2.1}$$

where $h(x,t)$ is the transverse displacement of the shape function as shown in Figure 2.4. A particular and non-trivial solution to this equation is shown to be derived in Vorus (2005), and a brief overview is given here.

After deriving a trivial motion that produces no fluid disturbance at all, Vorus (2005) specifies the velocity term on the right-hand side of the linearized slender-body theory equation as the Biot-Savart law in terms of an axis vortex distribution:

$$h_t(x,t) + U_o h_x(x,t) = \frac{1}{2\pi} \int_0^L \frac{\gamma(\xi,t)}{x-\xi} d\xi \tag{2.2}$$

where ξ is the coordinate in the x-direction on the $y = 0$ axis and is used to distinguish from the general x coordinate. In typical lifting wing vortex-sheet theory, this integral equation is to be inverted for the vortex strength, $\gamma(\xi,t)$. However, for this application, equation 2.2 assumes explicitly that no net vorticity is left in the downstream wake of the element. It is consistent with minimum work, since the wake-induced drag is zero. The value $h(x,t)$ is the unknown function to be determined in achieving the condition of no wake (Vorus (2005)).

An additional condition is required on $\gamma(\xi, t)$ in that "wakeless" motion requires that the time rate-of-change of element circulation remain continuously zero. That is, the net circulation of the element, as represented by the integral of γ over the element length, must be zero at all time. This necessary constraint is accomplished with γ specified as periodic in both space and time, with body length L now being some multiple m of the fundamental spatial wave length of the vortex distribution, L/m. Figure 2.1 shows a simplified schematic of the vortex distribution along the x-axis modeling the unknown anguilliform shape, $h(x, t)$, in a uniform flow.

The vortex distribution is specified as a traveling wave of length L and frequency ω; the wave length of $h(x, t)$ is defined as λ, which is equal to L only for the trivial case. The form of the prescribed vortex distribution is therefore:

$$\gamma(x, t) = \Gamma(x) \cos\left(\frac{2\pi x}{L} - \omega t\right) = \Re\left[\Gamma(x)e^{i\left(\frac{2\pi x}{L} - \omega t\right)}\right] \tag{2.3}$$

The amplitude $\Gamma(x)$ is taken as real but, at this point, as unspecified.

The following non-dimensionalization's are used by using the nominal length, L, and wave displacement speed, V (r_o is the radius of the circular cross section):

$$\bar{r}_o = \frac{r_o}{L} \qquad\qquad \bar{h}(\bar{x}, \bar{t}) = \frac{h(x, t)}{L}$$

$$\bar{x} = \frac{x}{L} \qquad\qquad \bar{t} = \frac{Vt}{L}$$

Substituting in the non-dimensionalization's but dropping the overbars for clarity, the equation above becomes

$$\gamma(x, t) = \Re\left\{\Gamma(x)e^{2\pi i(x-t)}\right\} \tag{2.4}$$

In addition to satisfying the condition that the integral of $\gamma(x, t)$ over the length L be identically zero at all t, the vortex distribution must satisfy the "shockless entry" condition $\gamma(0, t) = 0$ at the leading edge, as well as the "Kutta" condition $\gamma(1, t) = 0$ at the trailing edge. These three conditions are all appropriately satisfied by interpreting $\Gamma(x)$ as the generalized function:

$$\Gamma(x) = \Gamma\left[H_e(x) - H_e(x - L)\right] \tag{2.5}$$

where the Heaviside step function, $H_e(X)$, is defined as (Lighthill (1964)):

$$H_e(X) = \begin{cases} 0 & \text{if } X < 0 \\ 1 & \text{if } X \geq 0 \end{cases} \tag{2.6}$$

Multiplication of this generalized function with the traveling wave exponential in equation 2.4 achieves the continuously zero-lift requirement. This box idealization is a valid theoretical approximation of the edge conditions at this level of analysis, as $\gamma(x,t)$ by 2.4 is involved only in integration at 2.2, and never in differentiation.

Substitution of 2.4 into 2.2 gives the following first-order linear differential equation for $H(x)$:

$$H_x(x) - \frac{2\pi i}{U}H_t(x) = \frac{\Gamma}{U}\Lambda(x) \tag{2.7}$$

with

$$\Lambda(x) \equiv \frac{1}{2\pi}\int_0^1 \frac{e^{2\pi i\xi}}{x-\xi}d\xi \tag{2.8}$$

The solution of this differential equation is

$$H(x) = e^{\frac{2\pi i x}{U}}\left(H(0) + \frac{\Gamma}{U}\int_0^x e^{-\frac{2\pi i}{U}\xi}\Lambda(\xi)d\xi\right) \tag{2.9}$$

The term $H(0)$ is the leading-edge displacement amplitude. The product of the leading factor and the $H(0)$ term in the brackets represent a sinusoidal wave in x, the amplitude of which is modified over the length of the element, $0 \leq x \leq 1$, by the second term. The dimensional wave length, λ, of the function is established by the leading factor in 2.9. This dimensional wave length is

$$\lambda = L\frac{U_o}{V} \tag{2.10}$$

and the time period, $T = L/V$, creates the following equation

$$T = \frac{L}{V} = \frac{\lambda}{U_o} \tag{2.11}$$

The above equality can be stated as "the time required for the strip to advance one wavelength λ

at strip speed U_o is the same as the time required for the wave to advance one strip length L at wave speed V." Reorganizing, it becomes

$$\frac{\lambda}{L} = \frac{U_o}{V} \tag{2.12}$$

and this states that "the wavelength ratio is equal to the advance ratio for wakeless swimming to occur." When both sides of this equality are unity, this becomes the trivial case. For other cases when this equality is true, this is the kinematic condition where non-zero axial load is developed but with necessarily unity ideal efficiency because vortex shedding does not occur.

Returning to the displacement amplitude distribution of equation 2.9, $H(0)$ and Γ are the unknown parameters to be found, assuming the advance ratio U is specified. The head amplitude can be eliminated in terms of the total mean thrust coefficient, C_T. Prior to this, a force consideration of the articulating anguilliform shape can be performed via a momentum integral analysis to obtain the thrust coefficient:

$$C_T(t) = 2(1 - U) \int_0^1 \gamma(x,t) h_x(x,t) dx \tag{2.13}$$

Substitute equations 2.1 and 2.4 to obtain

$$C_T(t) = \Gamma(1 - U)\Re \left\{ \int_0^1 H_x(x) e^{-2\pi i x} dx + e^{-4\pi i t} \int_0^1 H_x(x) e^{2\pi i x} dx \right\} \tag{2.14}$$

Using the derivation by Vorus (2005) of $C_P(t) = U C_T(t)$ in the above, the head amplitude can be eliminated in terms of the total mean thrust coefficient:

$$C_T = \frac{C_P}{U} = 2\pi \frac{\Gamma}{U}(1 - U)\Re \left\{ i \int_0^1 H(x) e^{-2\pi i x} dx \right\} \tag{2.15}$$

With another definition of C_P:

$$C_P(t) = \int_0^1 C_p(x,t) h_t(x,t) dx \tag{2.16}$$

and substituting equation 2.9 into 2.15, one obtains after reorganizing:

$$H(0) = \frac{1}{e^{2\pi i \frac{1-U}{U}} - 1} \left[\frac{C_T}{\Gamma} - 2\pi i \frac{1-U}{U} \int_0^1 e^{2\pi i \left(\frac{1-U}{U}\right) x} \Delta H(x) dx \right] \tag{2.17}$$

22

with

$$\Delta H(x) \equiv \frac{\Gamma}{U} \int_0^x e^{-\frac{2\pi i \xi}{U}} \Lambda(\xi) d\xi \tag{2.18}$$

The formulas 2.9, 2.17, and 2.18 give the element displacement amplitude in terms of the single unknown parameter Γ, when U and C_T are assumed to be specified. Γ must be evaluated to proceed further with the analysis, but Γ is not a physically controllable variable, so that some closure condition is needed for uniqueness of the solution. Vorus (2005) uses a "minimum displacement" criterion, which determines Γ to minimize the maximum of the modulus of $H(x)$ for specified C_T and U:

$$\Gamma = \Gamma \left[\min(\bmod H(x)_{\max}); C_T, U \right] \tag{2.19}$$

This condition states that of the family of displacements that give no wake and 100% ideal efficiency, the animal selects the one that requires the minimum maximum displacement. Figure 2 in Vorus (2005) is a plot of this formula versus U.

In the scenario studied in Vorus (2005), there are 2 practical points along the axis of U values where $H(x)_{\max}$ is minimized: a supercritical condition at $U > 1$ and a subcritical for $U < 1$. The first is noted for it not being intuitive yet possible in terms of propulsion. The second is the one of more typical interest because of its similarity to that of serpentine animals seen in nature, in addition to its propulsive capabilities.

Linear time-domain analysis Vorus (2005) performs a linear time-domain analysis to check the preceding steady-state frequency-domain solution and to provide a more general model for other cases such as a transient analysis or off-design speeds. The linearized boundary condition now includes a shed vortex wake of strength γ_w:

$$h_t(x,t) + U(t)h_x(x,t) = \frac{1}{2\pi} \int_0^1 \frac{\gamma(\xi,t)}{x-\xi} d\xi + \frac{1}{2\pi} \int_1^{l(t)} \frac{\gamma_w(\xi,t)}{x-\xi} d\xi \tag{2.20}$$

The shed vortex wake spans downstream from the anguilliform shape's trailing edge element $(x = 1)$ to $l(t)$, with this increasing in time as

$$l(t) = \int_0^\tau U(\tau)d\tau \tag{2.21}$$
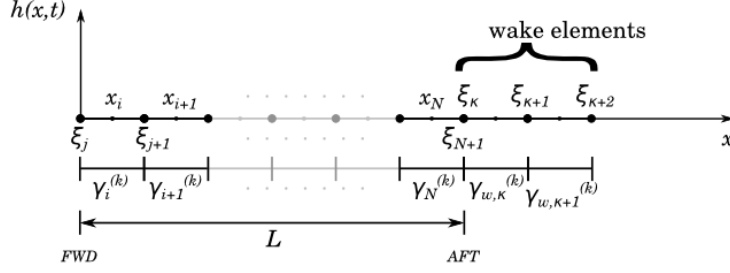
Figure 2.2: Anguilliform element and wake geometry with associated variable naming.

For this formulation, the vortex distribution is considered as the unknown, to be determined by inverting equation 2.20 numerically, for specified $h(x,t)$ as predicted by the foregoing steady-state solution. The right-hand-side of equation 2.20 is discretized as a line of point vortices, with each at segments' ends. This generates N algebraic equations, for the number of segments generated over time, in terms of $N+1$ unknown vortices. The additional relation, based on Kelvin's Theorem, is that the net total circulation at any time remain continuously at the initial value of zero.

This method is explained in more detail in the 3-D case in Section 2.2.2, but an overview of the equations are given here. Equation 2.20 can be discretized as

$$h_{t,i}^{(k)} + U^{(k)} h_{x,i}^{(k)} = \sum_{j=1}^{N+1} \frac{1}{2\pi} \frac{\gamma_j^{(k)}}{x_i - \xi_j} + \sum_{\kappa=0}^{k} \frac{1}{2\pi} \frac{\gamma_{w,\kappa}^{(k)}}{x_i - \xi_\kappa} \qquad i = 1, \ldots, N; k = 0, 1, \ldots \qquad (2.22)$$

where the i and j indices represent the anguilliform element's mid- and endpoints, respectively. The term $\gamma_{w,\kappa}$ denotes the discretized vortex distribution of the wake elements, with κ signifying the physical locations of the wake element endpoints. The number of wake elements grows at the same rate and is equal to the number of time steps, k. Figure 2.2 shows the anguilliform and its wake element geometry with its associated variables. This formula produces a linear system consisting of N equations with $N+1$ unknowns for each time step k. The unknowns are the discretized vortex distribution values $\gamma_j^{(k)}$ at each element endpoint. The $N+1^{\text{th}}$ condition to make the solving of the system possible is the fact that the circulation—the summation of the vortex distribution—is continuously zero for each time step:

$$\sum_{j=1}^{N+1} \gamma_j^{(k)} + \sum_{\kappa=0}^{(k)} \gamma_{w,\kappa}^{(k)} = 0 \qquad (2.23)$$

The initial value of the vortex distribution for the first wake element is $\gamma_{w,0}^{(0)} = 0$. This solution method is different from before—where the vortex distribution was prescribed as a periodic function over the body length—in that the vortex distribution is now the unknown for the already prescribed steady-state motion of $h(x,t)$.

The solutions to these equations are used to calculate the force coefficient

$$C_F(t) = C_T(t)\hat{i} + C_L(t)\hat{j} = \left[2(1-U)\int_0^1 \gamma h_x dx\right]\hat{i} - \left[2\int_0^1 \gamma dx\right]\hat{j} \tag{2.24}$$

Vorus (2005) plots the thrust and lift coefficients of this equation versus time with a slowly increasing value for U. In the vicinity of $U = 0.75$, the design steady-state condition of continuously zero lift (circulation) and non-zero thrust is approximately achieved, which can be seen in Figure 4 of Vorus (2005).

Non-linear steady-state analysis   Up to this point, linearized slender body theory has been assumed with acceptable results showing low-speed, small-thrust, and large-amplitude motion ($\approx$ 20% of body length). This large amplitude is not in agreement of the small angle assumption used in the derivation of slender-body theory, so an analysis using non-linear boundary conditions was performed by Vorus (2005), using the linear solution as the first approximation to the iterative scheme used. The iterative scheme is defined as

$$h_t^{(i)}(x,t) + \left\{U + u\left[x, h^{(i-1)}(x,t),t\right]\right\}h_x^{(i)}(x,t) = v\left[x, h^{(i-1)}(x,t),t\right] \quad \text{on } y = h^{(i-1)}(x,t) \quad (2.25)$$

where the superscript (i) denotes the ith iteration of the element displacement distribution $h(x,t)$, with $h^{(i-1)}(x,t)$ known from the previous iteration, starting with the linear solution. This equation is still a linear partial differentiation equation in terms of its known coefficients and application domain $y = h^{(i-1)}(x,t)$. Fortunately, it can be reduced to an ordinary differential equation using Fourier decomposition in time for $U(x,t)$, $v(x,t)$, and $h(x,t)$. For brevity, only $h(x,t)$ is shown here:

$$h(x,t) = \Re \sum_0^\infty H_m(x)e^{-2\pi imt} \tag{2.26}$$

25

and the solution is shown to be

$$H_m^{(i)}(x) = \frac{1}{p_m^{(i)}(x)} \left[H_m^{(i)}(0) + \int_0^x p_m^{(i)}(\xi) R_m^{(i)}(\xi) d\xi \right] \tag{2.27}$$

with $p_m^{(i)}(x)$ being an integrating factor and $H_m^{(i)}(0)$ being determined from the first iteration solution.

Figure 5 in Vorus (2005) shows three timesteps of the solution computed from 8 harmonics (m) and 5 iterations, compared to the original linearized solution. As one can see, the displacement difference between the two solutions is almost unnoticeable, with the larger displacements toward the tail, reaching a maximum percent difference of approximately 5% between the two solutions. The effect of the non-linearity is in the shape changes from the sinusoidal periodic case, and not in the magnitude of the motion itself. Due to the small differences between the two solutions, the linear solution method of using linearized slender body theory is deemed sufficient, and thus the non-linear case is not used but its contribution to the solution difference is acknowledged.

2.1.2   3-D Formulation

The following gives a brief overview of the formulation of the three-dimensional theory for the derivation of the anguilliform swimming as given in more detail in Vorus and Taravella (2011). The authors derive the equation for the ideal anguilliform swimming motion to be

$$\bar{h}(\bar{x}, \bar{t}) = \Gamma \left[\sin \left(2\pi \left(\frac{\bar{x}}{U} - \bar{t} \right) \right) - \sin \left(2\pi \left(\bar{x} - \bar{t} \right) \right) \right]$$

which is plotted in Figure 2.6 for specific parameters, which will be explained in more detail below. This formulation is based on slender-body theory as derived by Lighthill (1960), which applies to low-aspect ratio bodies where the cross-sectional dimensions are small relative to length. Slender-body theory still employs two-dimensional hydrodynamics but in cross-sectional planes normal to the longitudinal axis, as opposed to planes parallel to the axial direction. The solution development follows the same general steps as the preceding 2-D analysis, which is explained in detail in Vorus (2005).

A circular cross-section is used for convenience of the development as shown in Figure 2.3. The
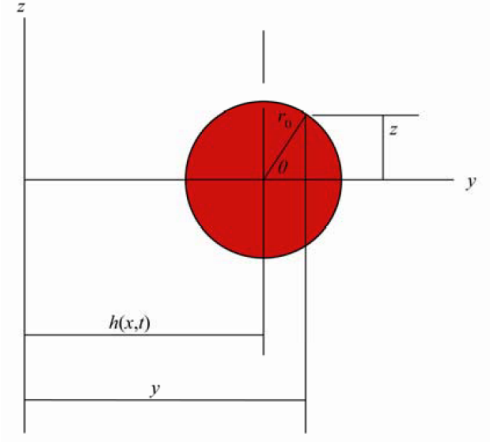
Figure 2.3: Coordinates of the body cross-section.
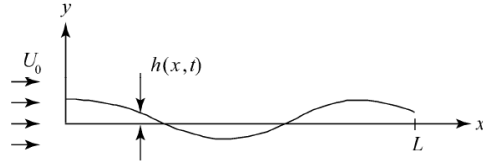
Figure 2.4: Coordinate description of generalized oscillating strip, modeling the anguilliform motion.

surface function is defined as

$$F(x, y, z) = -y + h(x, t) + \sqrt{\bar{r}_o{}^2 - z^2} \qquad (2.28)$$

which is the boundary condition for the oscillating strip as in Figure 2.4

With velocity vector $\mathbf{V} = (U_o + u)\hat{\mathbf{i}} + v\hat{\mathbf{j}} + w\hat{\mathbf{k}}$, the substantial derivative of F gives the same linearized boundary condition as in the previous development but now on a cylindrical surface (in the correct context, subscripts denote the variable to which partial differentiation is taken):

$$h_t(x, t) + U_o h_x(x, t) = v(x, t) \qquad on \ \ r = r_o; \ \ 0 \le x \le L \qquad (2.29)$$

From typical ideal flow theory, the 2-D perturbation potential for the circular section with velocity v in y is

$$\phi(x, r, \theta, t) = -\frac{v(x, t)r_o{}^2 \cos\theta}{r} \qquad (2.30)$$

27

Equation 2.30 is based on the assumption that no stream-wise vortex shedding occurs in the sectional planes, which is required for the reactive "wakeless" swimming solution sought. On the cylinder surface r_o, substitution of 2.29 into 2.30 gives

$$\phi(x, \theta, t) = -(h_t + U_o h_x) r_o \cos \theta \tag{2.31}$$

Using the Bernoulli equation, the linearized pressure on the surface is

$$p(x, \theta, t) = -\rho(\phi_t + U_o \phi_x) \tag{2.32}$$

By substituting 2.31 into 2.32, one arrives at

$$p(x, \theta, t) = \rho k(x, t) r_o \cos \theta \tag{2.33}$$

defining $k(x, t)$ as

$$k(x, t) \equiv h_{tt} + 2U_o h_{xt} + U_o{}^2 h_{xx} \tag{2.34}$$

The surface normal stress vector (inward positive) is written as

$$p\mathbf{n} = \rho k(x, t) r_o \cos \theta (-\hat{\mathbf{e}}_\mathbf{r} + h_x \cos \theta \hat{\mathbf{i}}) \tag{2.35}$$

Sectional forces are computed in the x and y directions as

$$f_x(x, t) = \int_0^{2\pi} p\mathbf{n} \cdot \hat{\mathbf{i}} r_o d\theta \tag{2.36}$$

$$f_y(x, t) = \int_0^{2\pi} p\mathbf{n} \cdot \hat{\mathbf{j}} r_o d\theta \tag{2.37}$$

Substitution of 2.35 into 2.36 and 2.37 gives

$$f_y(x, t) = -\rho \pi r_o{}^2 k(x, t) \tag{2.38}$$

$$f_x(x, t) = \rho \pi r_o{}^2 k(x, t) h_x(x, t) \equiv -f_y(x, t) h_x(x, t) \tag{2.39}$$

which are the sectional forces per unit length.

The sectional absorbed power can be defined as

$$p_d(x,t) = -\int_0^{2\pi} p\mathbf{n} \cdot h_t \hat{\mathbf{j}} r_o d\theta$$

$$= -h_t(x,t) f_y(x,t) \equiv f_x(x,t) \frac{h_t(x,t)}{h_x(x,t)} \tag{2.40}$$

Non-dimensional sectional coefficients for pressure, sectional forces, and power are determined by the following formula:

$$C_{p,\text{sec}}(x,\theta,t) \equiv \frac{p(x,\theta,t)}{\frac{1}{2}\rho V^2} = 2k(x,t)r_o\cos\theta \tag{2.41}$$

$$C_{fy,\text{sec}}(x,t) \equiv \frac{f_y(x,t)}{\frac{1}{2}\rho V^2} = -2\pi r_o^2 k(x,t) \tag{2.42}$$

$$C_{fx,\text{sec}}(x,t) \equiv \frac{f_x(x,t)}{\frac{1}{2}\rho V^2} = 2\pi r_o^2 k(x,t) h_x(x,t) \equiv -C_{T,\text{sec}}(x,t) \tag{2.43}$$

$$C_{P,\text{sec}}(x,t) \equiv \frac{p_d(x,t)}{\frac{1}{2}\rho V^3} = 2\pi r_o^2 k(x,t) h_t(x,t) \tag{2.44}$$

with U_o in $k(x,t)$ now non-dimensionalized by V so that it becomes

$$k(x,t) \equiv h_{tt} + 2U h_{xt} + U^2 h_{xx} \tag{2.45}$$

C_T is the sectional thrust coefficient, and the $2\pi r_o^2$ factors are the non-dimensional added mass of the circular cross-section. The subscript "sec" denotes that these are sectional coefficients. Figure 4.44 shows a plot of the sectional force coefficient in the x-direction over the length of the robot for equally-spaced time steps.

These coefficients can be substituted into the Froude propulsive efficiency equation

$$\eta_i = \frac{UC_T}{C_P} \tag{2.46}$$

to obtain

$$\eta_i(x,t) = \frac{-UC_{fx}}{C_P} = \frac{-Uh_x(x,t)}{h_t(x,t)} \tag{2.47}$$

Rearranging the above equation and setting $\eta_i = 1.0$ for the ideal swimming case, the equation

becomes

$$\eta_i h_t + U h_x = 0 \qquad (2.48)$$

which shows that the perturbation potential in 2.31 is also zero. Furthermore, the solution to this equation for periodic oscillation at dimensional frequency $f = V/L$ is just the same sinusoidal, traveling wave deduced previously as a trivial solution creating no disturbance and producing no thrust for the 2-D formulation:

$$h(x,t) = Re\left\{ H(x)e^{-2\pi it} \right\} \qquad (2.49)$$

with

$$H(x) = He^{\frac{2\pi ix}{L}} \qquad (2.50)$$

This trivial solution, with no slip, has 100% ideal efficiency. Non-trivial displacement shapes which do produce thrust, and which do slip, but also have 100% ideal efficiency are formulated below for the 3-D case.

Following the 2-D development, the explicit requirements on $h(x,t)$ for ideal wakeless propulsion are

1. the total body side lift, $C_{Fy}(t)$, is continuously zero for all t

2. the Froude efficiency of the mean hydrodynamic processes is unity for all x and t

3. the maximum of the real displacement amplitude in x is minimum

The first of the above conditions is equivalent to the restrictions imposed on the vortex distribution in the two-dimensional analysis in avoiding a shed vortex wake in that case. The condition of continuously zero circulation resulted in no net lift in time. In the 3-D case, any lateral vorticity shed in the body section planes has already been excluded in the formulation, enforced by 2.30. The vortex wake shed from the tail does not directly enter the slender-body formulation; its upstream induction, while not zero, is inherently treated as higher order in the sectional flow components by slender body theory and is thus neglected due to the linearization. Net unsteady lift, however, must still be the manifestation of circulation change and associated shed wake from the tail (Lighthill (1960) and Lighthill (1970)). *Non-zero shedding off the animal tail is indirectly eliminated here by requiring that the net lift be continuously zero in both space and time.*

Moving on from the trivial, generalized periodic form in 2.49, this equation is used to determine the 3-D displacement shape. The amplitude is considered to be complex

$$H(x) = e^{\frac{2\pi i x}{U}} H^*(x) \tag{2.51}$$

with

$$H^*(x) = H(0) + \Delta H^*(x) \tag{2.52}$$

which is the form selected on the basis of the character of the 2-D solution developed, where the leading factor in 2.51 incorporates the relationship of the displacement wave length to the body length. $H(0)$ is the unknown head amplitude and $\Delta H^*(x)$ is the function to be established in satisfying the above three conditions 1, 2, and 3.

The solution to the amplitude $H(x)$ can take on any number of solutions, and Vorus and Taravella (2011) provides a detailed formulation of the solution that minimizes the modulus of the maximum displacement $H(x)_{\max}$ for a specified U and C_T, which is enforced by the Froude efficiency being set to the ideal case of 1.0. It is determined that the minimum occurs on the boundary $H(0) = 0$ (it is unrealistic to have a negative head amplitude). Vorus and Taravella (2011) ends up with the equation

$$H(x) = i\sqrt{\frac{\Lambda^*}{\beta(1 - \cos\beta)}} \left(e^{2\pi i x} - e^{\frac{2\pi i x}{U}}\right) \tag{2.53}$$

which is compacted by

$$\Gamma \equiv \sqrt{\frac{\Lambda^*}{\beta(1 - \cos\beta)}} = \sqrt{\frac{C_T}{4\pi^3 \bar{r}_o^2 (1 - U)(1 - \cos\frac{2\pi}{U})}} \tag{2.54}$$

Then, finally, the three-dimensional displacement amplitude is the exceedingly simple function

$$H(x) = i\Gamma \left(e^{2\pi i x} - e^{\frac{2\pi i x}{U}}\right) \tag{2.55}$$

The time dependent displacement is then determined by substituting 2.55 into 2.49. Using Euler's

formula and taking the real part, the three-dimensional displacement wave form becomes

$$\overline{h}(\overline{x}, \overline{t}) = \Gamma \left[\sin \left(2\pi \left(\frac{\overline{x}}{U} - \overline{t} \right) \right) - \sin \left(2\pi \left(\overline{x} - \overline{t} \right) \right) \right] \tag{2.56}$$

where $\overline{x}$ and $\overline{t}$ are the normalized position along the body's length and normalized time, respectively (described below), and U is the advance ratio, which is the ratio of advance speed to displacement wave speed.

In the amplitude term Γ, $\overline{r}_o$ is the normalized length of the semi-major axis of the ellipse that forms the body's cross-section, and C_T is the thrust coefficient. All distance variables (r_0, h, and x) have been non-dimensionalized by the nominal length, L, as follows:

$$\overline{r}_o = \frac{r_o}{L} \qquad\qquad \overline{h}(\overline{x}, \overline{t}) = \frac{h(x, t)}{L}$$

$$\overline{x} = \frac{x}{L} \qquad\qquad \overline{t} = \frac{Vt}{L}$$

$$C_T = C_f 2\pi U^2 \overline{r}_o \tag{2.57}$$

The thrust coefficient computation is derived from the condition that the thrust and drag must equal each other for equilibrium at the mean speed:

$$C_D \equiv C_T \tag{2.58}$$

The total resistance due to drag, C_D, for an articulating, submerged body such as a robotic eel consists of pressure resistance and a frictional resistance. The pressure resistance is due to wave resistance and viscous pressure resistance, but since the robotic eel is deeply submerged and not generating gravity waves, the pressure resistance consists only of the viscous pressure resistance. The viscous pressure resistance is computed as the integration of components of normal stresses due to viscosity and turbulence in the direction of motion. The frictional resistance consists of two components: frictional resistance as calculated by a specific formulation (such as Blasius flat plate drag prediction (Blasius (1908)) or the Hughes prediction line (Hughes (1954) and Hughes (1966))) and an additional friction due to body curvature (form factor). (Other analytical skin friction drag formulations assuming laminar boundary layers include Falkner and Skan (1930) for

accelerating and decelerating flows and Sowerby (1954) for three-dimensional flows; these were not investigated within due to finding these sources late.) In coefficient form, the total drag resistance can be modeled by the following formula:

$$\frac{D}{\frac{1}{2}\rho U_o^2 A} = C_D \equiv C_{pv} + C_{df} + C_{ff} \tag{2.59}$$

with pv denoting viscous pressure, df for frictional drag (flat plate), and ff for the form factor. Because this propulsion is theorized to have zero induced drag, a coefficient for the induced drag is not included. However, an induced drag coefficient will be included for the off-design scenarios (see Sections 2.2.2 and 4.3).

The key is being able to accurately compute this overall drag coefficient. Due to the assumptions of ideal flow theory applied here, the viscous pressure resistance can be neglected here as it accounts for the effects of normal stress in a turbulent boundary layer that exhibits signs of separation from the body. Because of the assumption of no separation on a dynamically swimming vehicle, which is verified experimentally by Anderson et al. (2001), the drag is only due to the fluid disturbance in the thin boundary layer around the entire circumference of the surface. Turbulence is expected to be occurring in the thin boundary layer, and a potential type flow is happening outside it, creating a patched description of the system.

Although the case of no separation implies negligible form drag, there is still an additional frictional resistance component due to curvature of the body, as opposed to that of a flat plate. This component is called the form factor resistance coefficient. (It will also be shown later that form drag can be attributed to factors such as the skin of the robot not being perfectly smooth over the entire length.) In typical ship model resistance calculation procedures, the form factor is determined by Prohaska's method (Prohaska (1962)). Prohaska's method is based on the Froude number of the test and hence physical effects due to gravity. The robotic eel does not produce gravity waves, so this form factor calculation is not applicable here. However, the ITTC-57 (International Towing Tank Conference) ship-model correlation line (ITTC (1957)) already includes a form factor, which is calculated using Hughes' method (Hughes (1954)). Since this line already contains the form factor, the ITTC-57 line is used to compute a combined coefficient of the form factor and flat plate

frictional drag coefficients, which is denoted as follows

$$C_f = C_{df} + C_{ff} \qquad (2.60)$$

So in the end, the drag coefficient decomposition from above (equation 2.59) has been simplified and equated to a total frictional resistance computed using the ITTC-57 line:

$$C_D \equiv C_f = \frac{0.075}{(\log_{10} \mathrm{Re} - 2)^2} \qquad (2.61)$$

where the Re number is calculated using the length of the robot, the kinematic viscosity of water, and the advance speed:

$$\mathrm{Re} = \frac{U_o L_r}{\nu} \qquad (2.62)$$

Interestingly, the International Towing Tank Conference of 1957 adopted this line as the "ship-model correlation line" but was careful to label it as "only an interim solution to this problem for practical engineering purposes" because they could not agree on a final solution at the time (ITTC (1957), p. 324). Yet, it is still used to this day.

Vorus and Taravella (2011) used the Blasius flat plate drag prediction to compute the drag coefficient, which has its obvious disadvantage of not accounting for the shape of the interested object and thus possibly under-predicting the drag resistance. Proving this point, this prediction method was deemed ineffective after observing initial swimming trials of the robotic eel. The drag coefficient has a direct affect on the computation of the amplitude of the anguilliform motion (as shown in equations 2.54 and 2.56), and it was concluded that the amplitude was not large enough to propel the robot at the desired speed. The ITTC-57 line predicted a larger coefficient value and thus larger amplitude, which was expected to account for the assumed under-prediction scenario of the Blasius method. Even with the warnings from the ITTC and this line being used for correlating ships and models, it was decided that the ITTC-57 line should be used for the viscous drag calculation due to its practicality as proven over the years and the inclusion of a form factor. Thankfully, this decision was confirmed later in the research with results from load cell measurements (see Section 4.2.1.3). After more test results were obtained from a load cell measuring the robot's thrust forces, a more accurate prediction of the frictional drag was obtained

by using force decomposition, and the ITTC-57 line was found to be accurate within XX% of the measured value (see Section 4.3).

The often-used parametric curve of the ITTC-57 line and the typical non-dimensional equations for thrust/drag coefficients are used to derive a formula for a non-dimensional thrust here. Going back to the equality condition of 2.58 and substituting in the usual formulas for thrust and viscous drag coefficients, the equation becomes

$$C_D = C_T$$
$$D = C_f \frac{1}{2} \rho U_o^2 A \equiv T_{th} = C_T \frac{1}{2} \rho V^2 L^2$$
$$C_f \frac{1}{2} \rho U_o^2 A = C_T \frac{1}{2} \rho V^2 L^2$$

where A is the surface area of the robot. Canceling and rearranging terms gives

$$C_T = C_f 2\pi U^2 \bar{r}_o \tag{2.63}$$

The terms T_{th}, ρ, and V in the thrust coefficient denote the thrust, density of water (or whatever fluid the eel is attempting to swim in), and displacement wave speed, respectively. The advance speed, U_o, is the speed of the eel relative to an earth-fixed coordinate system, and the speed of the displacement wave, V, is relative to a coordinate system fixed on the robot.

Enforcing some of the theoretical variables to comply with dimensions of the actual robot requires some assumptions. The theoretical length, L, requires that the the arc length of the articulating displacement wave be extending and contracting in time to enforce a constant distance in the x-direction from the head to the tail. The nominal length, L, used in the theoretical derivation is different from the actual length of the robot, L_r, in that it is the time average of the longitudinal straight-line distance from the head to a line both perpendicular to the horizontal axis and intersecting the tail of the articulating eel for one cycle of motion. Figure 2.5 shows a visual description of these length parameters for time step n of the motion. The following equation shows how the nominal length is computed:

$$L = \frac{1}{N} \sum_{n=0}^{N} L_n \tag{2.64}$$

35
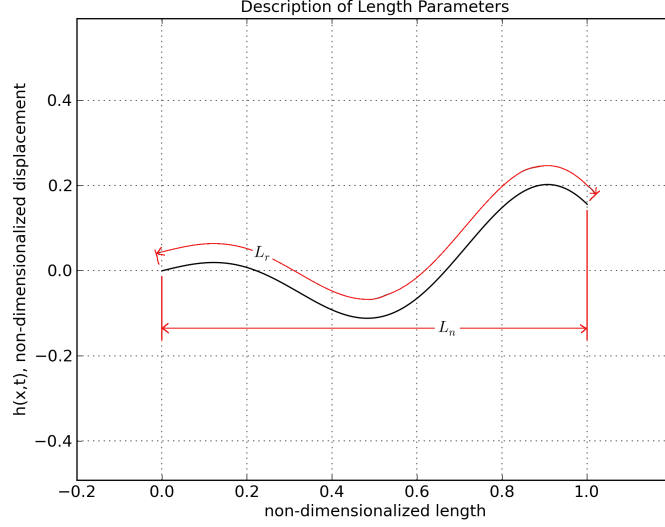
Figure 2.5: Annotations denoting the length parameters of the anguilliform shape for one time step of the motion.

where N is the number of time steps, computed by

$$N = \frac{T}{dt} - 1 \tag{2.65}$$

The nominal length is determined by this time-averaged method so that it follows the dimensional convention of Vorus and Taravella (2011). However, Vorus and Taravella (2011) assumes that the arc length of the anguilliform shape, equal to L_r in this paper, is able to change in time and keep the nominal length constant, a result of the slender body theory linearization. This, along with the non-dimensionalizations, is done to make the mathematical derivations of the hydrodynamic theory more easily possible. With current, practical robots this is physically infeasible, particularly with the one described within; so, instead, the constant time-averaged length in the x-direction is used to approximate the length specified by Vorus and Taravella (2011).

This motion described by the parameters and equations above is theorized to produce "wakeless" swimming when traveling at the prescribed steady-state forward speed, and the motion is shown in Figure 2.6 for specific parameters over 10 equally spaced time steps in one cycle with $t = 0$ as a solid line.

As explained in the 2-D formulation of the theory in Section 2.1.1, the kinematic condition

36
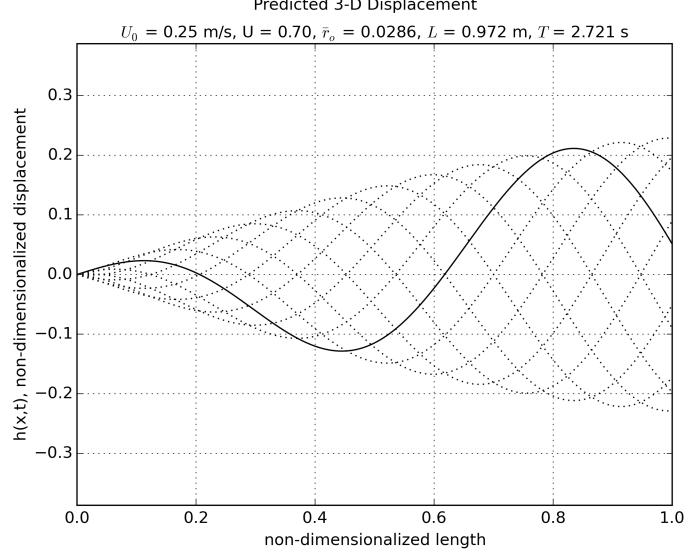
Figure 2.6: Theoretical anguilliform motion plotted for 10 equally spaced steps in time.

defines the possible non-trivial cases of the motion that produce non-zero axial thrust with 100% Froude efficiency because of the absence of vortex shedding:

$$f = \frac{V}{L} = \frac{1}{T} \tag{2.66}$$

This defines the frequency, or time period, at which the robotic eel will operate.

Table 2.1 lists the values for the various parameters that were determined mostly due to the physical constraints of the actual robot. This set of values that defines its unique displacement wave form is referred to as the nominal design throughout the rest of the text. Since the amplitude term, Γ, is a function of the length due to the reliance on the thrust coefficient, it is necessary to iterate to a converged nominal length by first performing the computation with the robot length as an initial guess to obtain a time-average nominal length, which is repeated for successive iterations. The nominal length is computed as in 2.64.

The above overview of the derivation given by Vorus and Taravella (2011) is based on the hypothesis that the steady anguilliform swimming of aquatic animals is purely reactive such that no net vortex wake is left downstream, which is in contrast to that of carangiform swimmers. Carangiform movements are such to produce partial vortex cancellation downstream in maximizing propulsive efficiency. A vortex wake persistent to large distances downstream necessarily accompanies circu-

37

Table 2.1: Current parameter values.

Parameter	Value
advance speed, U_o	0.25 m/s
advance ratio, U	0.7
disp. wave speed, $V = U_o/U$	0.3571 m/s
robot length, L_r	1.3 m
nominal length, L	0.972 m
time period, T	2.721 s
normalized radius, $\bar{r}_o$	0.02855
thrust coefficient, C_T	0.0007985
amplitude, Γ	0.11767

lation generation with unsteady motions in carangiform fish, such as tuna (Lighthill (1969)). In anguilliform swimming, it is argued that the swimming motions are configured by the animal such that vortex shedding does not occur at all since the circulation about the oscillating body is continuously zero. The wake-induced drag is then also zero, implying high propulsive efficiency. However, the propulsive thrust in this case is higher order in motion amplitude, so that relatively large coils are needed to produce relatively small thrust, making the speeds of anguilliform swimmers less. Carangiform swimmers develop first order thrusts via lifting processes, but their high efficiency is still achieved by cancellations in the shed free-stream vortices.

Vorus and Taravella (2011) states that for animals such as lamprey, relatively higher Reynolds number and thinner boundary layer flows prevail as shown in Lighthill (1971). This implies ideal flow theory, which can be used due to thin boundary layer assumptions, with vortex shedding, in general, and with simple skin friction corrections to explicitly account for viscosity (Lighthill (1960). Carangiform swimming has also generally been modeled as high Reynolds number ideal flow, and ideal flow theory with vortex shedding has been applied extensively to this case, e.g. Taylor (1952), Lighthill (1960), Wu (1961), Lighthill (1970), and Lighthill (1971). The difference in the formulation within is the proposition that lift and vortex shedding does not occur in high Reynolds number anguilliform swimming in achieving the highest possible propulsive efficiency.

The general hydromechanic theory for body thrust generation in ideal fluids without vortex shedding first appeared in Saffman (1967), with more recent work by Miloh and Galper (1993).

Essentially, the thrust is inertial, or reactive, and is produced by body accelerations acting through hydrodynamic added mass. This is in contrast to lifting processes where the associated lifting forces and circulation are generated through body and stream relative velocity.

The theoretical anguilliform undulation formulated here that generates reactive swimming thrust through fluid inertial reaction without generating circulation only applies in the context of thin boundary layer flows (Vorus (1995)), which may limit its applicability to a robotic eel (discussed in Chapter V).

Conclusions of Vorus, 2011: Ideal fluid theory has been used for the hydrodynamics, on the basis that the normal stress effects are separable and independent of the tangential. This requires a thin boundary layer flow, for which case the normal stress is the Bernoulli pressure. The mean flow Reynolds number for the swimming lamprey is around 23,000, so that the unsteady boundary layer should be laminar, but in the absence of separation, it should conform to the assumption of thinness (I disagree that their is no separation, as noted earlier with respect to Sarpkaya saying that separation on cylinders in oscillating flows happens readily.) Boundary layer thinness and attachment are promoted both by the flow unsteadiness and by the premise that the animal slides tangentially with minimum lateral distrubance in avoiding the creation of a vortex wake. Ideal flow theory with a separately estimated drag coefficient has been applied extensively in the fish swimming research of the past, e.g. Lighthill (1960). Any transient operations of the animal would generally involve hydrodyanamic lift, vortex shedding, accompanying the transient displacement distributions required to execute the maneuver.

2.2 Extensions to the Original Theory

For incompressible flows, the instantaneous solution is independent of time derivatives (Katz and Plotkin (2001)), i.e. the influence of the momentary boundary condition is immediately radiated across the whole fluid region. Therefore, steady-state solution techniques can be used to treat the time-dependent problem by substituting the instantaneous boundary condition at each moment in time.

The wake shape however does depend on the time history of the motion, and consequently an appropriate vortex wake model has to be developed.

2.2.1 Far-field Velocity Field

The velocity potential due to a 3-D point doublet of strength μ pointing in the y-direction using spherical coordinates is

$$\phi_{3D}(r, \theta, \psi) = -\frac{\mu \cos \theta}{4\pi r^2} \tag{2.67}$$

One needs to obtain the doublet strength as a function of the body boundary condition, in that the fluid velocity is known at the surface of the robot based on linearized slender body theory:

$$v_r(r, \theta, \psi, t)|_{r=r_o} = h_t + U_o h_x \equiv \nu(r_o, \theta, \psi, t) \tag{2.68}$$

The doublet strength for a doublet modeling a circular cross-section is

$$\mu = \nu 2\pi r_o^3 \tag{2.69}$$

where ν comes from the previous equation. Note that ν is still a function of the spatial and temporal variables.

This doublet strength is then substituted back into the original velocity potential of a point doublet (equation 2.67).

$$\phi_{3D}(r, \theta, \psi) = \frac{\nu r_o^3 \cos \theta}{2r^2} \tag{2.70}$$

To model the anguilliform shape, this point doublet can be integrated along a line. The equation is also placed back in the original coordinates.

$$\phi_{3D}(x, r, \theta, t) = \frac{r_o^3 \cos \theta}{2} \int_{\xi=0}^{L} \frac{\nu(\xi, t)}{(x - \xi)^2 + r^2} d\xi \tag{2.71}$$

Adding in wake elements modelled by doublets gives

$$\phi_{3D}(x, r, \theta, t) = \frac{r_o^3 \cos \theta}{2} \int_{\xi=0}^{L} \frac{\nu(\xi, t)}{(x - \xi)^2 + r^2} d\xi + \frac{r \cos \theta}{4\pi} \int_{L}^{L(t)} \frac{\mu_w(\xi, t)}{[(x - \xi)^2 + r^2]^{\frac{3}{2}}} d\xi \tag{2.72}$$

The intermediate and far-field perturbation potential can be modeled as a line of 3-D doublets, which have a line strength determined by the linearized boundary condition in equation 2.68.

The velocity potential due to a 3-D point doublet of strength μ in the y-direction is defined as

$$\phi(x, y, z) = -\frac{\mu(y - y_0)}{[(x - x_0)^2 + (y - y_0)^2 + (z - z_0)^2]^{-\frac{3}{2}}} \tag{2.73}$$

The strength can be determined by knowing the radius of the intended sphere and fluid velocity on-flow and substituting these boundary conditions into the above equation

$$\phi(x, y, z) = \phi(x, y, z) \tag{2.74}$$

The field points x, y, and z are changed into a cylindrical coordinate system with $r^2 = y^2 + z^2$. The locations of the doublets denoted by y_0 and z_0 are set to 0 since the shape is only modeled on the x-axis, and x_0 is changed to ξ for ease of notation.

After showing that the 3-D far-field potential approaches that of the near-field 2-D potential, Vorus (2013) shows the formula for the potential as a line of 3-D doublets:

$$\phi_{3D}(x, r, \theta, t) = \frac{r_o^2 r \cos\theta}{4\pi} \int_{\xi=0}^{L} \frac{\nu(\xi, t)}{[(x - \xi)^2 + r^2]^{\frac{3}{2}}} d\xi \tag{2.75}$$

Discretizing this for ease of computation in a computer code and assuming the velocity boundary condition, ν, is constant over each discretized segment, the equation becomes

$$\phi_{3D}(x, r, \theta, t) = \frac{r_o^2 r \cos\theta}{4\pi} \sum_{j=1}^{J} \overline{\nu}_j(t) \int_{\xi=\xi_j}^{\xi_{J+1}} \frac{d\xi}{[(x - \xi)^2 + r^2]^{\frac{3}{2}}} \tag{2.76}$$

where ξ_j are at the ends of the J equal segments spanning the discretized length from 0 to L. The barred quantity $\overline{\nu}$ are evaluated at the center of their respective elements:

$$\overline{\nu}_j(t) \equiv h_{tj}(t) + U h_{xj}(t) \tag{2.77}$$

and

$$h_j(t) = \Gamma \left[\sin\left(2\pi \left(\frac{\overline{x}_j}{U} - \overline{t}\right)\right) - \sin\left(2\pi \left(\overline{x}_j - \overline{t}\right)\right) \right] \tag{2.78}$$

Apply equation 2.264.5 from Gradshteyn and Ryzhik (1980) to achieve the integral term as a

41

series in J:

$$\phi_{3D}(x,r,\theta,t) = -\left(\frac{r_o}{r}\right)^2 \frac{\cos\theta}{\pi} \sum_{j=1}^{J} \overline{\nu}_j(t)(x-\xi)\left[(x-\xi)^2 + r^2\right]^{-\frac{1}{2}}\Bigg|_{\xi=\xi_j}^{\xi_{j+1}} \tag{2.79}$$

Taking the partial derivative with respect to the desired coordinate direction gives the velocity components at the field points:

$$u(x,r,\theta,t) = \frac{\partial\phi_{3D}}{\partial x}$$

$$= -\left(\frac{r_o}{r}\right)^2 \frac{\cos\theta}{\pi} \sum_{j=1}^{J} \overline{\nu}_j(t)\left\{\left[(x-\xi)^2 + r^2\right]^{-\frac{1}{2}} - (x-\xi)^2\left[(x-\xi)^2 + r^2\right]^{-\frac{3}{2}}\right\}\Bigg|_{\xi=\xi_j}^{\xi_{j+1}} \tag{2.80}$$

$$v_r(x,r,\theta,t) = \frac{\partial\phi_{3D}}{\partial r}$$

$$= \left(\frac{r_o}{r}\right)^2 \frac{\cos\theta}{\pi} \sum_{j=1}^{J} \overline{\nu}_j(t)\left\{\left[-\frac{2}{r}(x-\xi)^2 + r^2\right]^{-\frac{1}{2}} - r\left[(x-\xi)^2 + r^2\right]^{-\frac{3}{2}}\right\}\Bigg|_{\xi=\xi_j}^{\xi_{j+1}} \tag{2.81}$$

$$v_\theta(x,r,\theta,t) = \frac{1}{r}\frac{\partial\phi_{3D}}{\partial\theta}$$

$$= \left(\frac{r_o}{r}\right)^2 \frac{\sin\theta}{\pi r} \sum_{j=1}^{J} \overline{\nu}_j(t)(x-\xi)\left[(x-\xi)^2 + r^2\right]^{-\frac{1}{2}}\Bigg|_{\xi=\xi_j}^{\xi_{j+1}} \tag{2.82}$$

At each field-point, x, r, θ, at each time step, t, the formulas above are evaluated to generate the velocity vector, $\mathbf{v}_{\text{tot}}$ due to the contribution of all the doublets along the length of the shape function:

$$\mathbf{v}_{\text{tot}}(x,r,\theta,t) = u\hat{\mathbf{i}} + v_r\hat{\mathbf{e}}_{\mathbf{r}} + v_\theta\hat{\mathbf{e}}_\theta \tag{2.83}$$

Figures 2.7 through 2.16 show the velocities in the wake of the anguilliform motion at increments of $0.1T$ in non-dimensional time, over one complete cycle. The ambient field velocity of 0.25 m/s in the positive x-direction has been subtracted in order to show only the perturbation velocities. The contour plots show the velocity magnitude, and vectors at equally-spaced spatial coordinates are shown. However, the perturbation velocities are so small that they do not appear in any of these plots.

Figure 2.7: Computed velocity field vectors and velocity magnitude downstream of the ideal robot shape motion for $t = 0.0T$. The superimposed shape function is what the doublets on the $y = 0$ m centerline are modelling.

The velocity anywhere in the intermediate/far-field around the anguilliform eel shape function can now be computed as a function of time and be compared to experimentally measured values of the wake. The above formulation is for the ideal motion case, which was derived under the assumption that there is no shedding of vortices, and thus there are no wake elements included. Since the actual, recorded motion of the robotic eel did not replicate this ideal motion, the assumption of no shed vortices cannot be guaranteed. Thus, the formulation above has been modified to include wake elements that are shed in time, which is shown in the next section.

2.2.2 Far-field Velocity Field with Shed Vortices

For this research, unfortunately, the ideal motion prescribed by the formula in 2.56 was never exactly replicated by the NEELBOT-1.1 robot, as will be reported in Section 3.2.2, on a consistent basis. Since the ideal motion was never replicated consistently, a different formulation of the theory derived above is generated to include wake elements downstream of the robot to model shed vortices. These shed vortices are modeled as discrete point doublets with a strength averaged over the length of the wake element. The wake element length is determined by the speed of advance and the time step size in the computation. The doublet strength for each shed wake element is equal and opposite in value to the circulation about the shape function at the time of the wake element being shed.

43
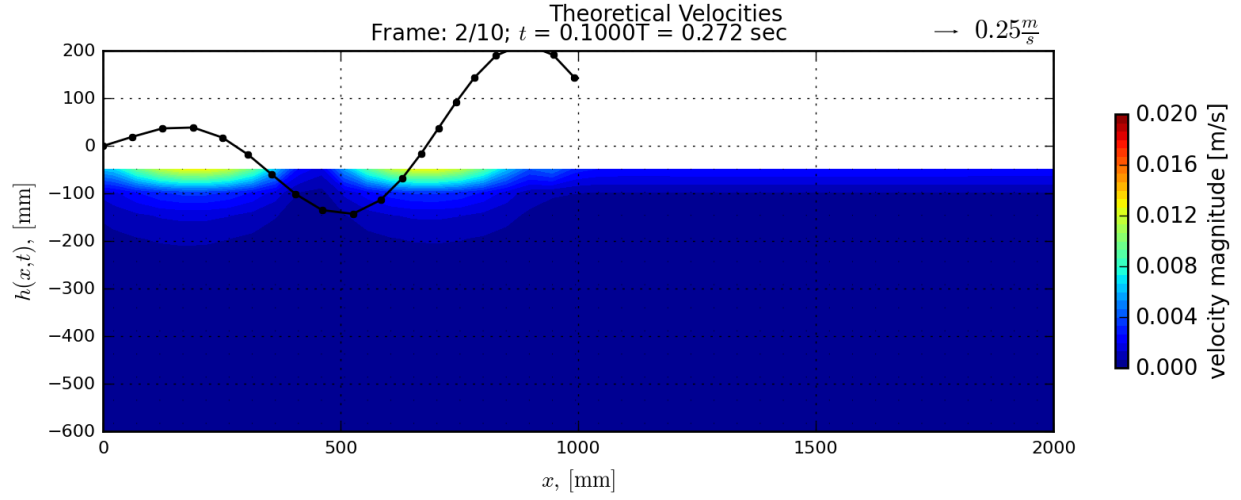
Figure 2.8: Computed velocity field vectors and velocity magnitude downstream of the ideal robot shape motion for $t = 0.1T$. The superimposed shape function is what the doublets on the $y = 0$ m centerline are modelling.
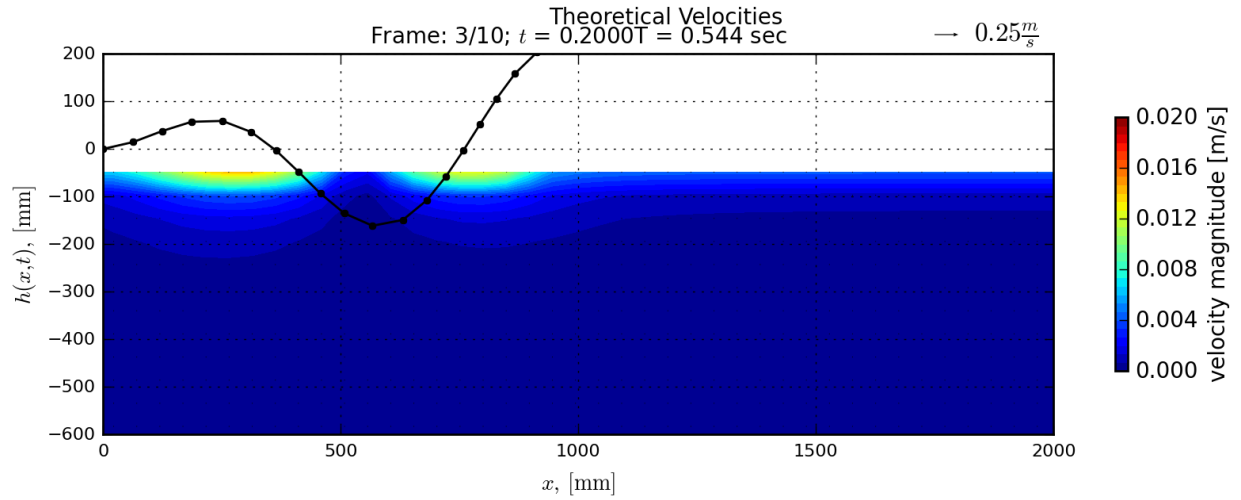
Figure 2.9: Computed velocity field vectors and velocity magnitude downstream of the ideal robot shape motion for $t = 0.2T$. The superimposed shape function is what the doublets on the $y = 0$ m centerline are modelling.
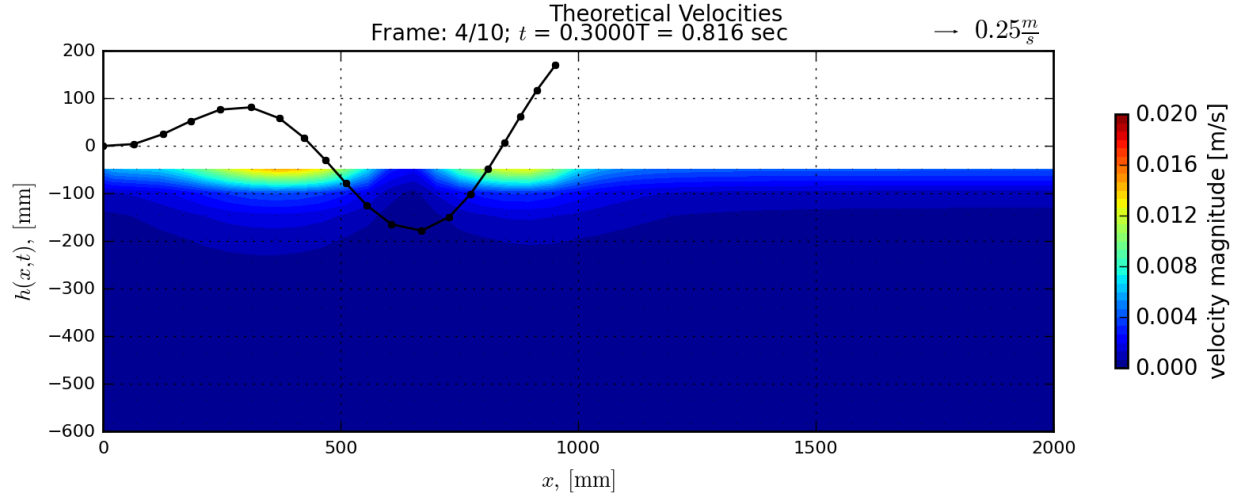
Figure 2.10: Computed velocity field vectors and velocity magnitude downstream of the ideal robot shape motion for $t = 0.3T$. The superimposed shape function is what the doublets on the $y = 0$ m centerline are modelling.
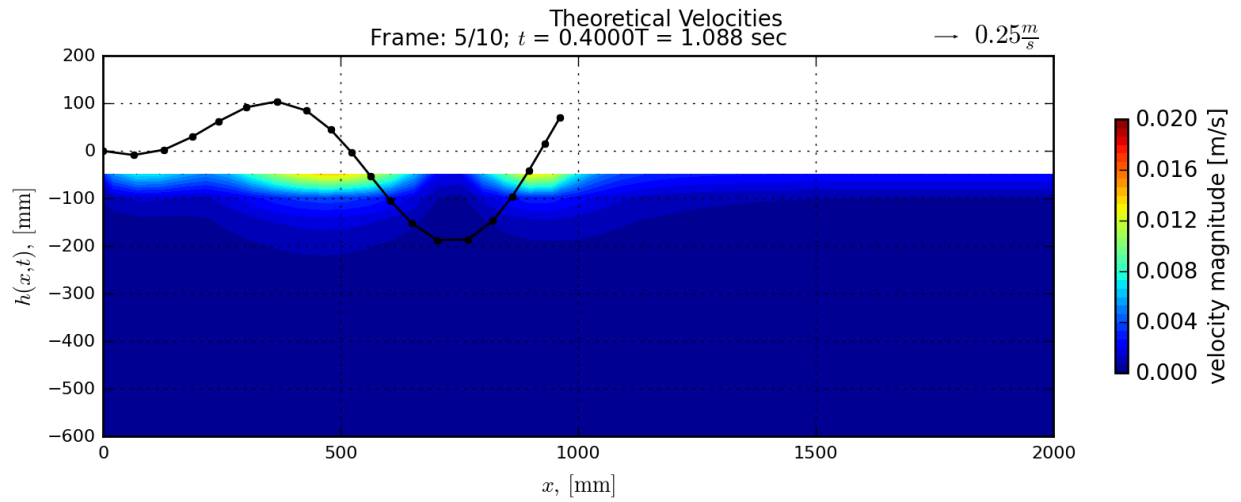
Figure 2.11: Computed velocity field vectors and velocity magnitude downstream of the ideal robot shape motion for $t = 0.4T$. The superimposed shape function is what the doublets on the $y = 0$ m centerline are modelling.
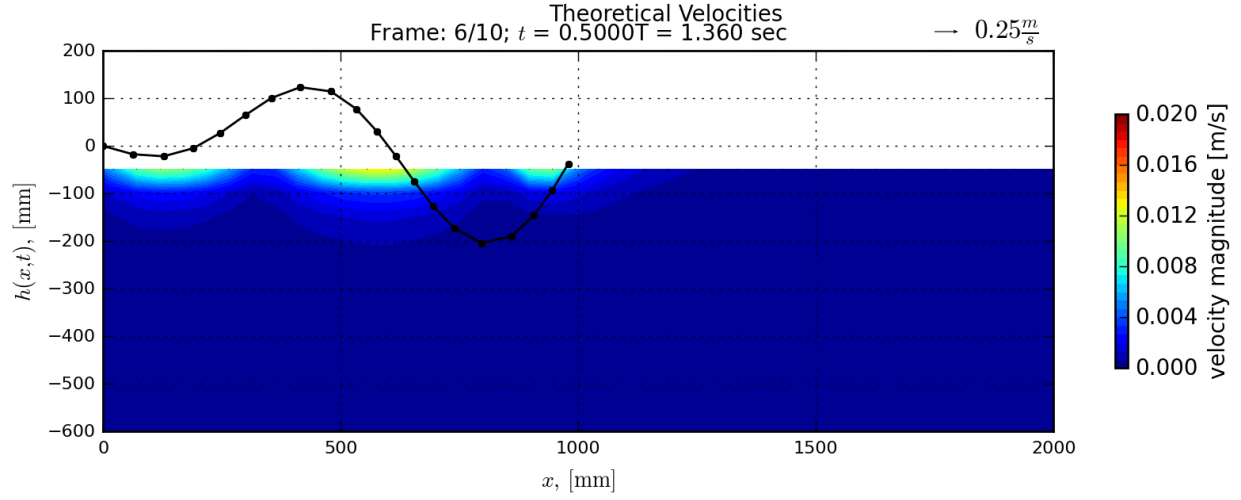
Figure 2.12: Computed velocity field vectors and velocity magnitude downstream of the ideal robot shape motion for $t = 0.5T$. The superimposed shape function is what the doublets on the $y = 0$ m centerline are modelling.
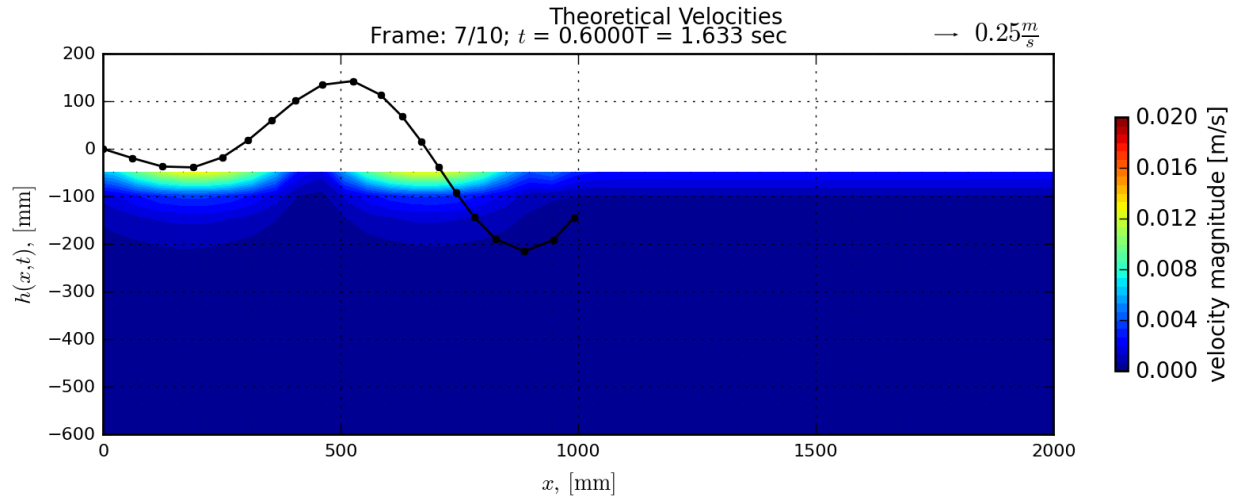
Figure 2.13: Computed velocity field vectors and velocity magnitude downstream of the ideal robot shape motion for $t = 0.6T$. The superimposed shape function is what the doublets on the $y = 0$ m centerline are modelling.
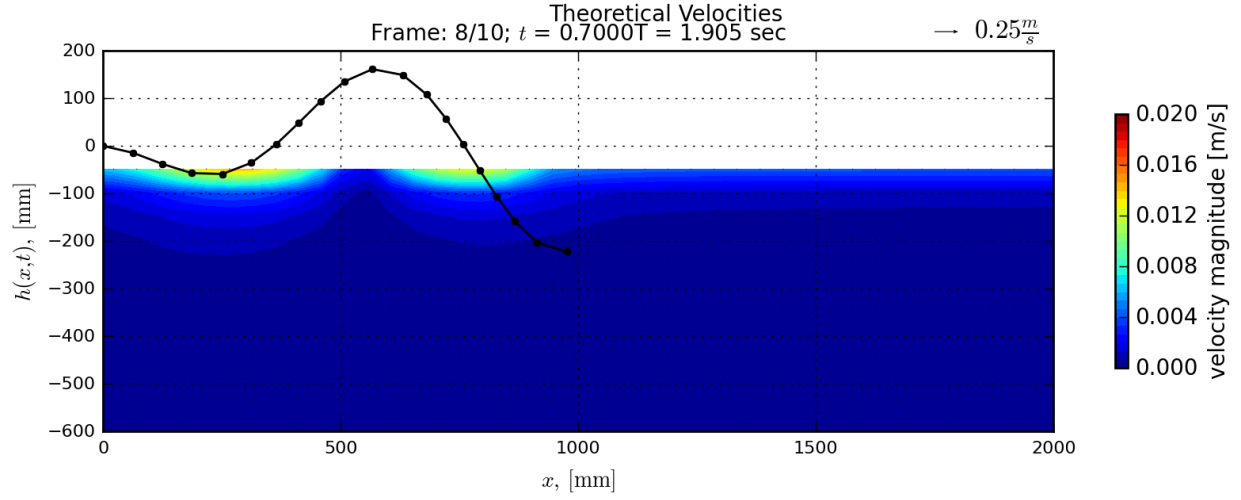
Figure 2.14: Computed velocity field vectors and velocity magnitude downstream of the ideal robot shape motion for $t = 0.7T$. The superimposed shape function is what the doublets on the $y = 0$ m centerline are modelling.
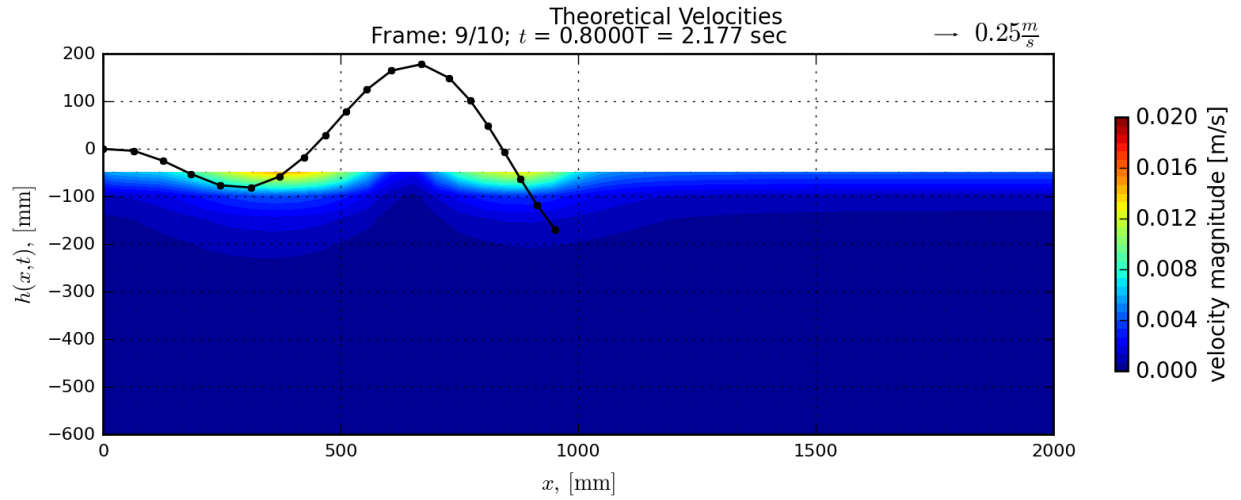
Figure 2.15: Computed velocity field vectors and velocity magnitude downstream of the ideal robot shape motion for $t = 0.8T$. The superimposed shape function is what the doublets on the $y = 0$ m centerline are modelling.
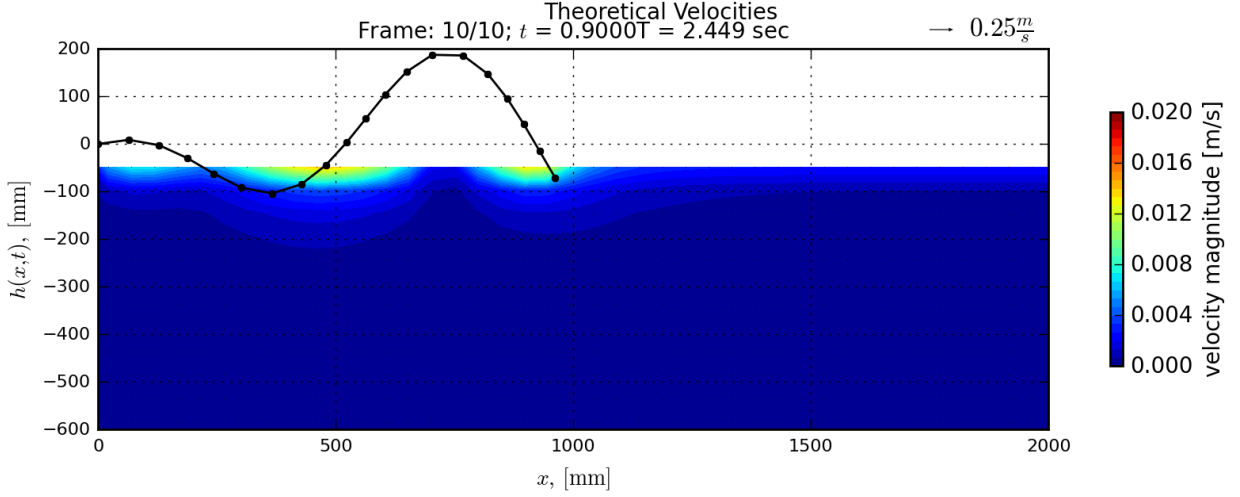
Figure 2.16: Computed velocity field vectors and velocity magnitude downstream of the ideal robot shape motion for $t = 1.0T$. The superimposed shape function is what the doublets on the $y = 0$ m centerline are modelling.

In agreement with the assumptions of the theory above, the shape function will only shed a vortex if the motion is not an imitation of the motion derived by Vorus and Taravella (2011). Therefore, the new formulation includes the option to manually define a custom motion. The custom motion used within replicates that of the actual motion, recorded by the angular position encoders in the servo-actuators of NEELBOT-1.1's joints (details of the servo-actuators are explained in Section 3.2.1, and the recorded motion is shown in Section 3.2.2).

With no loss in generality, the wake elements of doublet strength μ_w can be easily added to equation 2.75 as a second integral of line doublets modeling the wake:

$$\phi_{3D}(x, r, \theta, t) = \frac{r_o^2 r \cos\theta}{4\pi} \int_{\xi=0}^{L} \frac{\nu(\xi, t)}{[(x-\xi)^2 + r^2]^{\frac{3}{2}}} d\xi + \frac{\cos\theta}{4\pi} \int_{L}^{L(t)} \frac{\mu_w(\xi, t)}{[(x-\xi)^2 + r^2]^{\frac{3}{2}}} d\xi \qquad (2.84)$$

After discretizing, the above equation becomes

$$\phi_{3D}(x, r, \theta, t) = \frac{r_o^2 r \cos\theta}{4\pi} \sum_{j=1}^{J} \overline{\nu}_j(t) \int_{\xi=\xi_j}^{\xi_{J+1}} \frac{d\xi}{[(x-\xi)^2 + r^2]^{\frac{3}{2}}}$$

$$- \frac{r \cos\theta}{4\pi} \sum_{k=0}^{K} \overline{\mu}_{w,k}(t) \int_{\xi=\xi_k}^{\xi_{k+1}} \frac{d\xi}{[(x-\xi)^2 + r^2]^{\frac{3}{2}}} \qquad (2.85)$$

where the first term is the same as that of the one in equation 2.76, and the doublet strength,

specified by $\bar{\mu}_{w,k}$ is assumed constant over the length of the wake element and specified at the center of the element. The index k denotes the discretized segments of the wake being shed into the wake over time and matches that of the time step. The length of each shed wake element for time step k is dependent on the speed of advance and the length of the time step by the formula

$$l_{w,k} = U_o \Delta t_k \tag{2.86}$$

The total wake length is then computed as

$$L(k\Delta t) = L + \sum_{k=0}^{K} l_{w,k} = L + \sum_{k=0}^{K} U_o \Delta t_k \tag{2.87}$$

The endpoints of the wake elements used in the discretization summation above are denoted by the points $L(k\Delta t)$.

Because of the assumption that the barred quantities are constant along the length of each element, the integrals are easily integrated to be

$$\phi_{3D}(x, r, \theta, t) = -\left(\frac{r_o}{r}\right)^2 \frac{\cos\theta}{\pi} \sum_{j=1}^{J} \bar{\nu}_j(t)(x - \xi)\left[(x - \xi)^2 + r^2\right]^{-\frac{1}{2}}\Big|_{\xi=\xi_j}^{\xi_{j+1}}$$

$$+ \frac{\cos\theta}{4\pi r} \sum_{k=0}^{K} \bar{\mu}_{w,k}(t)(x - \xi)\left[(x - \xi)^2 + r^2\right]^{-\frac{1}{2}}\Big|_{\xi=\xi_k}^{\xi_{k+1}} \tag{2.88}$$

Similar to equations 2.80 to 2.82, the potential is partial differentiated with respect to each of the spatial coordinate directions to obtain the velocity components at each field point:

$$u(x, r, \theta, t) = \frac{\partial \phi_{3D}}{\partial x}$$

$$= -\left(\frac{r_o}{r}\right)^2 \frac{\cos\theta}{\pi} \sum_{j=1}^{J} \bar{\nu}_j(t)\left\{\left[(x - \xi)^2 + r^2\right]^{-\frac{1}{2}} - (x - \xi)^2\left[(x - \xi)^2 + r^2\right]^{-\frac{3}{2}}\right\}\Big|_{\xi=\xi_j}^{\xi_{j+1}}$$

$$+ \frac{\cos\theta}{4\pi r} \sum_{k=0}^{K} \bar{\mu}_{w,k}(t)\left\{\left[(x - \xi)^2 + r^2\right]^{-\frac{1}{2}} - (x - \xi)^2\left[(x - \xi)^2 + r^2\right]^{-\frac{3}{2}}\right\}\Big|_{\xi=\xi_k}^{\xi_{k+1}} \tag{2.89}$$

$$v_r(x, r, \theta, t) = \frac{\partial \phi_{3D}}{\partial r}$$

$$= \left(\frac{r_o}{r}\right)^2 \frac{\cos\theta}{\pi} \sum_{j=1}^{J} \bar{\nu}_j(t) \left\{ \left[-\frac{2}{r}(x-\xi)^2 + r^2 \right]^{-\frac{1}{2}} - r\left[(x-\xi)^2 + r^2\right]^{-\frac{3}{2}} \right\}\Bigg|_{\xi=\xi_j}^{\xi_{j+1}}$$

$$+ \frac{\cos\theta}{4\pi r} \sum_{k=0}^{K} \bar{\mu}_{w,k}(t) \left\{ -r(x-\xi)\left[(x-\xi)^2 + r^2\right]^{-\frac{3}{2}} \right\}\Bigg|_{\xi=\xi_k}^{\xi_{k+1}} \tag{2.90}$$

$$v_\theta(x, r, \theta, t) = \frac{1}{r}\frac{\partial \phi_{3D}}{\partial \theta}$$

$$= \left(\frac{r_o}{r}\right)^2 \frac{\sin\theta}{\pi r} \sum_{j=1}^{J} \bar{\nu}_j(t)(x-\xi)\left[(x-\xi)^2 + r^2\right]^{-\frac{1}{2}}\Bigg|_{\xi=\xi_j}^{\xi_{j+1}}$$

$$- \frac{\sin\theta}{4\pi r^2} \sum_{k=0}^{K} \bar{\mu}_{w,k}(t)(x-\xi)\left[(x-\xi)^2 + r^2\right]^{-\frac{1}{2}}\Bigg|_{\xi=\xi_k}^{\xi_{k+1}} \tag{2.91}$$

At this point, there is still the unknown doublet strength of the wake elements, so an additional equation is needed for each time step. Luckily, Kelvin derived his theorem that the circulation around a fluid curve of the same fluid elements in an incompressible, inviscid, irrotational flow remains constant over time:

$$\frac{D\Gamma}{Dt} = 0 = -\oint_C d\frac{p}{\rho} + \oint_C \mathbf{f} \cdot d\mathbf{l} \tag{2.92}$$

since the integral of a perfect differential around a closed path is zero and the work done by a conservative force around a closed path is also zero. Kelvin's theorem is based on the fact that angular momentum cannot change. Applied to the 3-D anguilliform displacement shape function, the following condition is enforced

$$\frac{D\Gamma}{Dt} = \frac{1}{\Delta t}(\Gamma_{\text{ang. shape}} + \Gamma_{\text{wake}}) = 0 \tag{2.93}$$

where the subscript "ang. shape" denotes the circulation about the anguilliform shape. For this case, it is assumed that the anguilliform shape motion starts from rest and thus there is no circulation to begin with. It is also assumed that when the motion starts, the starting wake circulation is

equal and opposite to the circulation of the anguilliform shape. Thus the above equation becomes

$$\Gamma(t_k) + \sum_{k=0}^{K} \Gamma_{w,k} = 0 \tag{2.94}$$

for time step k. From Katz and Plotkin (2001), it is shown that the circulation $\Gamma(x)$ around a path surrounding a segment in space is

$$\Gamma(x, y, z) = -\mu(x, y, z) \tag{2.95}$$

which is substituted into the current formulation going forward. Thus, the doublet strength of the anguilliform shape and the wake elements is

$$\mu_{ang.shape}(t_k) + \sum_{k=0}^{K} \overline{\mu}_{w,k} = 0 \tag{2.96}$$

where the first term is the total doublet strength of the anguilliform shape and the second term is now a summation of average doublet strengths for each segment included in the summation. This mean doublet strength at each wake element segment matches that of the wake elements in equations 2.89 to 2.91. Figure 2.17 shows a schematic of the circulation of the anguilliform shape (robot) and wake elements.

For this ideal flow theory case, the shed vortex (or doublet) strength does not change in time, i.e. the energy does not dissipate. The circulation, or doublet strength, of the shed vortex at time step k is equal and opposite to the circulation of the anguilliform shape plus all the shed vortex strengths prior to times step k. For example, at $t = 2\Delta t$, using equations 2.89 to 2.91 and Kelvin's constant circulation theorem in 2.94 with the substitution of 2.95, the set of equations is solved for $\overline{\mu}(t_2)$ and $\overline{\mu}_{w,2}$ while $\overline{\mu}_{w,1}$ is known from the previous time step.
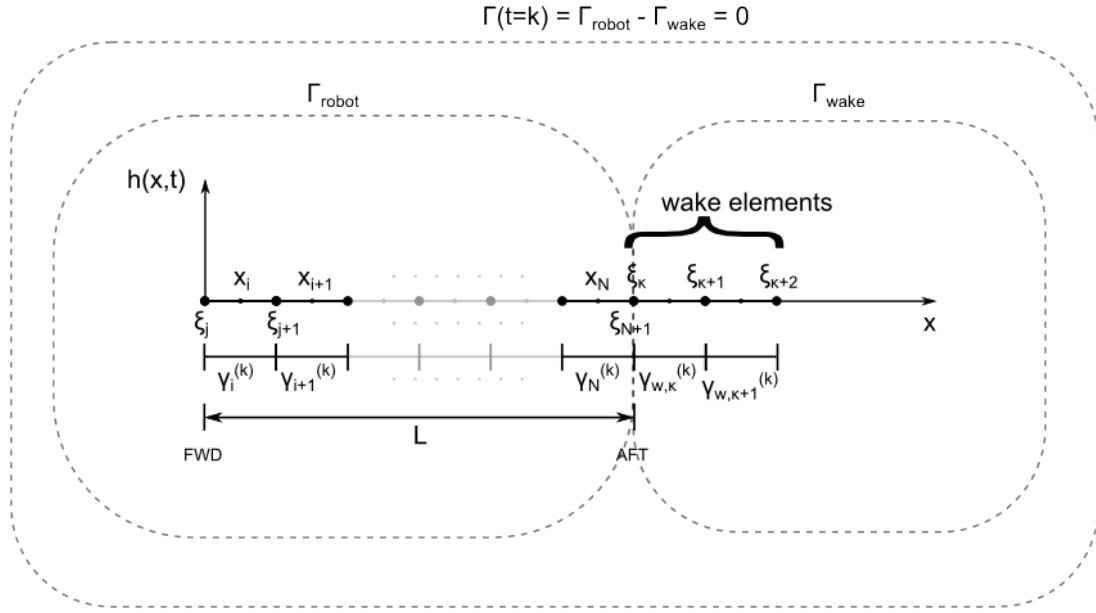
Figure 2.17: Schematic showing line integrals of circulation for the complete system and the individual robot and wake systems, each of which is composed of discrete elements.
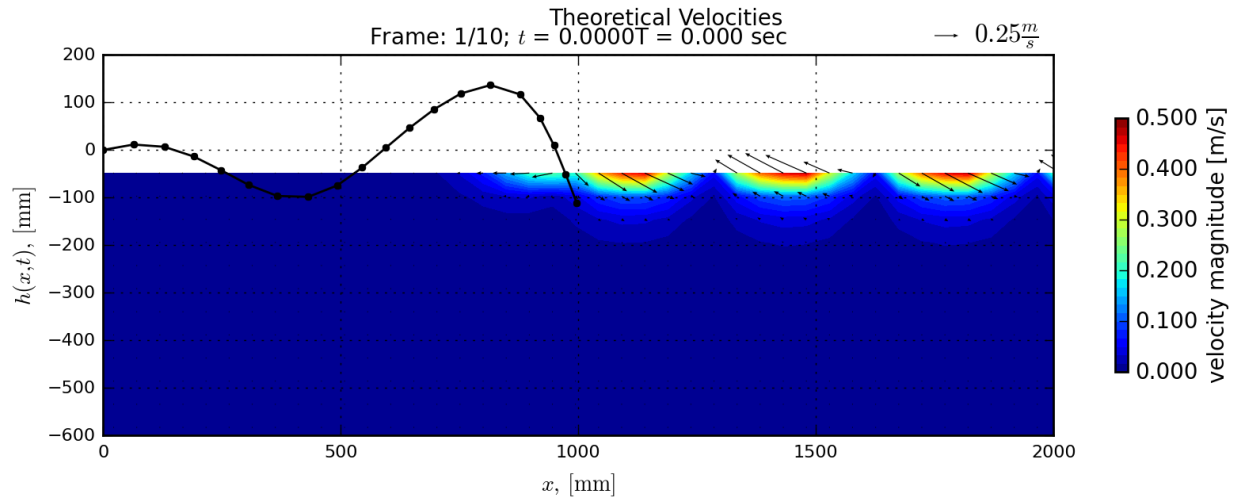
Figure 2.18: Computed velocity field vectors and velocity magnitude downstream of the actual robot shape motion for $t = 0.0T$. The superimposed shape function is what the doublets on the $y = 0$ m centerline are modelling.
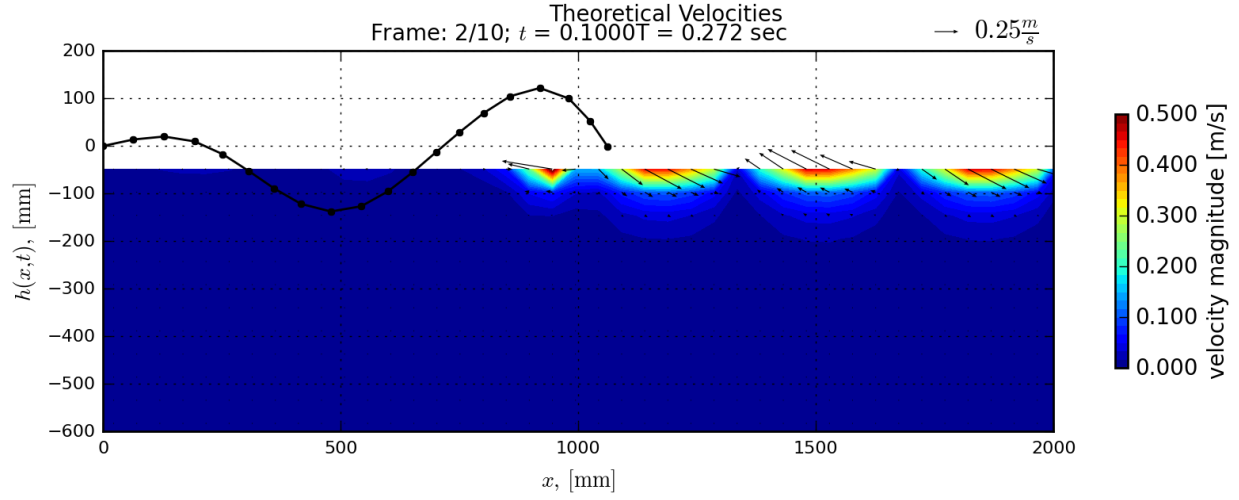
Figure 2.19: Computed velocity field vectors and velocity magnitude downstream of the actual robot shape motion for $t = 0.1T$. The superimposed shape function is what the doublets on the $y = 0$ m centerline are modelling.
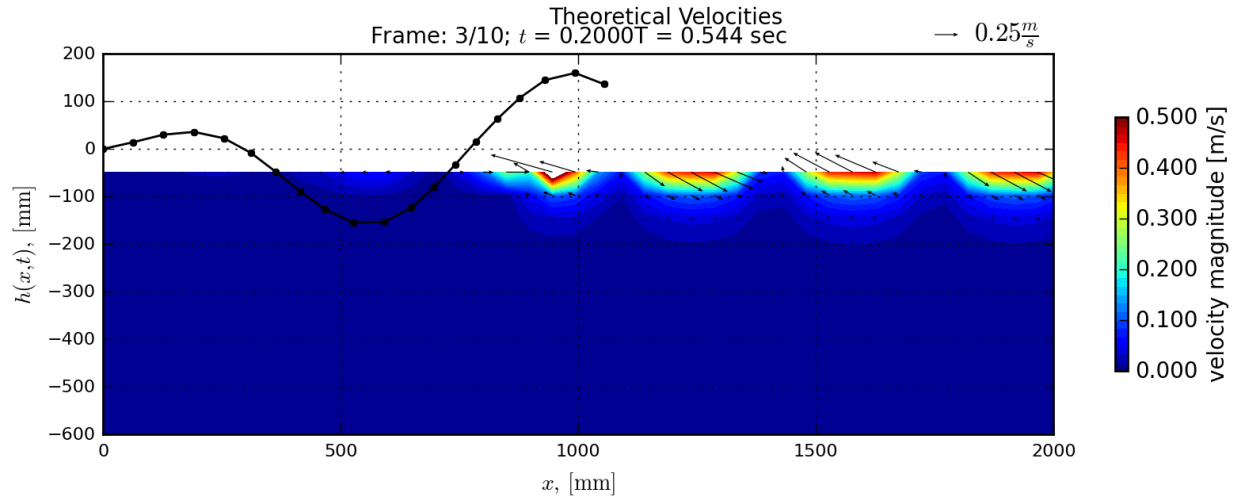
Figure 2.20: Computed velocity field vectors and velocity magnitude downstream of the actual robot shape motion for $t = 0.2T$. The superimposed shape function is what the doublets on the $y = 0$ m centerline are modelling.
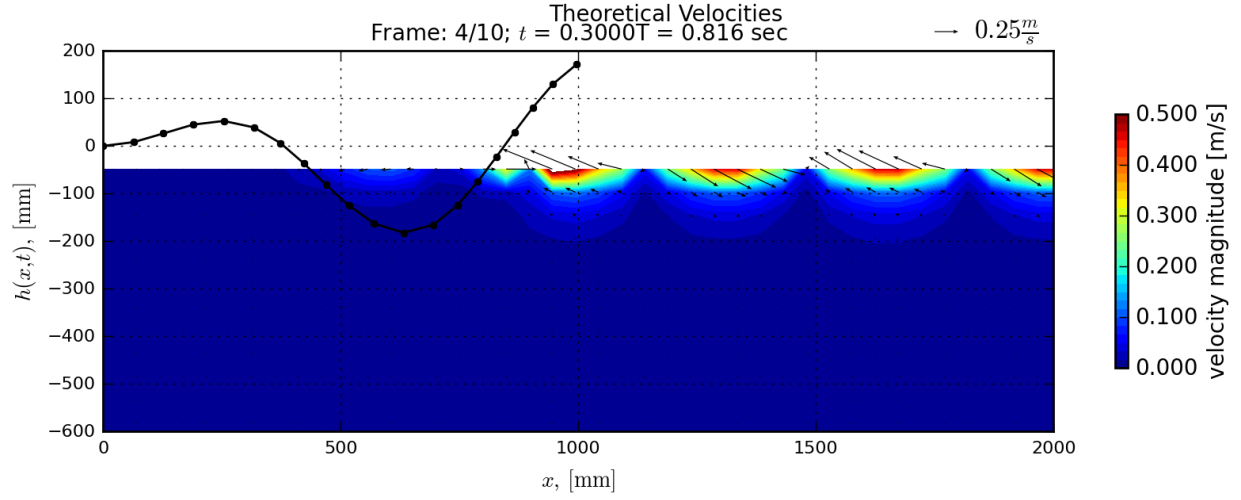
Figure 2.21: Computed velocity field vectors and velocity magnitude downstream of the actual robot shape motion for $t = 0.3T$. The superimposed shape function is what the doublets on the $y = 0$ m centerline are modelling.
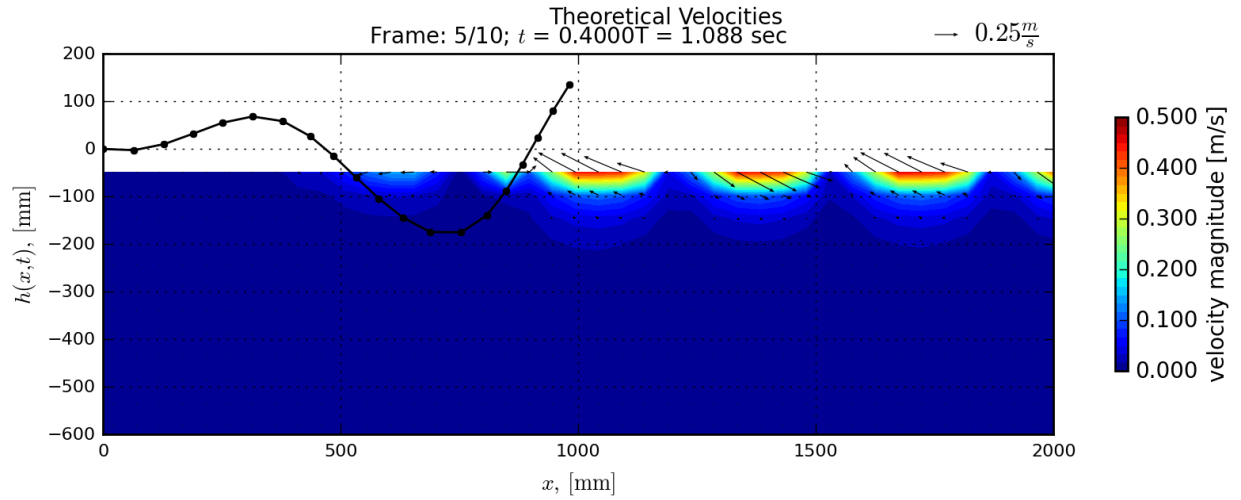
Figure 2.22: Computed velocity field vectors and velocity magnitude downstream of the actual robot shape motion for $t = 0.4T$. The superimposed shape function is what the doublets on the $y = 0$ m centerline are modelling.
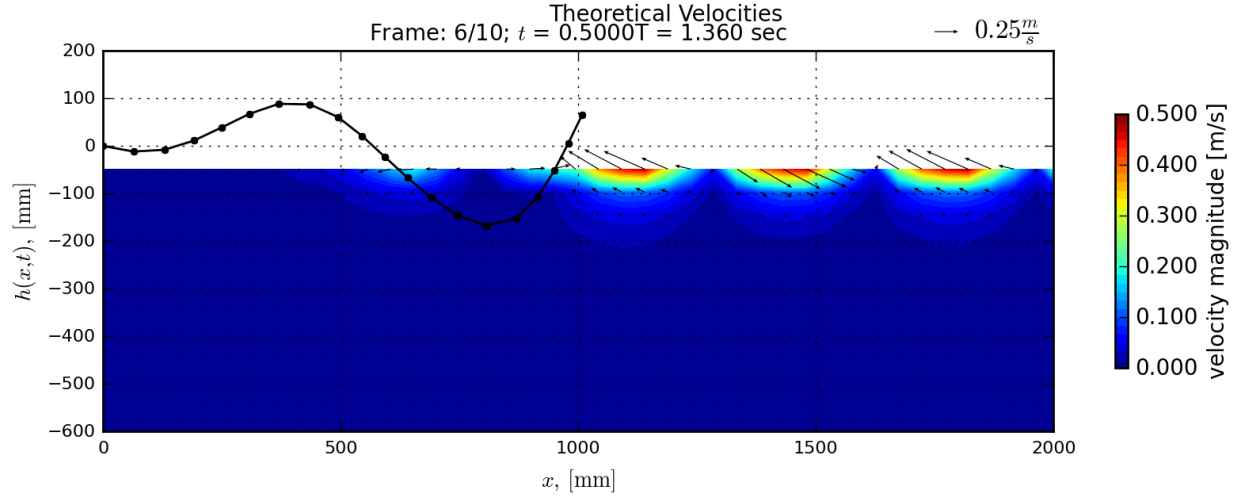
Figure 2.23: Computed velocity field vectors and velocity magnitude downstream of the actual robot shape motion for $t = 0.5T$. The superimposed shape function is what the doublets on the $y = 0$ m centerline are modelling.
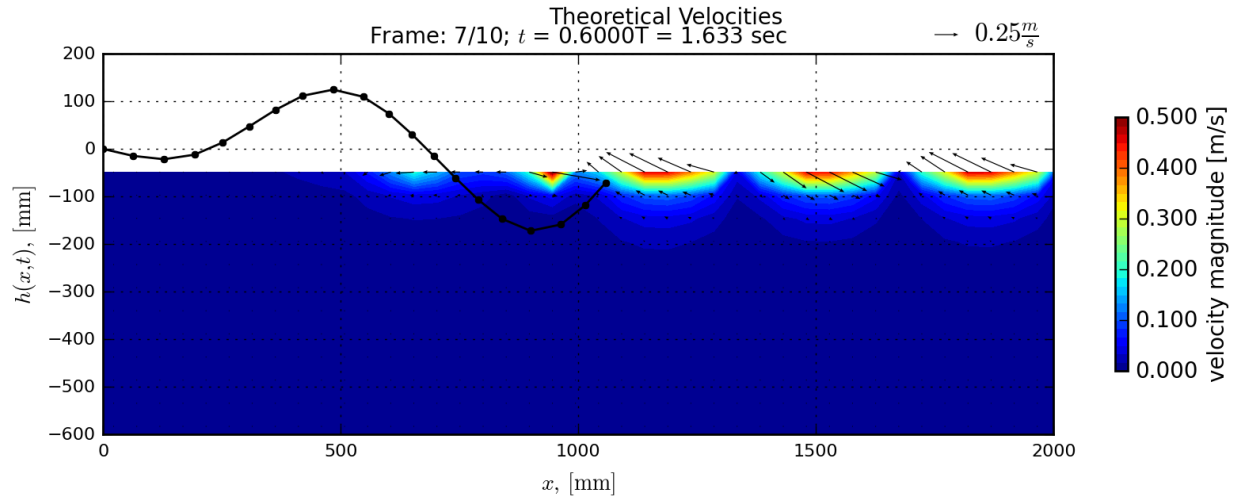
Figure 2.24: Computed velocity field vectors and velocity magnitude downstream of the actual robot shape motion for $t = 0.6T$. The superimposed shape function is what the doublets on the $y = 0$ m centerline are modelling.
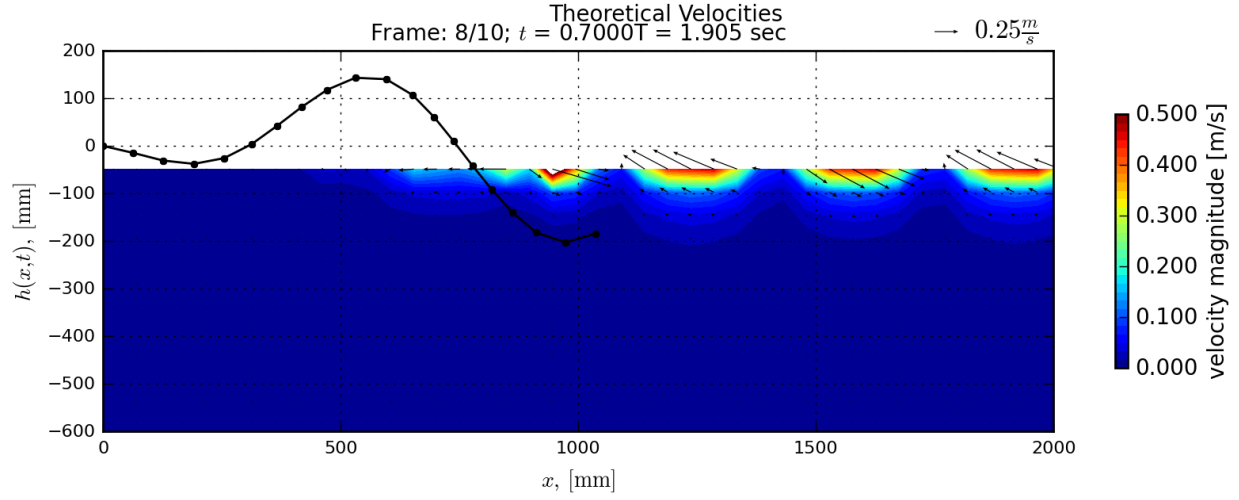
Figure 2.25: Computed velocity field vectors and velocity magnitude downstream of the actual robot shape motion for $t = 0.7T$. The superimposed shape function is what the doublets on the $y = 0$ m centerline are modelling.
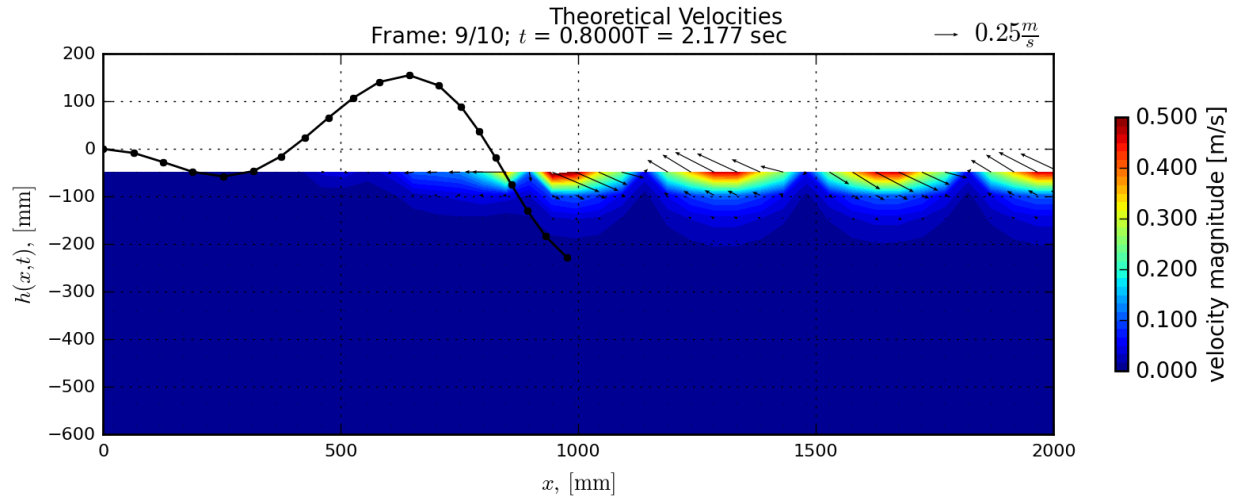
Figure 2.26: Computed velocity field vectors and velocity magnitude downstream of the actual robot shape motion for $t = 0.8T$. The superimposed shape function is what the doublets on the $y = 0$ m centerline are modelling.
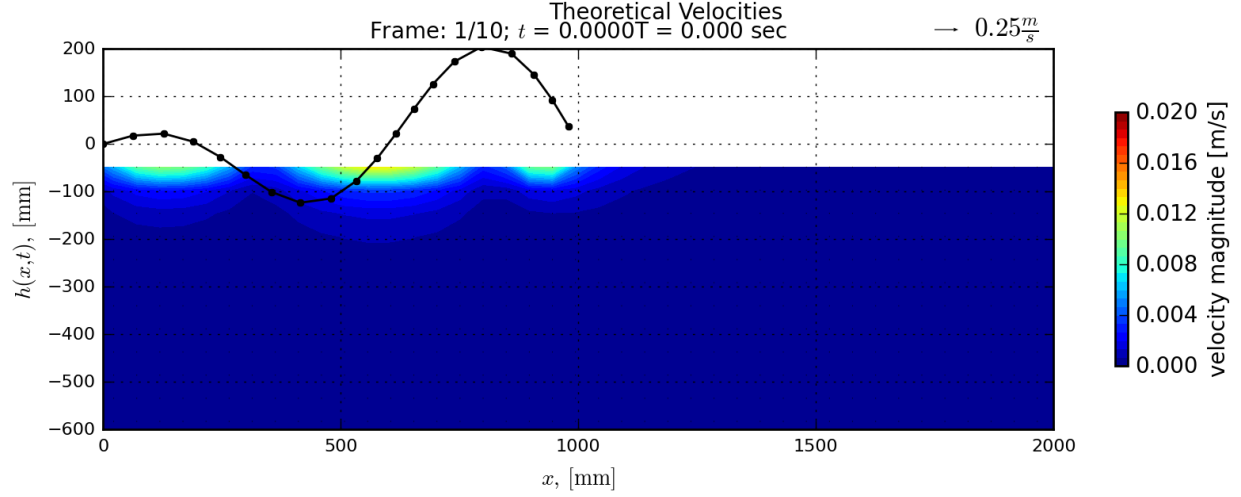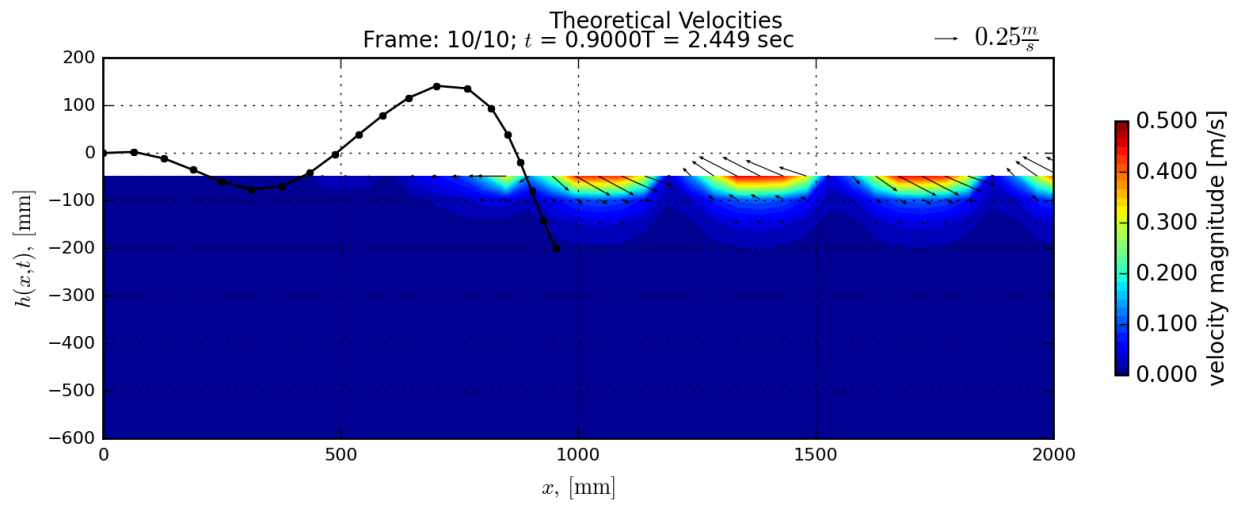
Figure 2.27: Computed velocity field vectors and velocity magnitude downstream of the actual robot shape motion for $t = 0.9T$. The superimposed shape function is what the doublets on the $y = 0$ m centerline are modelling.

CHAPTER III

Anguilliform Robot Development

In order to understand how well a theory works (or does not work), it is imperative that theories undergo experimental testing. For this research, two major systems were required to perform experiments with the theory. The first, development of anguilliform robot prototypes to replicate the theoretical motion, is explained in detail in this chapter. The second, which is the acquisition and setup of the Particle Image Velocimetry wake measuring system, is explained in more detail in Chapter IV.

For this research, anguilliform robot prototypes were developed to be the test beds for the theory developed in Chapter II. The design was driven by the demands of the interested research, which is to replicate the theoretical motion and measure the propulsive wake downstream of this motion. Two prototypes (NEELBOT-1.0 and NEELBOT-1.1) were developed to take advantage of the iterative design approach with several lessons learned from the first one. Prototyping provided ideal scenarios to experience "expected unknowns" and "unexpected unknowns" and compensate for them before the final testing was performed.

Lessons learned from the first prototype (Section 3.1) confirmed the expected and most important need for precise and accurate control of the robotic motion, which was the focus of the second robot (Section 3.2). An initial, linearized system of equations of motion was used to predict the required torques at each joint, aiding in the initial specifying of servo-actuators (Section 3.1.1). Improvements to the second prototype allowed the angles of the robotic joints to be recorded in order to verify the motion (Section 3.2.2). Control theory methods were applied to the second prototype to improve the accuracy of the motion (Section 3.2.3). Unfortunately, the ideal motion was not able to be accurately replicated consistently, but this problem was accounted for by adjusting the

theory appropriately as explained in Section 2.2.2.

3.1 NEELBOT-1.0

The first anguilliform swimming robot was developed to imitate the motion described by the wakeless swimming theory derived in Vorus and Taravella (2011) and to provide a proof of concept and knowledge for the next robotic design revision which will be used for experimental validation (or invalidation) of the theory using the PIV testing equipment. The concept design was initially open-ended with the only constraints being the length, cross section, and the theoretical shape function to be attained. Various component options were researched and decided upon for each aspect of the robot's design such as the waterproofing skin, flexible joint assembly, motion actuators, motion control, power source, wiring, and material properties of the robot's supporting structure.

In parallel, a tethered testing apparatus was designed around the robot for it to be attached to a marine testing facility's tow tank carriage (described in more detail in Section 4.1.1). While tethered to the testing mechanism, the NEELBOT-1.0's underwater swimming motion was measured with image processing software. This image processing analysis has been very successful in comparing the robot's motion to that proposed by the theory. The results of the analysis have quantitatively described the slight errors in the motion and what is needed to improve the results. This initial robotic design and motion measuring method has proven to be very successful and reliable at differentiating the recorded and theoretical motions. Design improvements applied to the robot (for the next prototype, NEELBOT-1.1) for hydrodynamic testing of the wakeless swimming theory are discussed.

3.1.1 NEELBOT-1.0 Dynamics

The following illustrates the simplified, linearized method for computing the forces and moments (torques) at each of the robot's joints. A more accurate, Lagrangian dynamics model was used in the application of the control theory (Section 3.2.3). This method was initially undertaken as an estimate for the expected torques. The forces and moments are computed by solving a matrix set of linear equations. The following dynamic analysis on the eel has only been performed for the case of planar motion in the x-y plane of the robot's frame of reference. The analysis is simply a

discretized model of the eel shape, which replicates the robotic eel nicely when the length of the elements match the segment lengths of the robotic eel. Since NEELBOT-1.1 has 20 segments with 19 joints, the analysis is that of a 19 degree of freedom system.

In all cases the motion of the elements is prescribed by the theoretical motion defined by Vorus and Taravella (2011) in equation 2.56. The forces (F_{Hx} and F_{Hy}) acting on the center of the elements are computed by summing the hydrodynamic sectional forces per unit length (f_x and f_y) along the segment length on which it acts.

$$F_{Hx,n} = l_n f_x \tag{3.1}$$

$$F_{Hy,n} = l_n f_y \tag{3.2}$$

Below are the equations to compute the sectional forces per unit length along the shape function. Vorus and Taravella (2011) derive f_y and f_x as the transverse and longitudinal sectional forces, respectively:

$$f_y(\bar{x}, \bar{t}) = -\rho \pi r_o^2 k(\bar{x}, \bar{t}) \tag{3.3}$$

$$f_x(\bar{x}, \bar{t}) = -f_y(\bar{x}, \bar{t}) h_x(\bar{x}, \bar{t}) \tag{3.4}$$

where h_x denotes the partial derivative with respect to x of equation 2.56. The function $k(\bar{x}, \bar{t})$ is defined by Vorus and Taravella (2011) to be

$$k(\bar{x}, \bar{t}) \equiv h_{tt} + 2U_o h_{xt} + U_o^2 h_{xx} \tag{3.5}$$

which is based on the linearized kinematic boundary condition applicable on the cylindrical surface of the eel and the 2-D perturbation potential for a circular cross-section with velocity in the y-direction. The subscripts denote partial derivatives with respect to the specified variable.

Figure 3.1 is a free body diagram illustrating the forces acting on eel segment n, where F_H denotes the hydrodynamic forces and F_x and F_y denote the internal forces at the nodes.

60
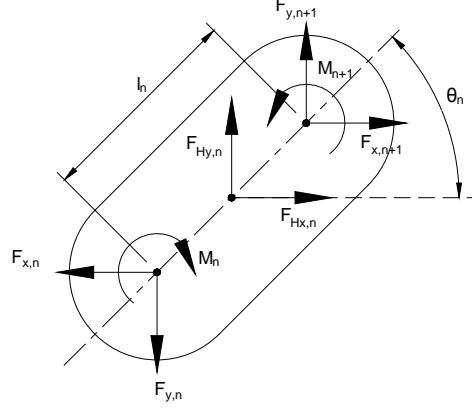
Figure 3.1: Free-body diagram of eel segment n.

3.1.2 Untethered Swimming (free swimming)

For this case, the boundary conditions are that the forward joint (or node) of the forward-most segment and the aft node of the last segment are set to zero:

$$F_{x,1} = 0 \qquad\qquad\qquad F_{x,N+1} = 0$$

$$F_{y,1} = 0 \qquad\qquad\qquad F_{y,N+1} = 0$$

$$M_1 = 0 \qquad\qquad\qquad M_{N+1} = 0 \qquad (3.6)$$

where N is the number of segments.

Going back to the free-body diagram of Figure 3.1, the x-direction forces, y-direction forces, and moment about the z axis can be equated to the inertia in each of these directions to obtain

$$\sum F_x = m_n A_x \qquad (3.7)$$

$$\sum F_y = m_n(a_{n,y} + A_y + \alpha_E l_n(-\frac{N}{2} + n - 0.5)) \qquad (3.8)$$

$$\sum M_z = I_n(\alpha_{z,n} + \alpha_E) \qquad (3.9)$$

$$n \in [1, N]$$

where m_n is the mass of segment n and A_x is the global acceleration of the robotic eel in the x-direction. The variable $a_{n,y}$ is the local acceleration of segment n at the midpoint of the segment in

61

the y-direction, and the global acceleration in the y-direction is denoted by A_y. The global angular acceleration is denoted by α_E.

Completing the left-hand side of the equation, the summation of forces and moments follows

$$\sum F_x = F_{x,n} - F_{x,n+1} + F_{H_x,n} \tag{3.10}$$

$$\sum F_y = -F_{y,n} + F_{y,n+1} + F_{H_y,n} \tag{3.11}$$

$$\sum M_z = -M_n + M_{n+1} + (F_{y,n+1} + F_{y,n})\frac{l_n}{2}\cos\theta - (F_{x,n+1} + F_{x,n})\frac{l_n}{2}\sin\theta \tag{3.12}$$

$$n \in [1, N]$$

Equating the forces/moments and their respective inertia terms and rearranging, one can place the system of equations in matrix form:

$$\mathbf{A}\underline{f} = \mathbf{B} \tag{3.13}$$

where

$$\mathbf{A} = \begin{bmatrix}
1 & 0 & 0 & -1 & 0 & 0 & \cdots & -m_n & 0 & 0 \\
0 & -1 & 0 & 0 & 1 & 0 & \cdots & 0 & -m_n & -m_n l_n(-\frac{N}{2}+n-0.5) \\
-\frac{l_n}{2}\sin\theta & \frac{l_n}{2}\cos\theta & -1 & -\frac{l_n}{2}\sin\theta & -\frac{l_n}{2}\cos\theta & 1 & \cdots & 0 & 0 & -I_n \\
\vdots & \vdots & \vdots & \vdots & \vdots & \vdots & \ddots & \vdots & \vdots & \vdots \\
1 & 0 & 0 & -1 & 0 & 0 & \cdots & -m_n & 0 & 0 \\
0 & -1 & 0 & 0 & 1 & 0 & \cdots & 0 & -m_n & -m_n l_n(-\frac{N}{2}+n-0.5) \\
-\frac{l_n}{2}\sin\theta & \frac{l_n}{2}\cos\theta & -1 & -\frac{l_n}{2}\sin\theta & -\frac{l_n}{2}\cos\theta & 1 & \cdots & 0 & 0 & -I_n
\end{bmatrix}$$

$$\tag{3.14}$$

$$\underline{f} = \begin{bmatrix} F_{x,n} \\ F_{y,n} \\ M_n \\ F_{x,n+1} \\ F_{y,n+1} \\ M_{n+1} \\ \vdots \\ A_x \\ A_y \\ \alpha_E \end{bmatrix} \tag{3.15}$$

and

$$\mathbf{B} = \begin{bmatrix} -F_{H_x,n} \\ m_n a_{n,y} - F_{H_y,n} \\ I_n \alpha_{z,n} \\ \vdots \\ -F_{H_x,N} \\ m_N a_{N,y} - F_{H_y,N} \\ I_N \alpha_{z,N} \end{bmatrix} \tag{3.16}$$

The dimensions of the above matrices are as follows:

$$\mathbf{A} : [3N \times (3N + 6)]$$

$$\underline{f} : [(3N + 6) \times 1]$$

$$\mathbf{B} : [3N \times 1]$$

One can immediately notice that the number of equations is less than the number of unknowns, making this system of equations unsolvable. However, this problem is resolved by applying the
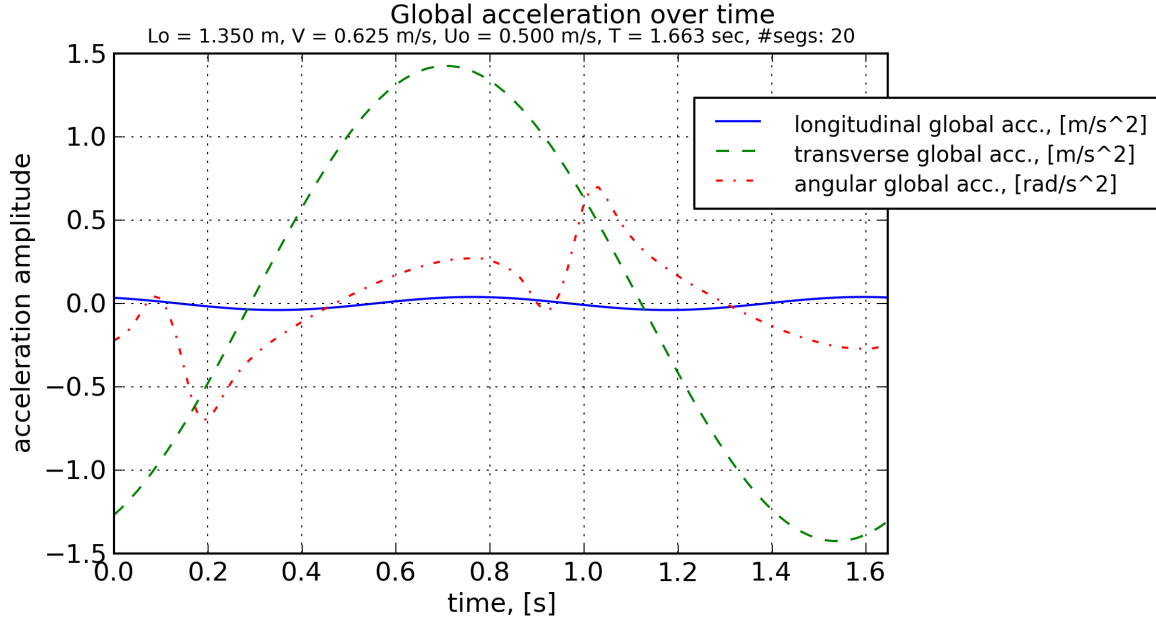
Figure 3.2: Global translational and angular accelerations of NEELBOT-1.1.

boundary conditions set in equations 3.6. The dimensions of the matrices become

$$\mathbf{A} : [3N \times 3N]$$

$$\underline{f} : [3N \times 1]$$

$$\mathbf{B} : [3N \times 1]$$

making the system solvable for the unknown vector $\underline{f}$.

This system of equations is solved for each time step over the cycle of motion giving the global accelerations (Figure 3.2), transverse and longitudinal forces at each joint (Figures 3.3 and 3.4), and the torques at each joint (Figure 3.5). For each of the plots, the servo number represents the interested joint, where 1 is at the head and 20 at the tail.

3.1.3 Tethered Swimming Case (PIV Testing)

This case is similar to the one above except that the forces/moment are set to zero solely on the aft point of the last segment. This is to model the transverse and longitudinal forces and moment about the z-axis at the head in order to predict what forces/moment will be induced on the tether apparatus. It is also used to predict the torques at each joint and ensure that the servo-actuators
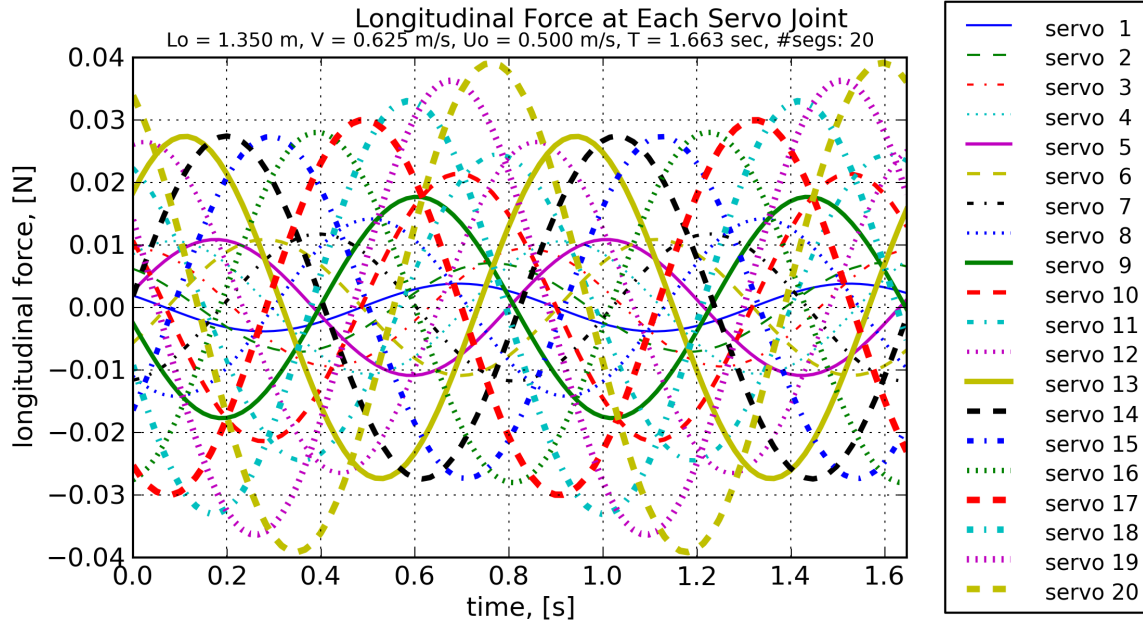
Figure 3.3: Longitudinal forces of NEELBOT-1.1 over time.
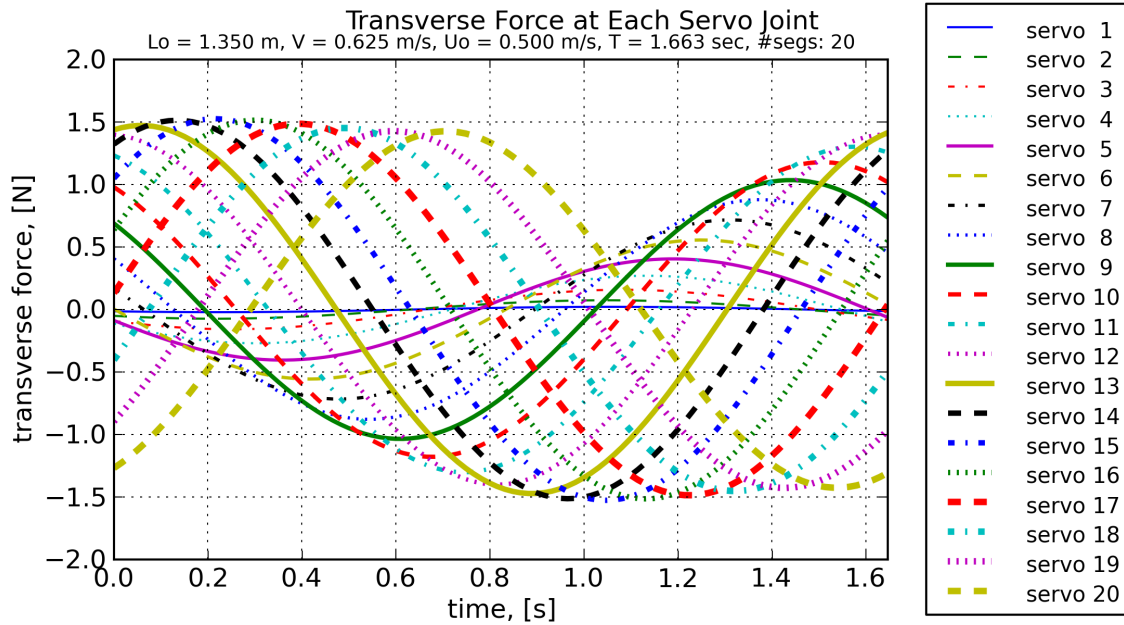
Figure 3.4: Longitudinal forces of NEELBOT-1.1 over time.
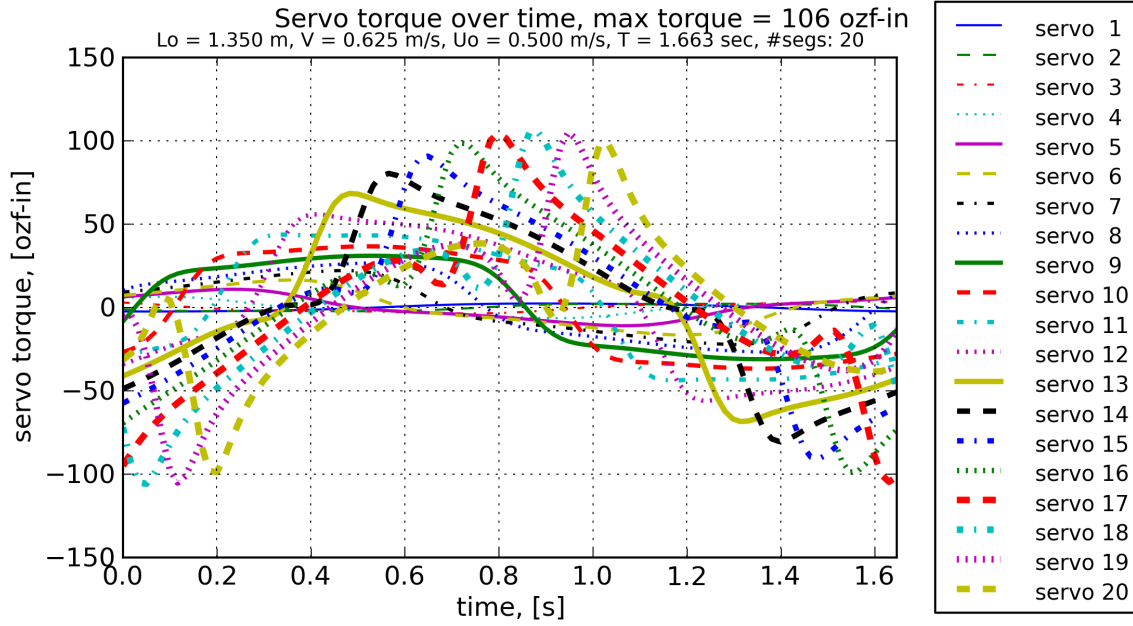
Figure 3.5: Servo torques of NEELBOT-1.1 over time.
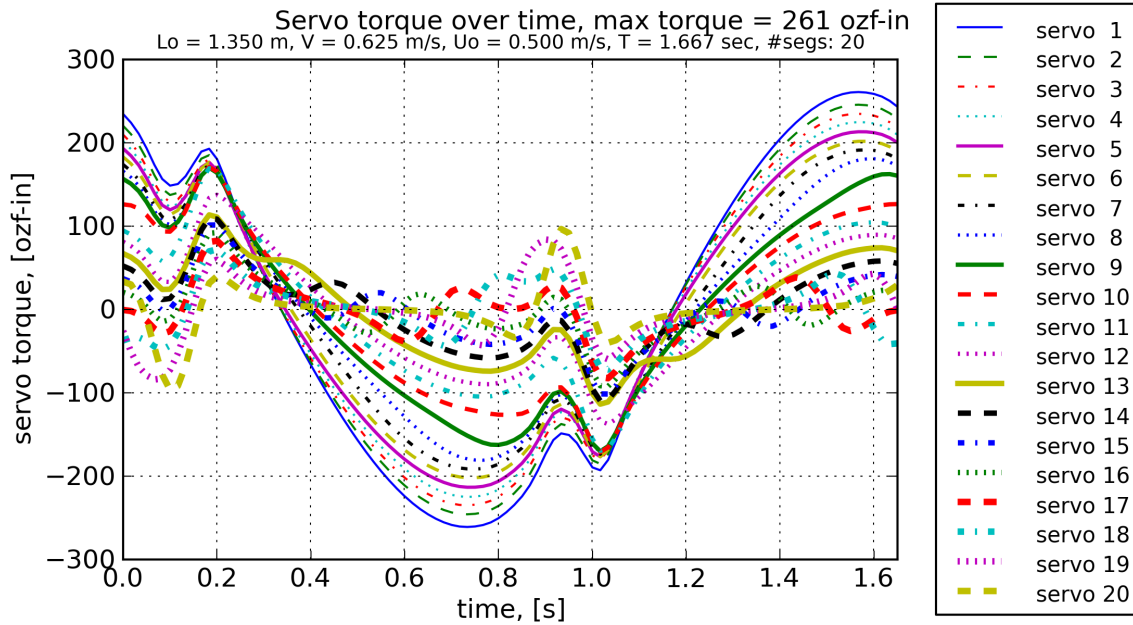
Figure 3.6: Servo torques of the robotic eel over time with head fixed.
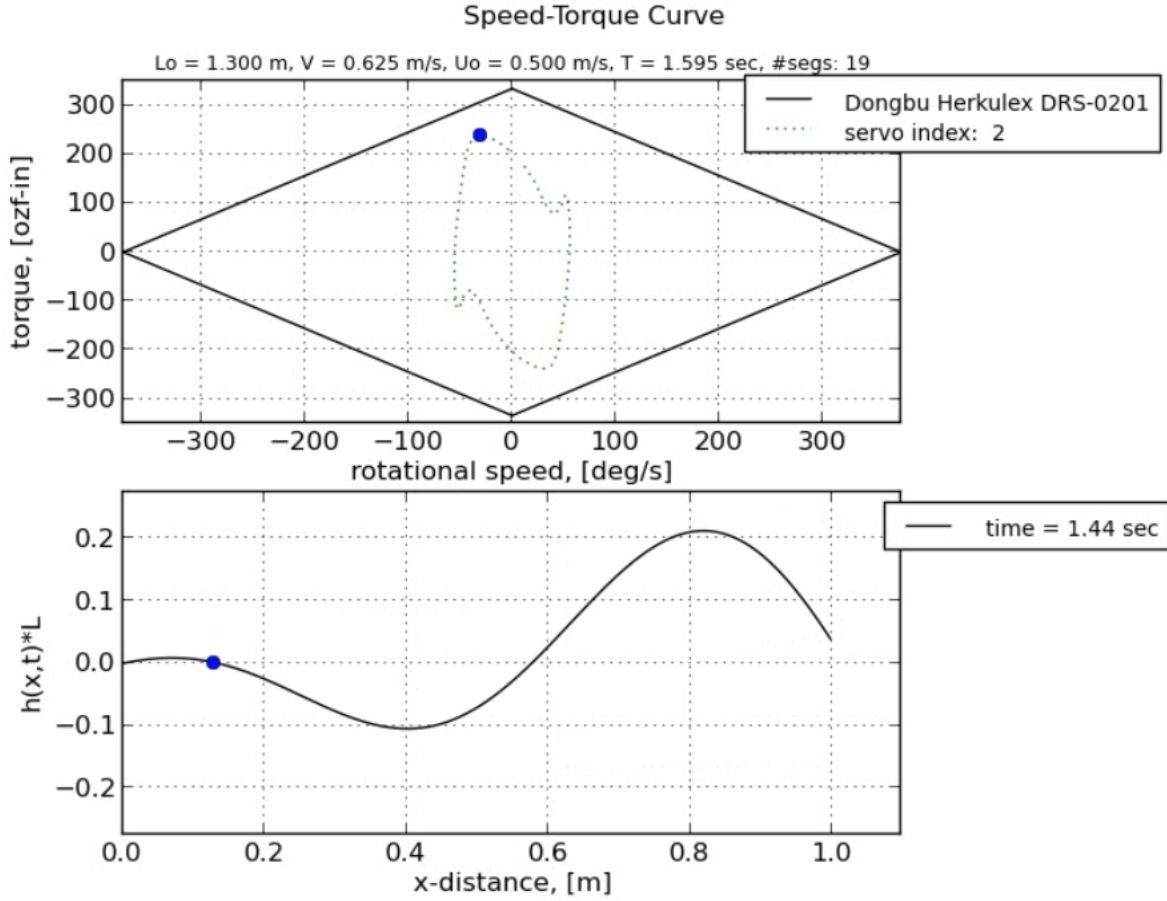
Figure 3.7: Rotational Speed-Torque curve for Dongbu Herkulex DRS-0201 (servo index 2).

can provide the required torque. Figure 3.6 shows the predicted torques for each joint over time, and the maximum predicted for this nominal speed case of 0.5 m/s is 261 ozf-in, which is 21% less than the vendor-supplied torque of 334 ozf-in.

Figure 3.7 shows a screen shot of a speed-torque curve with the limits of the specifications of the Dongbu Herkulex DRS-0201. The servos are actuated with a permanent-magnet direct-current (PMDC) motor, giving it a linear limit specifications curve. The green dotted curve inside the diamond-shaped limit specifications is the path in speed-torque space that the servo traverses over time. In this plot, the path is traversed in a clock-wise direction, and the predicted phase-space curve is within the vendor-supplied torque-speed specifications. This shows that the predicted, required torque can be achieved with the specified servos. The bottom half of the figure shows the position of the anguilliform shape in physical space for the moment in time at which it coincides with the position on the aforementioned phase-space curve.
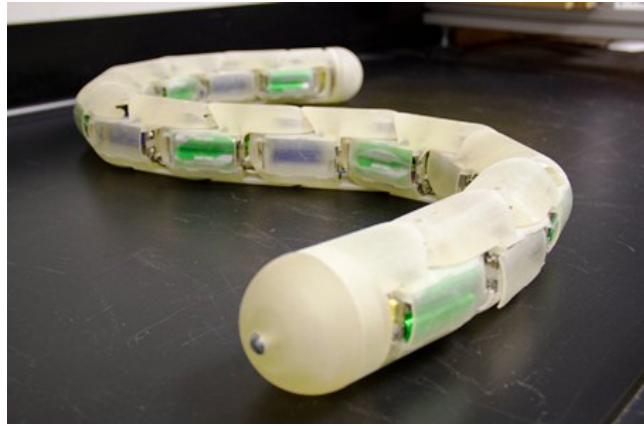
Figure 3.8: NEELBOT-1.0 robot design (without waterproofing skin). (photo courtesy of UNO Marketing Dept.)

3.1.4   Development of NEELBOT-1.0

The process of designing the first functional robot required several design iterations, and more detail on the product design process is provided in Potts et al. (2013), but a brief overview is given here. Each iteration within the first prototype design provided much needed knowledge about how the robot is to actually function considering the interaction of the individual components and their assemblies. This effectively turned into a trial and error exercise with product design principles for component and design selection borrowed from Ulrich and Eppinger (2008). Designing the product on paper (or in a CAD modeling program) can only go so far. It was necessary to actually fabricate components and see how they interact with one another. Before design fabrication and during concept generation, several other current designs of eel-like robots were researched and compared to the goals of our robot. Researched designs include but is not limited to those from Wilbur et al. (2002), Stefanini et al. (2012), Yamada et al. (2005), Leftwich and Smits (2011), and Hultmark et al. (2007), with the design described in this paper standing out from the others since the motion is based on the very efficient hydrodynamic theory of Vorus and Taravella (2011). The completed first prototype of NEELBOT-1.0 without its waterproofing skin is shown in Figure 3.8.

This first prototype used commercially available Traxxas 2075 servos with internal proportional control, using pulse-width modulation (PWM) to specify the angular position. A servo control board was used to send PWM signals to the 13 servos from a pre-programmed motion script. The segments were fabricated with a 3-D printer, the Objet Eden 350, using a fused deposition
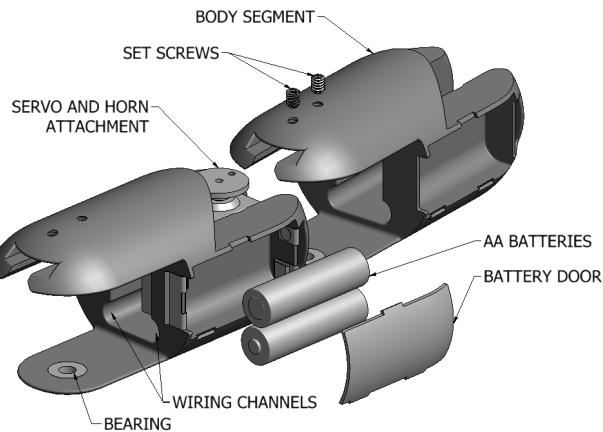
Figure 3.9: Exploded view of two body segments and internal components (wiring omitted) of NEELBOT-1.0.
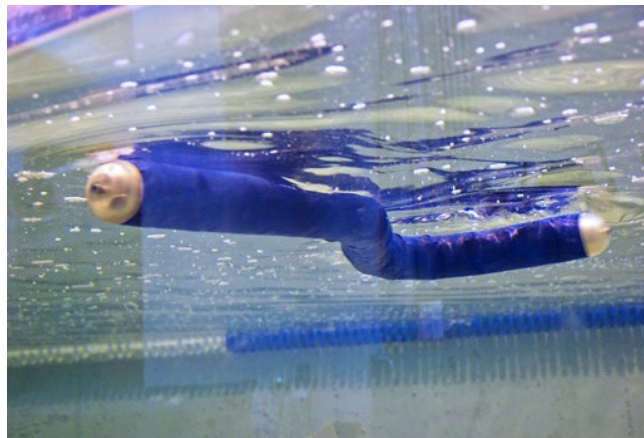
Figure 3.10: NEELBOT-1.0 swimming with waterproof skin. (photo courtesy of UNO Marketing Dept.)

modelling process. Figure 3.9 shows an exploded diagram of the NEELBOT-1.0 segments. As one can see, each segment contains four AA batteries, which are wired in a combination of series and parallel configurations to provide the correct amount of voltage and current. The pathways for the power and signal wires were significantly widened since the initial iteration to allow ample freedom of movement of the wires during segment rotation and to minimize rotative resistance.

The waterproofing membrane is a very critical component that must completely seal the inner workings of the robot from the aquatic environment. The skin was created by brushing several layers of the latex on to a cylindrical mold until an approximate thickness of 1/32" was achieved. This material has proved to be very useful since it minimally constricts the movement. Figure 3.10 shows the robot swimming just below the water surface with its waterproofing skin.

As stated above, Potts et al. (2013) provides much more detail on the general particulars and development process of the first prototype.

3.1.5 Lessons Applied Towards NEELBOT-1.1 Development

The goal of the research at this stage was to show a proof of concept robot can be created to mimic the ideal anguilliform swimming motion prescribed by Vorus and Taravella (2011) and to practice the expected tethered testing to be done on the next prototype. Motion verification was completed by using an image processing software algorithm that has been fine-tuned to be used for future prototypes. Although there are slight discrepancies, the current results show reasonably good accuracy between the theoretical motion and the actual robotic motion. One reason for the discrepancies is attributed to the most critical component of the design—the servo-style actuators. The Traxxas 2075 servos only provide proportional control, allowing for steady-state errors to arise due to the omission of integral control that sums the angular error over time.

The next design revision will include motion actuators that contain PID (proportional-integral-derivative) control, which will eliminate the steady state error (Ogata (2001)). In addition to the feedback within the closed-loop control system, these proposed actuators will also provide positional feedback to a data acquisition system, which can be analyzed for comparison with the theoretical motion, eliminating the need for image-processing verification, or at least making it redundant. These actuators chosen will also be stronger in terms of torque and speed provided which will overcome any unexpected inertial, rotative spring constant, or added mass resistance.

The NEELBOT-1.0 design could not be remotely operated. The motion was pre-programmed onto the servo control board, and the robot undulated upon the immediate push of the on-off switch, resulting in poor usability on the carriage during testing. NEELBOT-1.1 has the capability to be operated remotely.

This first prototype design allowed for unknowns to be tested without risking unwanted consequences of damage or monetary loss to a final prototype and thus a time-schedule setback.

Figure 3.11: Rendering of NEELBOT-1.1 showing off its sleek curves. The green cylinders are the AAA batteries with 2 per segment, and the dark blue boxes are the servo-actuators.

Figure 3.12: Shown is the NEELBOT-1.1 without its waterproofing skin, but showing off its translucent body segment shells. The translucence allows the LED status lights of the servos to be visible during use.

3.2 NEELBOT-1.1

NEELBOT-1.1 is a vast improvement over NEELBOT-1.0 in terms of servo-actuator torque and angular speed, size, programmability, more continuous shape attributed to segment design, neutral buoyancy and stability, and usability during testing. The servos are much more powerful than the original ones and are now able to be programmed serially and on the fly, allowing for maneuvering testing. Additionally, they contain proportional-integral-derivative controllers and can report their angular position over time back to the mainframe. The segments are designed to more compactly contain its internal equipment, including the wiring, batteries, and servos. The segments are also much shorter longitudinally, giving a much more continuous shape when replicating the ideal motion. The mass of each segment and its contents was much more precisely controlled to obtain a neutral buoyancy. The robot is also more robustly designed in terms of its structure, allowing for more testing to be endured.

NEELBOT-1.1 ended up being 20 segments with 19 servo-actuators at an overall length of 1.35 m (the length used for analysis spans from the centers of the forward and rear hemispheric domes,

hence the length of 1.3 m used for analysis). The diameter is 55 mm with the latex waterproofing skin, and each segment's length from joint axis to joint axis is 65 mm.

The dimensions were finalized through a combination of a parametric analysis and physical constraints of the system design. The shortest attainable segment length was 65 mm due to the length of the servos and the batteries. With 2 AAA batteries per segment, 20 segments provides just the right amount of capacity, voltage, and current to power the actuators and wireless communications. The servos are very new and were imported into the US less than a month before we ordered them.

Varying the length, segment diameter, and segment length, the parametric analysis using the discrete dynamics equations of motion determined that the required torque decreased with the ratio of diameter to length. Intuitively, this makes sense. The analysis suggested smaller diameters to decrease the mass and added mass, which decreases the inertia required to be overcome by the actuator torque. The analysis forced the segment length to decrease infinitesimally, but this was physically constrained by the internal components, as stated earlier. The provided torque of the chosen actuators is more 2.5 times that of the original ones, at the same angular velocity.

3.2.1 NEELBOT-1.1 Design Details

3.2.1.1 Segment Design

Here is a rendering of the 3-D model of the entire NEELBOT-1.1, excluding the wiring. Unfortunately, it is rather difficult to model the wiring in Inventor and was deemed unnecessary for the amount of effort. Actual prototyping and testing out the physical product overcame this problem. This full 3-D model within the computer allowed for the inspection of any interferences at any of the joints during full rotational displacements. It's amazing how fast a design can be made and verified within a 3-D modeling program, and I have tons of respect for those that performed complex product development before the advent of computer modeling.

3.2.1.2 Dongbu Herkulex DRS-0201 Servo-actuators

Each servo actuator has a closed-loop PID position controller with programmable PID gains. The servo contains a permanent magnet direct current (PMDC) motor with a gearbox reducing
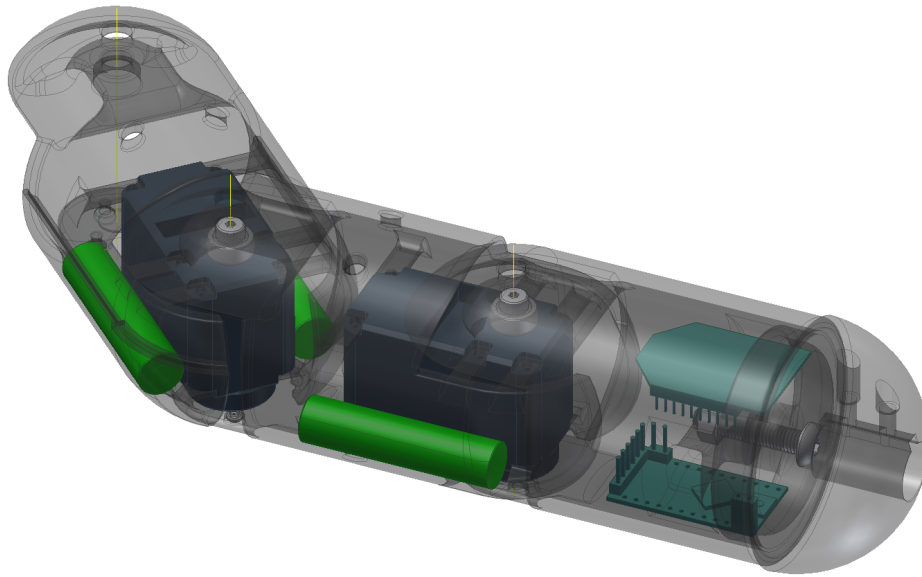
Figure 3.13: Rendering of three segments and their joints of NEELBOT-1.1. The green cylinders are the AAA batteries with 2 per segment, and the dark blue boxes are the servo-actuators. The turquoise components in the head, which is the right-most segment, are the circuit boards used to communicate wirelessly with a desktop PC and transmit the servo commands down the length of the robot. Wiring is omitted, but it passes through the top of the segments inside very smooth passageways, minimizing friction.

the speed of the motor and increasing the torque. The angular position output of the gear box is measured by a 10-bit encoder which is read by a micro-controller connected to the motor driver. The micro-controller handles closing the feedback loop of the actuator and communicates with the outside world via serial UART (Dongbu Robotics (2012)). This is how it communicates with the LabVIEW program (Section 3.2.1.4) via an XBee wireless controller (Section 3.2.1.5).

The servo uses pulse-width-modulation (PWM) to change the motor voltage. The batteries supply a constant voltage but the motor is controlled by varying the voltage, which is accomplished by PWM. The servo-actuators' specifications and physical characteristics are listed in Table 3.1. This combination of parameters fit the needs of the NEELBOT-1.1 and the constraints of the project budget the best of all the actuators of a similar type found on the market. In fact, this actuator had the highest torque and angular speed for its physical size, mass, and cost, compared to similar models available on the commercial market.

If money and time were unlimited, a custom servo-actuator would be designed to fit within the physical constraints of the NEELBOT-1.1 body. This custom actuator would most likely surpass any commercially available options by a wide margin. The actuator would be designed with mass and center of mass parameters in mind. This contrasts with the DRS-0201 in that the actuator is confined to a pre-defined prism, limiting the product design options with regards to orientations available.

3.2.1.3   Latex Rubber Waterproofing Skin

The latex rubber skin is extremely critical in that it protects all the internal components of the robot from getting wet, and thus destroying them. Initial design ideas consisted of obtaining waterproof components for the servo-actuators and communication board, but this proved too difficult to make everything waterproof. As a result, a waterproofing skin was deemed the best solution to protecting the important internal devices. Figure 3.2.1.3 shows the blue latex rubber skin installed on NEELBOT-1.1.

Brushable latex rubber proved to be the best material to use as the skin because of its cost, ease of fabrication, and elasticity. The latex rubber was brushed on to a male mold, totaling 8-10 coats, until a thickness of 0.5 mm was obtained. The dried product was peeled off the mold. Fabricating it this way prevented it from being completely enclosed like a sealed balloon, so both ends were

Table 3.1: Dongbu Herkulex DRS-0201 physical characteristics and specifications.

Parameter	Value
width	45 mm
depth	24 mm
height	31 mm
mass	60 g
gear ratio	1:266
voltage	7-12 VDC
current	670 mA @ 7.4 V
stall torque	2.4 N-m
max speed	408 deg/s
resolution	0.325°
cost	$125

open to the elements. Each end was sealed with hemispheric domes as described earlier.

The elasticity of latex rubber is very high, reducing any constraints on the angular movement of the joints. In addition, the skin was 0.5 mm thin, reducing the force of the elasticity. Dry lubricant such as baby powder was placed on the inside of the skin to minimize dynamic friction between it and the body. The skin was pre-tensioned slightly along the length of the eel during installation to minimize any wrinkles that may occur.

These aspects contributed to achieving the goal of minimal wrinkles along the length and minimizing the resistance due to angular displacement of the joints. Minimal wrinkles contributed to the robot replicating the desired motion shape as best as possible. Minimal resistance of the angular joints allowed the servo-actuators to focus more of their torque on overcoming the inertial, centripetal, coriolis, and added mass loads.

3.2.1.4 NEELBOT-1.1 Motion Program

The program that manipulates any actions of NEELBOT-1.1 was written in-house using LabVIEW™ software. This programming language was chosen for its ease of interaction with external hardware, specifically hardware provided by National Instruments™ that is fully customizable. The LabVIEW Real-Time (RT) program controls all data going in or pout from the robot, i.e. any mo-
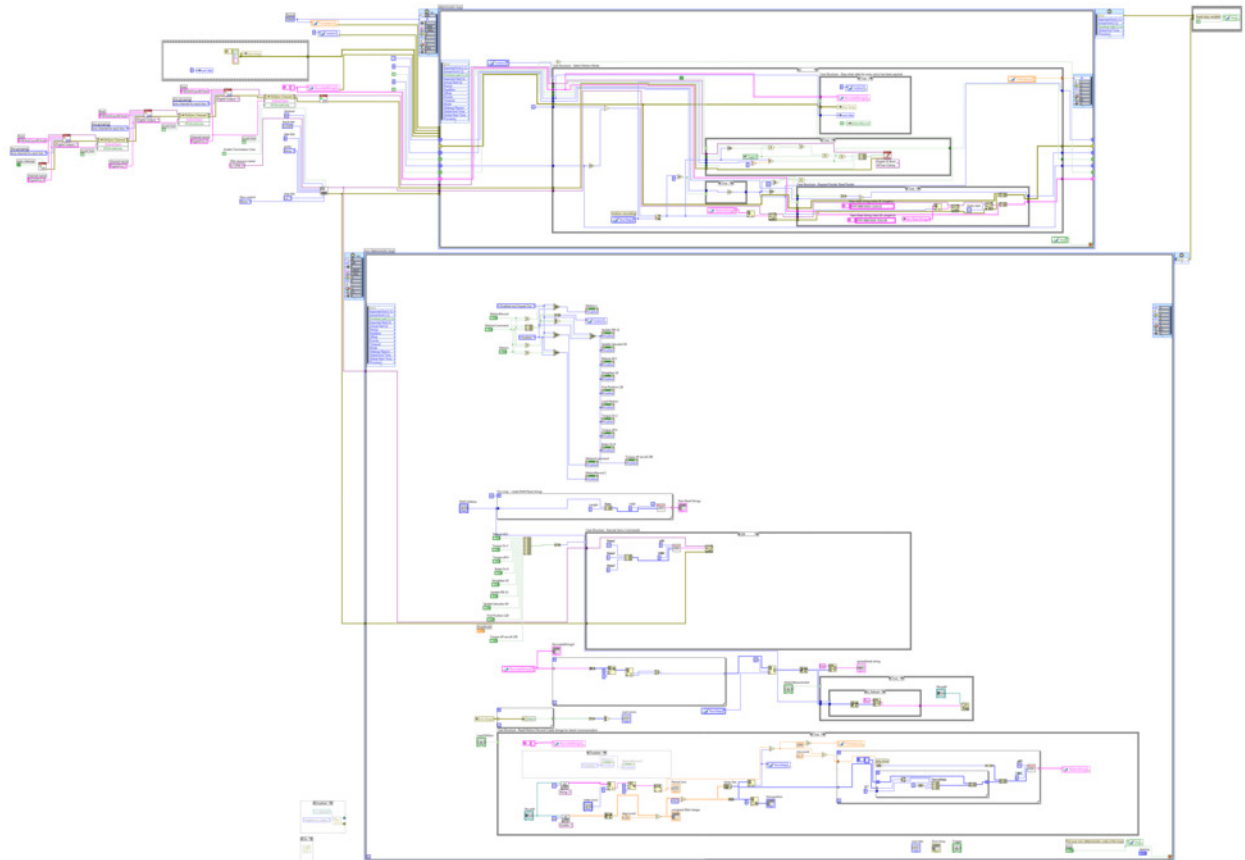
Figure 3.14: LabVIEW code of the program that controls all motion aspects of NEELBOT-1.1. It reads in a shape function file, transmits the encoded data to a wireless transceiver, and receives and records the servo-actuator angles.

tion programming or servo angle reporting. The program consists of 2 main parts: a time-critical loop and a front-panel communication loop. The time-critical part consists of a very accurately time-controlled loop to control the timing of all motions and sending of motion data. It was found that the minimum period of this loop could be 66.3 ms, which consists of sending motion commands and feedback position recording. This was only for a single servo reporting feedback too, prohibiting the use of a more advanced control scheme that requires knowledge of all the servo's positions. The short time period of the loop makes it difficult for inverse dynamics computations to be performed for the advanced control schemes. These problems are discussed in more detail in Section 3.2.3.

Conservatively, the minimum timestep length used was 68.0 ms which coincides with 40 timesteps for the NEELBOT-1.1 motion with a 2.72 second nominal time period. This time-critical loop period length consisted of a timeout portion of the period, in which data sent back from the servos is recorded. The timeout portion of the period was found to be somewhat unpredictable, necessitating an additional margin of time. A 7.5% increase was chosen rather arbitrarily from trial and error, and it was found that this decrease the number of packet errors significantly while adhering to a relatively large number of time steps to prevent the motion from becoming jerky.

The other major part of the motion program is the front-panel communication loop, which pertained to any user interactions occurring in the graphical user interface (GUI) of the program. Any user inputs were contained in this loop and then passed to the time-critical loop at opportune times to not affect the system and bog it down. The front-panel contains actions such as resetting the robot or starting the sending of motion commands. All commands are sent using a serial communication protocol specific to the servo-actuators via the XBee wireless communication board, described in the next section.

Figure 3.14 shows the LabVIEW program of the motion program application, where one can see the two loops and the data paths between the two. Figure XXX shows the front-panel GUI that is used for user-inputted actions.

3.2.1.5   XBee Wireless Communication Board

NEELBOT-1.1 communicated with the external computer using an XBee-PRO® ZB RF Module (ZB: ZigBee; RF: radio-frequency), which was powerful enough to communicate through several

inches of water even the electromagnetic spectrum. The XBee-PRO® ZB RF Modules are designed to operate within the ZigBee protocol and support the unique needs of low-cost, low-power wireless sensor networks. The modules require minimal power and provide reliable delivery of data between remote devices. The modules operate within the ISM (Industrial, Scientific, & Medical) 2.4 GHz frequency band (Digi International (2009)).

This device can transmit a signal up to 1 mile in distance outdoors or up to 300 feet indoors. Its peak current for transmission is 295 mA at 3.3 V. This agrees with the available voltage and current provided by the battery circuitry. However, a voltage regulator and divider was required for the decrease in voltage required compared to the supplied amount.

Its small form factor and mass fit well within the constraints of the robot design. Its length and width is 2.438 cm by 3.294 cm. It can withstand a temperature range of -40 to 85°C.

Its serial data rate range of 1200 bps to 1 Mbps agreed with the range required for direct communication links with the Dongbu servos. The module is wired directly to the signal wires of the servos and communicates serially using an asynchronous method, with the key being that the baud rates for the XBee module and servos are equal.

This necessary electrical component was chosen mainly because of its cost, small size, and small mass. It is the six-sided object in the head of the NEELBOT-1.1 segments shown in Figure 3.13.

3.2.1.6   Mass Distribution

The buoyancy and mass distribution of NEELBOT-1.1 is absolutely critical to prevent the robot from floating or sinking relative to the PIV measurement plane. Since the cross-sectional area of the robot is constant along the length, except for the hemispheres at the ends, the buoyancy per unit length is constant. In the fresh water of the UNO Towing Tank at a temperature of 16° C, the water density is nominally 998.905 kg/m^3 with a gravitational constant of 9.793165 m/s^2 (ITTC (2011) and USGS (2006)). The displacement of this water by the robot with a circular cross-sectional radius of 27.75 mm (includes thickness of latex skin) provides a buoyancy per unit length of 2.417 g/mm (0.02367 N/mm) along the constant cross-section part of the robot (see the dotted curve in Figure 3.15 for the buoyancy distribution along the length). Including the ends, the volume of the robot as calculated from the design displaces 3231.0 g. This desired mass was set as the goal for the total mass of the robot for the finalized design.
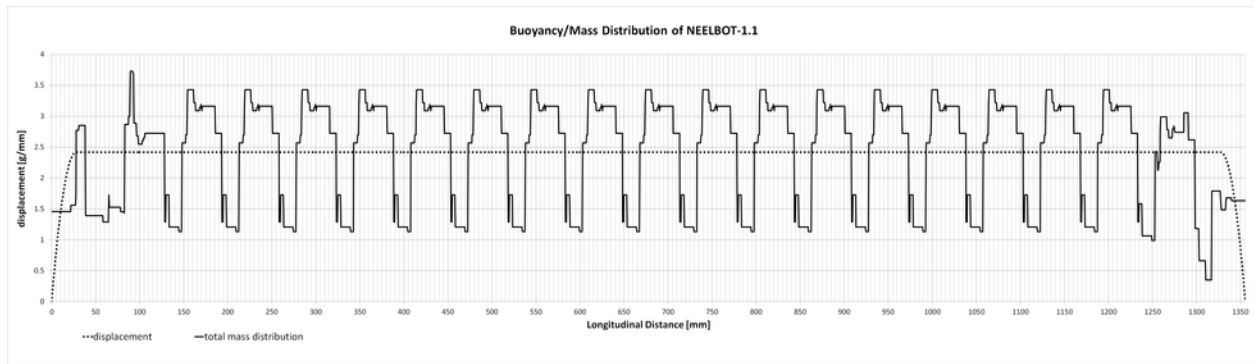
Figure 3.15: Buoyancy/mass distribution of NEELBOT-1.1.

During the build, all components were accurately measured on a scale with a precision of ±0.1 grams to aid in keeping within the desired mass. A main objective of the design is to match the mass distribution to that of the buoyancy distribution along the length. This minimizes any bending moments in the longitudinal direction that can place unnecessary stresses on the rotational joints and increasing the dynamic friction, forcing the servo-actuators to waste energy that could be used to properly define the motion. Bending moment can also possibly force the robot to sag or hog along the length, preventing NEELBOT-1.1 from staying within the measurement plane of the PIV.

It is almost impossible to design a physical system containing internal discrete, commercial-off-the-shelf (COTS) components to have a uniform mass distribution across the entire length. However, a constant eye towards this goal was kept during the design-build process. Components were placed to the best ability with this goal in mind even while acknowledging other constraints such as the physical limitations of space. The dark line in Figure 3.15 shows the mass per unit length of NEELBOT-1.1 due to all the individually weighed components. As one can see, the line is not nearly as uniform as the buoyancy distribution due to the discrete nature of physical components. The components not only included the obvious ones such as the servo-actuators, body shell, batteries, latex skin, wireless communication board, and wiring, but also the tiny screws attaching the servos to the body shell, the solder for the wiring, joint bearings, and lead-tape ballast. It was very difficult to measure everything accurately before the system was completely built because it was hard to pre-determine how much solder or wiring would be used. In the end, ballast was added to attain the final, desired mass and mass distribution.

Figure 3.16: Bottom side of NEELBOT-1.1 showing attached lead tape used as ballast.

During the product development process, it was easier to keep the design under the desired mass and then add small increments of ballast at the end to obtain an accurate mass. This was indeed the case with the addition of thin lead-tape to the underside of the robot. The lead-tape is the same as that used by golfers to change the center of mass of their golf clubs to aid in their swinging motion. Figure 3.16 shows the lead tape attached to the underside of NEELBOT-1.1 on the last couple of segments. Attaching it to the underside also lowered the center of gravity of the robot relative to the center of buoyancy, thus keeping it stable in roll. The lead tape was very thin and minimally affected the surface smoothness of the robot; the elastic latex skin smoothed out the transitions between tape and no tape. The tape also had the advantage of being able to distribute the mass over a long length giving a very uniform mass distribution per unit length, over concentrated ballast such as bee-bee's or pellets.

One concern was the depressing of the latex skin due to hydrostatic pressure on areas of the body that couldn't provide support against this problem. The depressions reduce the volume of the robot and thus decrease its buoyancy, possibly forcing a sinking situation, so it was very important

Table 3.2: Comparison of computed and actual masses and buoyancy.

	mass [g]
design buoyancy, M_{b}	3231.0
individually measured mass, M_{sum}	3285.4
total measured mass, M_{total}	3216

to minimize this action. These areas are located around the circumference of the robot at each joint along the length of the robot. The robot must be able to rotate freely but still provide a surface which can act against the pressure of the fluid. The cavity provides space for the succeeding segment to rotate inside the preceding one without interference. At the same time, the succeeding segment includes a curved segment that provides support to the latex skin during rotation. Details of this design feature can be seen in Figure 3.13 around the axis of rotation of the joints. Once built, the robot was placed at the intended depth for testing and remained at equilibrium without sinking, so the robot did not appear to experience any sinking motions due to depressions of the skin. The same was attempted for the robot while articulating, but it was difficult to judge whether the robot was rising or sinking due to the propulsive forces of the eel or the depressions of the skin. It was hard to place the robot perfectly horizontal without any initial condition of pitching rotation.

In the end, several buoyancy/ballasting trials were performed in order to attain the perfect amount of ballast by placing the robot in the water repeatedly with slightly different amounts of lead-tape ballast each time. Before and after each trial, the total mass of the robot was measured on a scale with an accuracy of 0.001 kg. Table 3.2 displays the values for the buoyancy as calculated from the geometry of the robot (M_b), the mass as measured by individually measuring the components during the build process and summing them up (M_{sum}), and the total mass of the robot measured during the ballasting trials after the robot was completely built (M_{total}). as one can see, there are slight discrepancies between all three measurements. The percent difference between the maximum and minimum of these three values is 2.1%, which is within reasonable acceptance of error. The error can be attributed to a number of factors in addition to the differences in accuracy of the scales used. Other factors include but are not limited to errors in measuring the amount of wiring and solder used since these could not be easily separable from the other components before or after installation. The lead-tape ballast was assumed to be constant in mass per unit length during the computation of how much was predicted to be needed, but it could have easily been
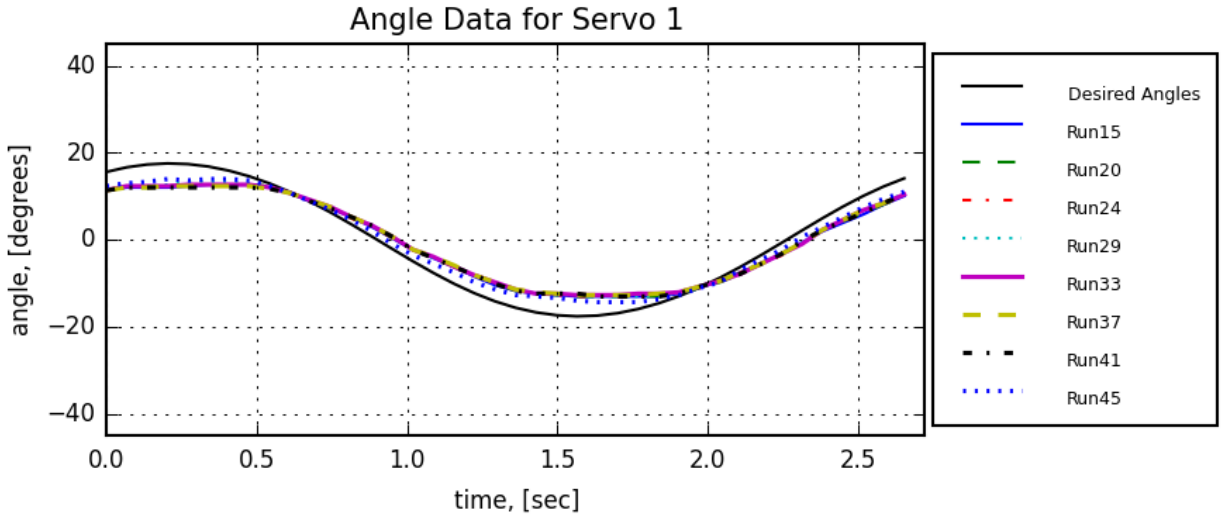
Figure 3.17: Comparison of angles from different PIV testing "runs" versus time for servo 1. Despite the inaccuracy of the angles over time, the servo angle versus time for each test precisely agree with one another.

variable due to manufacturing quality. There were some slight depressions in the skin at each of the joints during ballasting trials, which would decrease the volume of the robot and thus provide less buoyancy. Less buoyancy means the mass of the robot must be less. This is most likely the reason for the total measured mass of the perfectly neutrally-buoyant robot being less than the design buoyancy for the perfect geometry.

3.2.2 Kinematic Verification

It is extremely important that NEELBOT-1.1 replicate the desired motion as accurately as possible since it enables equal comparisons of theory and experiment. However, this was not always the case for the testing of this study. Unfortunately, the robot could not replicate the desired motion consistently during all testing. Thus, the inaccurate motion had to be deemed acceptable, and the theoretical computations were adjusted as necessary to model the new off-design cases, which is already discussed in Section 2.2.2. The joint angular positions in time and space are shown in the Figures in Section 3.2.3, which also explains the control theory analysis and design performed on NEELBOT-1.1 to attempt to replicate the desired motion to the best of its ability. This section only illustrates and discusses the angular position of individual servos over time.

The motion of the robot was verified by inspecting the recorded servo angles as reported back to
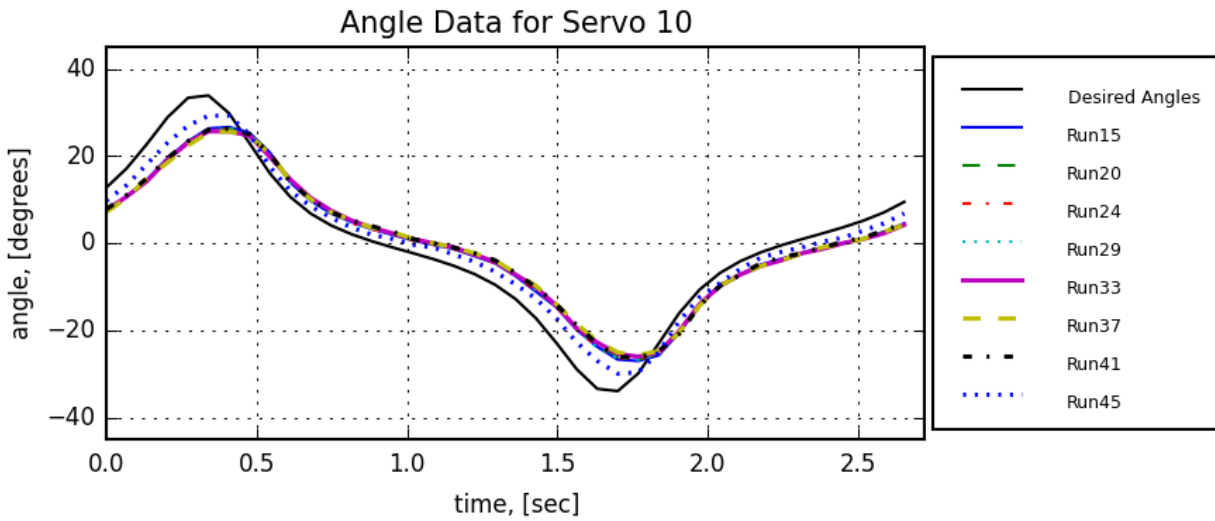
Figure 3.18: Comparison of angles from different PIV testing "runs" versus time for servo 10. Despite the inaccuracy of the angles over time, the servo angle versus time for each test precisely agree with one another.
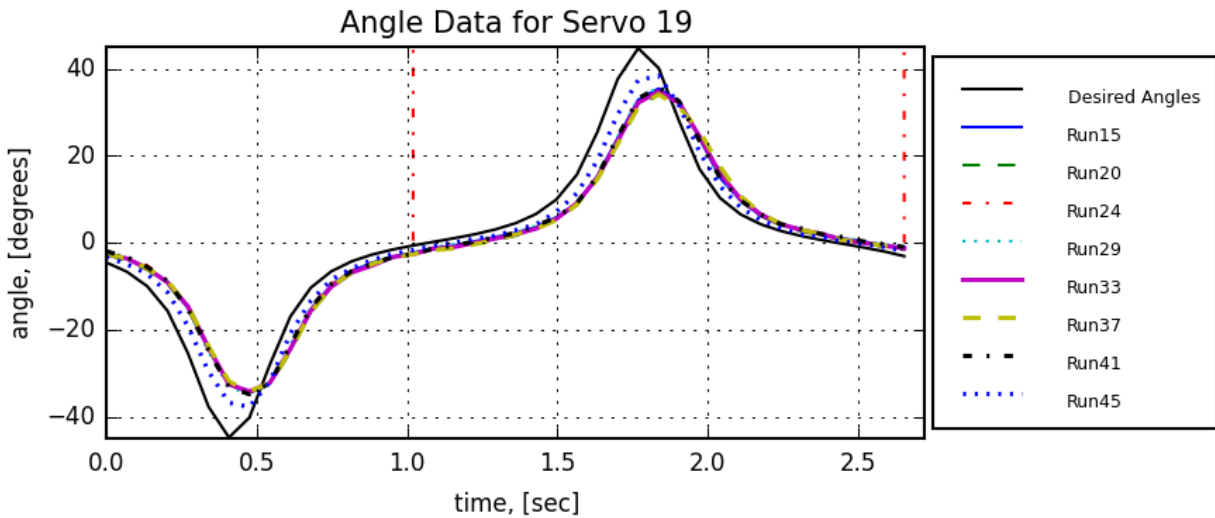
Figure 3.19: Comparison of angles from different PIV testing "runs" versus time for servo 19. Despite the inaccuracy of the angles over time, the servo angle versus time for each test precisely agree with one another.

the mainframe by the Dongbu Herkulex DRS-0201 servos. With a resolution of 0.325°, the servos were able to record their angular position over time at acceptable levels of precision. The angular positions are recorded at a sampling rate of 14.7 Hz.

Figures 3.17 through 3.19 show the comparison of desired and actual joint angles versus time. The plots show the angles versus time for servos 1, 10, and 19, respectively. Plots for the other 16 servos show similar characteristics to these and are not shown here. Each of these is for the same carriage advance speed of 0.25 m/s. Each plot shows several "runs," and each run is associated with a tether position (shown in Table 4.1).

Although there is a slight error between the desired and actual servos over the entire time period, the angular positions over time from various runs agree with one another within an acceptable level of error. These position results were also compared for varying levels of servo voltage levels between 7.4 V and 10.5 V, and there was no discernible error found due to voltage levels.

3.2.3 Control Theory Application

Introduction For an accurate comparison of the theoretical prediction with the experimental results, it is very important to have the robot follow the preplanned, desired trajectory that replicates the motion explained in Chapter II and shown in Figure 2.6. Enforcing the robot to attain this goal requires the application of control theory to accurately manipulate the servo actuators in time. At its core, applying a control theory method requires a dynamic model of the system called the plant, feedback of the state variables which are the joint angles in this case, and a controller, also known as a compensator, to eliminate any errors between the desired and actual joint angles. The ultimate goal of the analyses to follow is to determine the compensator's proportional, integral, and derivative gains that minimize the position errors.

The chosen servos can provide feedback both internally to itself and to an external mainframe acting as a microcontroller, although at a very limited rate for the latter which has proven to be problematic. A mathematical, dynamic model of the plant is derived both analytically and heuristically. The Lagrangian equation of motion is used for the analytical model of the entire system. For the heuristic approach, a Newtonian formulation is used to model the torques about a single joint to create a transfer function for each joint, and this model along with recorded responses to step inputs of each joint is used to derive the coefficients of the polynomials in the transfer

function using system identification techniques. This is performed for each unique combination of servo j's input affecting servo i's output to create a coupled matrix of transfer functions. Both of these models are used to determine the proportional-integral-derivative (PID) gains for the controller.

For each model, an independent joint control law was used for the application of the gains, i.e. each joint is ignorant of the angular position of other joints. There are several types of control schemes that have been derived over the years, and due to physical limitations of the NEELBOT-1.1 system components, the classical manipulator control scheme of PID independent joint control was chosen, which is the simplest method, with respect to computational load, of the computed-torque controllers (see the next section for more details).

Determining each of the gains for each servo's joint controller was performed differently for each of the models. For the heuristic model, an optimization routine was wrapped around the entire system to minimize the error in the state variables by varying the gains. For the solely computer simulated Lagrangian model, a computational approach was used to obtain optimal sets of PID values similar to the approach in Chapter 10 of Ogata (2001).

In addition to the methods performed above, classical tuning rules for PID controllers were applied, specifically that of the Ziegler-Nichols method (Ogata (2001)). This method was the easiest to accomplish with a slight improvement in the motion control.

The heuristic model proved to be the least difficult to implement but also applied the most simplifying assumptions of the other two models due to non-linearities and time-varying phenomenon of the matrix set of equations modeling the dynamics of the system for the Lagrangian equations of motion. The accuracy of the motion in time and space improved to replicate the desired, theoretical motion, but it could not be consistently replicated during all the experimental testing.

Independent Joint Control Law   Computed-torque controllers require the robot arm parameters to be known fairly accurately and be able to compute the required torque in real time. Control in the presence of uncertainties or unknown parameters (e.g. friction, payload mass, etc.) requires refined approaches, such as robust or adaptive control (Lewis et al. (1993)). Robot control schemes can be classified into "computed-torque-like" and "noncomputed-torque-like" algorithms. Robust, adaptive, learning, and the eponymously-named one are computed-torque-like schemes. Indepen-

dent joint control, the simplest of the computed torque ones, does not require nearly as much of a computational effort as the others.

The more advanced schemes such as computed-torque, robust, adaptive, and neural network require a significant amount more up-front development of the algorithm and real-time computational effort during manipulation. Lewis et al. (1993) states that it is important to realize that computed-torque depends on the inversion of the robot dynamics, which is sometimes called inverse dynamics control. This can be troublesome due to zeros becoming poles, locations on the complex domain where the system becomes severely unstable. Computing the computed-torque control law, $\underline{\tau} = \underline{\underline{M}}(\underline{\ddot{q}}_d - \underline{u}) + \underline{N}$, requires matrix multiplication at each sample time step and should be avoided. A good way to compute the torque is to use the efficient Newton-Euler inverse dynamics formulation with $\underline{\ddot{q}}_d - \underline{u}$ in place of $\underline{\ddot{q}}$ (Craig (1988) and Walker and Orin (1982)), but this method proved to be too computationally taxing for NEELBOT-1.1's hardware in real-time.

To overcome this scenario of computational load, the timesteps of the motion can be lengthened to allow more time for the computation to be executed. However, increasing the timestep means fewer timesteps for each cycle and provides the opportunity for the motion to become jerky, or not as smooth (additional programming would be needed to control the acceleration and deceleration curves of the servos). For the nominal time period of 2.72 seconds, it was determined that 40 timesteps provided a timestep length that was conservatively long enough to allow for any data acquisiton, sending of signals, and real-time computations between the robot and the computer. Using shorter timesteps, errors were unpredictably experienced in the data acquisition and sending of signals, causing the robot to manipulate very inaccurately. These errors were experienced without even a heavy load of computation. The most limiting factor of the Dongbu Herkulex DRS-0201 servos was the number of servo angles that could be reported back to the mainframe at one time.

The feedback of the servo angles to the external mainframe severely limited the capabilities of the system and was the main reason for not being able to choose one of the more advanced control schemes. The serial communication of the system can report back to the mainframe only one servo's feedback at a time, during each timestep. Trying to report back more than one servo at a time caused several errors in the motion since the data could not be retrieved correctly before the next timestep. Executing more computationally intense control schemes that require feedback of all the servos for each timestep require a more detailed analysis and design of hardware-software

interaction than the costs and time allowed for this project. Hardware that can provide higher rates for downloading and uploading data would be needed to overcome the external feedback problem. Mainframe hardware designed specifically for the algorithms of the more advanced control schemes, such as field-programmable-arrays (FPGA), would be able to overcome the problem of executing the computational effort at the fastest possible rate.

Independent joint control, also known as classical joint control, is considered a computed-torque-like control scheme but does not require the computational intensity that other computed torque schemes require (Lewis et al. (1993)). For classical joint control, the computed-torque control law is specified as $\tau_c = -u(t)$, and u is selected as u_j so as to depend only on joint variable j. This describes n decoupled individual joint controllers and is the reason for being called independent joint control.

Implementation is relatively easy since the control input for joint j only depends on locally measured variables, not on the variables of the other joints. Moreover, the computations are easy and do not involve solving the complicated nonlinear robot inverse dynamics (Lewis et al. (1993)). During the early days of robotics, independent joint control was popular (Paul (1981)) since it allows a decoupled analysis of the closed-loop system using single-input-single-output classical techniques. This statement is now outdated, but should be noted for the technique used within: there are strong arguments even today by several researchers that this control scheme is always suitable in practical implementations (Lewis et al. (1993)).

However, as will be shown next, deriving the highly non-linear dynamics for the 19 degree-of-freedom NEELBOT-1.1 proved to be very difficult. The dynamical equations of motion are needed to simulate as accurately as possible the plant model of NEELBOT-1.1 in the time-series computations to determine the PID gains.

Analytical Model using Lagrange-Euler Dynamics   The system of equations defining the dynamics of a simplified model representing the robotic eel can be derived using Lagrange-Euler dynamics of a set of generalized coordinates. As an example, the equations for a 2-segment robotic eel are derived here, assuming the segment masses are concentrated at the ends, gravity force can be neglected since the robot segments are all at the same potential in the plane horizontal to the ground, and the friction terms are ignored for now to make the derivation simpler.
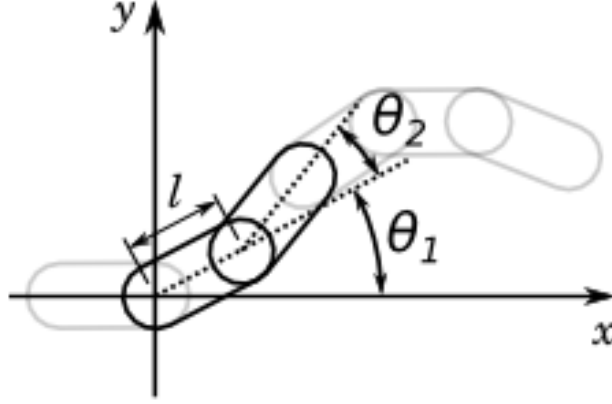
Figure 3.20: Coordinate system for 2 degree-of-freedom robot overlaid on multi-DOF robot.

Lagrange's equation of motion for a conservative system is given by

$$\frac{d}{dt}\frac{\partial L}{\partial \dot{q}} - \frac{\partial L}{\partial q} = \tau \tag{3.17}$$

where $\underline{q}$ is an n-vector of generalized coordinates q_j, $\underline{\tau}$ is an n-vector of generalized forces τ_j, and the Lagrangian, L, is the difference between the kinetic and potential energies

$$L = K - P \tag{3.18}$$

The variable $\underline{q}$ is the joint-variable vector, consisting of joint angles θ_j as in Figure 3.20. The vector $\underline{\tau}$ represents the n components of torque corresponding to joint j.

The joint variable vector is

$$\underline{q} = \begin{bmatrix} \theta_1 \\ \theta_2 \end{bmatrix} \tag{3.19}$$

where θ_1 and θ_2 are the angles of the first and second joints, respectively. The generalized force vector is

$$\underline{\tau} = \begin{bmatrix} \tau_1 \\ \tau_2 \end{bmatrix} \tag{3.20}$$

with τ_1 and τ_2 torques supplied by the actuators.

The kinetic and potential energies for each segment can be derived relatively easily, with in-

90

creasing difficulty for the second segment. The potential energy can actually be ignored since the potential is the same for all of the planar robot. The Lagrangian for both segments (with potential energy eliminated) becomes

$$L = K_1 + K_2 \tag{3.21}$$

Taking the necessary derivatives of this and substituting it into Lagrange's equation of motion (equation 3.17), the set of equations for the robot dynamics, after some rearranging, can be written as

$$\begin{bmatrix} (m_1 + m_2)l_1^2 + m_2l_2^2 + 2m_2l_1l_2\cos(\theta_2) & m_2l_2^2 + m_2l_1l_2\cos(\theta_2) \\ m_2l_2^2 + m_2l_1l_2\cos(\theta_2) & m_2l_2^2 \end{bmatrix} \begin{bmatrix} \ddot{\theta}_1 \\ \ddot{\theta}_2 \end{bmatrix}$$
$$+ \begin{bmatrix} -m_2l_1l_2(2\dot{\theta}_1\dot{\theta}_2 + \dot{\theta}_2^2\sin(\theta_2) \\ m_2l_1l_2\dot{\theta}_1^2\sin(\theta_2) \end{bmatrix} = \begin{bmatrix} \tau_1 \\ \tau_2 \end{bmatrix} \tag{3.22}$$

This matrix set of equations is in the standard form:

$$\underline{\underline{M}}(\underline{q})\ddot{\underline{q}} + \underline{V}(\underline{q}, \dot{\underline{q}}) = \underline{\tau}(t) \tag{3.23}$$

The generalized version, now including the friction and gravity terms, of the set of non-linear coupled dynamics equations modeling the planar robotic eel with n joints is

$$\underline{\underline{M}}(\underline{q})\ddot{\underline{q}} + \underline{V}(\underline{q}, \dot{\underline{q}}) + \underline{\underline{B_m}}\dot{\underline{q}} + \underline{\underline{B_L}}(\dot{\underline{q}}) + \underline{G}(\underline{q}) + \underline{\underline{K_s}}\underline{q} + \underline{\tau_d} = \underline{\tau}(t) \tag{3.24}$$

with $\underline{q}(t) \in \mathbb{R}^n$ the joint variable vector and n being the number of generalized coordinates. Doubly-underlined terms represent a matrix, and single underlines represent a vector. The term $\underline{\tau}(t)$ is the control input, $\underline{\underline{M}}(\underline{q})$ is the inertia matrix, $\underline{V}(\underline{q}, \dot{\underline{q}})$ the Coriolis/centripetal vector, $\underline{\underline{B_m}}\dot{\underline{q}}$ the viscous friction matrix, $\underline{\underline{B_L}}(\dot{\underline{q}})$ the dynamic friction matrix, $\underline{G}(\underline{q})$ the gravity vector, $\underline{\underline{K_s}}$ the spring constant matrix, and $\underline{\tau_d}$ the uncertain disturbance to account for inaccuracies in the modeling. The gravity term can be ignored due to it being constant over the entire, planar robot.

The friction terms can be considered to be local effects, so it is assumed that each matrix is uncoupled among the joints, thus containing elements only along the diagonal. The friction

coefficients are among the parameters most difficult to determine, and these represent only an approximate mathematical model for their influence (see Lewis et al. (1993); Craig (1988); Schilling (1990); and Corke (2011) for more discussion).

The $\underline{\underline{B_m}}$ matrix, modeling each of the joint's motor viscous friction is considered to be independent of each other and thus decoupled. This viscous friction describes that of both the motor and gearbox lumped together. For simplicity, the friction is considered constant with respect to rotational speed, thus linearizing the term. The matrix can be written as a diagonal one:

$$\underline{\underline{B_m}} = \mathrm{diag}\left\{B_m\right\} \tag{3.25}$$

where B_m is the servo-actuator's lumped viscous friction. This viscous friction term was measured empirically, and its value is shown in Table 3.4.

Similarly, the dynamic friction is assumed to be independent of the rotational speed and is also decoupled. Realistically, $\underline{B_L}$ is coupled but it is assumed to be decoupled due to how dominant it is along the diagonal (as shown in the heuristic transfer function matrix modeling method, but remember that this method is quasi-static), and it is written as

$$\underline{\underline{B_L}} = \mathrm{diag}\left\{B_L\right\} \tag{3.26}$$

where B_L was determined from system identification as described later and is listed in Table 3.4. The $\underline{\underline{B_L}}$ models the dynamic friction acting on the joint segments as a result of the fluid environment. This is the same as the damping coefficient for an oscillating structure in a fluid.

In addition to these terms, reactive forces due to rotational spring-like loading have been included due to their significant contributions. The reactive forcing of the segments' angular displacement is due to the wires moving within the articulating channels of the robot and the elasticity of the latex rubber skin. Similar to the friction terms, the spring constants for each joint are considered independent of angular displacement and decoupled. The spring constant matrix becomes

$$\underline{\underline{K_s}} = \mathrm{diag}\left\{k_s\right\} \tag{3.27}$$

where k_s is the spring constant, measured empirically and displayed in Table 3.4.

In addition, the added mass due to the accelerations of the segments and the fluid surrounding it are accounted for in the mass matrix. The sectional forces due to added mass are computed using Vorus' equations 2.39 from Section 2.1.2 and are added to the inertia matrix, denoted by the term $\underline{\underline{M_a}}$. The added mass varies along the length of the robot and with time, making the system time-varying, significantly increasing the complexity of the system.

With changes to all the terms described above, the complete equation modeling the system is written as

$$\left(\underline{\underline{M}}(q) + \underline{\underline{M_a}}(q,t) \right) \ddot{\underline{q}} + \underline{V}(q,\dot{q}) + \underline{\underline{B_m}}\dot{q} + \underline{\underline{B_L}}(\dot{q}) + \underline{\underline{K_s}}q = \underline{\tau}(t) \tag{3.28}$$

This equation can be solved for $\ddot{\underline{q}}$ to generate the inverse dynamics modeling the robot

$$\ddot{\underline{q}} = \left[\underline{\tau}(t) - \underline{V}(q,\dot{q}) - \underline{\underline{B_m}}\dot{q} - \underline{\underline{B_L}}(\dot{q}) - \underline{\underline{K_s}}q \right] \left(\underline{\underline{M}} + \underline{\underline{M_a}} \right)^{-1} (q,t) \tag{3.29}$$

This equation is solved using a Runge-Kutta integration scheme and initial conditions. As can be seen, this equation is highly non-linear and time-varying, making it computationally difficult to compute with simple hardware such as a commercial-off-the-shelf unit like an Arduino UNO, as explained earlier. Thus, this complicated equation is only used for the time-series computer simulation.

As stated several times before, this equation models the dynamics of the NEELBOT-1.1 and is considered to be the plant, which is the box labeled H in Figure 3.21. However, the output of the compensator is a voltage, so the above equation must be placed in terms of an input voltage vector. Using a simplified model based on the characteristics of a permanent magnet direct current (PMDC) motor, the torque can be related to voltage input by the following equation:

$$\underline{\tau}(t) = \frac{k_m}{R_a}\underline{v_a} \tag{3.30}$$

where $\underline{v_a}$ is the armature voltage of each joint's servo-actuator. The terms k_m and R_a are constant for each joint and are explained in the next section and listed in Table 3.4.

Using the methods in Chapter 10 of Ogata (2001), the PID gains, $\underline{K_p}$, $\underline{K_i}$, and $\underline{K_d}$, that best minimize the angular position error are determined. However, there will still be some small amount of overshoot, time delay, oscillation, etc. which will cause some errors in the system.
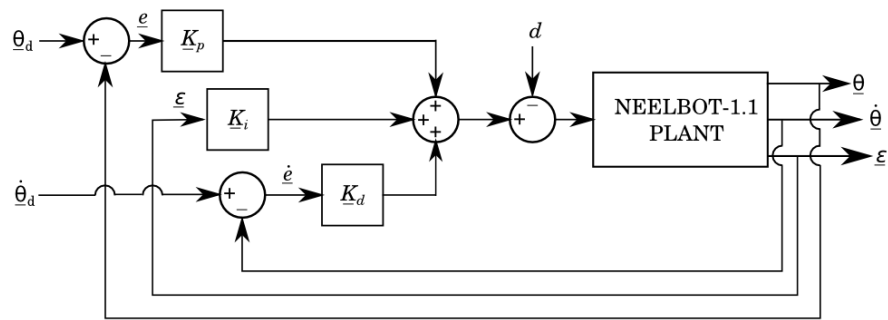
Figure 3.21: PID independent joint control diagram.
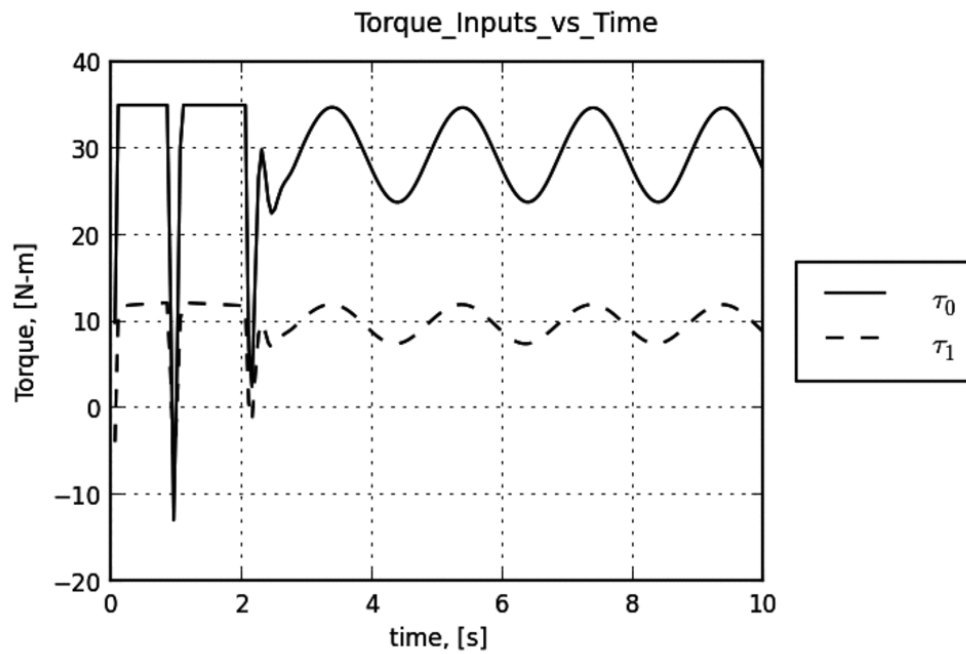
Figure 3.22: Torque input versus time for each joint, for a 2 degree of freedom system.
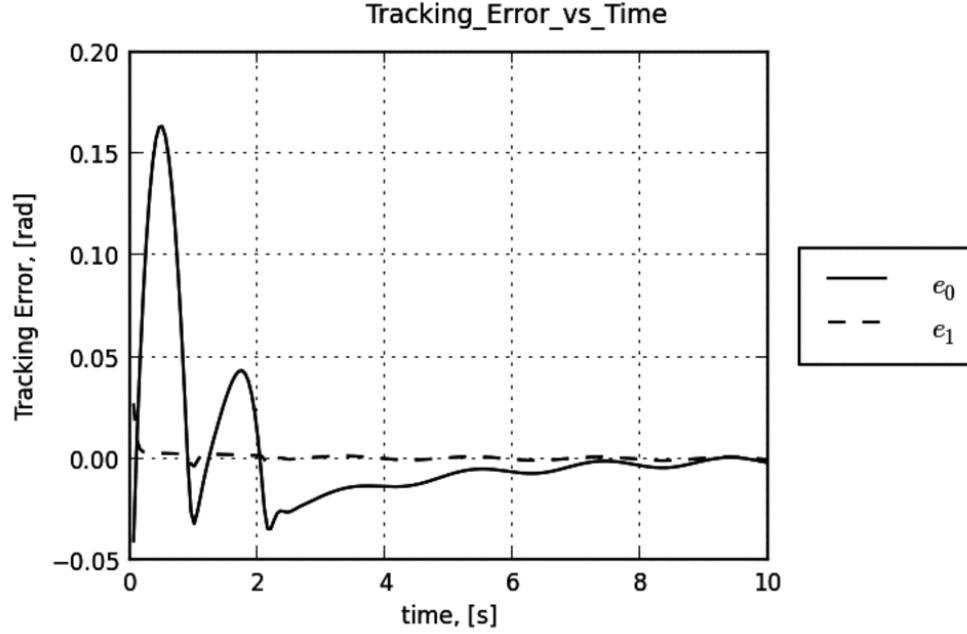
Figure 3.23: Tracking error versus time for each joint, for a 2 degree of freedom system.

Figures 3.22 and 3.23 show results of the computer code created to perform these numerical simulations.

Ziegler-Nichols Tuning As opposed to the theoretical simulation approach above, a heuristic method known as Ziegler-Nichols tuning was used to find suitable gains for the PID controller of each servo. The researchers who invented this method found that it provided the gains for an optimal combination of overshoot, response time, and minimal oscillations for plant response. It is easily implemented in-situ and doesn't require any off-site computational analysis. This method is advantageous when the mathematical models of plants are not known, as can be the case here since the mathematical model is very difficult to compute. Specifically, Ziegler-Nichols' Second Method of tuning rules was used, which is based on critical gain, K_{cr}, and critical period, P_{cr}.

First, set the derivative gain, K_d, to zero, and using proportional control action only, increase K_p from 0 to a critical value, K_{cr}, at which the output first exhibits sustained oscillations. The period at which the oscillations occur is the critical period, P_{cr}. These two critical values are plugged into the formulas in Table 3.3 for the PID controller to determine the PID gains.

For the robotic eel, the critical oscillation occurred when the entire robot oscillated, which is a

Table 3.3: Ziegler-Nichols tuning rules for the Second Method.

Type of controller	K_p	K_i	K_d
P	$0.5K_{cr}$	-	-
PI	$0.45K_{cr}$	$1.2K_p/P_{cr}$	-
PID	$0.6K_{cr}$	$2K_p/P_{cr}$	$0.125K_pP_{cr}$

global instability as opposed to local instabilities for each joint. We could not get local instabilities to occur and thus used the global instability criteria as the specification for the critical gain and period, and thus the PID gains obtained were the same for all joint controllers.

Oscillations were induced with the initial conditions of the robot being in a straight line and articulated to its first timestep in the motion routine, i.e. the robot was statically placed in the initial orientation of its motion. There was no discernible difference between the critical proportional gain and period obtained for either set of initial conditions. The critical proportional gain was determined to be 300, and the critical period was 0.333 seconds for the global oscillations. Table XXX shows the finalized gains determined from the Ziegler-Nichols tuning. The integral gain determined from the Ziegler-Nichols tuning method was extremely low and may have contributed to this method not succeeding. The results of the Ziegler-Nichols method improved the motion of the robot compared to the default controller settings, but the motion was still unsatisfactory.

Heuristic Transfer Function Matrix Modeling Simultaneously being performed during the computer simulations explained above, a matrix of transfer functions of the dynamic model similar to the one above was developed in order to perform the task of optimizing the proportional-integral-derivative gains for each servo.

Due to difficulties deriving the nonlinear equations of motion for a 19 degree-of-freedom system and also not having a sufficient point in the state space to linearize about, we felt that this simulation method would be insufficient to model the actual robot. Thus, in addition to the Ziegler-Nichols method, another heuristic method was derived to determine the PID gains. This method consists of modeling the dynamics, including the actuator, of each robot joint independently in a frequency-domain form to derive a transfer function for each. Transfer functions are derived to model a servo's own input-output relation or the output response due to the input of each other servo. Each transfer function models the response of one servo due to an input of another servo. For

this system of 19 servos, there are 361 independent transfer functions modeling these unique input-output response pairs. The mathematical form is the same for each of the transfer functions, but the coefficients for the polynomials in the numerator and denominator differ for each unique pair. For each unique pair, a unit step was inputted and the angular displacement response of the interested servo was recorded. From this data recorded by the LabVIEW program as reported by the servos, the coefficients were determined heuristically using a system identification toolbox in MATLAB. This single-input-single-output (SISO) transfer function system for each joint was then placed in a 19×19 coupled matrix to model the entire system. This modeling can then be thought of as a multi-input-multi-output (MIMO) system of SISO transfer functions. A compensator with variable PID gains was added to each SISO transfer function along with feedback to form a closed loop controller. This large MIMO transfer function was then wrapped with an optimization routine to determine the optimal PID gains for each servo-actuator.

First, let us derive the dynamics of the actuators from an electrical point of view. The actuator consists of a permanent magnet direct current (PMDC) motor, which defines the electrical laws applied to this derivation. The sum of the voltages for a PMDC is

$$v_a - i_a R_a - L_a \frac{di_a}{dt} - k_v \omega_a = 0 \tag{3.31}$$

where v_a is the armature voltage, i_a is the armature current, R_a is the armature resistance, L_a the inductance, k_v the motor velocity constant, and ω_a the rotational velocity of the armature, or rather, the motor. Several texts describe the characteristics of PMDC motors such as Siciliano and Khatib (2008), Siciliano et al. (2010), de Silva (2007), and Spong (2006). For the Dongbu Herkulex DRS-0201, the high-speed motor is geared down in speed to provide more torque at the output shaft. Thus, there is a difference in the shaft angular velocity from that of the armature angular velocity by a gear ratio, $r_{j/a}$:

$$\omega_a = \dot{\theta}_j r_{j/a} \tag{3.32}$$

where $r_{j/a} = 266$ for the Dongbu Herkulex DRS-0201 servo-actuators.

Substitute the above equation into 3.31 to get

$$v_a - i_a R_a - L_a \frac{di_a}{dt} - k_v \dot{\theta}_j r_{j/a} = 0 \tag{3.33}$$

Since the servo-actuators were not custom fabricated, it was much harder to determine some of the constants of the internal components, such as the motor constant. To overcome this difficulty, intrinsic parameters describing the servo-actuator's internal components were determined end-to-end, i.e. the whole system of the motor and gearbox were included. Going forward, any constants describing the servo-actuator characteristics have been lumped together to describe the whole system. For example, the gear ratio in the above equation has been lumped into the motor constant, and the equation becomes

$$v_a - i_a R_a - L_a \frac{di_a}{dt} - k_v \dot{\theta}_j = 0 \qquad (3.34)$$

Thus, keep in mind that the gear ratio has now been lumped into the motor constant. The motor velocity constant describes the XXXXXX characteristics of the motor. It was measured empirically by timing how long it took the motor to spin down from a known torque input. The measured value is listed in Table 3.4, along with other heuristically determined constants.

A summation of torques acting on the motor can be described as

$$\tau_e - \tau_J - \tau_B - \tau_L = 0 \qquad (3.35)$$

where τ_e is the torque due to electromagnetic torque, τ_J is the torque due to rotor and gearbox inertia, τ_B is the torque due to rotor and gearbox friction, and τ_L is the load torque consisting of external and intrinsic loads such as added mass and rotational inertia, respectively.

The first three terms can be substituted with the following formulas, based on the characteristics of a PMDC:

$$\tau_e = k_t i_a \qquad (3.36)$$

$$\tau_J = J_m \ddot{\theta}_j \qquad (3.37)$$

$$\tau_B = B_m \dot{\theta}_j \qquad (3.38)$$

where k_t is the torque constant, J_m is the rotor and gearbox inertia coefficient, and B_m is the rotor and gearbox friction coefficient. The subscript m denotes motor, and θ is the relative joint angle with subscript j denoting the jth joint. As explained above, all parameters describe the end-to-end characteristics of the servo-actuator, and the gear ratio has been lumped into the coefficients so

that the state variable, θ_j, describes the relative angles between joints and not the motor armature angle. The viscous damping coefficient B_m, which describes the rotor and gearbox friction (or viscous damping), is equivalent to the same named term in the simulated formulation described later.

The motor torque constant, k_t, describes the XXXXXX characteristics of the motor. Thankfully, in SI units for a PMDC motor, the motor torque constant and motor velocity constant are equivalent:

$$k_v = k_t \equiv k_m \tag{3.39}$$

with k_m being the nomenclature used from here forward, m denoting motor.

The fourth term above describes the load torque on the joint, which is due to the inertial and viscous damping of the rotating joint:

$$\tau_L = J_L \ddot{\theta}_j + B_L \dot{\theta}_j + k_L \theta_j \tag{3.40}$$

where J_L is the inertia of the robot segment and included added mass. B_L is the external dynamic friction and the internal friction of the wiring and skin sliding across the surface of the body. The third and final term models the force due to angular displacement which stretches and contracts the latex rubber skin. The skin's elasticity acts as a spring and thus has spring constant, k_L, which was measured experimentally and is listed in Table 3.4. In addition, the wiring inside the eel also induces some unexpected forcing on the angular displacement.

Substituting equations 3.36 to 3.38 and 3.40 into 3.35 gives

$$k_m i_{a,j} - J_m \ddot{\theta}_j - B_m \dot{\theta}_j - J_L \ddot{\theta}_j - B_L \dot{\theta}_j - k_L \theta_j = 0 \tag{3.41}$$

The inertial and viscous damping terms are lumped together to form total inertia and viscous damping for each joint, denoted by the subscript T:

$$k_m i_a - J_T \ddot{\theta} - B_T \dot{\theta} - k_L \theta = 0 \tag{3.42}$$

Rearranging equation 3.34 for the differential of the armature electrical current gives

$$\frac{di_a}{dt} = -\frac{R_a}{L_a}i_a - \frac{k_m}{L_a}\dot{\theta}_j + \frac{v_a}{L_a} \tag{3.43}$$

and then taking the Laplace transform of both equations above with zero initial conditions gives

$$k_m I_{a,j} - J_T \Theta_j s^2 - B_T \Theta_j s - k_L \Theta_j = 0 \tag{3.44}$$

$$-\frac{R_a}{L_a}I_{a,j} - \frac{k_m}{L_a}\Theta_j s + \frac{V_{a,j}}{L_a} = I_{a,j}s \tag{3.45}$$

Substitute the latter equation into the former to give

$$\frac{-k_m^2 \Theta_j s + k_m V_{a,j}}{L_a s + R_a} - J_T \Theta_j s^2 - B_T \Theta_j s - k_L \Theta_j = 0 \tag{3.46}$$

We assume the armature inductance is small compared to the resistance, which is reasonable from experience and then rearrange to get the left-hand side in the form of output over input, $\Theta_j/V_{a,j}$:

$$\frac{\Theta_j}{V_{a,j}} = \frac{k_m}{J_T R_a s^2 + (B_T R_a + k_m^2)s + k_L R_a} \tag{3.47}$$

This is the transfer function modeling a single servo-actuator joint (joint j) that will be the basis for each term in the coupled MIMO matrix describing the entire 19-joint system. The equation above actually describes the input-output relationship of solely the jth servo, i.e. those joints along the diagonal of the coupled matrix. For the off-diagonal transfer functions, the equation formally becomes

$$\frac{\Theta_i}{V_{a,j}} = \frac{k_m}{J_{T,i,j} R_a s^2 + (B_{T,i,j} R_a + k_m^2)s + k_L R_a} \tag{3.48}$$

where subscript i denotes the column index location in the matrix, and j denotes the row index. This input-output relationship can be thought as a description of input V_a at servo j induces an output of Θ at servo i.

The key is determining the numerical values for the terms on the right-hand side of the equation. Some of the values have been determined experimentally on their own, as described above, and their confidence of accuracy is reasonably high. However, others are more difficult to determine

accurately and require another method to confirm their experimental values. This other method is that of system identification, a widely used tool in control theory to determine a model of a plant when it cannot be analytically derived with confidence.

System identification requires recorded time-series data that will be used to determine the coefficients of the transfer function modeling the system. For each of the 361 unique input-output pairs, the angular response over time of servo i was recorded as a result of a unit-step input to servo j. Each of these time-series curves were entered into MATLAB's system identification toolbox in order to perform an algorithm of fitting its own curve to match the recorded data by varying the polynomial coefficients. Equation 3.48 above can be placed in polynomial form with the coefficients on the right lumped together to match the output from MATLAB:

$$\frac{\Theta_i}{V_{a,j}} = \frac{d_{i,j}}{a_{i,j}s^2 + b_{i,j}s + c_{i,j}} \tag{3.49}$$

For each input-output pair, MATLAB's system identification toolbox determined numerical values for $a_{i,j}$, $b_{i,j}$, $c_{i,j}$, and $d_{i,j}$. These numerical values were compared to the coefficients in equation 3.48, with the armature resistance and motor constant reliably known from experiments, thus the inertia and viscous damping terms varied for each input-output pair. Table 3.4 shows the inertia and viscous damping terms as an average of those determined from the results along the diagonal of the matrix. These ended up being the values used in the time-series computer simulation too.

The entire matrix of open-loop SISO transfer functions will be denoted as $\underline{\underline{\mathbf{H_o}}}$, with the subscript o denoting that it consists of open-loop transfer functions. Multiplying this matrix by the vector of state variable input V_a will produce the open-loop output Θ vector for the entire system.

We have yet to describe how the PID gains and the minimization of desired to actual error factor into this control scheme for the angular displacements of the joints. The loop of each element of the transfer function matrix $\underline{\underline{\mathbf{H_o}}}$ is closed by providing feedback of the state variables. Also, a controller, also called a compensator, is added to the signal flow before the state variable vector is multiplied by the transfer function matrix in state space. This compensator contains the varying PID gains that will attempt to minimize the error of the output compared to the desired output. This closed-loop, PID compensated matrix of transfer functions is now denoted as $\underline{\underline{\mathbf{H_c}}}$.

Lastly, the matrix $\underline{\underline{\mathbf{H_c}}}$ is wrapped with an optimization routine in MATLAB to determine the

Table 3.4:
Heuristically/empirically determined values of Dongbu Herkulex DRS-0201 servo-actuator (insert columns showing measured and sys identification calculated values and maybe a range of values for confidence).

Parameter	Value
armature resistance, R_a	
armature inductance, L_a	$L_a \ll R_a$
motor constant, $k_v = k_t \equiv k_m$	
servo-actuator inertia, J_m	2.6×10^{-7} kg-m^2
viscous damping constant, B_m	1.7×10^{-7} kg-m^2/s
spring constant, k_L	
,	
,	

PID gains that minimize the error of the output compared to the desired output. The optimization algorithm consisted of an "fmin" search routine. The algorithm returned a vector of PID gains, which were then used in some trial runs. Due to lack of specifications of the servo-actuators, the PID gains had to be reverse-engineered to determine what units the gains are in for the internal micro-controller board.

Unfortunately, the results of the runs were not a reasonable improvement over the initial results, and sometimes the motion was even worse than before and erratic. The motion could not be consistently repeated.

In the end, these computed vectors of PID gains were not used due to too much erratic motion and no consistency of repeatability. Table XXX shows the value of PID gains tried for various runs, eventually settling on Set D.

Problems with Non-linearities of the Plant   As discussed earlier, the equations of motion describing the physics-based model of the plant are highly non-linear and time varying. This poses problems for applying control theory methods because non-linear systems cannot be handled by these methods. A state-variable formulation is still capable of handling non-linear systems. However, the transfer function and frequency-domain methods fail, making modeling much more difficult. Deriving a transfer function of a system requires the physics describing it to be linear and time-invariant. Ogata (2001) explains the state-variable methods but only for linear systems, and
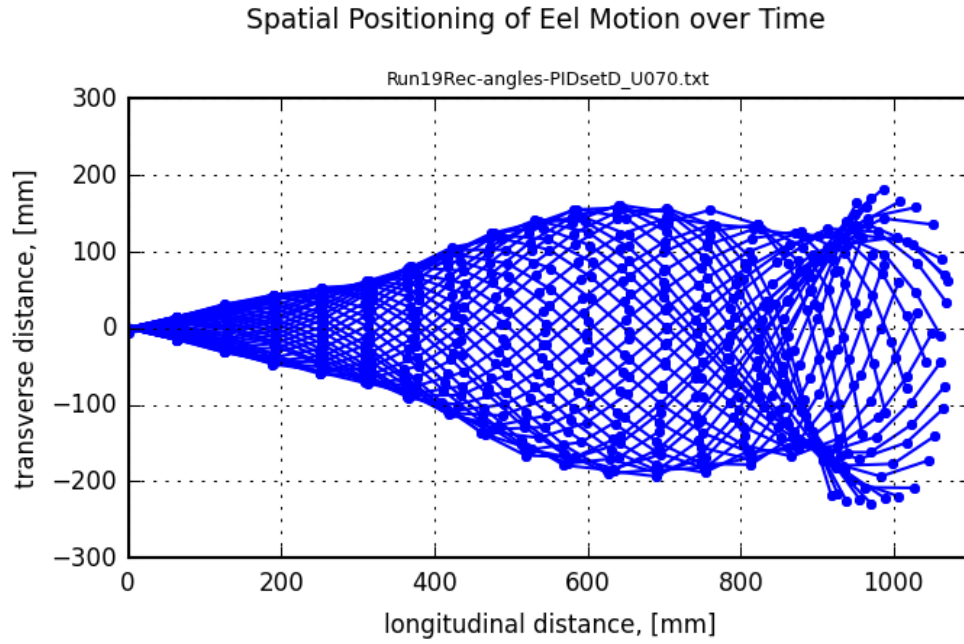
Figure 3.24: Spatial superposition of servo angles for all time steps for an advance speed of 0.0 m/s.
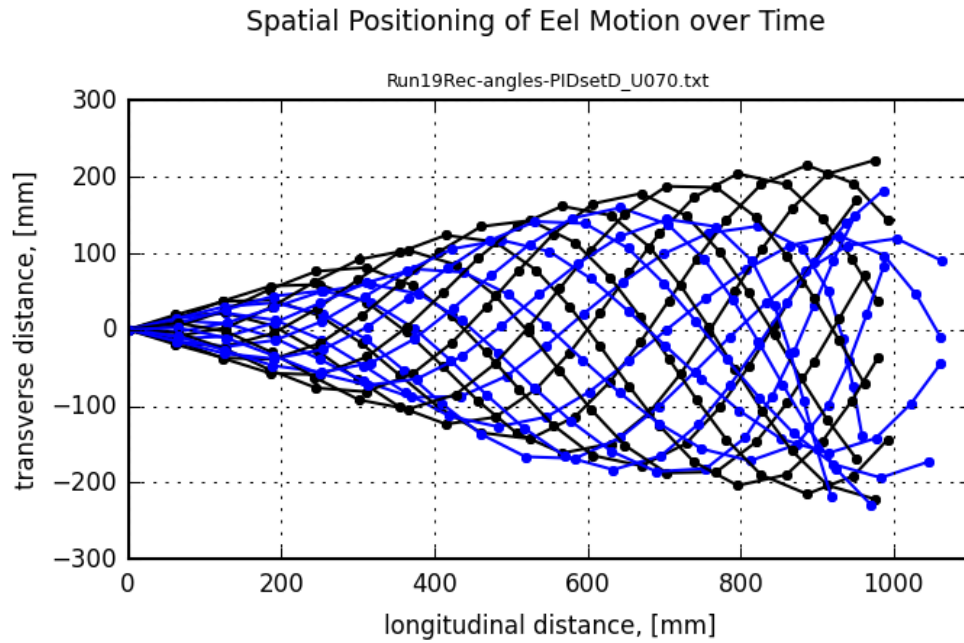
Figure 3.25: Spatial superposition of servo angles (blue) compared to the desired motion (black) for 10 evenly spaced time steps for an advance speed of 0.0 m/s.
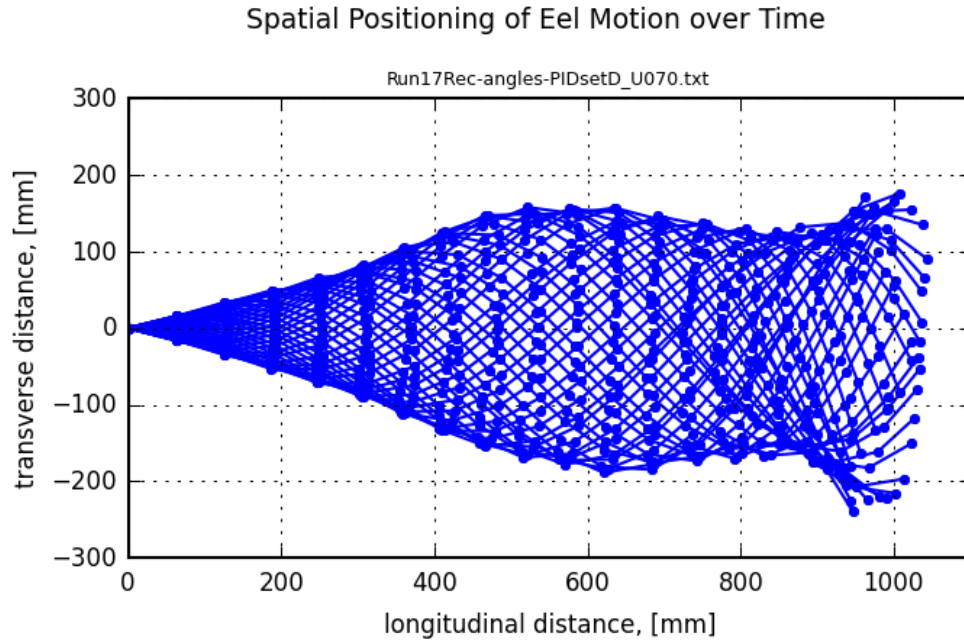
Figure 3.26:
Spatial superposition of servo angles for all time steps for an advance speed of 0.16 m/s.
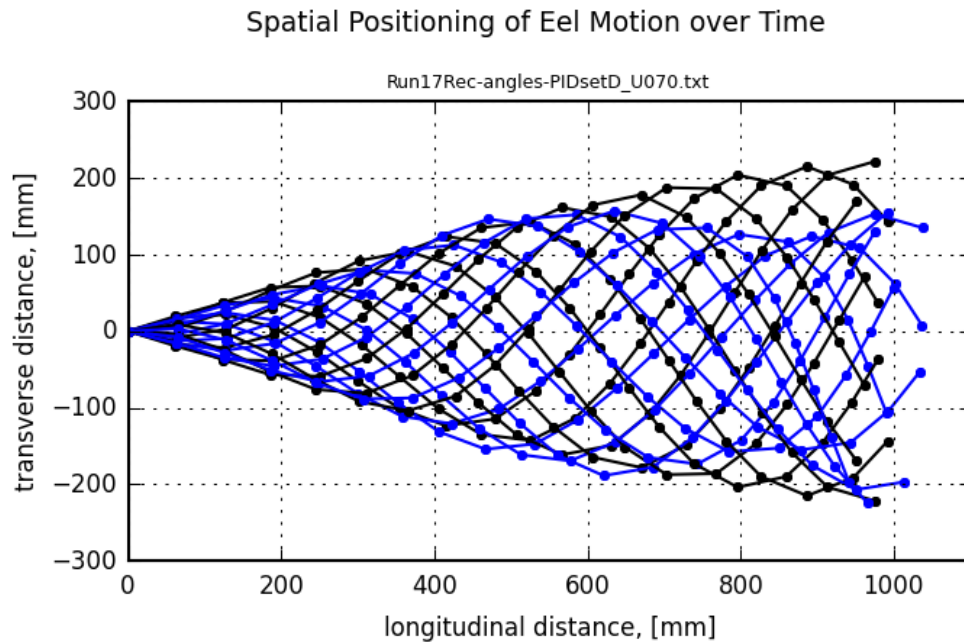
Figure 3.27:
Spatial superposition of servo angles (blue) compared to the desired motion (black) for 10 evenly spaced time steps for an advance speed of 0.16 m/s.

Spatial Positioning of Eel Motion over Time

Run15Rec-angles-PIDsetD_U070.txt
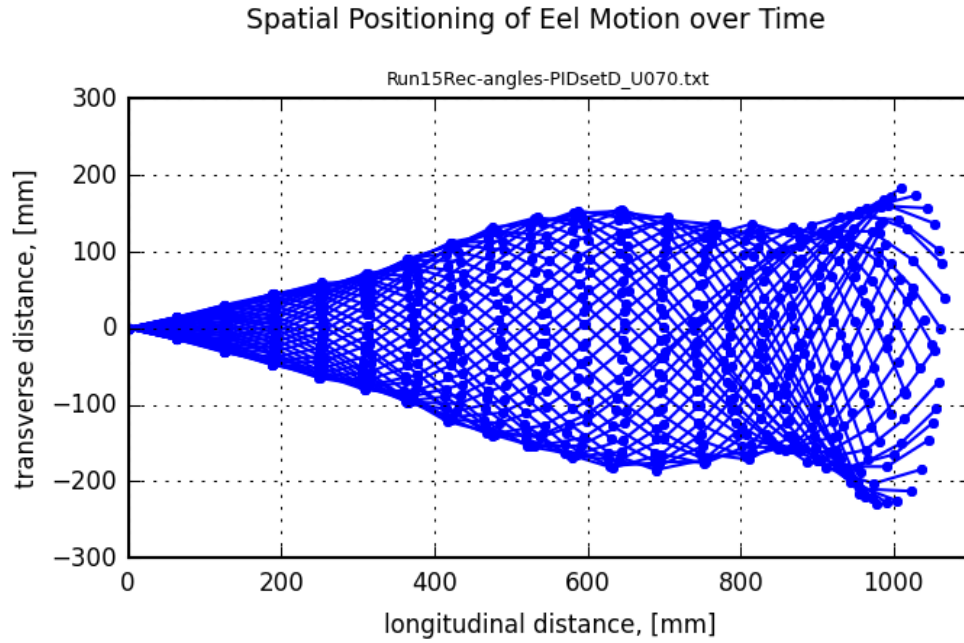
Figure 3.28:
Spatial superposition of servo angles for all time steps for an advance speed of 0.25 m/s.

Spatial Positioning of Eel Motion over Time

Run15Rec-angles-PIDsetD_U070.txt
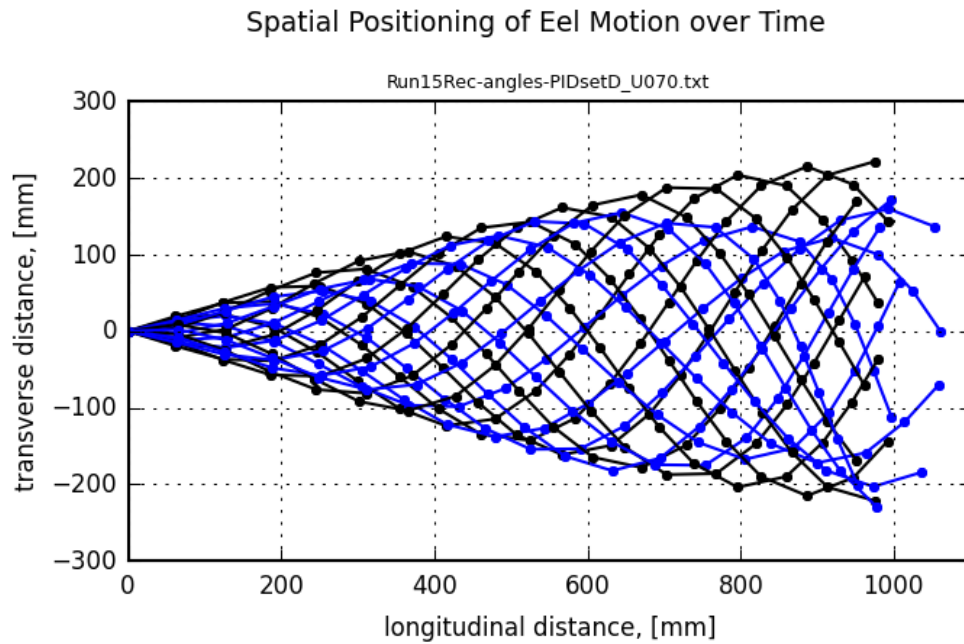
Figure 3.29:
Spatial superposition of servo angles (blue) compared to the desired motion (black) for 10 evenly spaced time steps for an advance speed of 0.25 m/s.
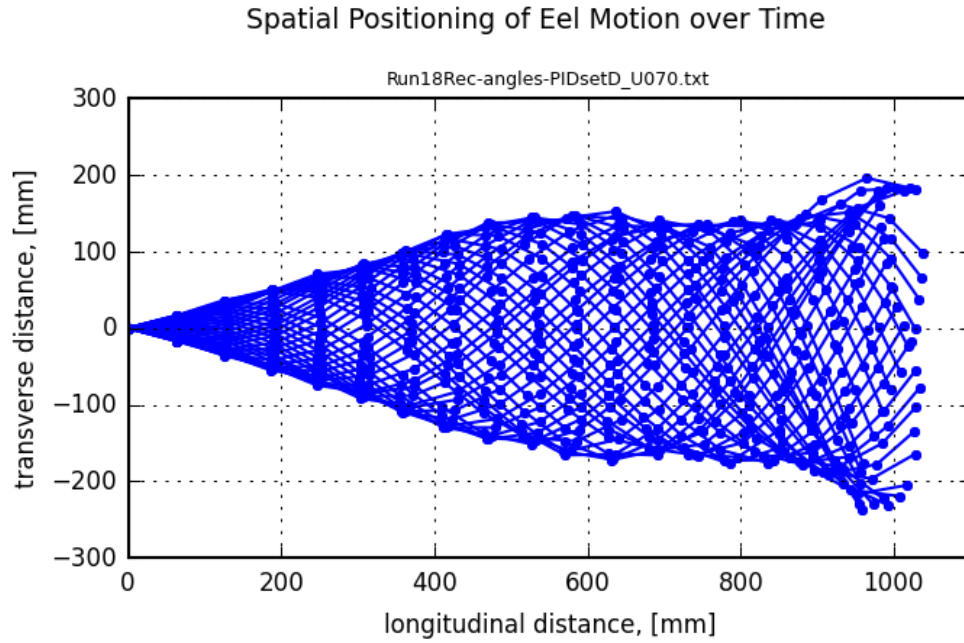
Figure 3.30:
Spatial superposition of servo angles for all time steps for an advance speed of 0.40 m/s.
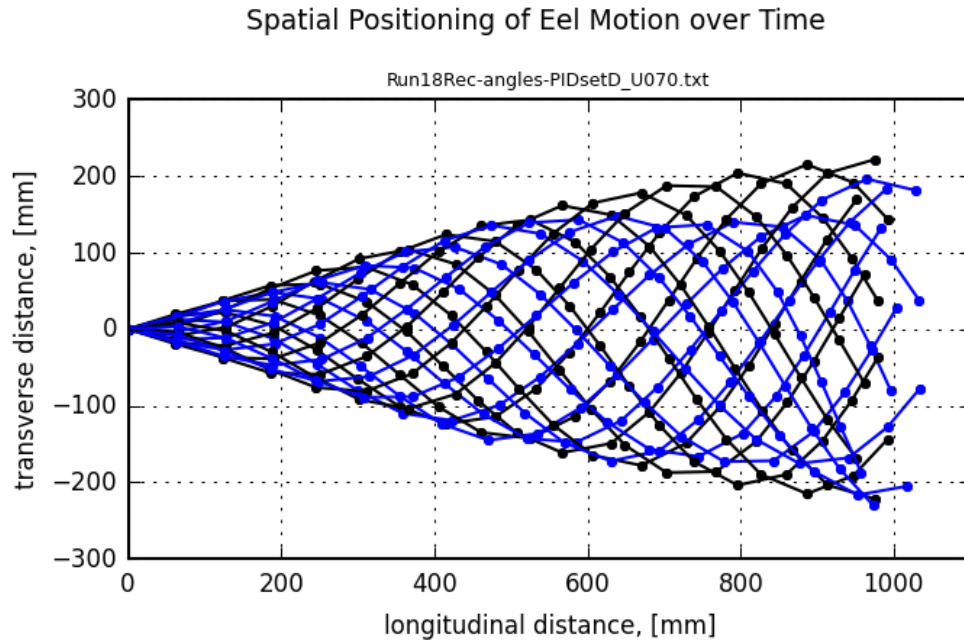
Figure 3.31:
Spatial superposition of servo angles (blue) compared to the desired motion (black) for 10 evenly spaced time steps for an advance speed of 0.40 m/s.

hence it can only work in the frequency domain. Other authors that discuss the classical approach to non-linear systems are Vidyasagar (1978), Slotine and Li (1991), Lasalle and Lefschetz (1961), Verhulst (1989), and Hahn (1967). Non-linear control analyses is beyond the scope of this research due to time and cost constraints.

A popular solution to dealing with non-linear systems is to linearize it. However, this method poses two challenges to the dynamics of NEELBOT-1.1. The first is where in the state-variable domain to linearize about, and the second is the perturbations about each of the linearization points are considered to be relatively large, extending outside the acceptable bounds of the linearized region. For the NEELBOT-1.1 system, there are 38 possible state variables to linearize, with an infinite number of operating points to linearize about. Additionally, the perturbations about an arbitrary operating point are considered to be fairly large, making the linearization quickly to become inaccurate.

CHAPTER IV

Experimental Testing

4.1 Experiment Setup

The parts of the research relating to the experimental testing and data acquisition are described. The results of each of the experiments are reported within and described.

The experimental testing consists of two major physical components, the anguilliform robot tether (Section 4.1.1) and the particle image velocimetry (PIV) equipment (Section 4.1.2). Figure 4.1 shows a rendering of the major physical components used in the experimental testing. The tether consists of its namesake which is used to steadily position the robot in the laser light sheet plane of the PIV equipment and a 6-DOF load cell which measured the thrust/drag (longitudinal) and lift (transverse) loads. The PIV equipment consists of TSI, Inc.'s Model 6800 PIV System, which is a waterproof PIV system that can be attached to a moving towing tank carriage to measure the fluid velocities in a planar region.

There are three sets of results being obtained from this equipment. The measurements from the tether load cell are used for both a time-series and steady-state analyses. The time-series analysis is used to compare the thrust/drag and lift of the robot to the theoretical predictions over its time period (Section 4.2). The steady-state analysis is used to investigate the thrust/drag characteristics of the robot and again compare this to the theoretical predictions of Vorus and Taravella (2011) (Section 4.3). This analysis is used to determine a better estimate for the thrust coefficient, C_T, which is one of the main parameters determining the thrust. The third and final area of measurements is a result of the PIV testing equipment (Section 4.4). These PIV results which are only in the plane of the robot's motion are then able to be compared to the theoretical
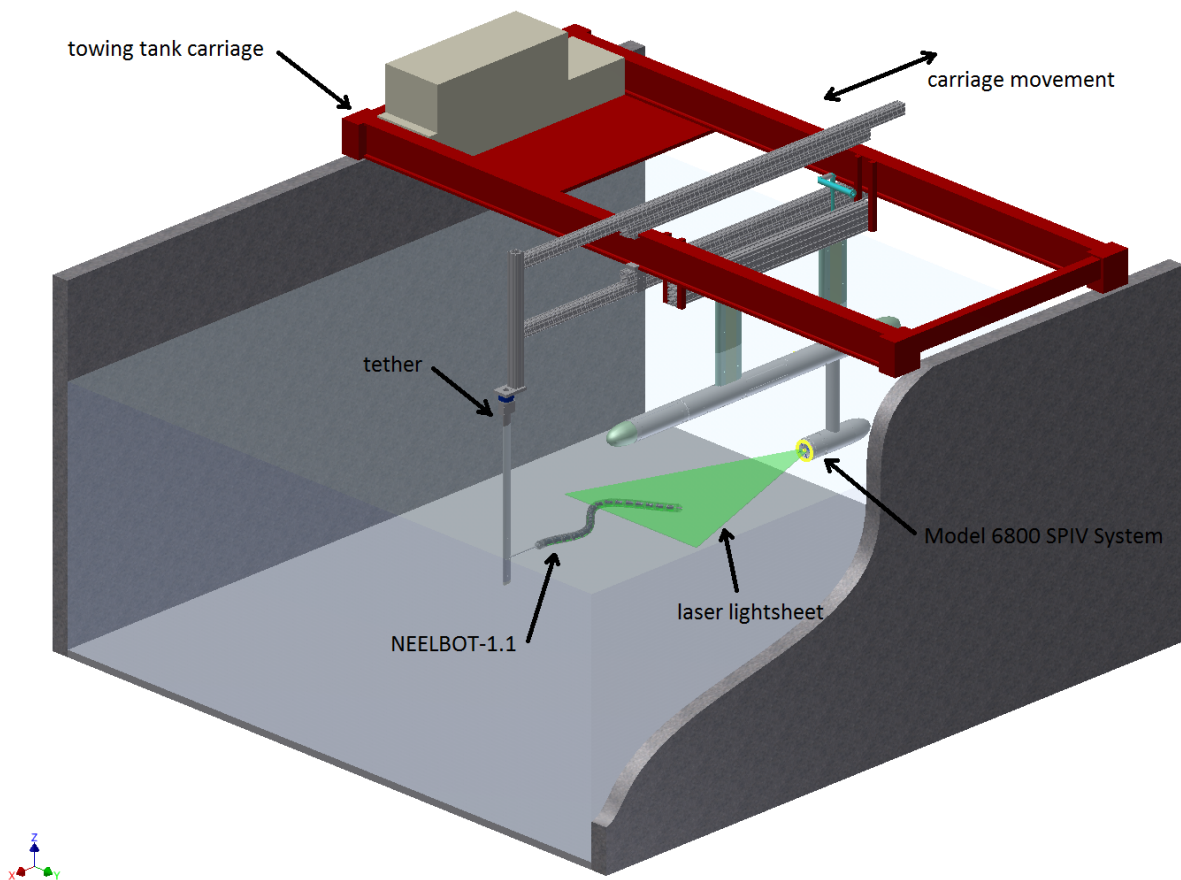
Figure 4.1: PIV equipment installed on UNO Towing Tank carriage with rendering of NEELBOT-1.1 and its tether.
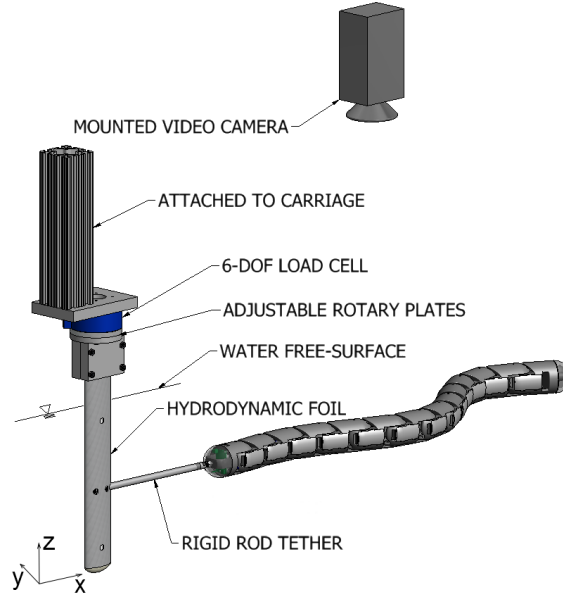
Figure 4.2: Components of the custom robotic eel tether and its coordinate system.

predictions with various techniques, including velocity magnitude comparisons and control volume momentum integral analysis.

4.1.1 Anguilliform Robot Tether

A testing rig has been designed to tether the robot to the carriage of the Univ. of New Orleans' towing tank so that the robot is swimming in a controlled state for easier processing of the motion measurements and PIV data acquisition. Figure 4.2 shows a rendering of the aforementioned rig. A video camera, which records the motion to be analyzed via image processing, can be mounted above the testing rig and pointed down to record the motion in the x-y plane. A six degree-of-freedom load cell has been placed at the interface between the hydrodynamic foil and the attachment to the carriage. The load cell was used to measure forces and moments caused by the propulsion of the robot. Beneath the load cell, the foil is mounted to an adjustable plate that allows the apparatus to be rotated for proper alignment.

The foil section was chosen so that there is minimal bending about the vertical z-axis due to transverse inertia forces at the head of the eel. (Theoretically, there are no transverse forces due to the hydrodynamics.) This tether design was chosen since it minimizes the flow disturbance around the eel's body. It also minimizes the effects of the free surface disturbance on the image data. Since
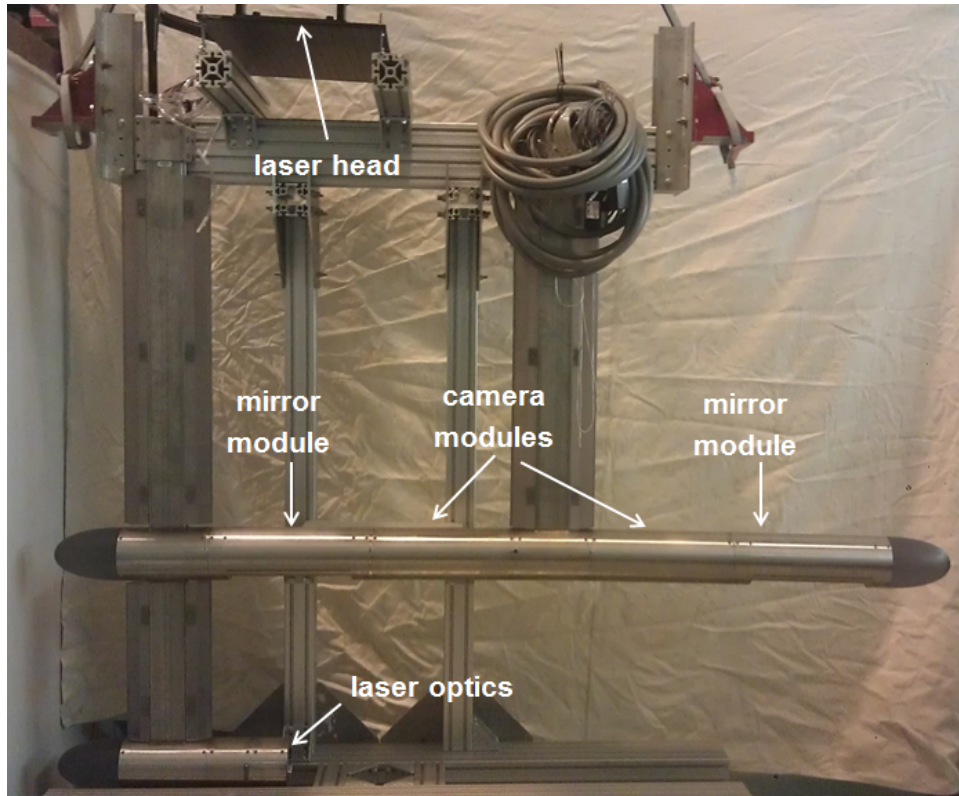
Figure 4.3: Components of the TSI Model 6800 SPIV System at University of New Orleans.

the foil pierces the free surface well ahead of the camera's view, the divergent waves are out of view (see Figure 4.42).

The coordinate system shown in Figure 4.2 matches that of the coordinates used to specify the anguilliform shape motion in the theoretical chapter, previously.

4.1.2 PIV Hardware Setup

The Particle Image Velocimetry (PIV) equipment hardware is the most expensive and contains some of the most delicate components of the testing. For this project, University of New Orleans obtained a Model 6800 SPIV system from TSI, Inc. through DURIP grant # N00014-12-1-0782. This equipment can measure fluid velocities in a large field field of view and is able to be attached to UNO's Towing Tank carriage, enabling it to measure velocities while underway.

Figure 4.3 shows some of the components in Model 6800. The laser head, which is just above the image frame, shines its laser beam into a 90-degree block and then into a light-bar, which directs it down the vertical strut on the left side of the picture and out to the right through the optics. Each

camera module contains a Powerview 4MP camera (not shown since they are inside the camera modules) that are each pointing to the right and left in the image frame. (These end up being fore and aft directions on the carriage, relative to the towing tank.) The mirror modules redirect the light into the camera modules so that the cameras can record the scene appropriately. It is critical that the mirrors are angled correctly so that the desired field of view is seen by the cameras. The coiled tubing contains all of the data acquisition wiring to download the data from the camera CCD's, and it contains the signal wiring for the aperture, Schiempflug, and focus control, as well as the camera triggering.

In addition to the components described above, the system consists of the following major components (with descriptions of each to follow):

- cameras: ×2 Model 630059 Powerview 4MP, 2048 x 2048 pixels, 12-bit, at 16 fps

- stereo calibration kit

- synchronizer: Model 610035 LaserPulse Synchronizer

- lasers: Model Nd:YAG 200-15 Dual YAG laser with 200 mJ/pulse at 15 Hz

- laser power supply

- 90-degree block

- carbon-fiber reinforces laser light bar

- laser optics

- software/data processing: Insight 4G$^{\text{TM}}$Stereo parallel processing PIV software package

- 48GB RAM computer

The stereo calibration kit is used to calibrate distances in the images acquired with the cameras. The kit consists of a 0.76 m by 0.46 m plate with an array of contrasting dots on a precise grid pattern. Due to the speed at which data can be downloaded from the CCD arrays of the cameras, the maximum sampling rate is effectively 7.25 Hz (not the 16 Hz specified). The synchronizer is a critical component that synchronizes the laser pulses and camera snapshots. The synchronizer
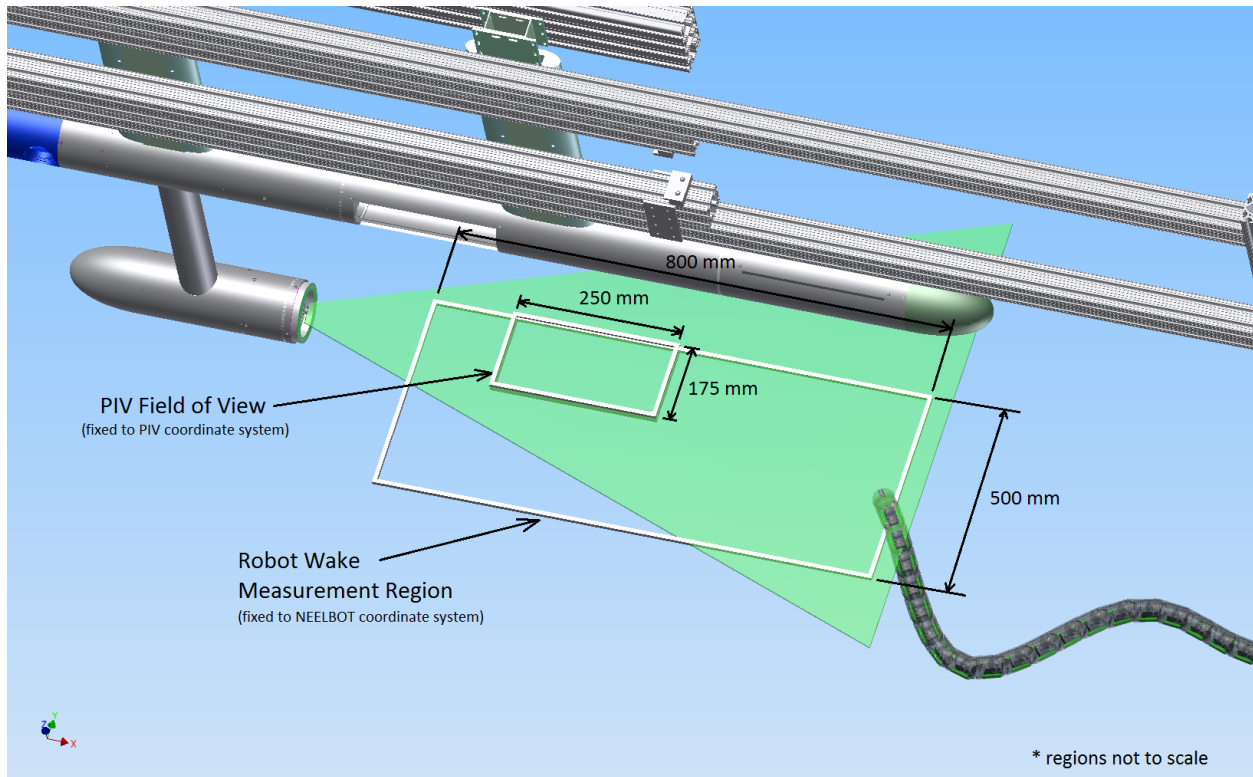
Figure 4.4: Annotations showing the exact locations of the interested measurement region and the field of view of the PIV.

timing can be adjusted to microsecond levels of precision. The laser power level can be adjusted to varying levels of intensity.

The laser head is pointed into the 90-degree block to direct the laser into the light bar, while also providing a method to aim the laser down the length of the light bar. The light bar, also called a periscope, directs the laser beam from the 90-degree block down to the bottom of the Model 6800, where it exits through the beam-forming optics. The light bar consists of several precision-tuned mirrors to help direct the laser through its numerous corners with minimal efficiency losses. The optics are used to shape the laser beam into a wide-angle fan with a width of 3-5 mm. Figure 4.4 shows the fan created by the optics.

Figure 4.4 also shows the different sizes of the PIV field of view and the wake measurement region, which is where the fluid dynamics of the robot are to be compared to the theoretical predictions. Because of this problem, several PIV "runs" had to be performed with different tether positions. It is not easy to move the PIV system relative to the robot, so the tether support

113
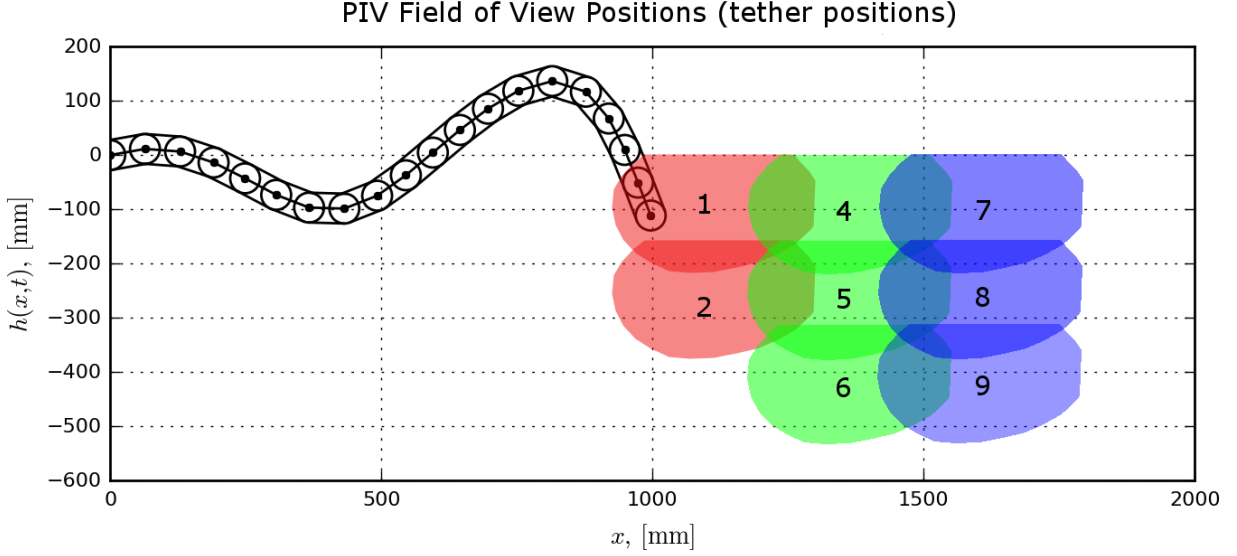
Figure 4.5: PIV field of view positions relative to the NEELBOT-1.1 frame of reference.

structure was designed to be adjustable in the xy-plane. Figure 4.5 shows the eight positions of the tether needed to cover the robot wake measurement region. Notice that region 3 is not shown. This is because it was found after initial testing that fluid dynamic phenomenon as a result of the robot motion is not occurring in this region of the wake. Eliminating this area of measurement reduced the testing runs needed by 11%.

Sufficient overlap between the regions was ensured so that the fluid velocities from different positions can be compared and ensure that the results are stationary in time. Each tether position consisted of at least four runs occurring at its spatial position, one for each of the four different testing speeds. Table 4.1 shows the testing matrix of run numbers, tether position, and advance speed. These run numbers are used to also denote the load-cell measurement results shown in Section 4.2.

Figures 4.6 and 4.7 show NEELBOT-1.1 tethered to the towing tank carriage during testin. The first image was taken during a full test, including the load-cell measuring and the PIV measuring. The robot is the brightly illuminated object in the center of the picture. The second image shows a close-up of NEELBOT-1.1 tethered in front of the Model 6800 PIV system but without PIV testing occurring.

Table of advance speeds and tether positions of the robot. The value for each unique speed-tether position combination denotes the label number for the "run" performed during the experiment. A run consists of the carriage traversing the length of the tank during DAQ.

Tether Position	1	2	4	5	6	7	8	9
0 rpm (0.0 m/s)	19	23	36	32	27	40	44	48
89 rpm (0.16 m/s)	17	21	34	30	25	38	42	46
139 rpm (0.25 m/s)	15,16	20	33	28,29	24	37	41	45
222 rpm (0.40 m/s)	18	22	35	31	26	39	43	47,49
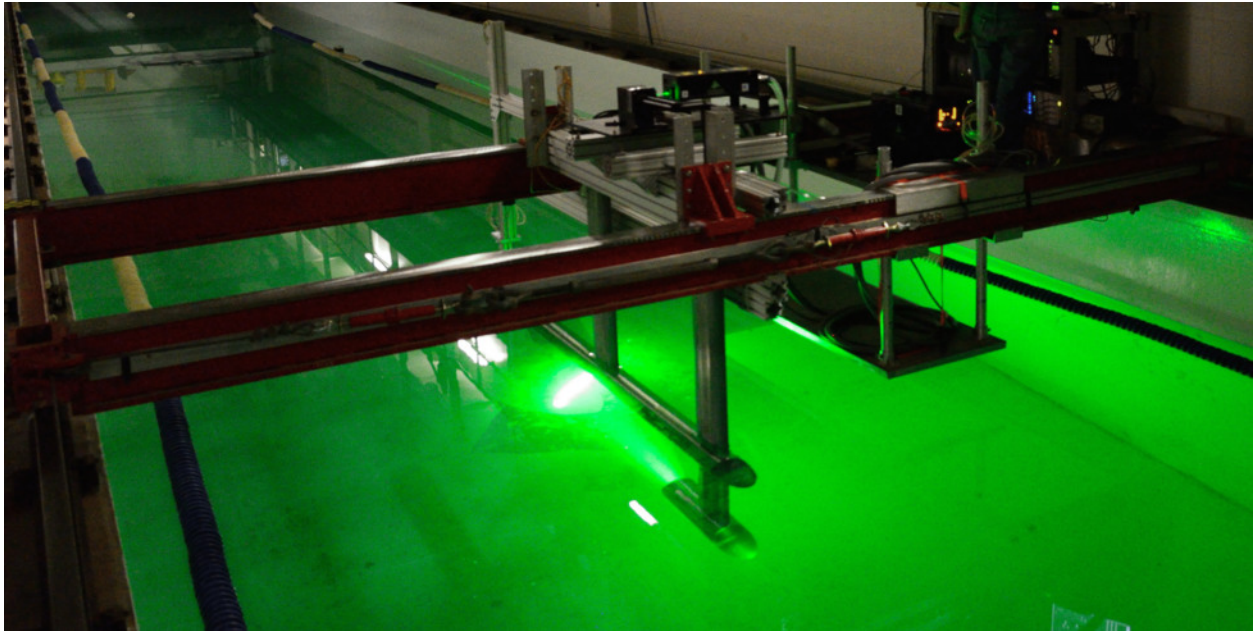
Figure 4.6: TSI Model 6800 SPIV system installed on UNO Towing Tank carriage, shown while underway during a test. NEELBOT-1.1 is the brightly illuminated object in the center of the picture.
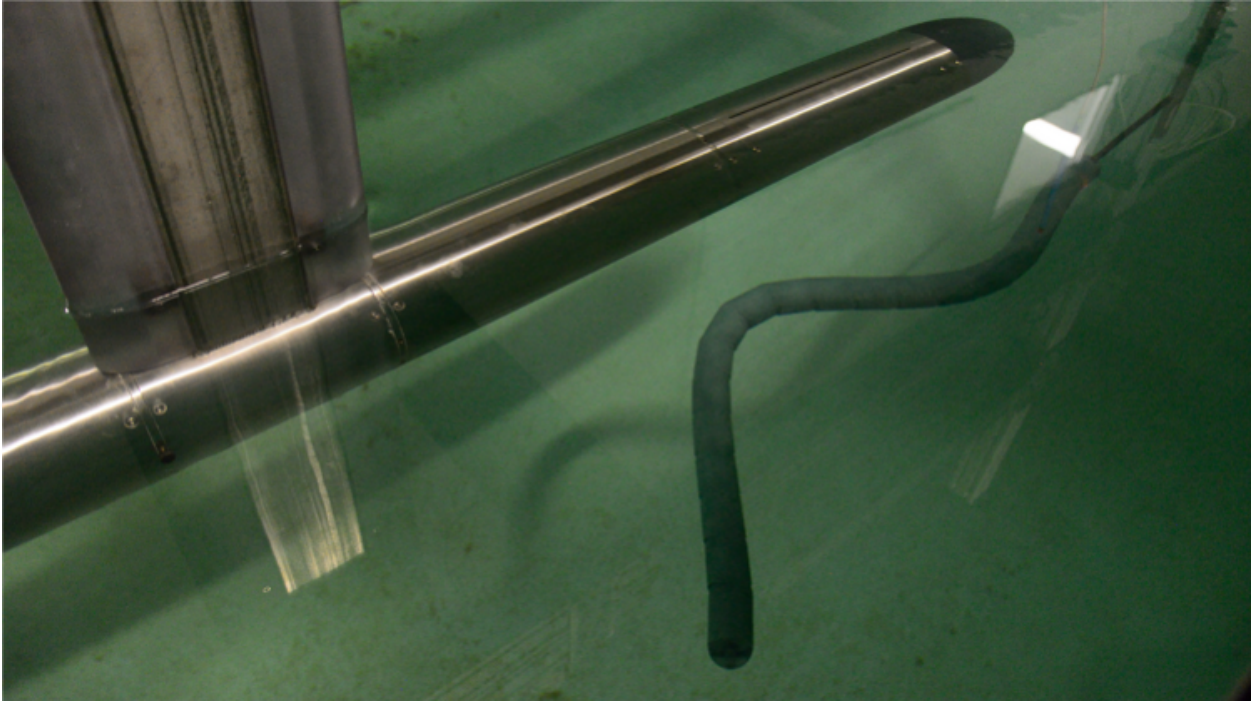
Figure 4.7: NEELBOT-1.1 shown tethered in position in front of the PIV system.

4.2 Lift/Drag Results

In addition to the PIV testing of the robot wake, the load cell was simultaneously recording the transverse and longitudinal forces at the head of the robot. This recorded data was then compared to the forces as predicted by the revised theoretical prediction applited to the actual motion. As reported earlier, the robot was not able to fully replicate the ideal motion. To compare the actual, non-ideal motion that was recorded to a theoretical prediction, the theoretical prediction of propulsive forces in Vorus and Taravella (2011) was computed for this non-ideal motion case. Comparisons were made for the 4 advance speeds, and the comparisons between the measured and predicted agree rather reasonably.

First, the ideal theory for propulsive forces is applied to a discretized kinematic model, resembling the segments of the robotic eel, and the forces and moments are computed for each joint (Section 4.3.3). The measurement procedure of the transverse and longitudinal forces is explained with details of the load cell and robotic eel coordinate systems (Section ??) and subtraction of the foil drag (Section 4.2.1.1) and straight-line robot drag (Section 4.2.1.2). The measurements are then compared to the theoretical predictions for the four advance speeds (Section 4.2.1.3). Discussion
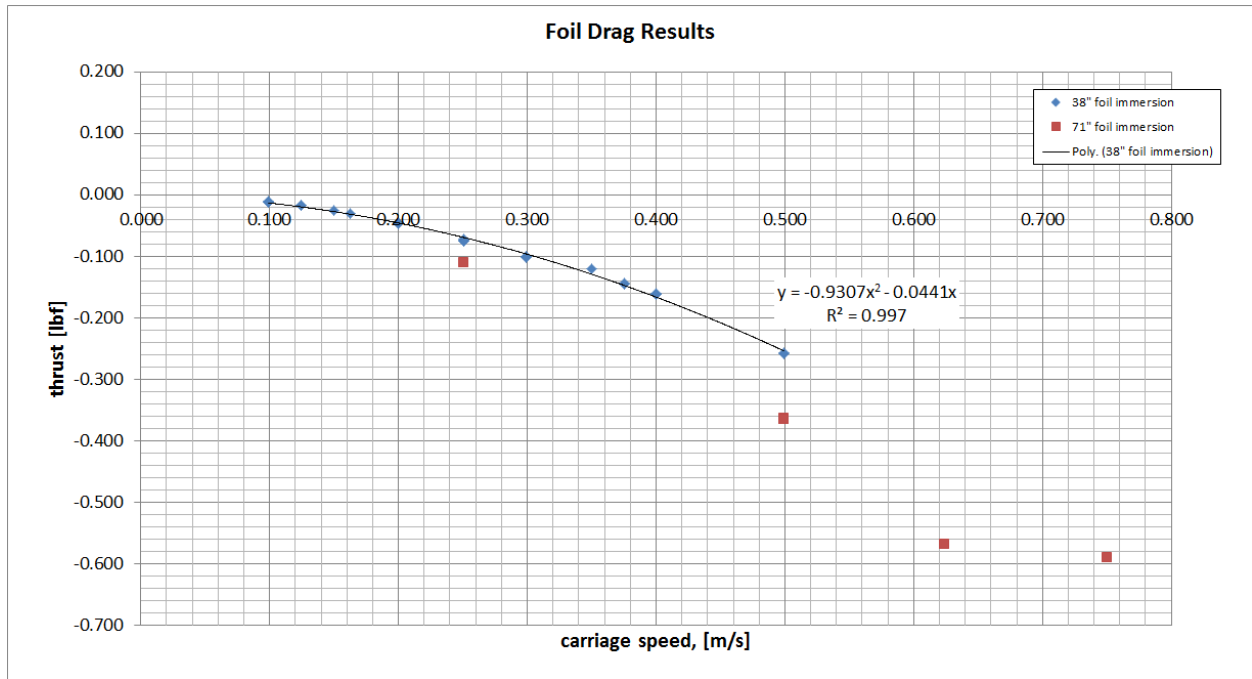
Figure 4.8: Foil drag of robot vs. advance speed (U_o).

of the results and the reasonably agreeable comparisons is contained within.

4.2.1 Load Cell Measurements

4.2.1.1 Foil Drag

4.2.1.2 Straight-line Robot Drag

4.2.1.3 Load Cell Measurements Compared to Theoretical Predictions

The transverse and longitudinal loads at the robot's head were recorded with a JR3 6-DOF load cell during each of the PIV measurement runs. The data was recorded at a sampling rate of 40 Hz and is shown on the next several plots. Figure 4.2 shows the coordinate directions of the forces as measured by the load cell. For each unique force direction-advance speed combination, there are four plots associated with it. In order for each combination, the four plots are the raw time-series data of each run, a time-series showing the average of all the runs, a Discrete Fourier Transform (DFT) of the raw data, and another time-series data set but with the raw data of each run filtered using a "brickwall" filter in the frequency domain. For the plots except for the DFT ones, the theoretical predictions are plotted for comparison. For example, for the 0 m/s advance speed case,
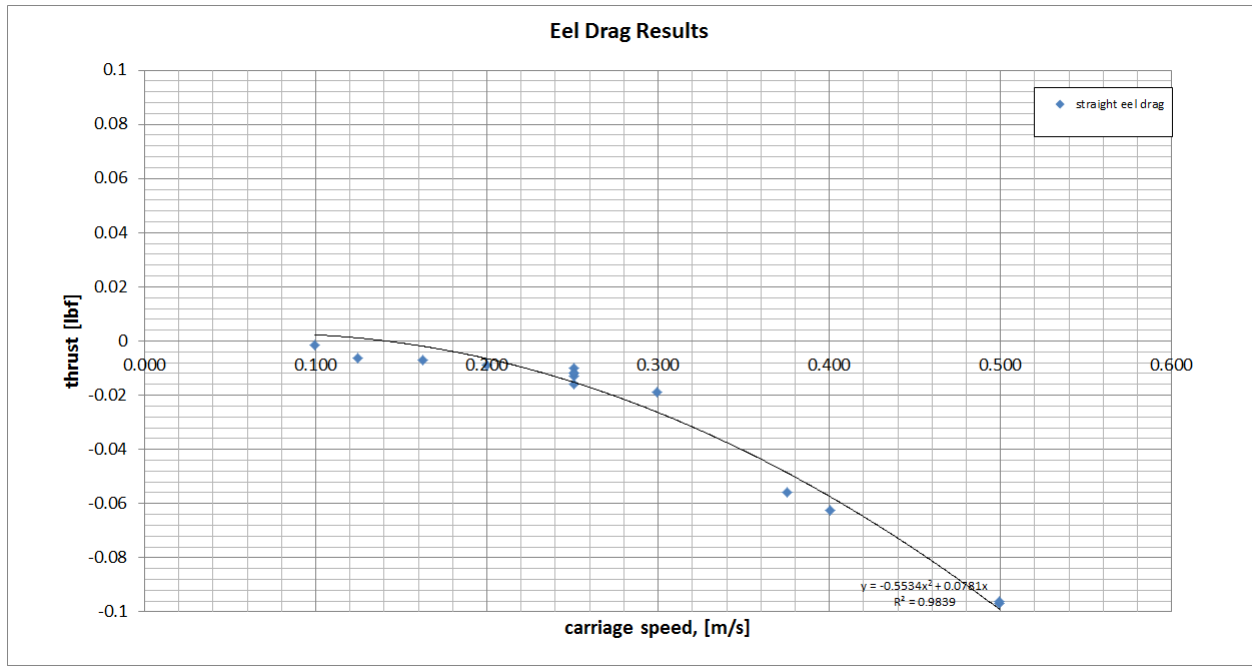
Figure 4.9: Straight-line drag of robot vs. advance speed (U_o).

Figures 4.10 and 4.11 show the raw and averaged time-series data for each run, respectively. Figure 4.12 shows the DFT of this raw data, and Figure 4.13 shows the raw data being filtered with a brickwall filter. The next 4 figures plot the same type of data but for the longitudinal force at 0 m/s advance speed. Then, this pattern of plots repeats itself every 8 figures for the next 3 cycles, up to Figure 4.41.

For the majority of the following plots, the respective force (either predicted or measured) is plotted versus time over one cycle of motion. For the load cell measurements, each speed consists of 8 Runs due to the different tether positions needed for the PIV to measure the whole field of interest. 19 cycles of motion were recorded for each Run since the motion was recorded for the entire length of the tow tank. These 19 cycles of motion for each of the 8 runs at each speed provides some reliable statistics and a good picture of the repeatability of the force measurements due to the robot motion over time.

The remaining plots contain frequency analyses of the data to give an idea of what is happening to the system from an oscillatory point of view. For each case, there are matching frequency components with possible causes explained in more detail within.

For each speed and force direction, a Fourier analysis was performed in order to understand

the oscillatory nature of the measurement data. The Fourier analysis for each set of data was computed by taking the DFT of the data and plotting it in the frequency domain. Figures 4.12 and 4.16 display the DFT for the 0 m/s case. Figures 4.20 and 4.24 show it for the 0.16 m/s case. Figures 4.28 and 4.32 are for the nominal design speed case of 0.25 m/s, and Figures 4.36 and 4.40 are for the 0.40 m/s case.

From the Fourier analysis, the amplitude of the frequency spike at 0 Hz is the average value for the force over the time period. As a quality assurance check, this value is in agreement qualitatively for all the speed cases, as can be seen by the theoretical predictions about this mean value. In each of the plots, there are several spikes at equal intervals, which are all lining up with the integer multiples of the fundamental frequency (which in these cases is 0.3675 Hz, the frequency of the eel motion).

For the DFT's of the transverse force plots, besides the 0-frequency component, the two largest spikes are located at the fundamental frequency and 13 times the fundamental frequency (4.78 Hz). The reason for the fundamental frequency spike has already been explained. It is unclear at the moment what the cause of the spike at 4.78 Hz is (but it is hypothesized that it is aligning close to the natural frequency of the tether in the transverse direction). A natural frequency analysis of the tether is performed and shown in the next section. Table 4.2 shows the parameters used to calculate the natural frequency. Unfortunately, this calculation estimates the natural frequency of the NEELBOT-1.1 and tether system, with added mass included, to be 8.5 Hz. This frequency value is very close to the 23rd harmonic of 8.45 Hz, but the spike at this position is relatively small for all speeds. (An earlier estimate for the natural frequency was computed to be 9.7 Hz, which is approximately twice that of the large frequency spike at 4.78 Hz for each speed case. This earlier estimate omitted the added mass of the tether column. The current analysis assumes the tether and robot are all rigid, when in fact the robot will have some freedom to move at its joints, affecting the amount of added mass included due to the body not being normal to the flow, as the assumed cylindrical cross-section model is.)

For the DFT's of the longitudinal force plots, there are spikes at all multiples of the fundamental frequency, with the largest (besides the 0-frequency component) occurring at double the fundamental frequency. The two cycles of propulsive force per one cycle of robot motion (as predicted by the theory in Vorus and Taravella (2011)) is causing this frequency spike. The other frequency

spikes are occurring at integer multiples of this propulsive frequency, but are relatively small and are ignored for the moment.

The fourth figure of each cycle of four plots shows the raw data being filtered to eliminate any noise. The frequency spectrum of each data set was filtered with a "brick-wall" filter at a threshold of 1 Hz, which was performed by multiplying this filter with the DFT in the frequency domain (Bracewell (2000)). The inverse Fourier transform of the resulting spectrum was taken to get the data back in the time domain, and the resulting plots are shown in Figures 4.13, 4.17, 4.21, 4.25, 4.29, 4.33, 4.37, and 4.41.

This computation is the same as filtering the time-domain data with a "sinc" filter, which is an ideal filter for a specified cut-off frequency, or threshold frequency. For this analysis, the threshold frequency was set at 1 Hz, thus eliminating any frequency content in the data above this value. This specific value was chosen since the rigid body motion and propulsive frequencies are lower than this. Any frequencies higher than these are considered to be noise. The robot's time period of motion is 2.721 seconds for the nominal design speed, resulting in a frequency of 0.3675 Hz. According to the theory in Vorus and Taravella (2011), there are two cycles of propulsive thrust for each cycle of motion, thus the propulsive thrust is occurring at a frequency of 0.735 Hz, still well below the cut-off frequency.

Other equipment or phenomenon that my be contributing to the frequency content of the spectrum are the carriage motor drive and gear train. This is proportional to the speed by a simple unit conversion, so for the 89 rpm (0.16 m/s case), the motor system is contributing a frequency of 9.3 Hz. The other two speeds are proportionally higher at 14.6 Hz and 23.3 Hz, respectively. The gear train of the motor drive contributes to the frequency content of the system too but at frequencies higher than the motor speeds. Since these frequencies are much higher than the majority of the frequency content of the data shown within, the contributions from this equipment that may be affecting the data have been neglected.

Natural frequency of tether: The natural frequency of the NEELBOT-1.1-tether system is estimated using Rayleigh's effective mass energy method (Thomson and Dahleh (1998)). The effective mass is computed by deriving the kinetic energy of the system, modelling it as a single degree-of-freedom system. The mass component of the kinetic energy formula is extracted and used

as the effective mass, which is used to improve the estimate of the frequency. The formula for the natural frequency is

$$\omega_n = \sqrt{\frac{k}{m_{\text{eff}}}} \tag{4.1}$$

where k is the stiffness of the system and m_{eff} is the effective mass. For Rayleigh's method applied to the tether, the mass of the column is included instead of assuming it to be negligible. The kinetic energy, KE, of a translating mass, m, is

$$KE = \frac{1}{2}m\dot{y}^2 \tag{4.2}$$

Using lookup tables in a text such as Young et al. (2011) for a vertical column fixed at one end, the deflection in the y-direction as a function of the vertical length, z is

$$y(z) = \frac{Fz^2}{6EI}(3l - z) \tag{4.3}$$

where F is the concentrated force at the end of the column, E is the modulus of elasticity of the column's material, and I is the 2nd moment of area of its cross section, and l is the length of the column. The max deflection is at the end and is

$$y_{max} = \frac{Fl^3}{3EI} \tag{4.4}$$

This formula can be substituted into equation 4.3 to get the deflection proportional to the maximum deflection and still as a function of z

$$y(z) = y_{max}\left(\frac{3z^2}{2l^2} - \frac{z^3}{2l^3}\right) \tag{4.5}$$

This can be substituted into the equation for kinetic energy (4.2) and integrated along the length of the column to get the maximum kinetic energy of the column

$$
\begin{aligned}
KE_{max} &= \frac{1}{2}\int_0^l \frac{m_t}{l}(\dot{y}(z))^2 dz \\
&= \frac{1}{2}(0.2357m_t)\dot{y}_{max}^2
\end{aligned}
\tag{4.6}
$$

where m_t is the mass of the tether column (included in the mass of the tether is its added mass, $m_{a,t}$, computed by modelling it as having an elliptical cross-section), and the term in parentheses is the mass of the column contributing to the kinetic energy of the system. Lumping this mass term with the mass and added mass for the NEELBOT-1.1, m_{tot}, gives the effective mass of the system:

$$m_{\text{eff}} = m_{\text{tot}} + 0.2357 m_t \tag{4.7}$$

and this, along with the stiffness for a vertical column $(k = \frac{3EI}{l^3})$, can be substituted into equation 4.1 to obtain

$$\omega_n = \sqrt{\frac{3EI}{l^3(m_{\text{tot}} + 0.2357 m_t)}} \tag{4.8}$$

The mass, m_{tot}, includes both the mass of the robot and its added mass:

$$m_{\text{tot}} = m_r + m_{a,r} \tag{4.9}$$

The added mass, $m_{a,r}$, for the robot is computed for a cylindrical cross-section assuming it is an infinitely long:

$$m_{a,r} = \rho \pi r_o^2 L_r \tag{4.10}$$

where ρ is the density of the water, r_o is the radius of NEELBOT-1.1, and L_r is the length of the robot. Using the above formulas and the parameters listed in Table 4.2, the natural frequency of the system is computed to be 8.5 Hz.

4.2.1.4   0 rpm (0 m/s)

Table 4.2: NEELBOT-1.1-tether system natural frequency analysis.

Parameter	Value
water density, ρ	998.905 kg/m^3
robot length, L_r	1.3 m
robot radius, r_o	0.0555 m
robot mass, m_r	3.216 kg
robot added mass, $m_{a,r}$	12.57 kg
column mass, $m_{a,t}$	20.12 kg
column mass, m_t	0.942 + 20.12 kg
column length, l	0.965 m
modulus of elasticity, E	69,000 MPa
2nd moment of area	6.54×10^{-9} m^4
natural frequency, ω_n	8.5 Hz
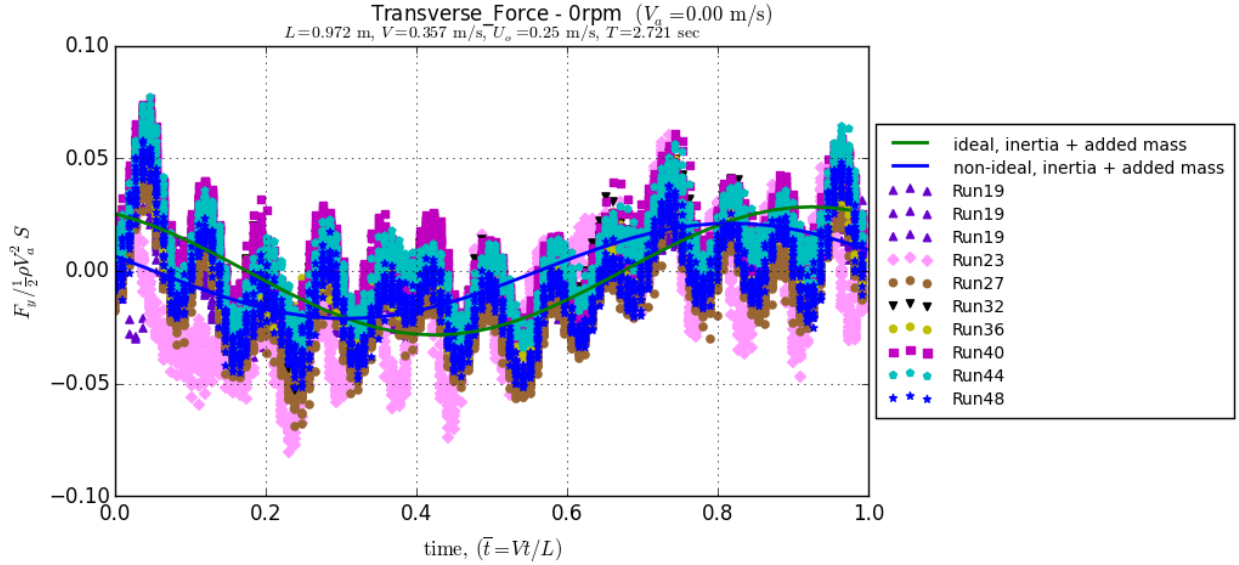
Figure 4.10: Transverse Force.

Figure 4.11: For the advance speed of 0.0 m/s, the mean of transverse force for each time step is shown, with error bars showing standard deviation of the mean, i.e. the uncertainty.

Figure 4.12: DFT of Transverse Force.

Figure 4.13: Filtered Transverse Force data.

Figure 4.14: Longitudinal Force.

125

Figure 4.15:
For the advance speed of 0.0 m/s, the mean of longitudinal force for each time step is shown, with error bars showing standard deviation of the mean, i.e. the uncertainty.

Figure 4.16: DFT of Longitudinal Force.

Figure 4.17: Filtered Longitudinal Force data.
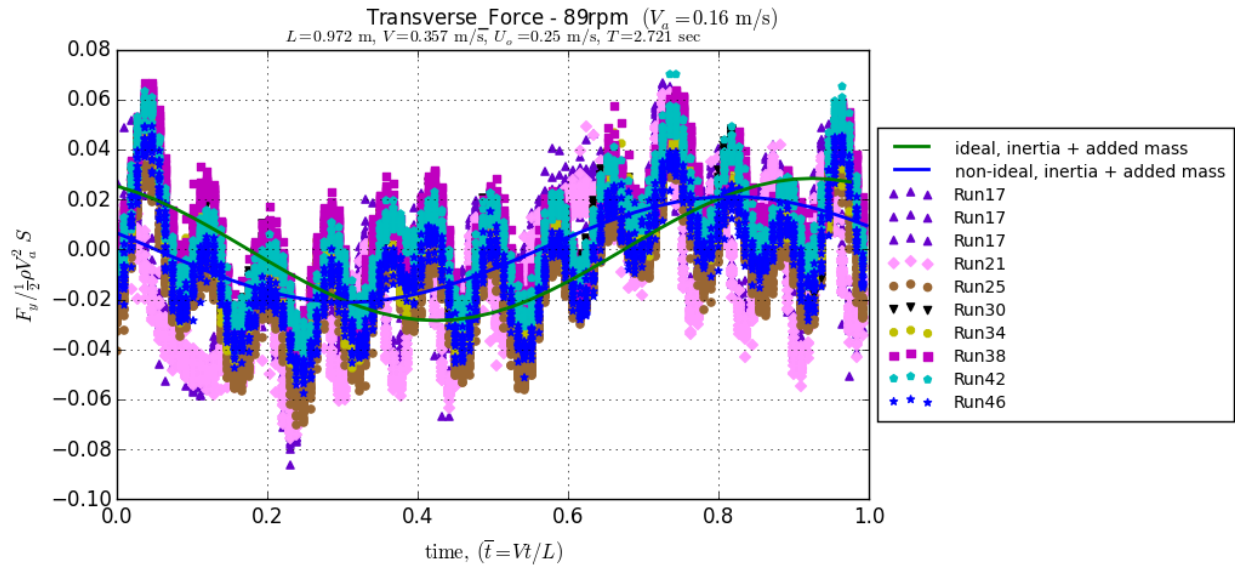
Figure 4.18: Transverse Force.

4.2.1.5   89 rpm (0.16 m/s)
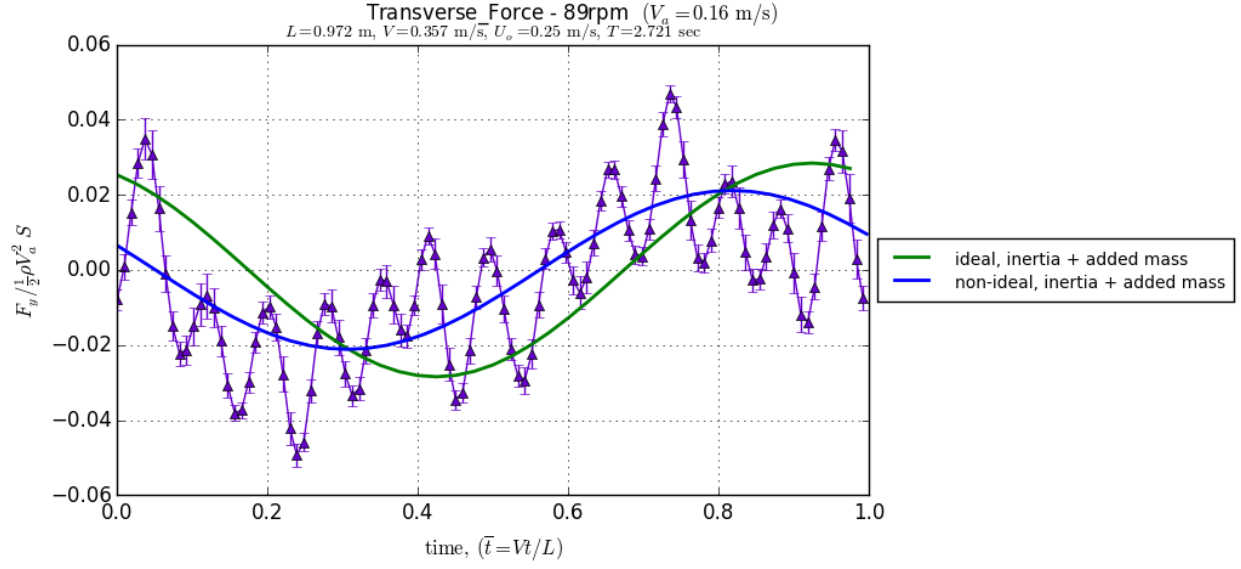
Figure 4.19:
For the advance speed of 0.16 m/s, the mean of transverse force for each time step is shown, with error bars showing standard deviation of the mean, i.e. the uncertainty.
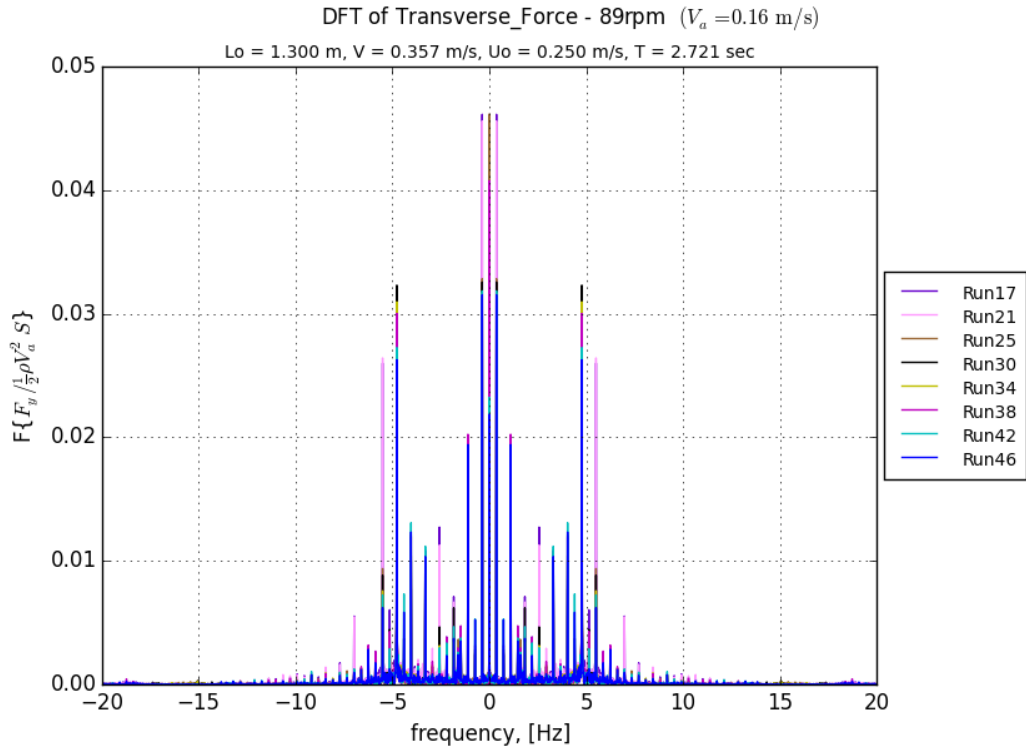
Figure 4.20: DFT of Transverse Force.
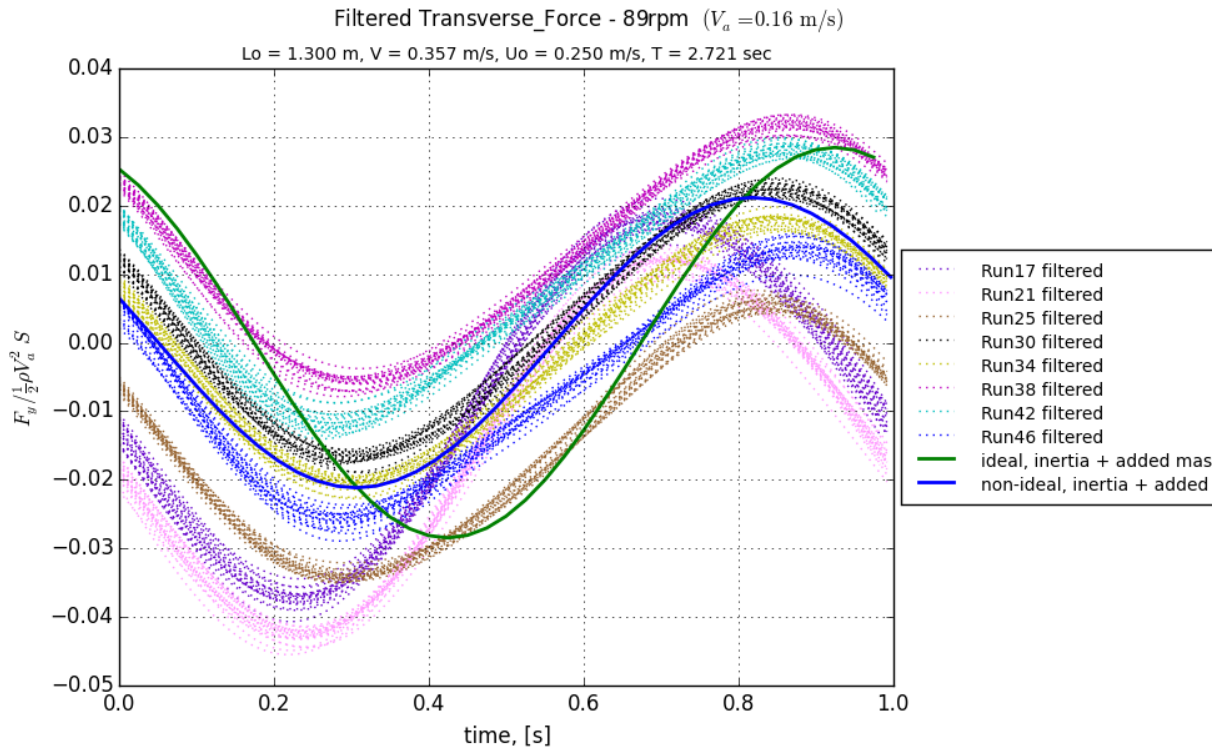
Figure 4.21: Filtered Transverse Force data.
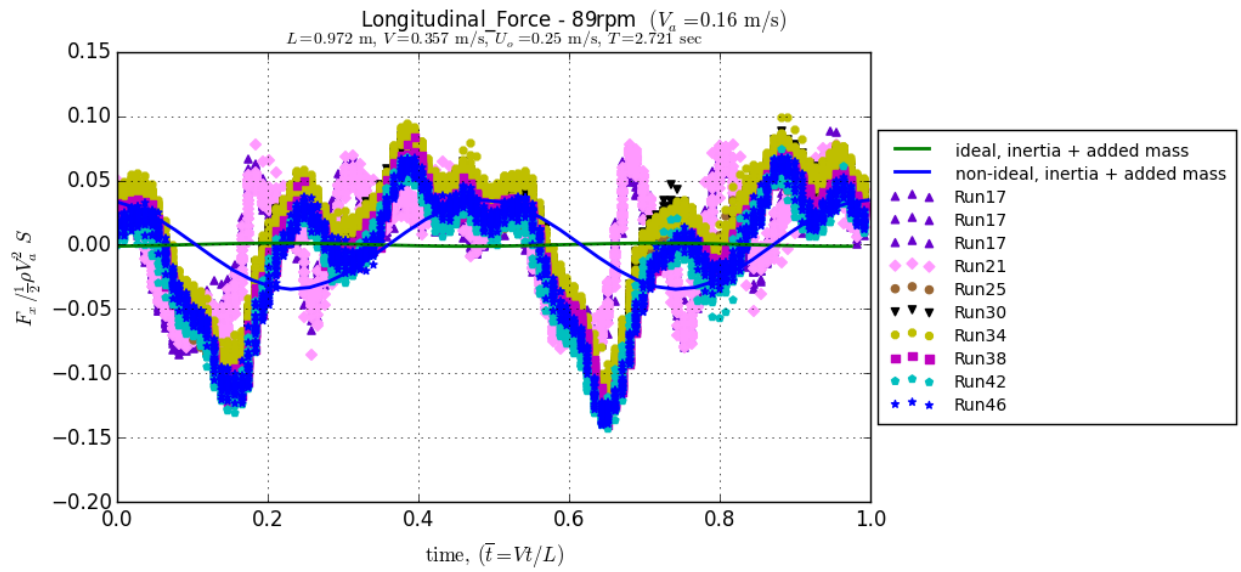
Figure 4.22: Longitudinal Force.

130
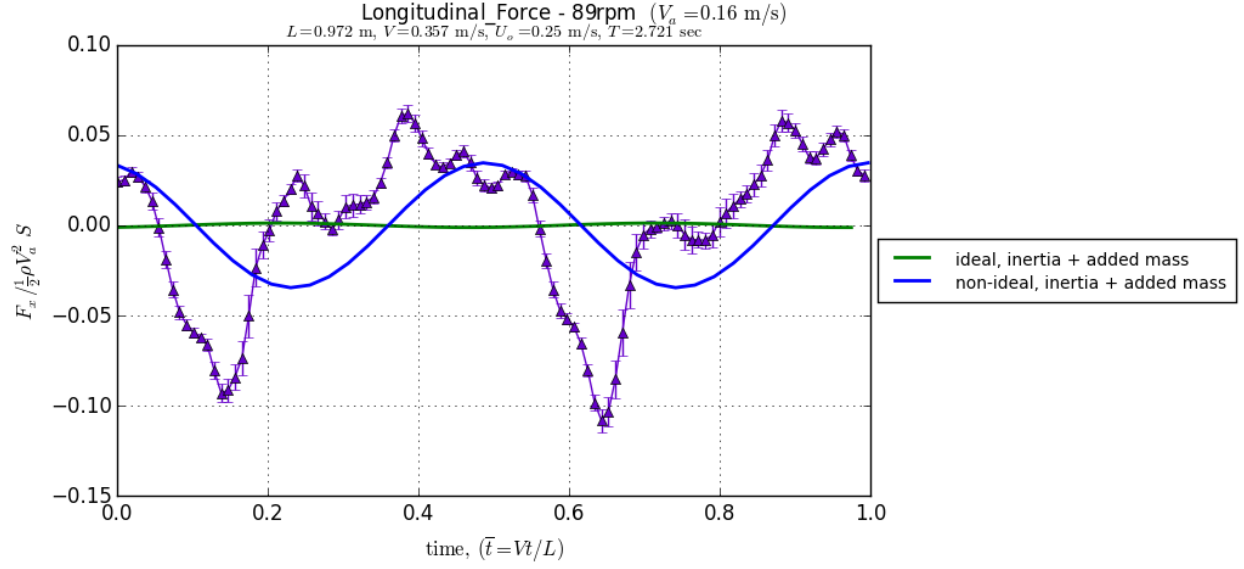
Figure 4.23:
For the advance speed of 0.16 m/s, the mean of longitudinal force for each time step is shown, with error bars showing standard deviation of the mean, i.e. the uncertainty.
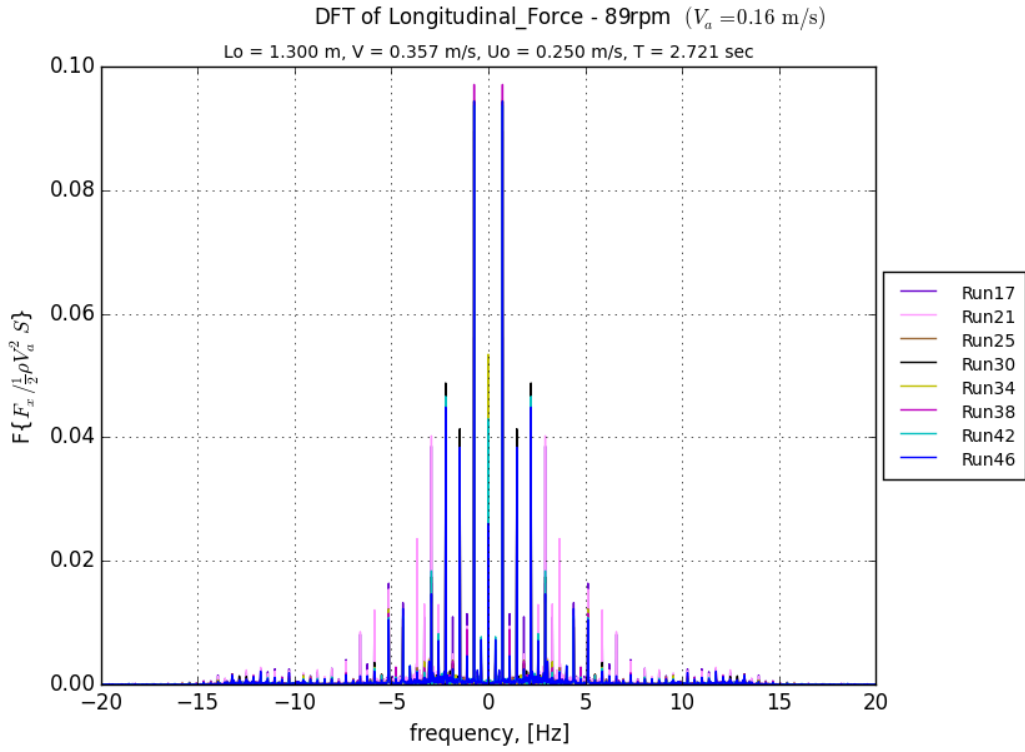
Figure 4.24: DFT of Longitudinal Force.
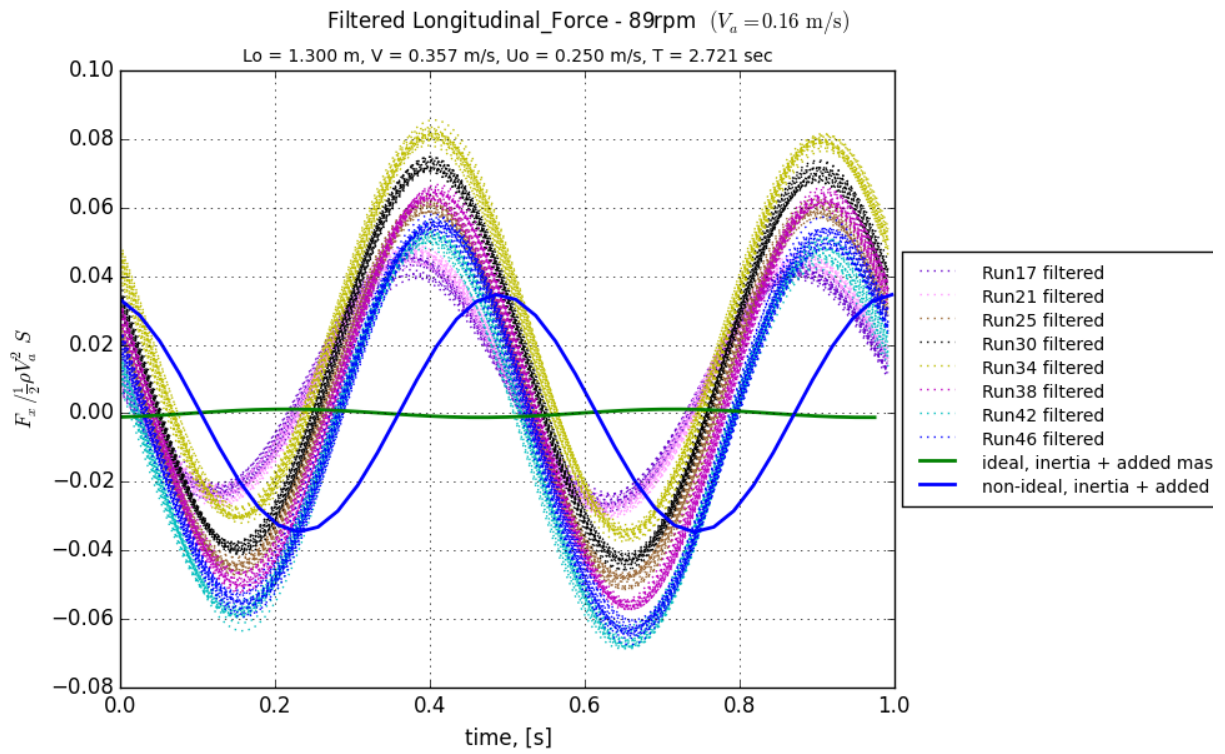
Figure 4.25: Filtered Longitudinal Force data.
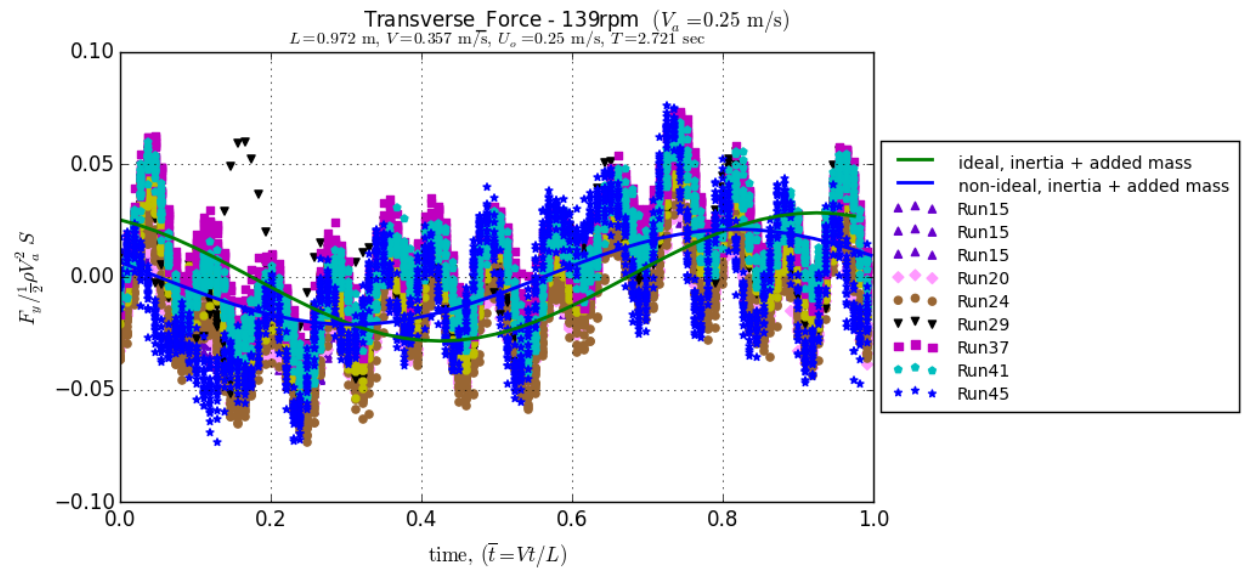
Figure 4.26: Transverse Force.

4.2.1.6   139 rpm (0.25 m/s)
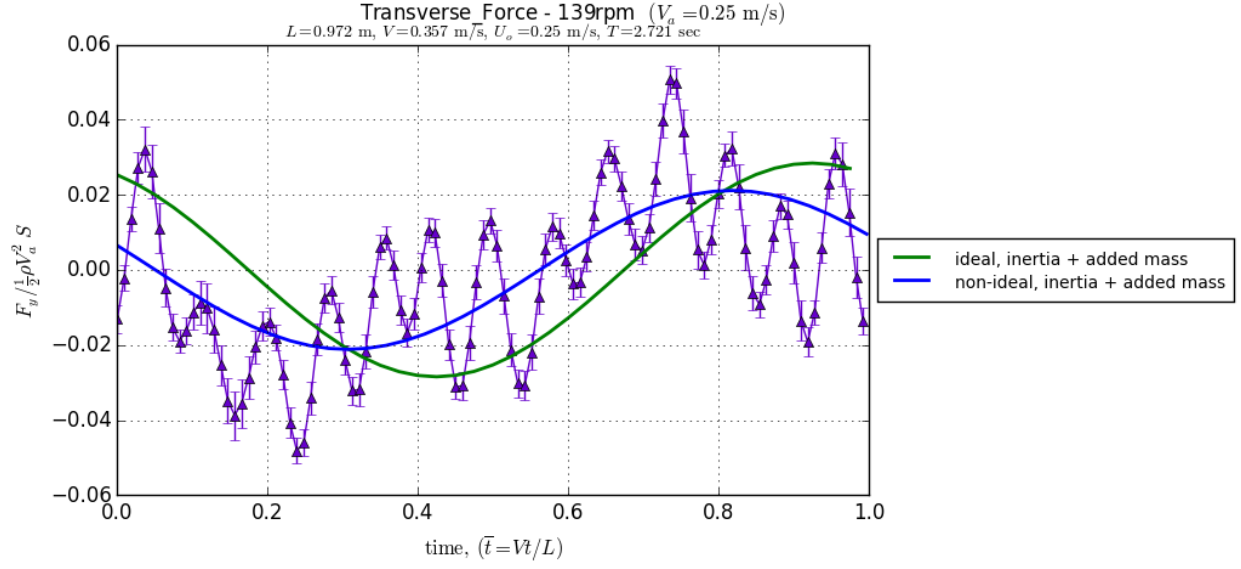
Figure 4.27: For the advance speed of 0.25 m/s, the mean of transverse force for each time step is shown, with error bars showing standard deviation of the mean, i.e. the uncertainty.
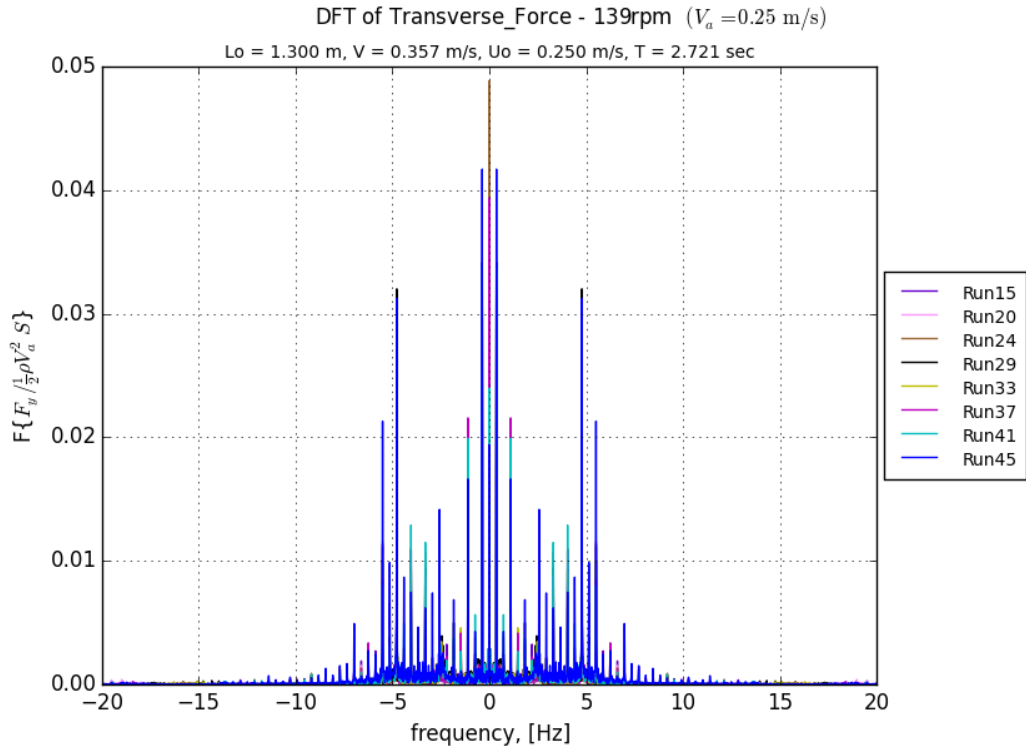
Figure 4.28: DFT of Transverse Force.
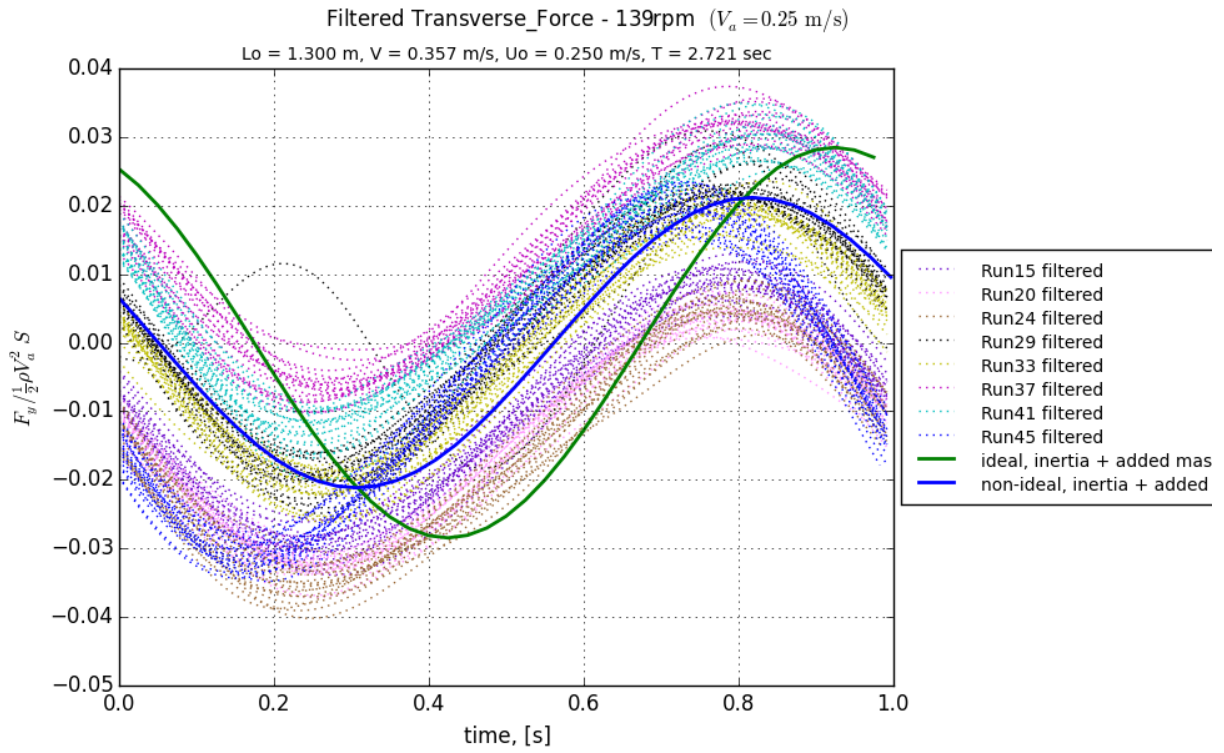
Figure 4.29: Filtered Transverse Force data.
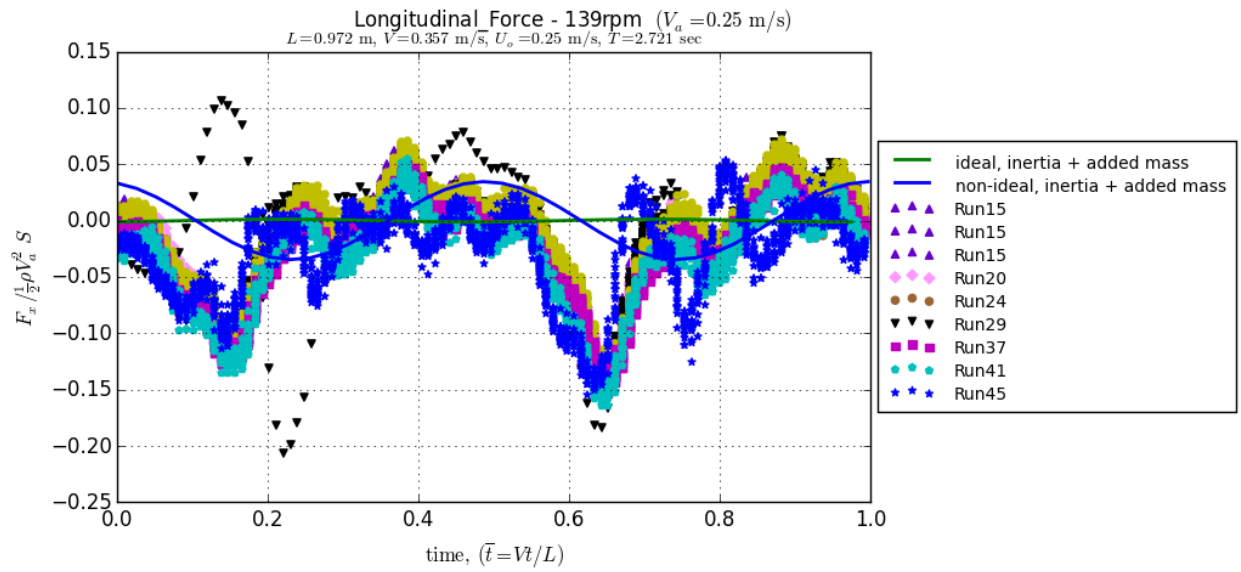
Figure 4.30: Longitudinal Force.

135
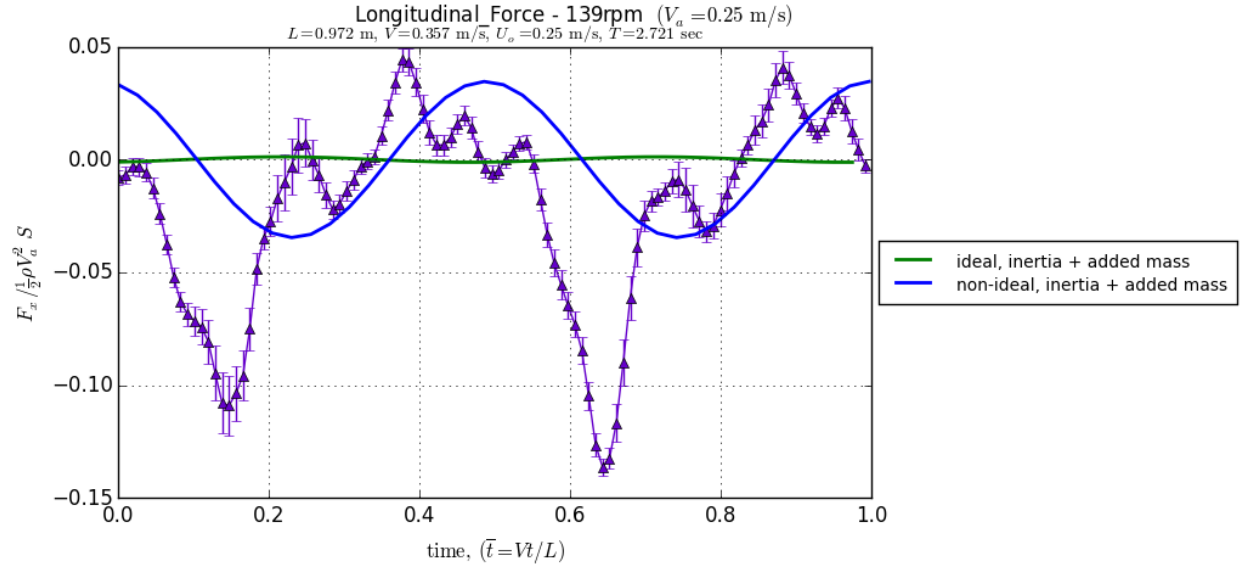
Figure 4.31: For the advance speed of 0.25 m/s, the mean of longitudinal force for each time step is shown, with error bars showing standard deviation of the mean, i.e. the uncertainty.
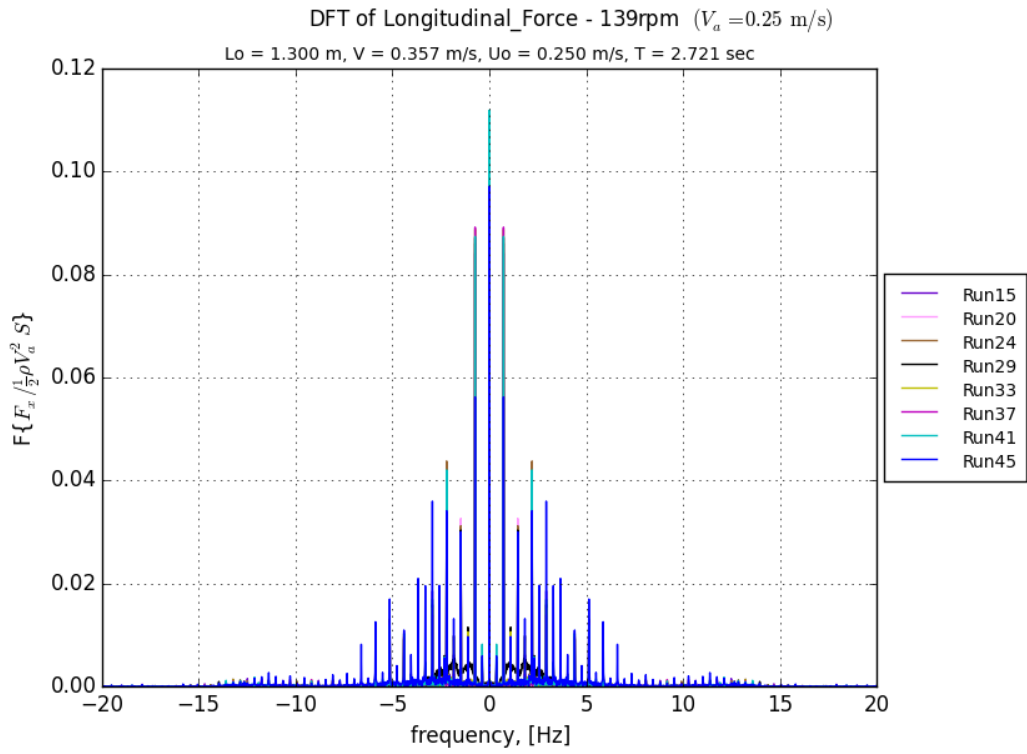
Figure 4.32: DFT of Longitudinal Force.
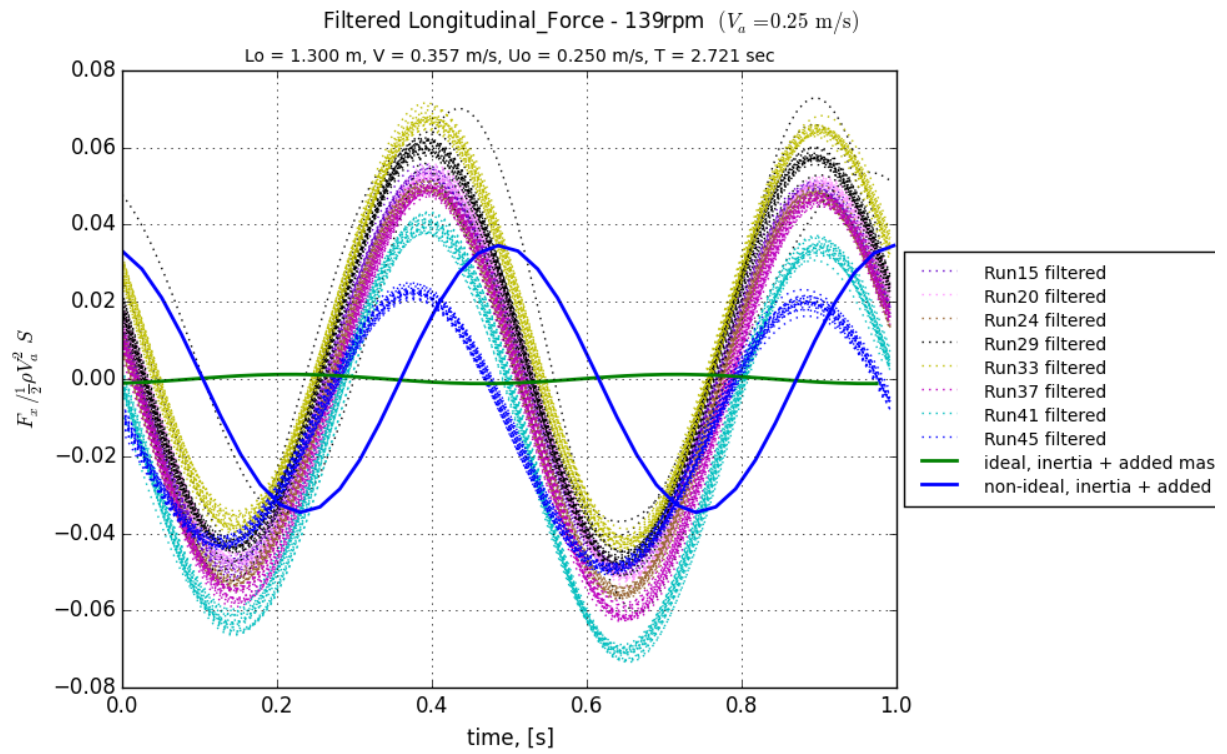
Figure 4.33: Filtered Longitudinal Force data.
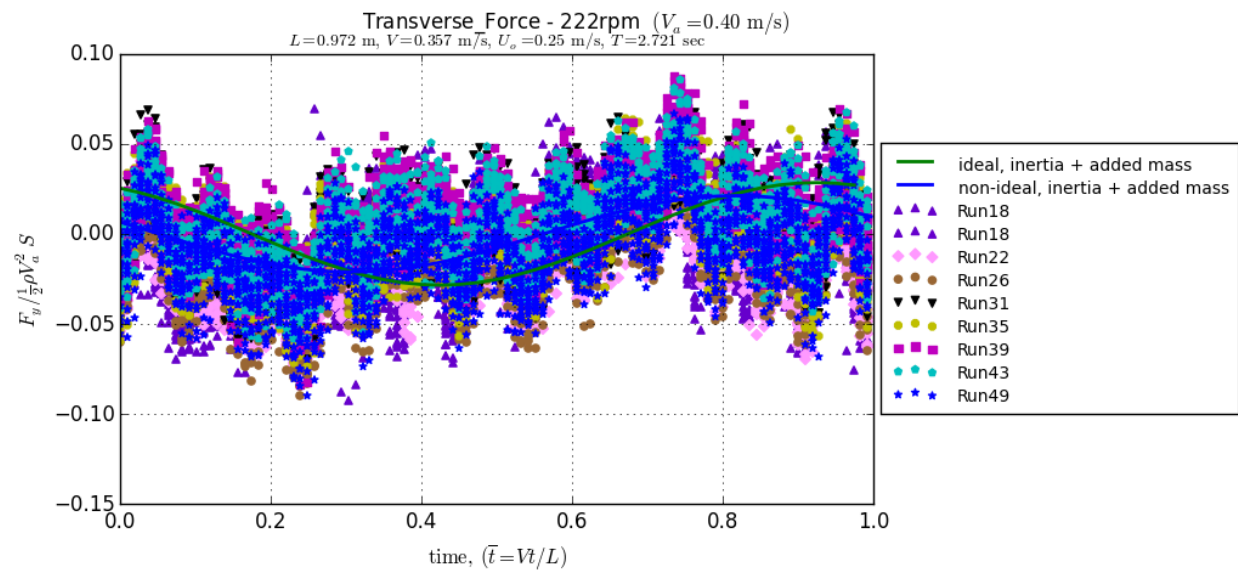
Figure 4.34: Transverse Force.

4.2.1.7 222 rpm (0.40 m/s)
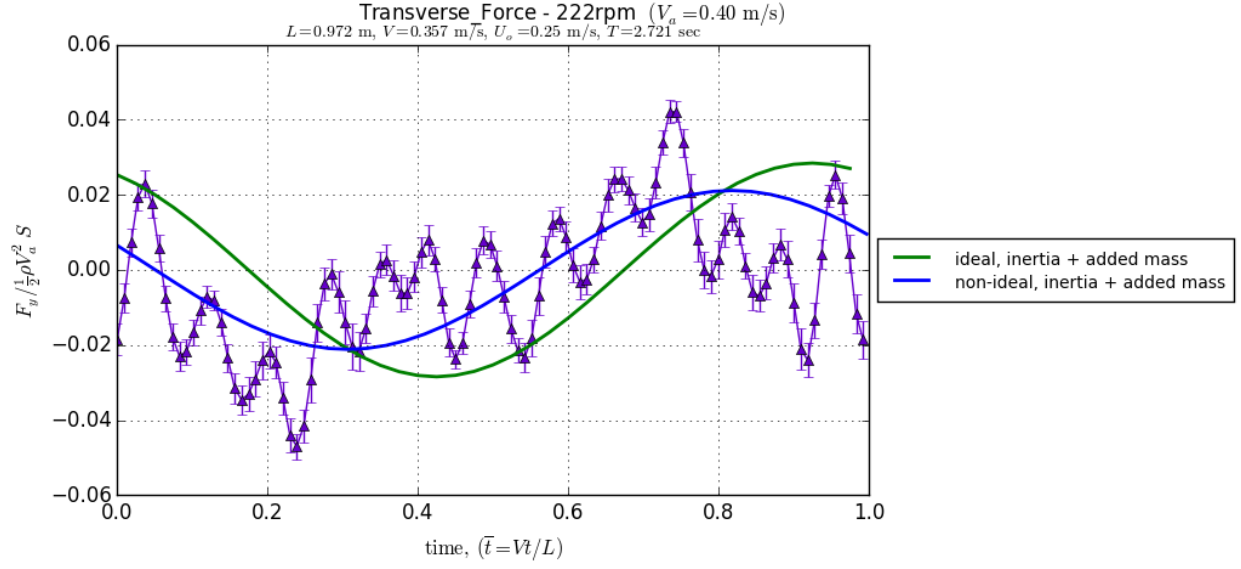
Figure 4.35: For the advance speed of 0.40 m/s, the mean of transverse force for each time step is shown, with error bars showing standard deviation of the mean, i.e. the uncertainty.
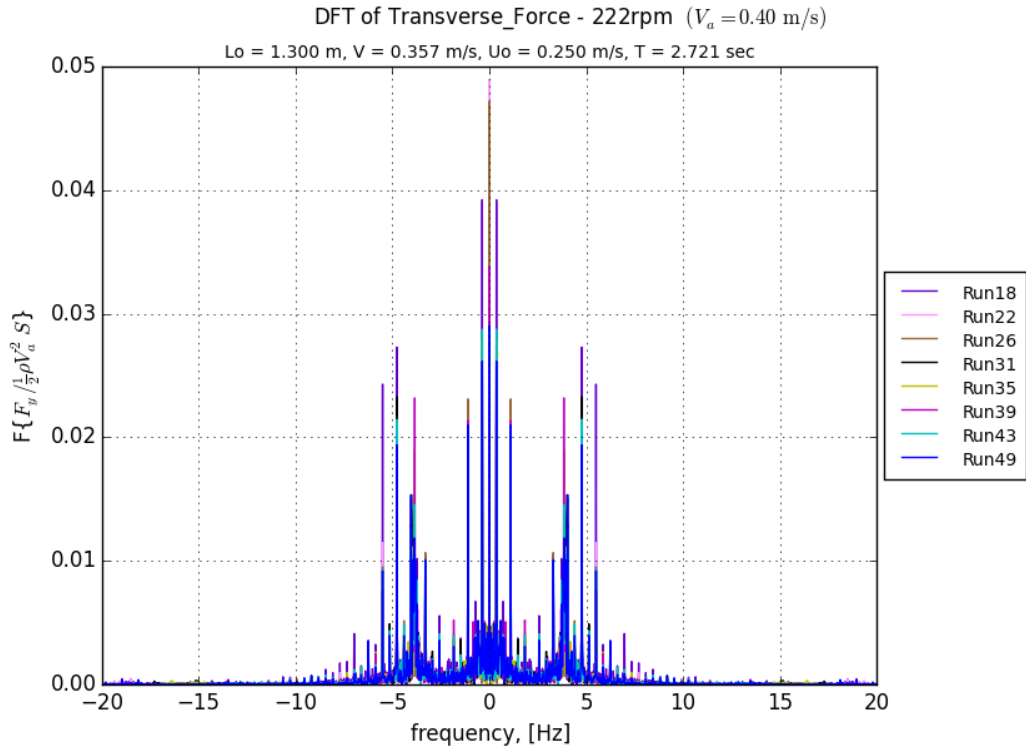
Figure 4.36: DFT of Transverse Force.
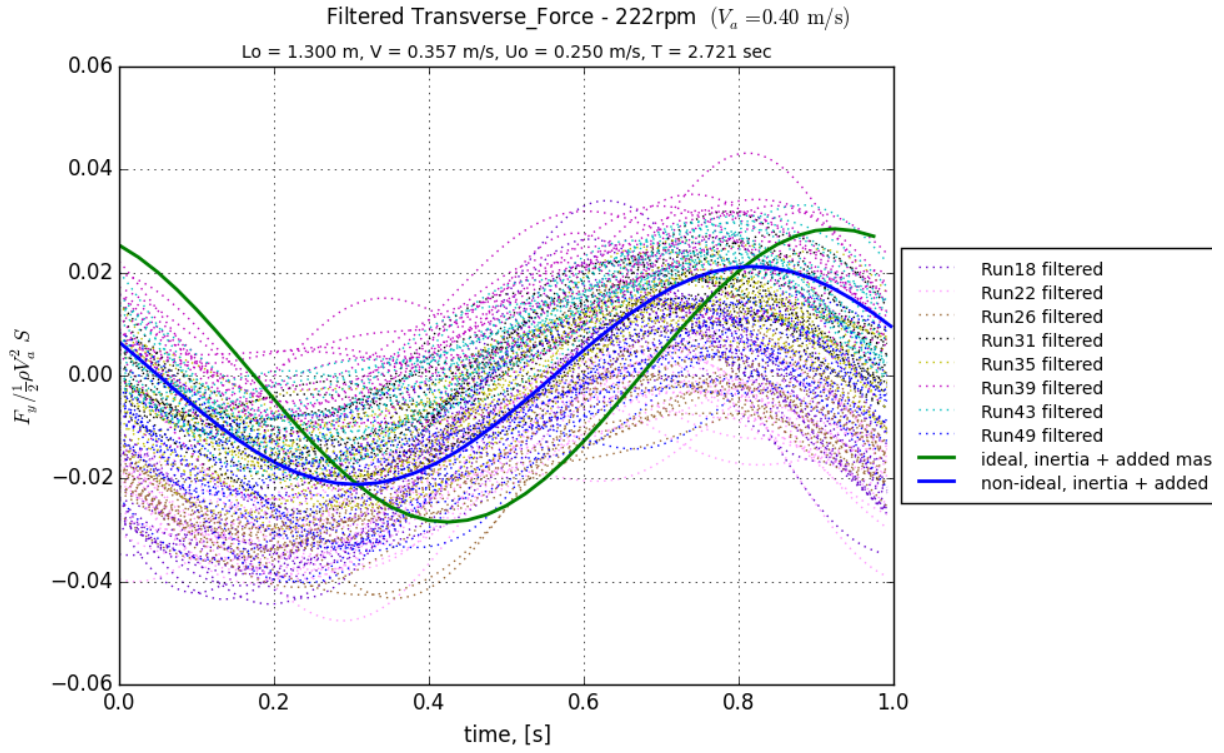
Figure 4.37: Filtered Transverse Force data.
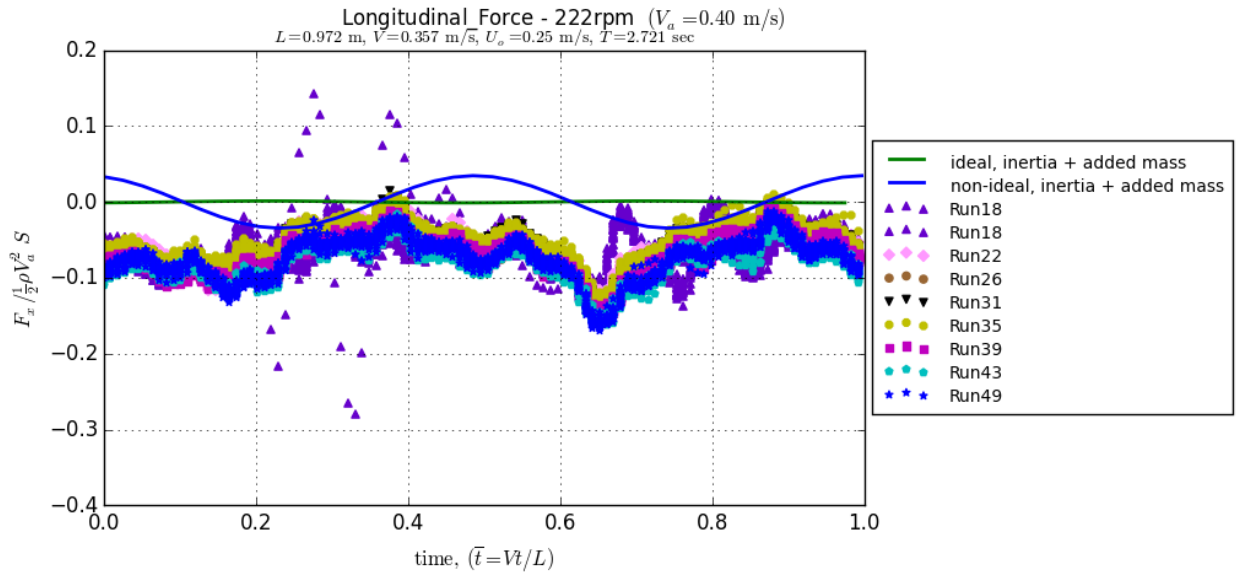
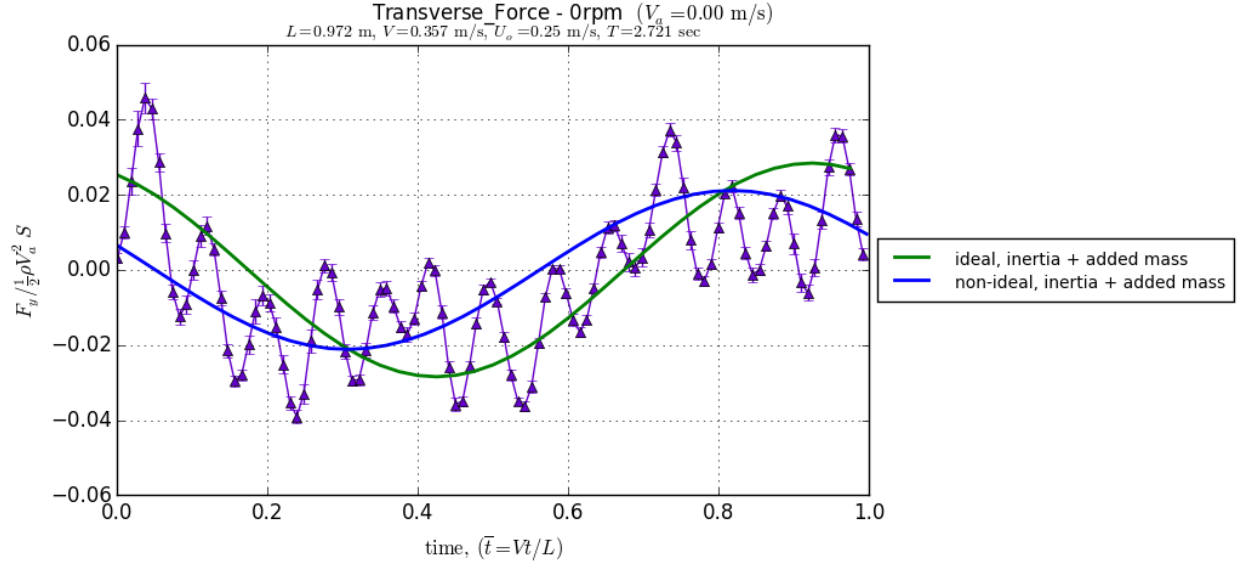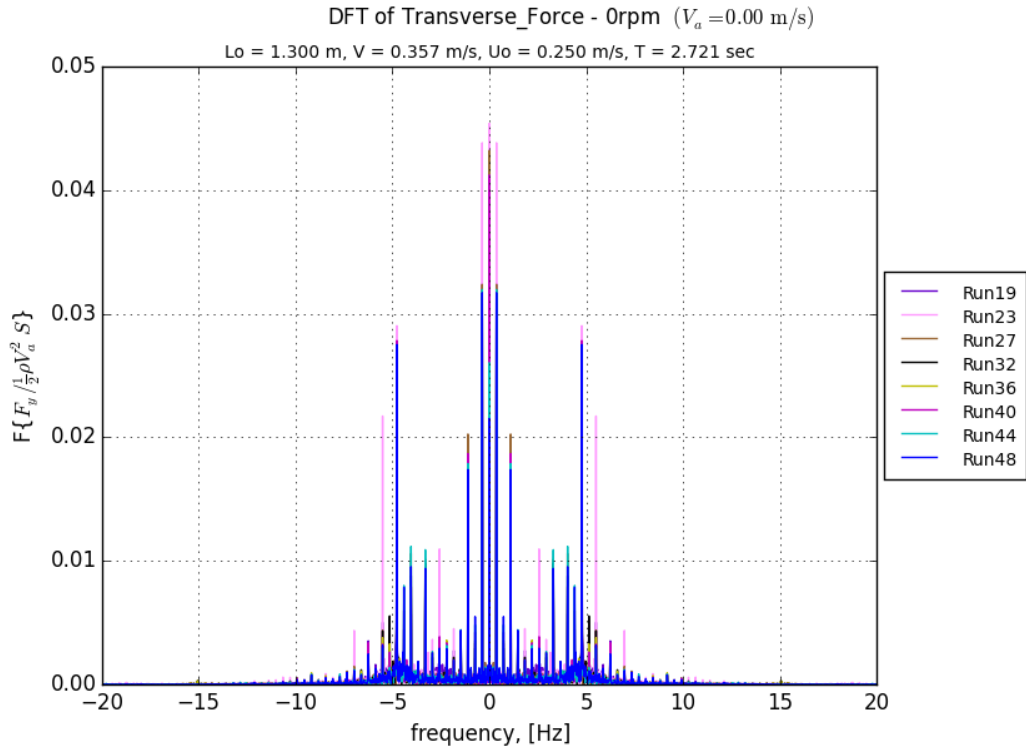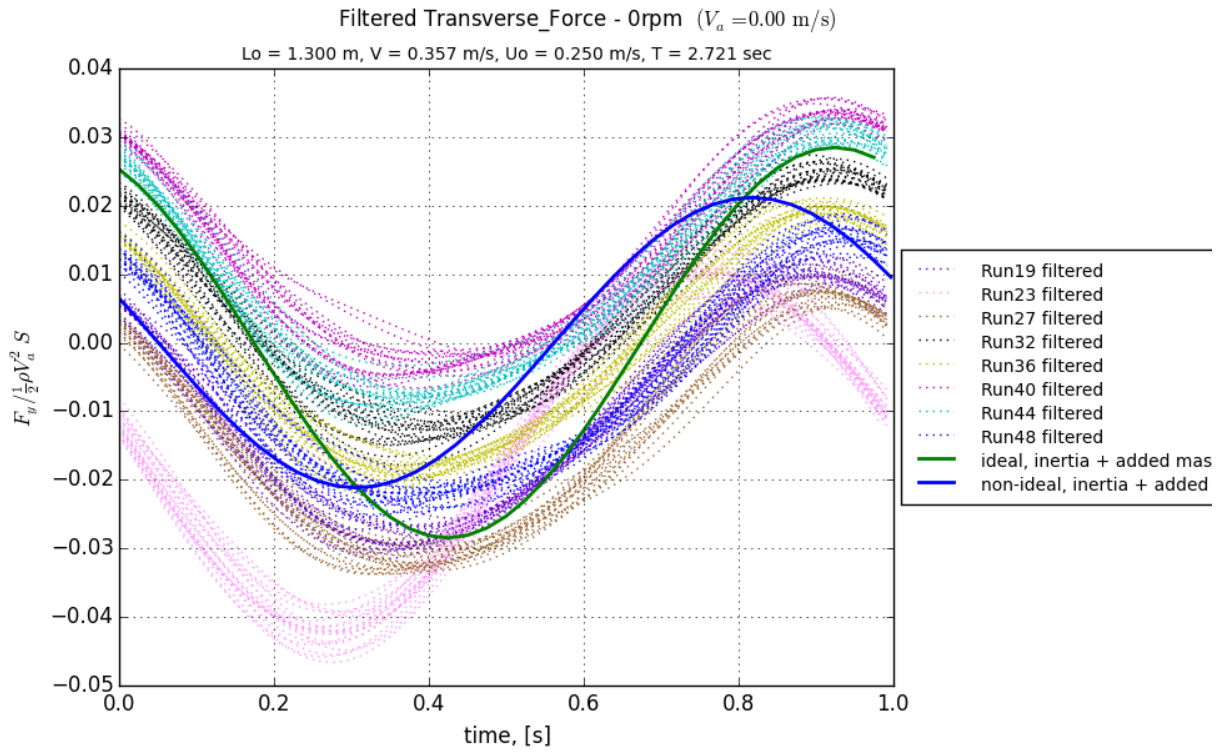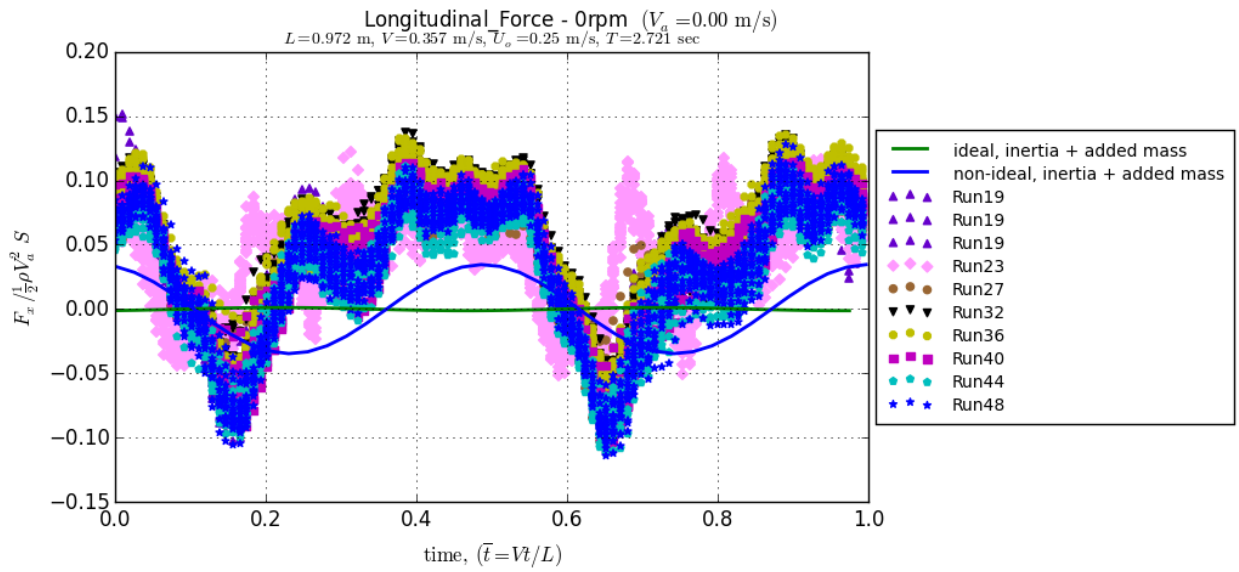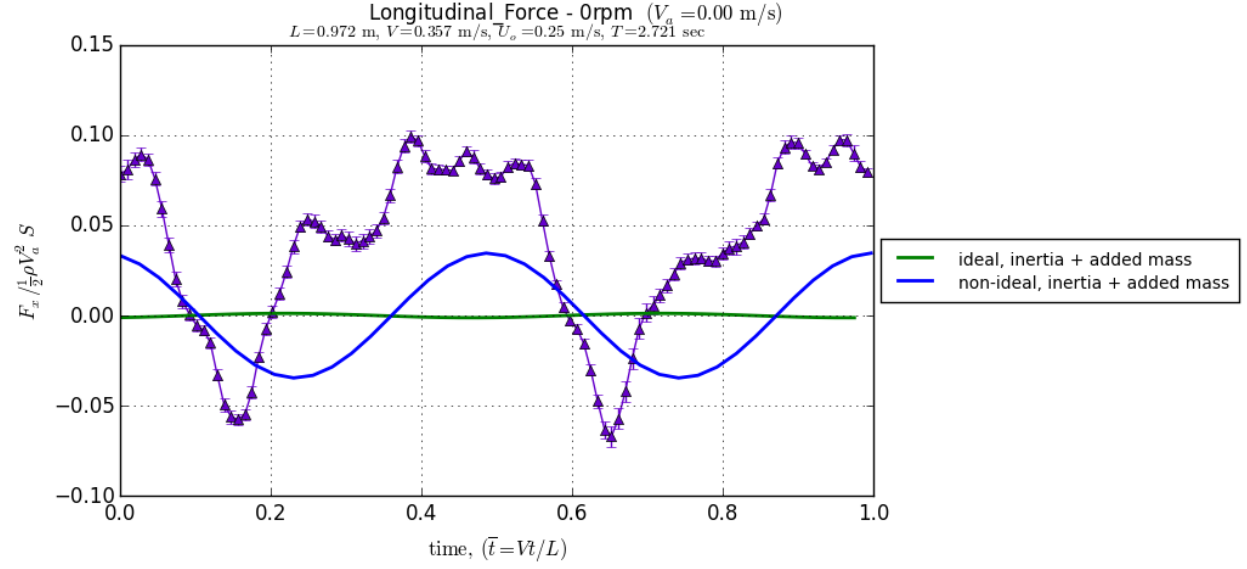Figure 4.38: Longitudinal Force.
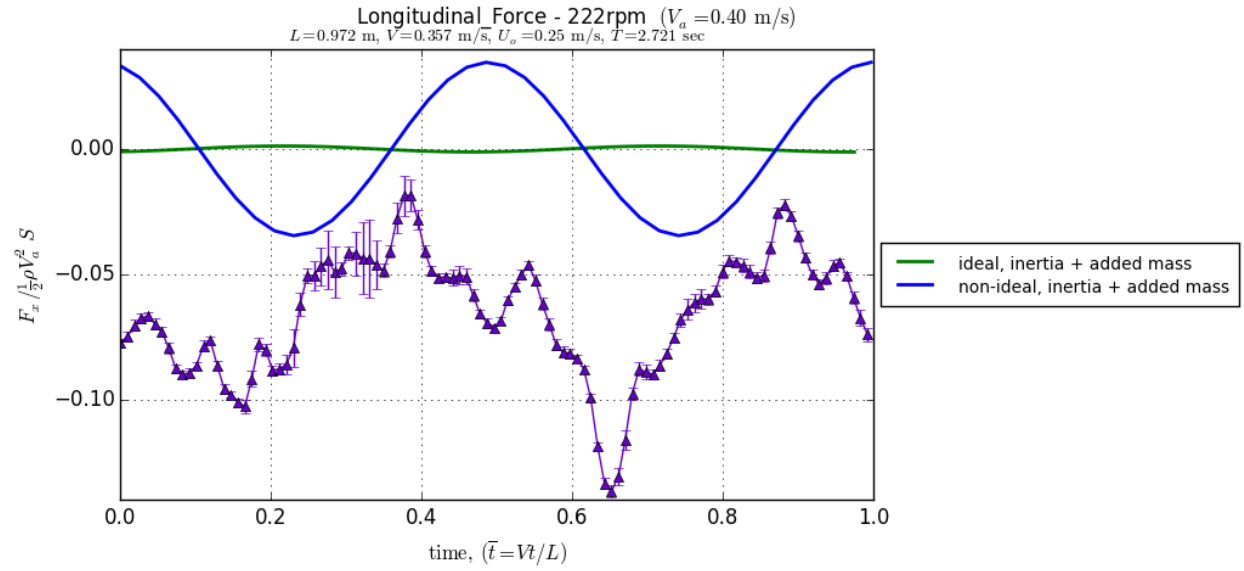
Figure 4.39: For the advance speed of 0.40 m/s, the mean of longitudinal force for each time step is shown, with error bars showing standard deviation of the mean, i.e. the uncertainty.
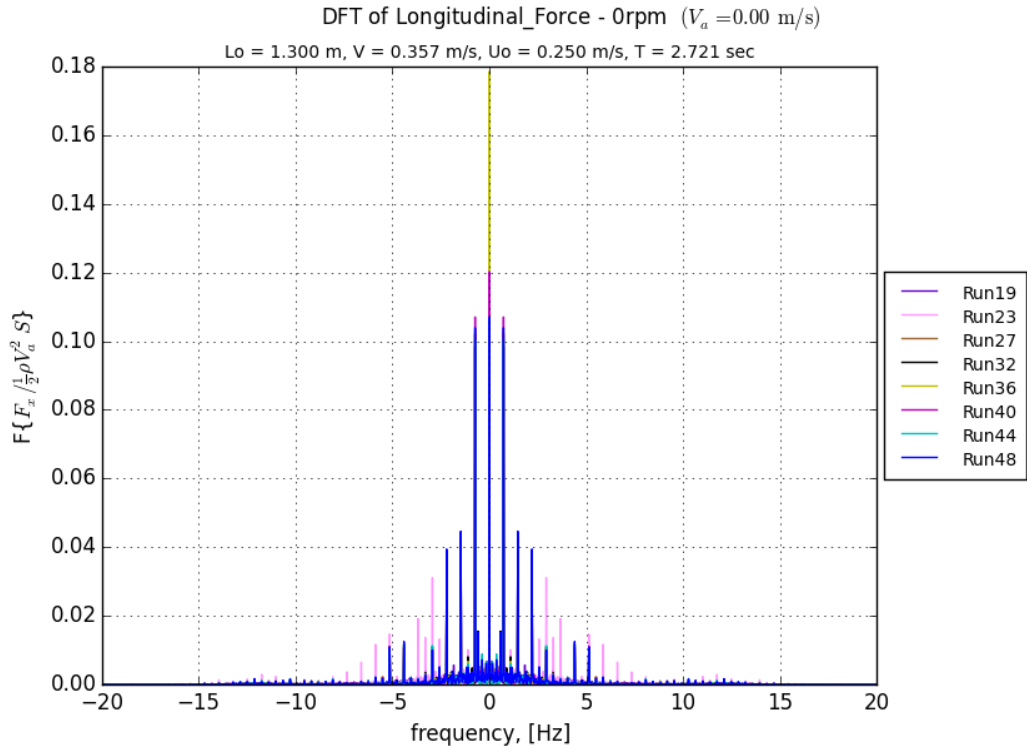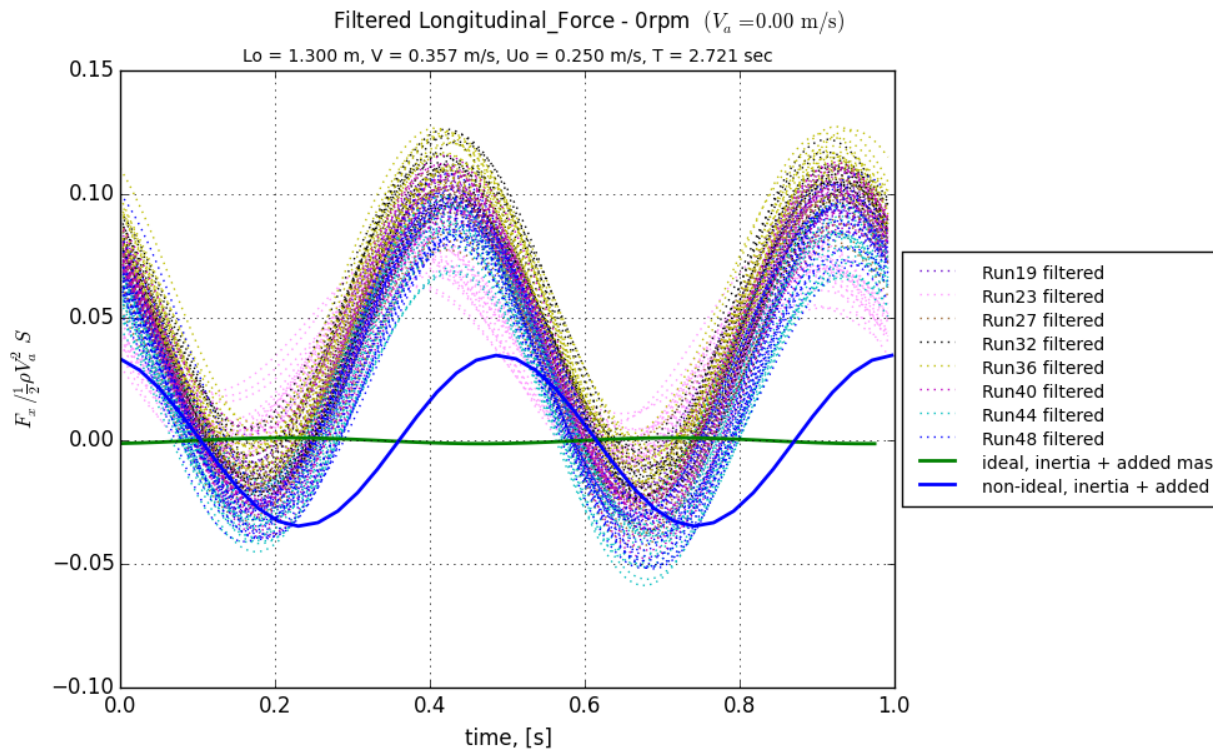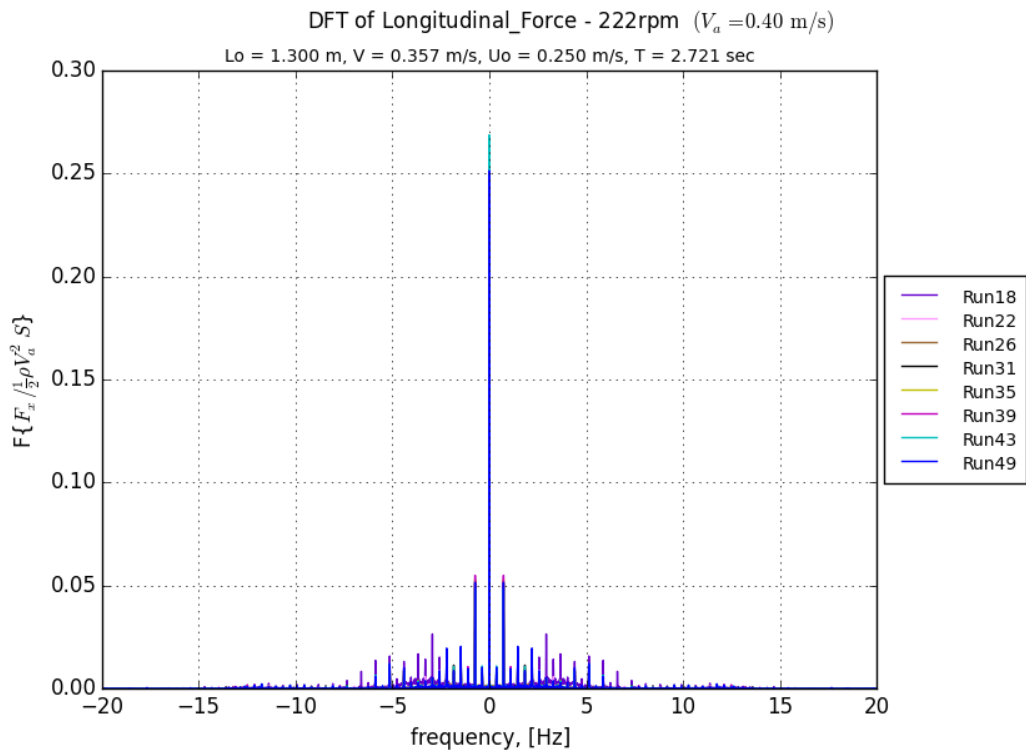

Figure 4.40: DFT of Longitudinal Force.
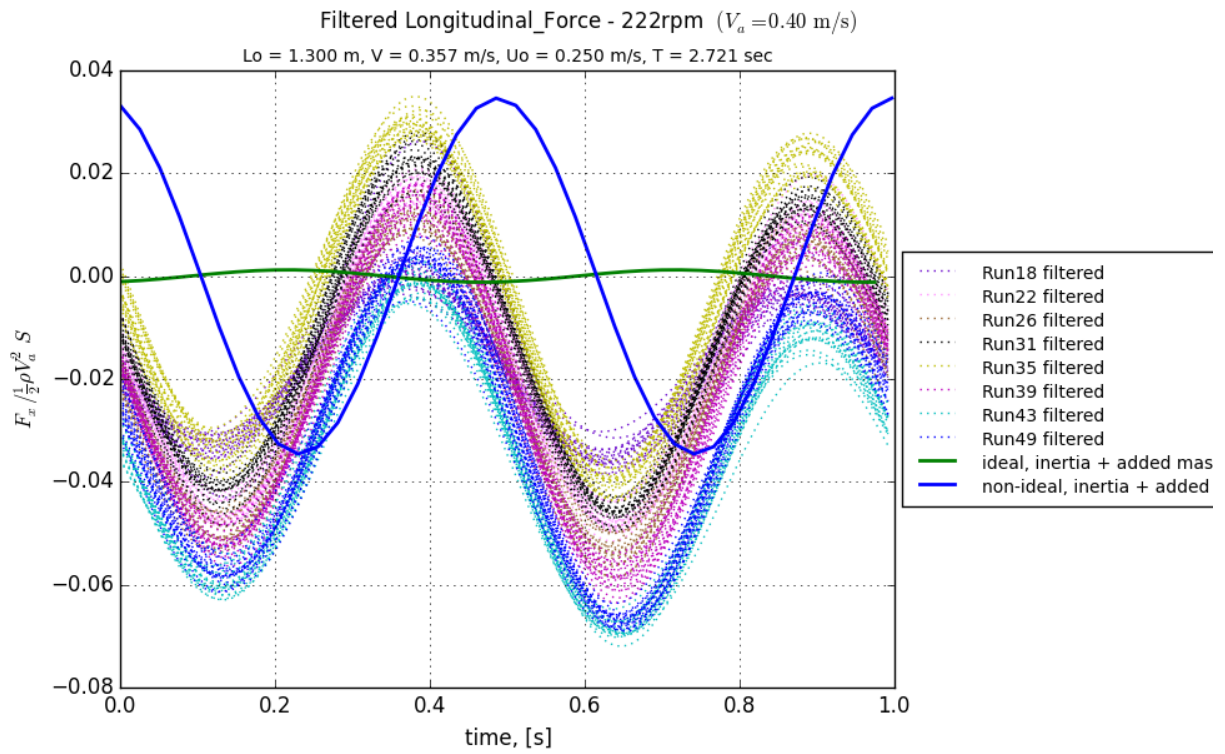
Figure 4.41: Filtered Longitudinal Force data.

Table 4.3: Percent difference between maximum amplitude of load cell measurements and theoretical predictions.

Speed [m/s]	Force Direction	Percent Difference
0.0	Transverse	3%
	Longitudinal	22%
0.16	Transverse	3%
	Longitudinal	11%
0.25	Transverse	5%
	Longitudinal	5%
0.40	Transverse	1%
	Longitudinal	21%

4.2.1.8 Load Cell Measurements Summary

Table 4.3 shows the percent difference between the theoretically and experimentally obtained values for the maximum amplitude over time.

4.3 Parameter Space Search (C_T Determination)

The goal of this experimental force decomposition is to determine how inaccurate the frictional drag force prediction using the ITTC-57 line (F_f from equation 2.61 via dimensionalization) is from the actual frictional drag ($F_{D,lumped}$) as computed via decomposition of measured and derived force components. The various force components acting on NEELBOT-1.1 can be decomposed, assuming linear superposition, in order to individually compute the actual frictional force. The various force components include tether drag, drag due to vortex shedding, frictional drag, form factor drag, forces measured by the load cell, and thrusts computed from the theory. However, not all components can be separated and are instead lumped together, hence the "lumped" subscript.

Different speeds for the same programmed motion were tested because we determined that the programmed motion was not producing the predicted thrust necessary to overcome the drag and obtain the desired speed. We decided to test a range of carriage advance speeds for the same programmed motion to search for the 0-net force point, with tether drag subtracted, where thrust equals the drag at the tested speed. This will then tell us how inaccurate our initial drag prediction

Figure 4.42: Screenshot of recorded video of a motion programming test, that measured the angular positions of the joints over time. PIV testing is not being performed in this video, but the green laser would be shining in from the right, parallel to the plane of the image.

was for the motion programming.

4.3.1 Background

As performed before, the thrust coefficient, C_T, is specified *a priori*, which is equivalent to the drag coefficient for steady swimming (equation 2.58). The force coefficients, C_{fx} and $C_{fx,\mathrm{non-ideal}}$, are computed using the theoretical equations from Vorus and Taravella (2011) but applied to each of the inputted ideal and non-ideal motions for varying advance speeds (U_o). These are computed as summations of sectional coefficients. The coefficient of drag due to vortex shedding (or rather, induced drag), $C_{D,\mathrm{vortex}}$, is hoped to be computed via decomposition but shown later that it is not possible. The coefficient of drag of the tether, $C_{D,\mathrm{tether}}$, is measured with the load cell for cases of only the tether foil dragging through the water. $C_{\mathrm{net,meas}}$ is measured with the load cell for the tether while NEELBOT-1.1 is articulating, producing thrust.

For steady swimming speeds in Vorus and Taravella (2011), the force of thrust must equal the

144

Table 4.4: Details of iterative spirals.

spiral #	date	U_o, [m/s]	U_a, [m/s]	U, [-]	C_T/C_D	PID gains	PIV quality	notes (also, see details)
1 (⋆1,⋆2)	7/2013	0.5	≈0.23 (F.S.)	0.8	Blasius	default	-	-
2	7/2013	0.5	≈0.28 (F.S.)	0.8	ITTC-57	default	-	-
3	7/2013	0.25	≈0.14 (F.S.)	0.8	ITTC-57	default	-	-
4 (⋆3)	8-11/2013	-	various	-	-	-	unacceptable	-
5 (⋆4)	12-2/2014	-	-	-	-	-	-	-
6	2/14/14	0.25	table-top	0.8	ITTC-57	default	-	-
7 (⋆5)	2/25/14	0.25	0.25	0.8	ITTC-57	default	-	-
8 (⋆6)	2/28/14	0.10-0.25	various	0.8	ITTC-57/Blasius	default	-	letter combo's
9	3/13/14	0.10-0.25	various	0.8	ITTC-57/Blasius	default	-	letter combo's
10	3/21/14	0.10-0.25	various	0.8	ITTC-57/Blasius	default	-	letter combo's (tested PWM)
11	3/26/14	0.10-0.25	various	0.8	ITTC-57/Blasius	default	-	letter combo's
(⋆7)	4/2014		researched robot manipulator control theory					
12 (⋆8)	4/25/14	0.25	0.25	0.8	ITTC-57	Ziegler-Nichols tuning	-	-
13	5/30/14	0.25	0.0	0.8	ITTC-57	various; Z-N tuning	-	step inputs
14 (⋆9)	7/9/14	-	various	-	-	-	better; 1-2% RSD	-
14.5 (⋆9.5)	7/18/14	-	0.25	0.8	ITTC-57	Set D	unacceptable	-
15	7/29/14	0.25	0.0	0.8	ITTC-57	Sets A,B,C,D	-	-
16 (⋆10)	8/4/14	0.25	0.25	0.8	ITTC-57	Set A,E	-	-
17	8/5/14	0.25	various	0.8	ITTC-57	Set A	-	-
18	8/15/14	-	various	-	-	-	-	foil drag tests
19	8/18/14	0.25	0.25	0.6-0.7	exp. drag	Set A	-	varied U
20 (⋆11)	8/22/14	0.25	0.25	0.7	exp. drag	Sets F,G,H,I	-	-
(⋆12)	8/26-8/14		PIV laser alignment successful					
21	8/29-9/17/2014	0.25	0.0,0.16,0.25,0.40	0.7	exp. drag	Sets A,D	unacceptable (OAPIV)	-
22 (⋆13)	10/14-27/14	0.25	0.0,0.16,0.25,0.40	0.7	exp. drag	Set D	excellent	-
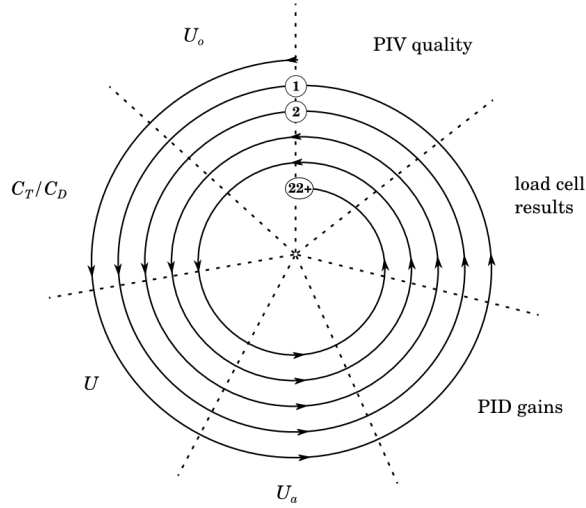
Figure 4.43: Schematic showing the iterative spirals occuring over the course of the research, with each spiral attempting to focus on all the aspects of the project related to determining the thrust/drag coefficients.

forces due to drag for the quasi-static scenario.

$$F_T = F_D \tag{4.11}$$

Vorus and Taravella (2011) computes the force coefficient by summing the axial sectional force, $f_x(x, t)$, along the length of the anguilliform shape function, averaging over time, and non-dimensionalizing to obtain C_{fx}. This is dimensionalized to obtain the computed thrust, F_{fx}:

$$F_T \equiv F_{fx} = C_{fx} \left(\frac{1}{2} \rho V^2 L^2 \right) \tag{4.12}$$

This force term F_{fx} is equivalent to F_T above but has different subscripts to denote that it is computed using the potential flow method of Vorus and Taravella (2011).

For the theoretical scenario described in Vorus and Taravella (2011) where the ideal motion produces the thrust based on the drag prediction, the force balance is

$$F_{fx} = F_D \tag{4.13}$$

Before (in Section 2.1.2), the right hand side was actually F_f from equation 2.61 via dimensional-

146

ization. In that discussion, it was reasoned that F_f is only due to frictional drag and additional resistance due to body curvature. Now, it is denoted as F_D because the method for calculating this component is different than before, in that it is a combination of theoretical and heuristic calculations. The variable F_D is considered to be for the ideal motion case, whereas what follows is for cases of vortex shedding.

For off-design cases experienced in the research testing explained within, the motion is possibly now shedding parasitic vortices, causing a loss of efficiency in the system. The above equation then becomes

$$F_{fx} = F_D + F_{D,\text{vortex}} \tag{4.14}$$

where $F_{D,\text{vortex}}$ accounts for the drag force due to the vortex shedding. As one can see, for a constant original drag prediction (F_D), the thrust on the left-hand side must increase by the amount equivalent to the vortex shedding drag for the force balance to be equal. As will be shown later, computing or measuring the drag due to the vortex shedding ($F_{D,\text{vortex}}$) cannot be performed and is instead lumped into the force term on the right hand side, creating a new term for bookkeeping tabulation:

$$F_{fx} = F_{D,\text{lumped}} \tag{4.15}$$

This term on the right hand side now includes the unseparable components of frictional drag, additional drag due to body curvature, drag due to vortex shedding (induced drag), and possibly viscous pressure resistance that was assumed negligible before due to assumptions of zero boundary layer separation. Boundary layer separation is most likely occurring experimentally now due to wrinkles in the latex rubber skin towards the tail. This term on the right is expected to be different, but hopefully not by much, from the originally computed F_f term (equation 2.61). The difference will show how inaccurate the assumption of thinking the ITTC-57 line models the drag of the anguilliform robot.

Additionally for this off-design case, the sectional force component on the left hand side is now computed differently than before in that it uses the ideal motion theory applied to an off-design case, denoted by $F_{fx,\text{non}-\text{ideal}}$:

$$F_{fx,\text{non}-\text{ideal}} = F_{D,\text{lumped}} \tag{4.16}$$

For the current experiment, a load-cell is attached to the head of NEELBOT-1.1 and is able to measure the axial forces during an articulating motion test. This load cell acts as a "branch cut" into the current system. Unfortunately, this load cell also affects the system. The force balance with the load-cell measuring the net force can be written as

$$- F_{\text{net,meas}} = F_{fx,\text{non-ideal}} - F_{D,\text{lumped}} \qquad (4.17)$$

where $F_{\text{net,meas}}$ is the reading on the load cell. The negative sign on the load cell reading is showing that the value is equal and opposite to that of the resultant force on the right hand side. The load cell actually sees an equal and opposite force of $F_{\text{net,meas}}$, making this value in the robot frame of view. Any imbalance between the computed thrust and yet-to-be-found drag force will be measured by the load cell. For the ideal scenario explained above and for the imaginary case where the tether connection between the head and the load cell doesn't affect the measurements, $F_{\text{net,meas}}$ would equal zero. The new force balance with the inclusion of the drag due to the tether becomes

$$- F_{\text{net,meas}} = F_{fx,\text{non-ideal}} - F_{D,\text{tether}} - F_{D,\text{lumped}} \qquad (4.18)$$

Luckily, the drag due to the tether can be easily measured on its own by dragging the tether through still water while measuring its resistance. The system is assumed to be linear in that the motions of the robot while attached to the tether do not affect its resistance and vice versa, allowing the separate force values to be linearly superimposed.

Along with the computed values for the theoretical thrust ($F_{fx,\text{non-ideal}}$), the equation can be rearranged to solve for the lumped drag:

$$F_{D,\text{lumped}} = F_{\text{net,meas}} + F_{fx,\text{non-ideal}} - F_{D,\text{tether}} \qquad (4.19)$$

This drag will then be compared to the original drag prediction (F_f from equation 2.61 via dimensionalization) to see how well it has lined up with the measured forces. A negative value of $F_{D,\text{lumped}}$ indicates a drag force, or rather, aft-directed force in the robot frame of view. Negative values for this lumped drag force are expected. A positive value would indicate that the computed thrust force of $F_{fx,\text{non-ideal}}$ is over-predicting what the theoretical thrust should be.

Several tests were performed with only the drag of the tether being measured as the carriage traverses the length of the tank. The tether can be seen in Figures 4.1 and 4.2. Several tests were performed at each speed, obtaining a reliable mean and standard deviation over the course of the research, and these are plotted in Figure 4.8. The interested results are listed in Table 4.6.

The measured forces recorded by the load cell are listed in Table 4.6. These were obtained by taking a time-average of the load over the course of an experimental run.

In addition to the above measured quantities, the drag of the robot was measured with it locked in a straight-line position, denoted as $F_{D,\text{str}}$, the results of which are shown for the various speeds in Table 4.6. These values were obtained from several tests over the course of the research, and these are plotted in Figure 4.9. This drag force should be the lower bound for the frictional drag of the articulating robot and was in fact the value used for the initial drag prediction. Anderson et al. (2001) showed that swimming fish were found to experience greater friction drag than the same fish stretched straight in the flow.

4.3.2 Theoretical - Ideal Motion

From equation 2.43, it is shown that

$$C_{fx,\text{sec}}(x,t) \equiv \frac{f_x(x,t)}{\frac{1}{2}\rho V^2 L} = 2\pi r_o{}^2 k(x,t)h_x(x,t) \equiv -C_{T,\text{sec}}(x,t) \tag{4.20}$$

which is the sectional force coefficient in the x-direction equated to the sectional thrust coefficient of equal and opposite magnitude. Note that this is a sectional force coefficient, to be summed over the length of the anguilliform shape.

Table 2.1 shows the parameters used to define the motion of the current analysis. It is important to note that the thrust coefficient in Table 2.1, C_T, is computed from a thrust force of 0.04804 N (0.0108 lbf). This value was chosen for the nominal design case. It is the value of the straightline robot's drag resistance and was thus assumed to be a sufficient initial estimate for the drag prediction. The accuracy of the drag changed after more testing was accomplished, but this value remained constant for the baseline, nominal speed case.

Figure 4.44: Sectional force coefficient distributions shown for every other timestep for the first half of the motion cycle of the ideal motion using the parameters from Table 2.1. This plot replicates the results graphed in Figure 8 of Vorus and Taravella (2011) except for different design parameters.

Remember the thrust coefficient is computed via the formula

$$C_T = \frac{F_T}{\frac{1}{2}\rho V^2 L^2} \tag{4.21}$$

where F_T is the value specified above from the straight-line drag.

For the current parameters, the distribution of sectional force coefficient along the length for selected timesteps is shown in Figure 4.44. Every other time step from the first half of the motion cycle is shown. The thrust cycle repeats itself twice for every cycle of motion, hence the reason for only showing the timesteps from the first half of the motion cycle. All values are non-dimensionalized.

For the ideal motion case using the parameters in 2.1, Figure 4.45 shows the integral of the sectional force coefficient over the length of the robot, plotted over time, using the following equation

$$C_{fx}(t) = \int_0^L C_{fx,\text{sec}}(x,t)dx \tag{4.22}$$

150

Figure 4.45: The sectional force coefficient is integrated over the length of the robot and then plotted over time for one cycle of motion clearly showing the two cycles of thrust production in that span. This is for the ideal motion case using the parameters listed in Table 2.1

The mean value of $C_{fx}(t)$ over time is computed by

$$C_{fx,\mathrm{avg}} = \frac{1}{T} \int_0^1 C_{fx}(\bar{t})d\bar{t} \qquad (4.23)$$

and is shown in the title of the plot (here, T is equal to 1, the non-dimensionalized time length of the cycle). As you can see, the value for $C_{fx,\mathrm{avg}}$ matches that of the specified thrust coefficient input listed in Table 2.1, and thus matching the condition of equation 4.20.

This summed and averaged sectional force coefficient is dimensionalized using equation 4.12, the value of which is shown in the first value of the first column of Table 4.6. The remaining values of the column are computed using formulas explained earlier.

4.3.3   Theoretical - Non-ideal Motion

The other four, non-ideal motion, columns are populated using the same analysis above but for cases of non-ideal motion for each speed. The theoretical thrust, $F_{\mathrm{non-ideal}}$, is computed by

Figure 4.46: Sectional force coefficient distributions shown for every other timestep for the first half of the motion cycle. This is for the non-ideal motion case at a carriage advance speed of 0.0 m/s.

applying the ideal motion theory to the actual, non-ideal motion. Figures 3.24 through 3.31 show the recorded, actual motion of the servo angles over time for each speed. As one can see, the attained motion does not exactly replicate that of the ideal situation, necessitating a new method for predicting the generated thrust and thus being able to compute the lumped drag force, $F_{D,\text{lumped}}$. It is assumed that this drag force will be accounting for all the unseparable force components.

With no loss of generality, equations 4.12, 4.22, and 4.22 are used to compute $F_{fx,\text{non}-\text{ideal}}$, the values of which are shown in Table 4.6.

Figures 4.46 through 4.53 show the sectional force coefficient distribution and its integral over time, similar to the plots above for the ideal case, for each of the advance speeds from 0.0 to 0.4 m/s.

4.3.4 Force Decomposition Summary

Table 4.6 shows the overview of the forces for all test speeds of the ideal and non-ideal motion. Positive values indicate a force in the negative direction of the NEELBOT-1.1 body-fixed frame

152
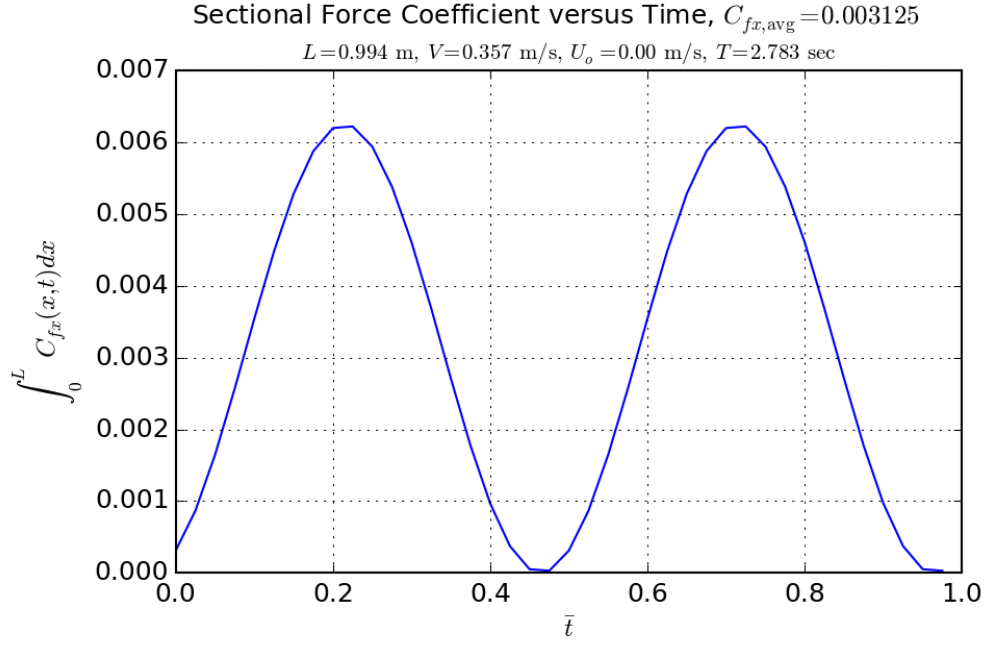
Figure 4.47:
The sectional force coefficient integrated over the length of the robot and then plotted over time for one cycle of motion clearly shows the two cycles of thrust production in that span. This is for the non-ideal motion case at a carriage advance speed of 0.0 m/s.
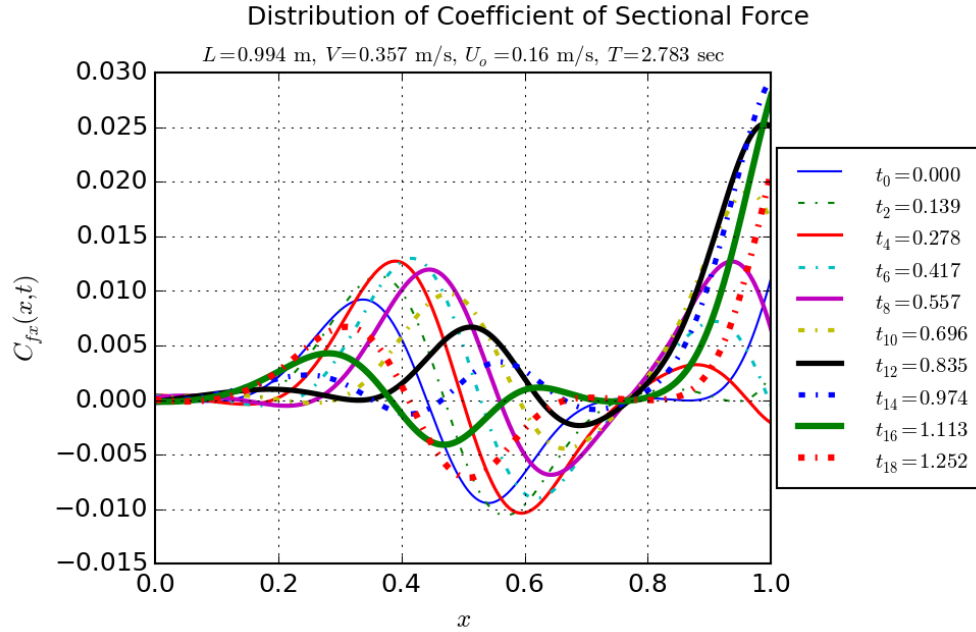
Figure 4.48:
Sectional force coefficient distributions shown for every other timestep for the first half of the motion cycle. This is for the non-ideal motion case at a carriage advance speed of 0.16 m/s.

153
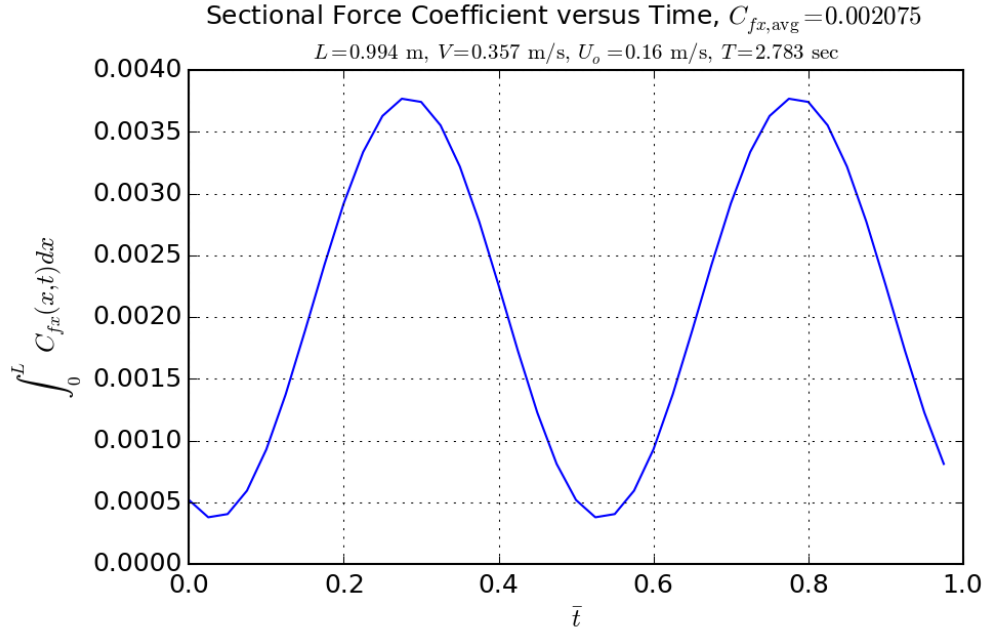
Figure 4.49:
The sectional force coefficient integrated over the length of the robot and then plotted over time for one cycle of motion clearly shows the two cycles of thrust production in that span. This is for the non-ideal motion case at a carriage advance speed of 0.16 m/s.
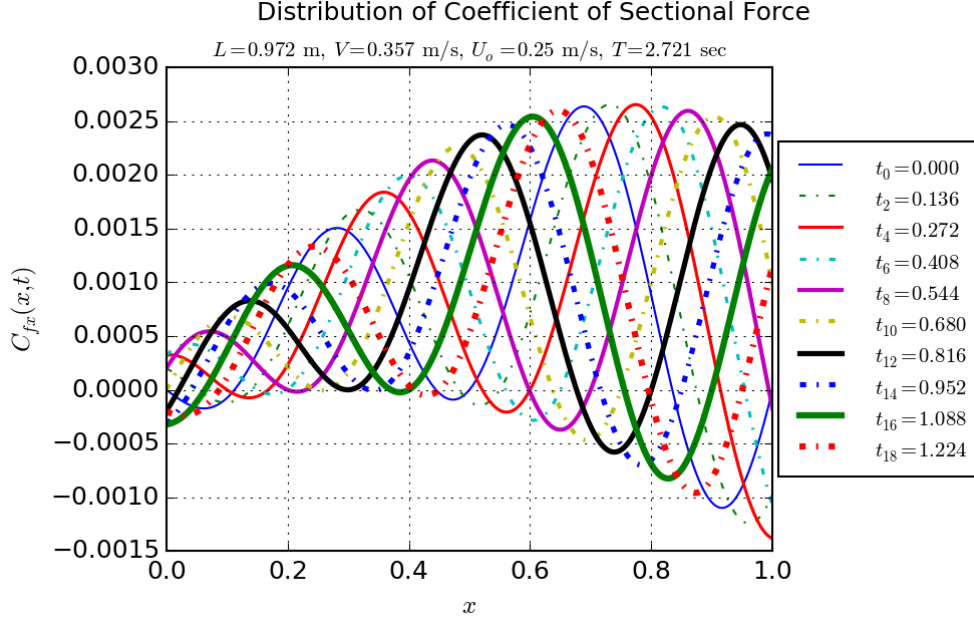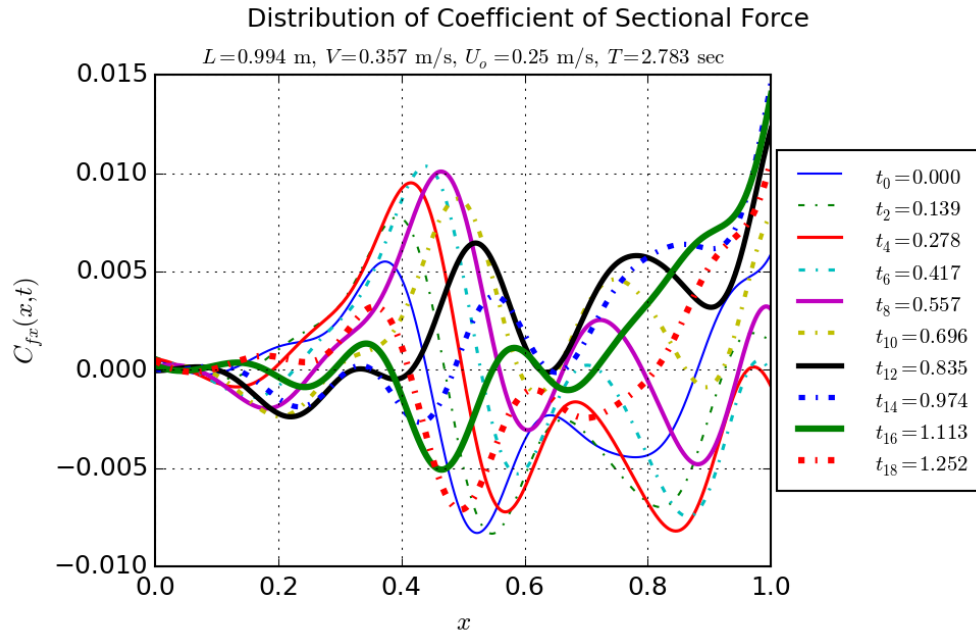

Figure 4.50:
Sectional force coefficient distributions shown for every other timestep for the first half of the motion cycle. This is for the non-ideal motion case at a carriage advance speed of 0.25 m/s.
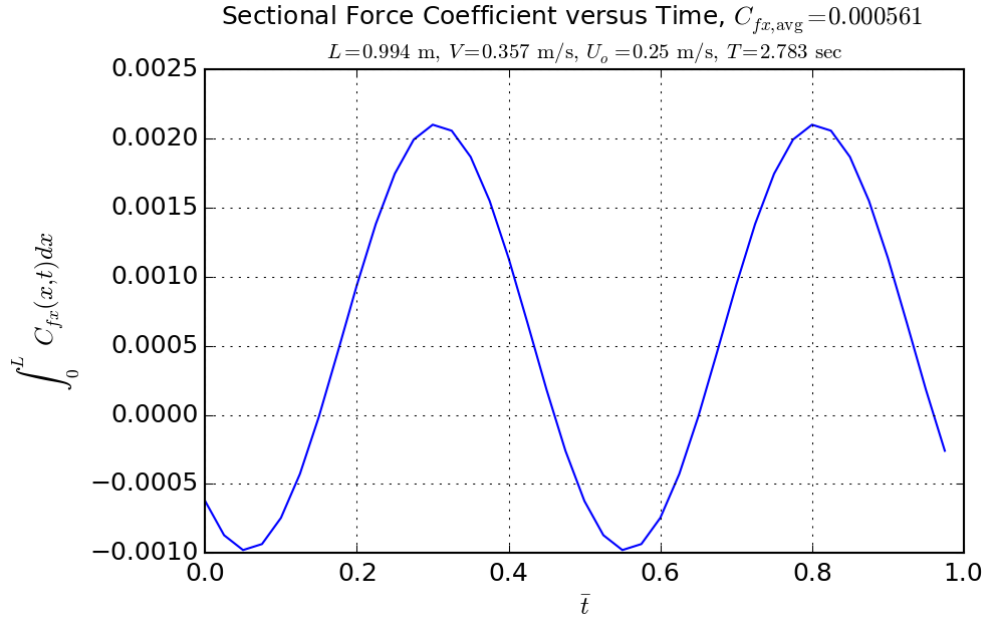
Figure 4.51: The sectional force coefficient integrated over the length of the robot and then plotted over time for one cycle of motion clearly shows the two cycles of thrust production in that span. This is for the non-ideal motion case at a carriage advance speed of 0.25 m/s.
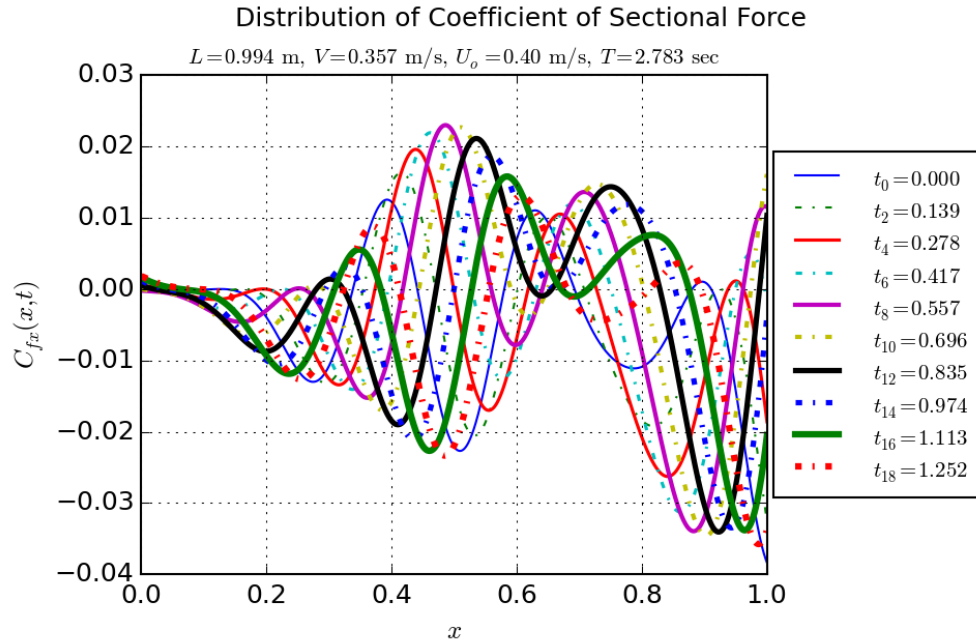
Figure 4.52: Sectional force coefficient distributions shown for every other timestep for the first half of the motion cycle. This is for the non-ideal motion case at a carriage advance speed of 0.40 m/s.
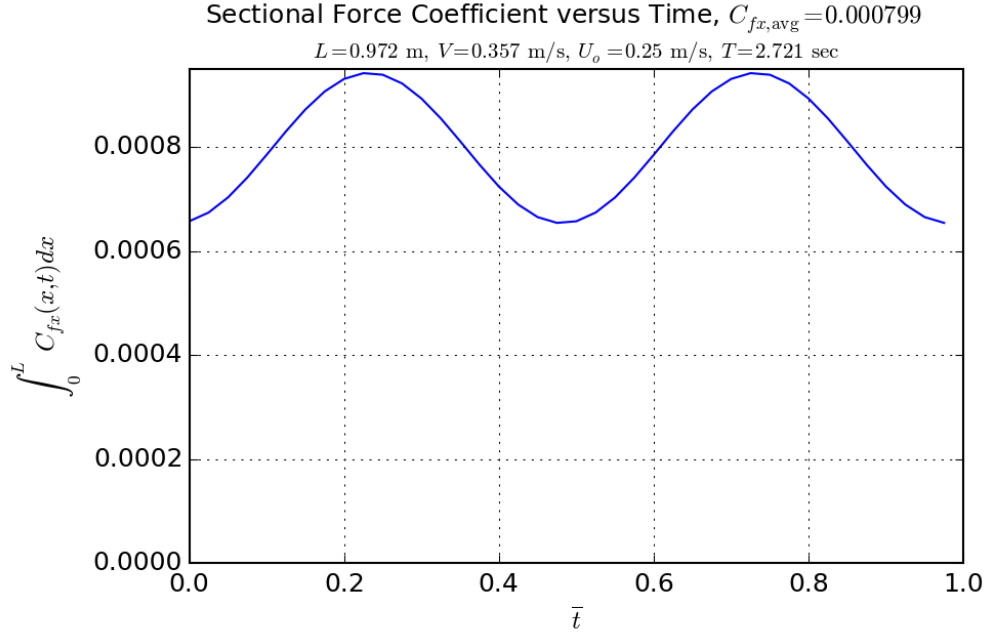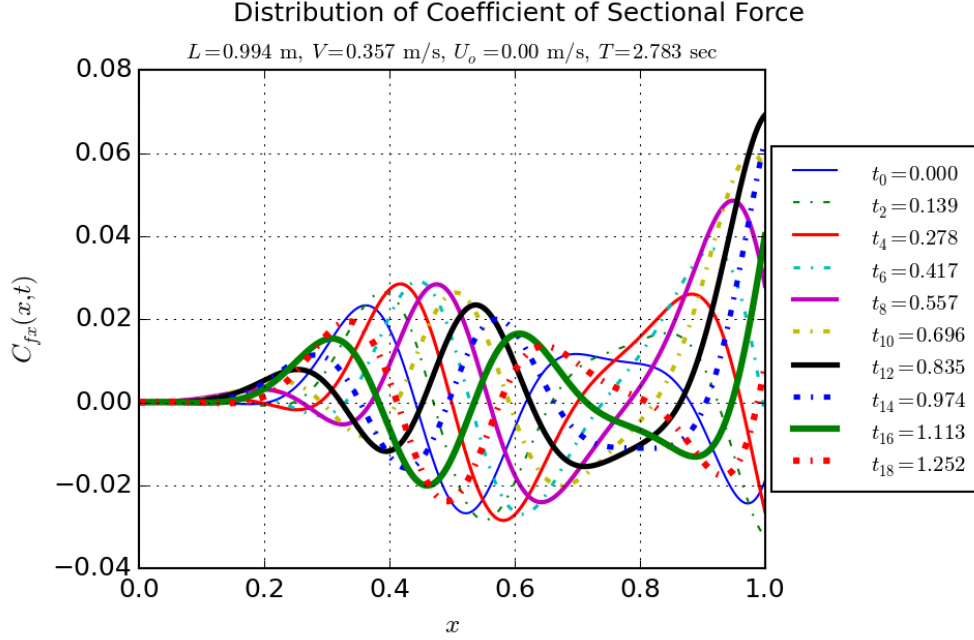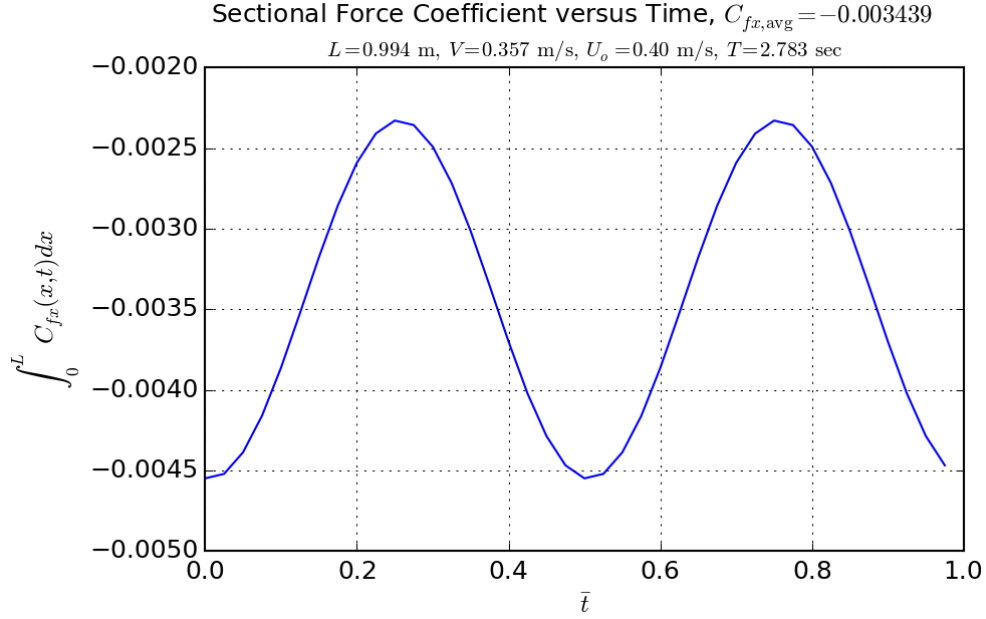
Figure 4.53: The sectional force coefficient integrated over the length of the robot and then plotted over time for one cycle of motion clearly shows the two cycles of thrust production in that span. This is for the non-ideal motion case at a carriage advance speed of 0.40 m/s.

of reference. Thus, positive indicates a production of thrust in the inertial frame of reference. Negative indicates drag. The Froude efficiency, η, was computed using equation 2.46. The row of figure numbers denotes the actual motion that the theoretical thrust production was calculated for.

The lumped drag and F_f rows are the two key values to compare for each speed. For the 0.25 and 0.4 m/s cases, the lumped drag is over 500% more than the predicted value. For the other cases, the results are actually predicting a positive thrust for what should be a drag, so this raises some questions. Maybe, the calculation for $F_{fx,\text{non-ideal}}$ is over-predicting its contribution for the lower speeds. Or the vortex shedding is not being as parasitic as it is expected to be.

Table 4.7 shows the sectional force coefficients and the efficiencies of the various advance speeds as calculated using equation 2.46. Even for the off-design case of 0.25 m/s, the results are showing that it is 60% efficient, which is on par with most propellers in the field.

4.4 PIV Results

Free Flow PIV Testing

$$F_{net,meas} - F_{D,tether} \pm F_{robot} = 0$$

$F_{net,meas}$

$F_{D,tether}$

F_{robot}

?
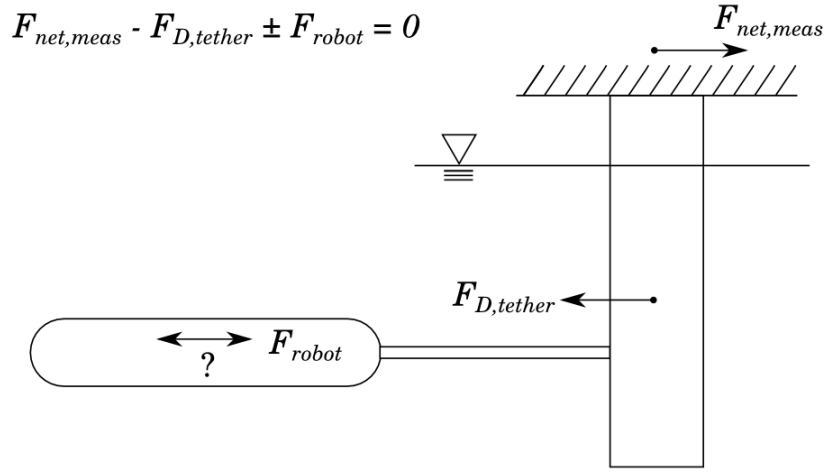
Figure 4.54: Free-body diagram showing forces acting on tether and the robot. It is unknown at this point in which direction the force is acting on the robot.

$$F_{robot} = F_T - F_D = F_{fx} - F_D$$
$$F_{net,meas} - F_{D,tether} + F_{fx} - F_D = 0$$
$$F_D = F_{net,meas} - F_{D,tether} + F_{fx}$$

$F_{net,meas}$

$F_{D,tether}$

F_D F_{fx}
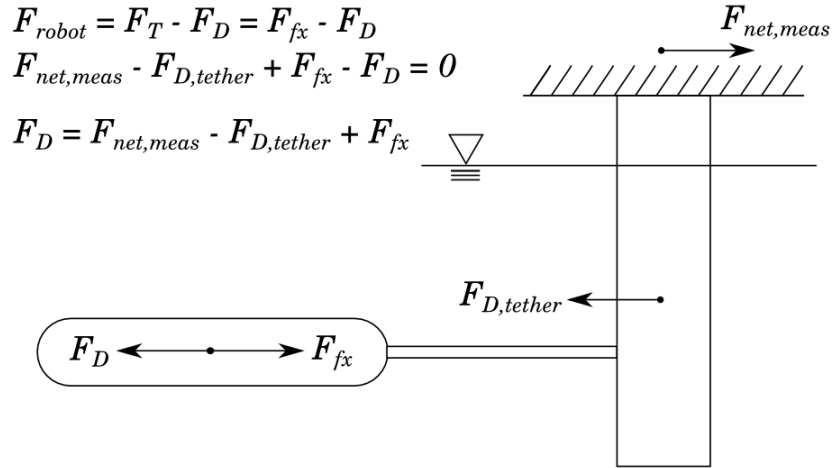
Figure 4.55: Free-body diagram showing the forces acting on the tether and robot, updated with computed thrust prediction, F_{fx}, of the robot motion. From this, the drag force acting on the robot can be predicted.

Table 4.5: Computed and measured forces of NEELBOT-1.1 for all test speeds (quasi-static).

	ideal motion	non-ideal motion			
U_a [m/s]	0.25	0.0	0.16	0.25	0.40
$F_{\text{net,meas}}$ [N]	n/a	-0.578±0.006	0.160±0.004	0.623±0.008	1.713±0.008
$F_{D,\text{tether}}$ [N]	n/a	0.0	-0.133±0.006	-0.311±0.006	-0.712±0.005
$F_{fx,\text{ideal}}$ or $F_{fx,\text{non-ideal}}$ [N]	0.04804	0.1880	0.1248	0.0337	-0.2069
$F_{D,\text{vortex}}$ [N]	0.0	-	-	-	-
F_D or $F_{D,\text{lumped}}$ [N]	-0.04804	0.390±0.006	-0.15±0.010	-0.35±0.014	-0.79±0.013

Table 4.6: Computed and measured forces of NEELBOT-1.1 for all test speeds (quasi-static).

	ideal motion	non-ideal motion			
	0.25 m/s	0.0 m/s	0.16 m/s	0.25 m/s	0.40 m/s
$F_{fx,\text{ideal}}$ or $F_{fx,\text{non-ideal}}$ [N]	0.048	0.1880	0.1248	0.0337	-0.2069
Γ [-]	0.11767	0.11767	0.11767	0.11767	0.11767
$F_{D,\text{vortex}}$ [N]	0.0	?	?	?	?
$F_{D,\text{tether}}$ [N]	n/a	0.0	-0.1334	-0.3114	-0.7117
$F_{\text{net,meas}}$ [N]	n/a	0.578	-0.160	-0.623	-1.713
F_D or $F_{D,\text{lumped}}$ [N]	-0.048	0.7660	0.0982	-0.2779	-1.2082
$F_{D,\text{str}}$ [N]	-0.048	0.0	-0.03114	-0.048±0.005	-0.2802
Re [-]	292898	0	187455	292898	468637
F_f [N]	-0.044	0.0	-0.020	-0.044	-0.101
$F_{D,\text{Blasius}}$ [N]	-0.017	0.0	-0.009	-0.017	-0.035
η [-]	100%	0%	72%	60%	154%
Figure number	2.6	3.24	3.26	3.28	3.30

Table 4.7: Axial force coefficient values for ideal and non-ideal motions at various carriage speeds.

	ideal motion		non-ideal motion	
U_o [m/s]	C_{fx} [-]	η [%]	C_{fx} [-]	η [%]
0.00	0.002662	0	0.003125	0
0.16	0.001899	78	0.002075	72
0.25	0.000799	100	0.000561	60
0.40	-0.002108	110	-0.003439	154
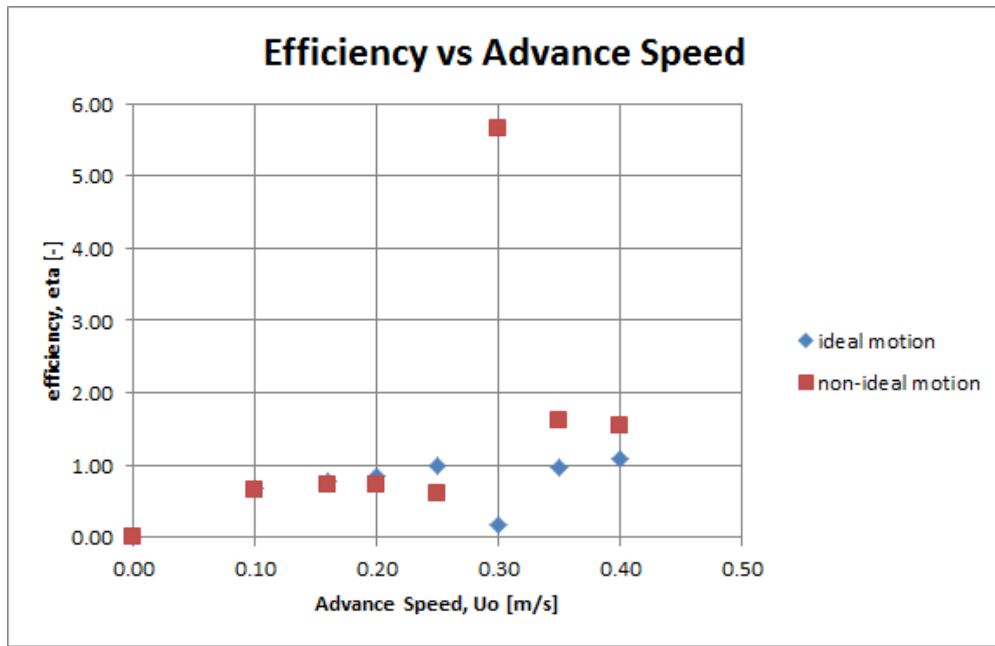
Figure 4.56: Efficiency versus carriage advance speed for ideal and non-ideal motions.

- rel. std dev < 5%

- used hot-wire anemometer

- various analysis macros used

- lessons learned about sufficient seeding (need lots)

Off-Axis PIV Testing (Aug. 2014)

- too much out-of-plane motion, even with small Δt

4.4.1 PIV Software Setup - Data Acquisition and Post-processing

- 4 carriage speeds: 0.0, 0.16, 0.25 (design speed), 0.4 m/s

- $\Delta t = 2000, 1560, 1000, 625$ μs

- Pre-Processing: subtraction of background image

- Processing:

    - image deformation used for areas of high shear
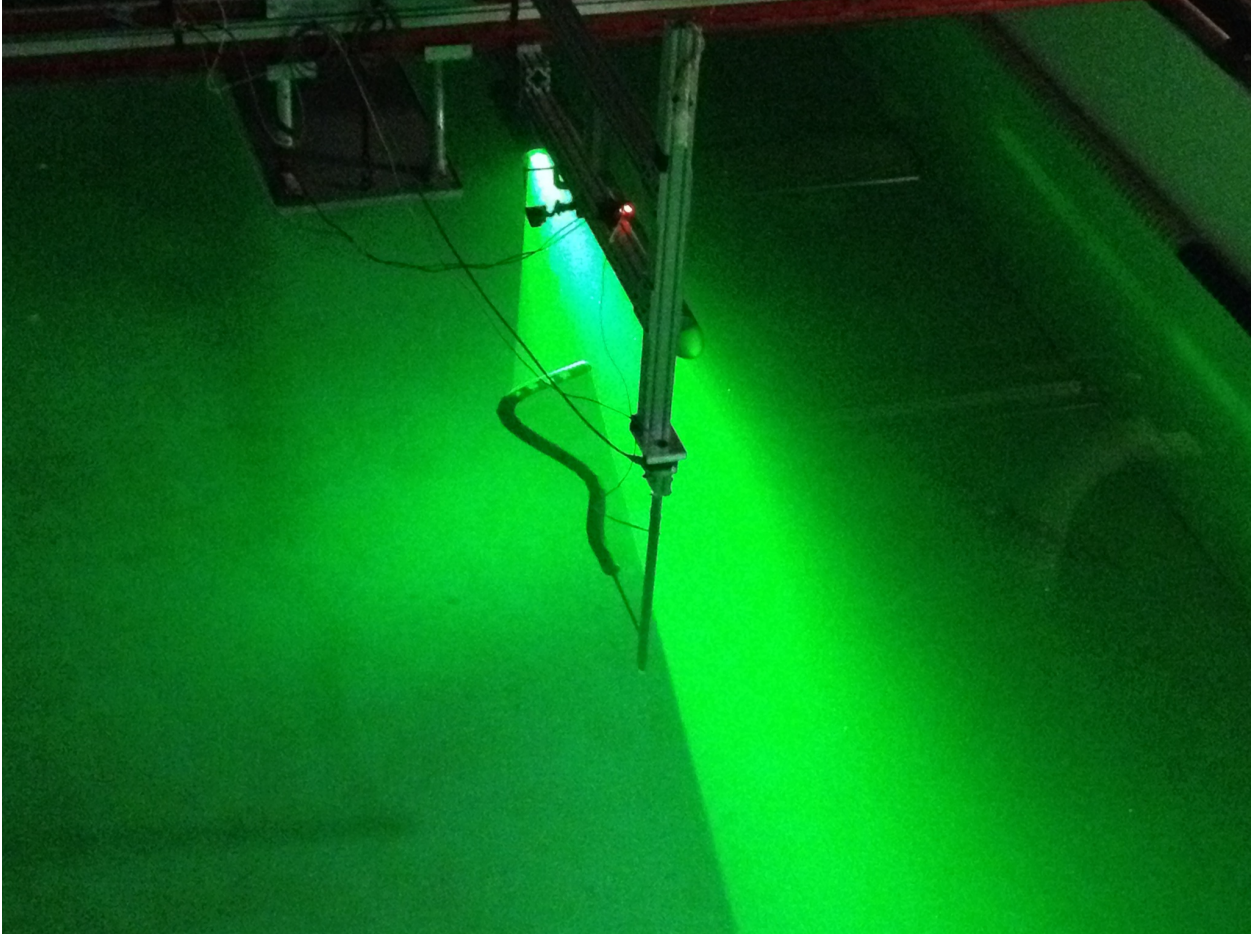
Figure 4.57: NEELBOT-1.1 underway during a PIV test.
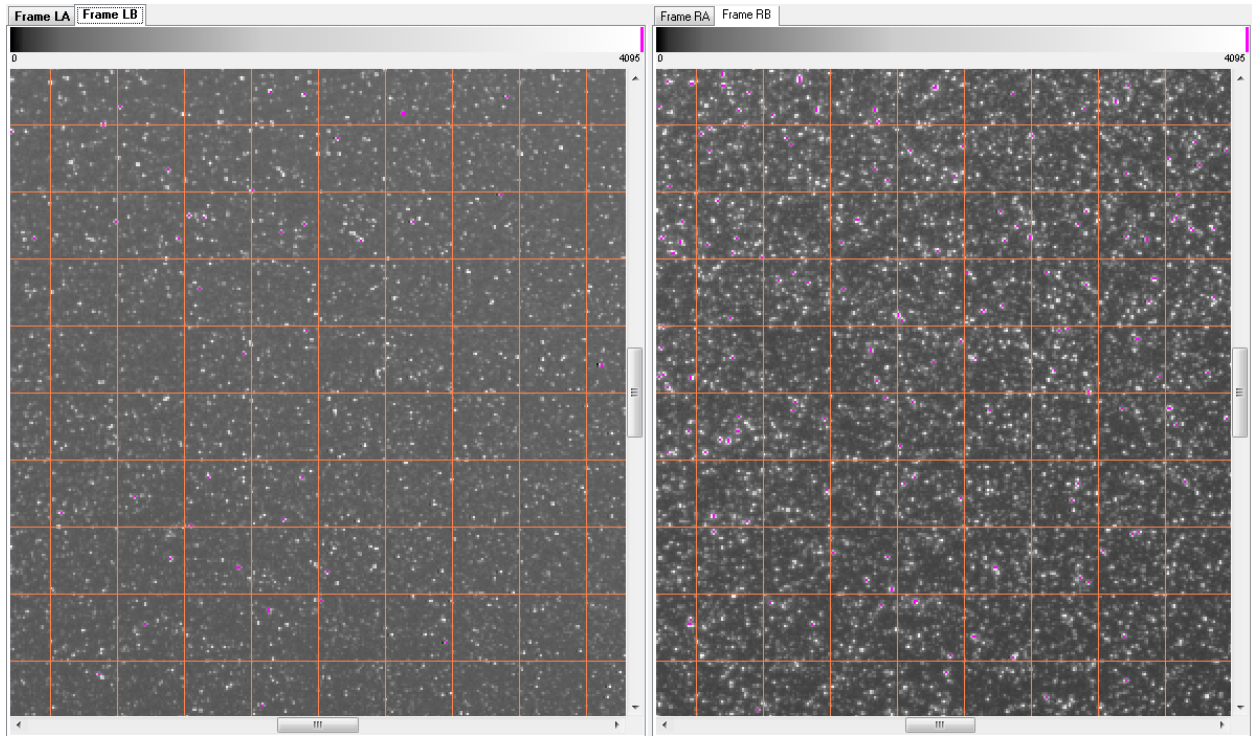
Figure 4.58: Screenshot showing example of seed particle density in the flow field (square grid of 32 pixels; 32 pixels = 5.72mm.

- omitted bad vectors

- 2D vector fields corrected for perspective and distortion using 3rd order polynomial (Soloff et al. (1997))

- combined vector fields using stereo process (Prasad and Adrian (1993))

- Starting/Ending Spot Dimensions: 64/32 pixels (FOV size: 250 x 175 mm, nominal)

- Vector validation/conditioning:

  - local validation: median filter (neighborhood size: 5x5; vel. tolerance: 3 px)

  - conditioning: holes filled with local mean method (measured vectors only)

As a rule of thumb in the field of PIV testing, a frame is considered to contain an acceptable set of velocity vectors if the percentage of good vectors is greater than 90%.

4.4.2 Propulsive Wake Results

- spatial resolution: 2.86 mm grid

161
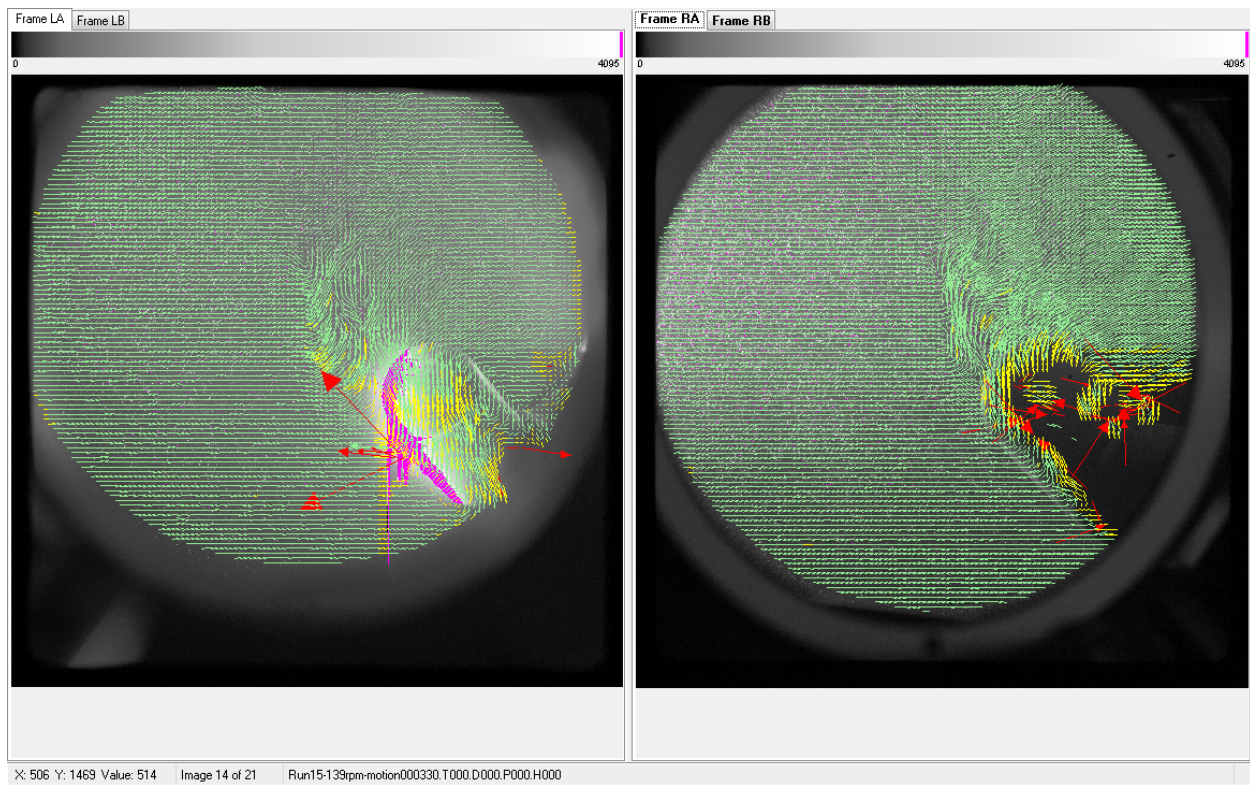
Figure 4.59: Example of processed vectors showing good (green), bad (red), and interpolated (yellow) vectors. Good vector percentage: Left frame: 95%; right frame: 91%.

- temporal resolution: 7.25 Hz (20 samples per NEELBOT-1.1 motion cycle)

- FOV's from 8 different tests of same motion/carriage speed are combined with the proper spatial transformations and phase synchronizing to create an analysis of the interested wake region

4.4.2.1 SPIV Testing (Oct. 2014)

After learning the seeding mistakes from the free flow testing and that there was too much out of plane fluid flow for the off-axis analysis, SPIV testing was finally performed on the wake velocities downstream of the eel. The unfortunate problem with this is that the field of view (FOV) is XX% smaller than that of the OAPIV testing. The total field of view ended up being 0.8 m × 0.5 m to the port side of the NEELBOT-1.1's centerline in the horizontal x-y plane.

SPIV testing was performed for 4 different advance speeds of the carriage: 0.0, 0.16, 0.25, and 0.4 m/s. The desired motion of the ideal anguilliform was replicated as best as possible (See Section XX for control theory and why motion was not attained; maybe add this as an appendix).

Motion control parameters used are listed herein.

Analysis macro parameters are listed herein.

Until I figure out a better way to explain this in writing, the following sections are listed in chronological order for the setup and analysis of the SPIV testing. Maybe place results and conclusions first and then have setup details explained in an appendix like structure for this chapter.

The contour plots of the velocity magnitudes in Figures **??** through **??** are somewhat noisy. To eliminate the noise, the plots are smoothed using an ideal "sinc" filtering technique. For each spatial point in the wake region, each of the components of that velocity vector is filtered over time. However, the raw data is not simply filtered as it is. The PIV system can record a maximum frequency of 7.25 Hz, so according to the Nyquist condition, this discrete data can capture phenomenon happening up to half of that frequency. The motion of the robot is cycling at a period of 2.721 seconds, and 22 cycles of motion were recorded by the PIV system. The first half of the cycles have been truncated due to transient fluid dynamics due to the acceleration of the towing tank carriage up to full speed. An example of this time series of data for a specific point in space of the fluid flow field is shown in Figure 4.60.
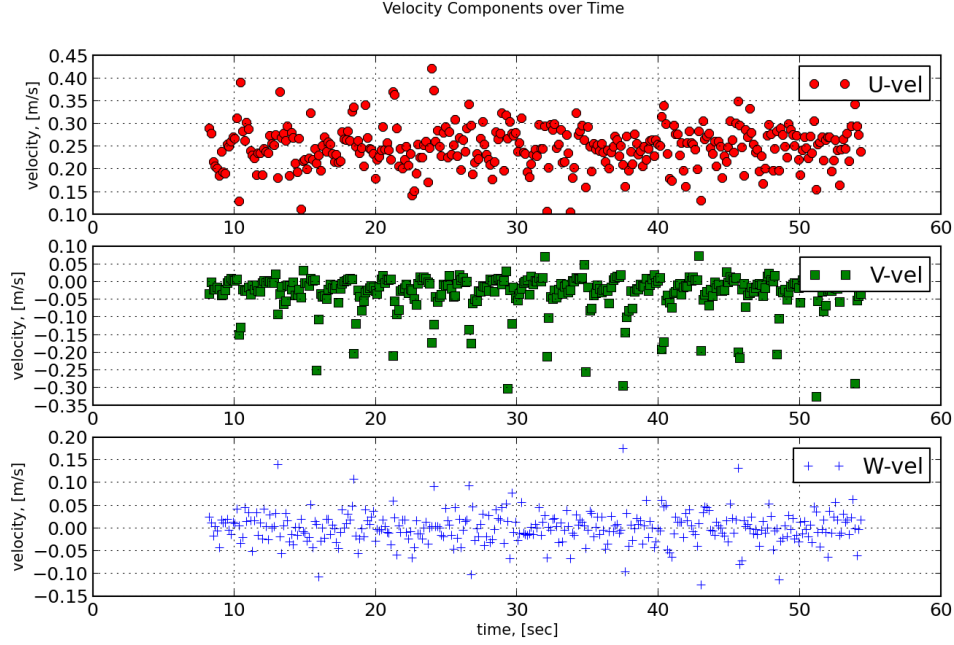
Figure 4.60:

Several cycles of the velocity components shown for the specific spatial point of $x = 1301.3$ mm, $y = -143.86$ mm.

The spatial point $x = 1301.3$ mm, $y = -143.86$ mm is shown by the red cross-hair target symbol in Figure 4.61.

Unfortunately, the frequency of the robot motion is not an integer multiple of the sampling frequency of the PIV system. Because of this, at the start of each robot cycle, the PIV samples will be slightly out of phase compared to the other cycles of motion. This prevents the application of a typical fluid dynamics analysis technique of computing phase-averaged velocities. However, the results can be superimposed into one motion cycle by ordering the data points in time based on their phase difference from the start of each motion cycle. A schematic of this is illustrated in Figure 4.62. The top image shows each of the three velocity components plotted over 11 cycles of motion at a sampling rate of 7.25 Hz. The bottom image shows the data points reordered over one cycle, now with an effective sampling rate of 80 Hz. This reordering is only acceptable if the motion is cyclic, and thus independent of time, which is assumed here.

The reordered data is shown in Figure 4.63, which is now one cycle of data at an effective sampling rate of 80 Hz, assuming the component data is cyclic for all time. The different marker styles are each for the different cycles of motion in the original time series, and these show that no
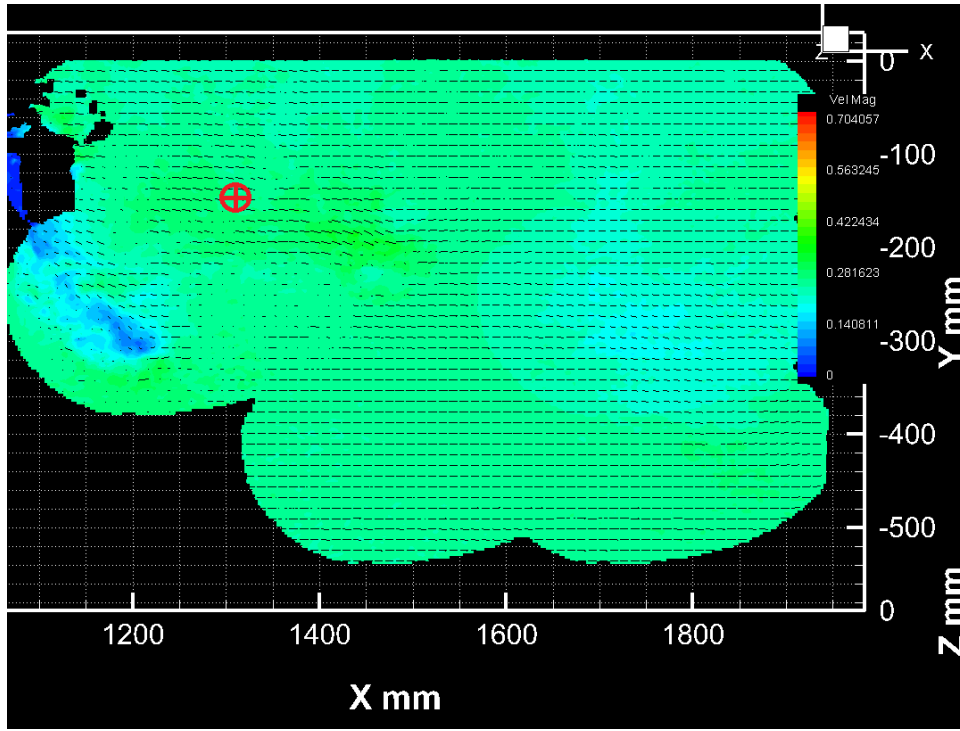
Figure 4.61: View of the fluid flow field showing the point in space where the time-series of data in Figure 4.60 was recorded.

single cycle is biased higher or lower than the other sets of data. This validates that the velocity component data is cyclic for all time and that this reordering of data is a valid technique. This technique was performed for all +55,000 points in space of the velocity flow field.

Once the velocity component data for each spatial point has been reordered, it was filtered using an ideal "sinc" filter (in the time domain), also called a "brickwall" filter in the frequency domain. This technique filters out any high-frequency noise above the threshold, or cutoff, frequency. Determining the frequency cutoff of the filter was fairly subjective, and it has been set at 3.625 Hz for the data here. Following is an explanation of this technique. Given a row vector of data, $\mathbf{V}$, that contains values evenly spaced in time, at the inverse of the sampling rate, f_s. The data vector contains N number of values, and the time step is Δt. Take the Discrete Fourier Transform (DFT) of $\mathbf{V}$:

$$\mathcal{F}(f) = \frac{1}{N} \int_{-\infty}^{\infty} \mathbf{V}(t)e^{-ift}dt \tag{4.24}$$

where f is the independent variable for the frequency domain. The DFT for the example set of data is shown in Figure 4.64. Of the replicated discrete Fourier transform now in the frequency

165

Velocity Components over Time

$T_{\text{NEELBOT}-1.1} = 2.721 \text{ sec}$

$f_{\text{s,NEELBOT}-1.1} = 0.368 \text{ Hz}$

$f_{\text{s,PIV}} = 7.25 \text{ Hz}$

11 cycles of robot motion

1 cycle

$f_{\text{s}} = 80 \text{ Hz}$
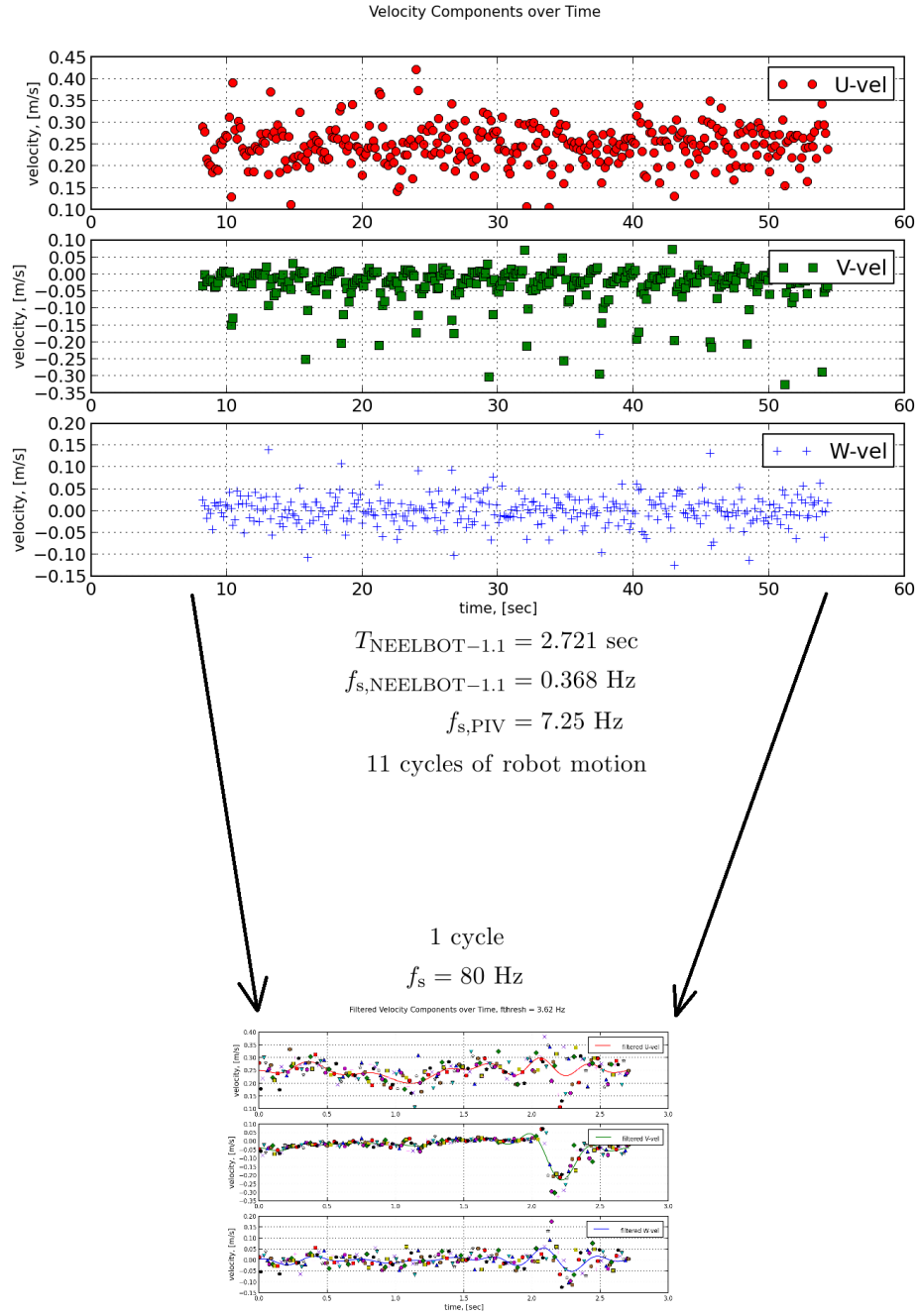
Figure 4.62: Data reordering technique to increase the sampling rate to an effective 80 Hz, assuming the fluid flow is perfectly cyclic.

166

Filtered Velocity Components over Time, fthresh = 3.62 Hz
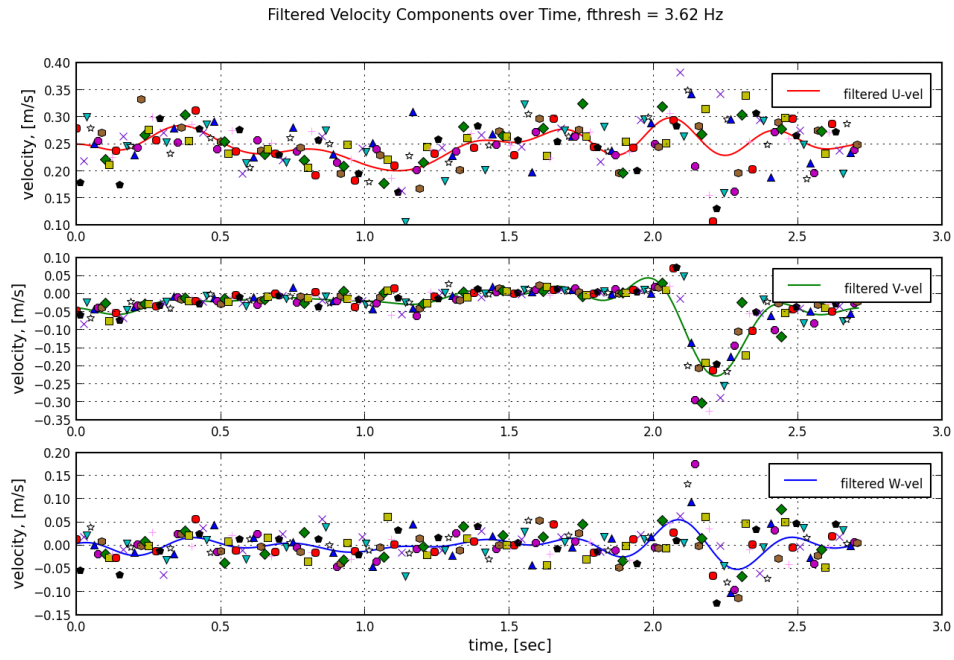
Figure 4.63: Reordered time series of velocity component data into one cycle to increase the effective sampling rate to 80 Hz, assuming the component data is cyclic for all time. The different marker styles are each for the different cycles of motion in the original time series. The solid lines represent that data filtered with a "sinc" filter at a cutoff frequency of 3.625 Hz.

domain, only the "base island" is of interest at the moment, which spans in frequency from $-f_s/2$ to $f_s/2$. The width of frequency steps between the complex values of the DFT is

$$\Delta f = \frac{1}{N\Delta t} \tag{4.25}$$

The rectangle function, also known as a boxcar or brickwall function,

$$\Pi_{f_c}(f) = \begin{cases} 0 & \text{if } |f| > f_c \\ 1 & \text{if } |f| \le f_c \end{cases} \tag{4.26}$$

is multiplied by the DFT in the frequency domain

$$\mathcal{F}_{\text{filt}}(f) = \mathcal{F}(f)\Pi_{f_c}(f) \tag{4.27}$$

where f_c is the cutoff frequency for the filter. The filtered function in the frequency domain is then transformed back into the time domain with the inverse Fourier transform:

$$\mathbf{V}(t) = N \int_{-\infty}^{\infty} \mathcal{F}_{\text{filt}}(f)e^{-ift}df \tag{4.28}$$

which is plotted as the solid lines in Figure **??** at a cutoff frequency of 3.625 Hz. The filtered velocity component data is then used to reconstruct the flow field as shown in the selected screenshots over the cycle in Figures XXX-YYY. For this data, there ends up being 217 time steps of velocity component data to complete one cycle of data at a time period of 2.721 seconds at a sampling frequency of 80 Hz.

Figures 4.65 and 4.66 show a snapshot in time of the velocity field plotted using raw and filtered data, respectively. The second figure clearly looks "cleaner" and less noisy, but it could also be omitting important high-frequency phenomenon. For now, the focus is the bigger-picture phenomenon, which have hopefully not been affected by the filtering techniques.
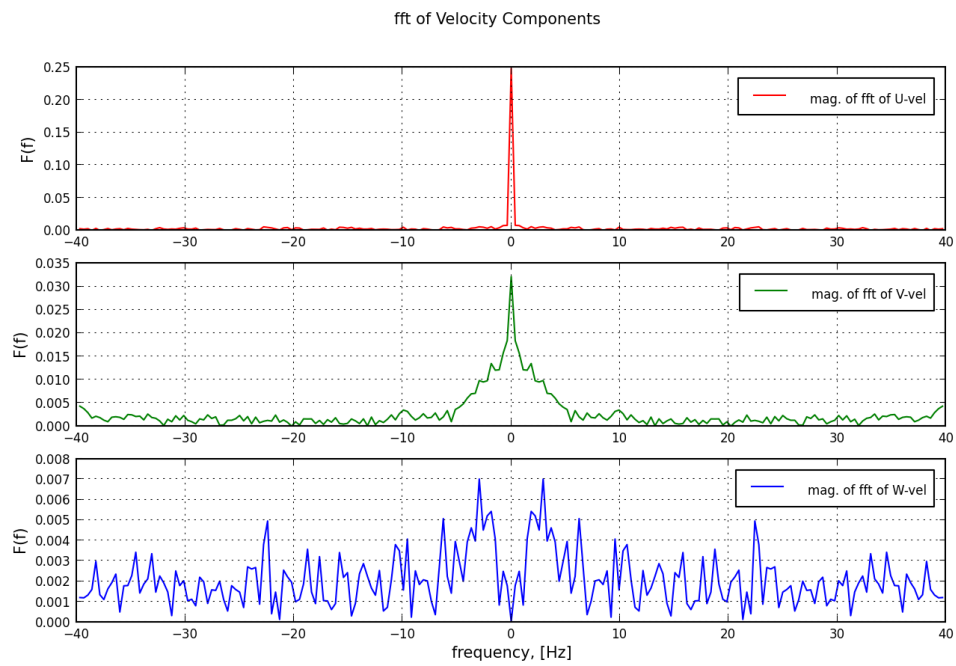
Figure 4.64: Magnitude of the Discrete Fourier Transform of the velocity component data in Figure ??
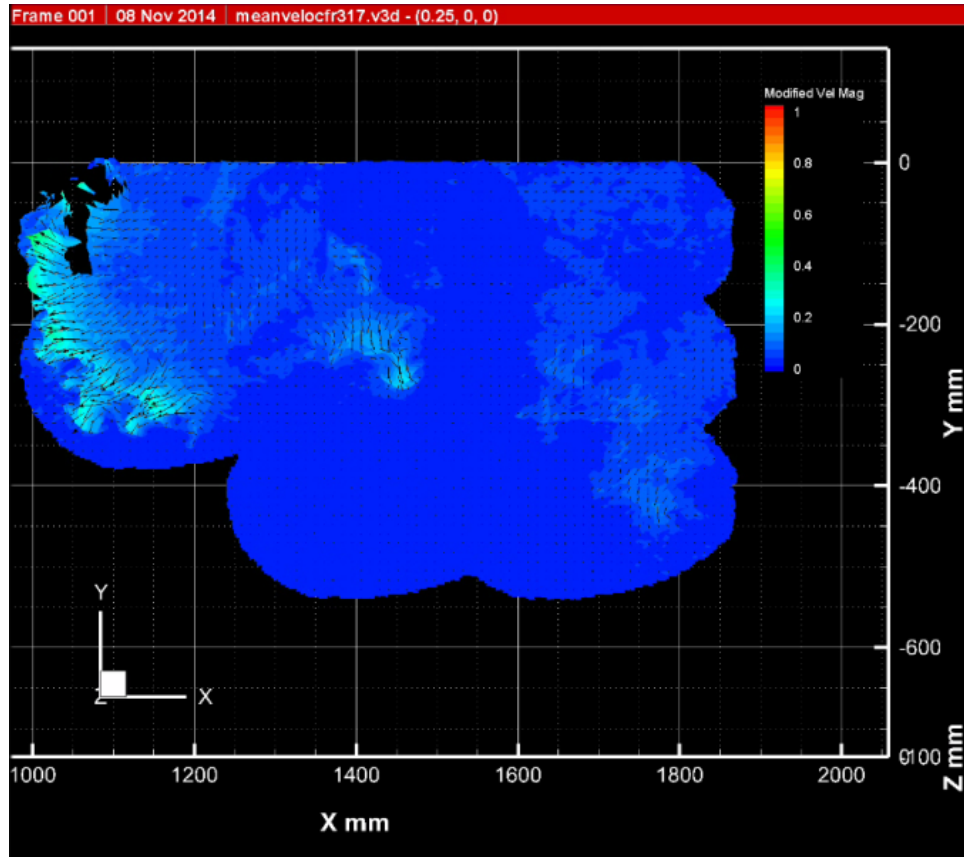
Figure 4.65: Flow field of raw velocity vectors at $t = 0.0T$ for $U_0 = 0.25$ m/s.
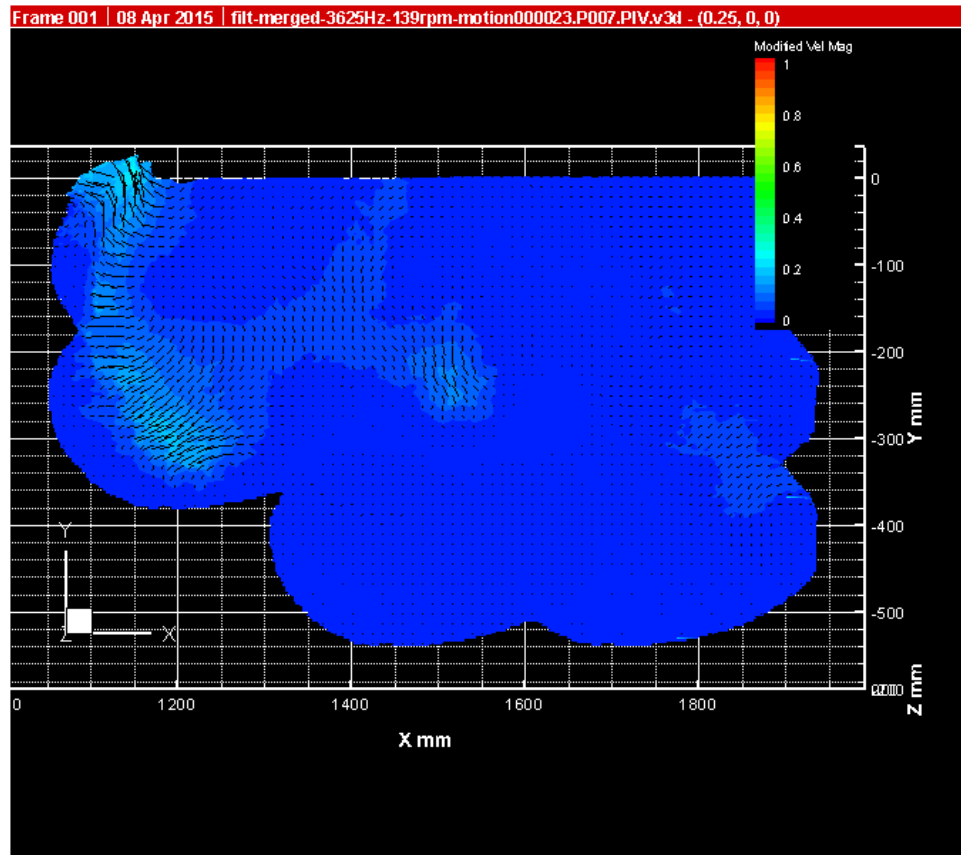
Figure 4.66: Flow field of filtered velocity vectors at $t = 0.0T$ for $U_0 = 0.25$ m/s.

4.4.2.2 Advance Speed: 0.25 m/s

The governing equation for an integral control volume analysis of momentum conservation that computes the forces acting on a control volume is

$$\frac{\partial}{\partial t} \iiint \rho \underline{V} d\mathcal{V} + \iint \rho \underline{V} (\underline{n} \cdot \underline{V}) dA = \iint -p \underline{n} dA + \iiint \rho \underline{g} d\mathcal{V} + \underline{F}_{\text{viscous}} \qquad (4.29)$$

where

$$\underline{F}_{\text{gravity}} \quad = \iiint \rho \underline{g} d\mathcal{V} \qquad (4.30)$$

$$\underline{F}_{\text{pressure}} \quad = \iint -p \underline{n} dA \qquad (4.31)$$

and $\underline{F}_{\text{viscous}}$ is not derived for purposes of simplicity.

Equation 4.29 needs to be applied to the control volume as shown in Figure 4.70. The gravity vector is equal throughout and perpendicular to the horizontal control volume, so the body force term can be ignored. Inspecting solely the surface integrals next helps simplify the equation. Each of the surface integrals can be broken up into individual pieces:

$$\iint ( ) dA = \iint_{abhi} ( ) dA + \iint_{def} ( ) dA + \iint_{cd} ( ) dA + \iint_{fg} ( ) dA \qquad (4.32)$$

Surfaces cd and fg have the same flow variables but opposite signs due to $\underline{n}$, so these integrals go away for each overall surface integral. The momentum flux integrals disappear for surface def since the flux through a solid surface is zero. The revised momentum integral equation is

$$\frac{\partial}{\partial t} \iiint \rho \underline{V} d\mathcal{V} + \iint_{abhi} \rho \underline{V} (\underline{n} \cdot \underline{V}) dA = \iint_{abhi} -p \underline{n} dA + \iint_{def} -p \underline{n} dA + \underline{F}_{\text{viscous}} \qquad (4.33)$$

The pressure acting on surface $abhi$, uniform and equal to p_∞, cancels out due to it being equal around the entire CV surface but with opposite normal vectors. The viscous term is assumed to act only on the surface def since it cannot act on surfaces normal to the flow, ia and bh, and there is assumed to be no velocity gradient (du/dy), which shear stress is proportional to, at the surfaces ab and hi, which are far away from the body.

172
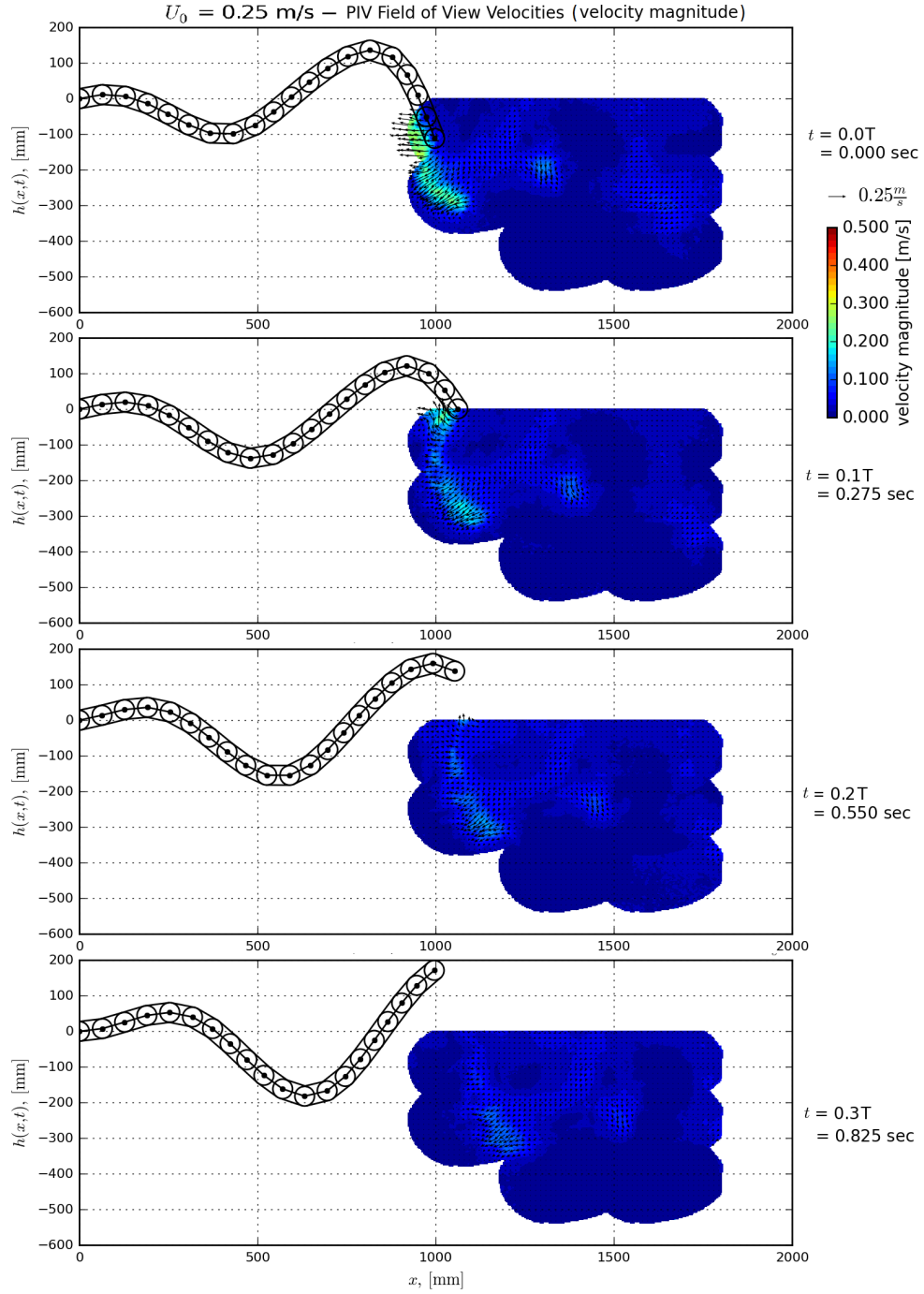
Figure 4.67:
Timesteps 0.0T, 0.1T, 0.2T, and 0.3T of filtered ($f_c = 3.625$ Hz) velocities at equal time steps over the robotic eel motion cycle for $U_0 = 0.25$ m/s. The uniform flow of $u = 0.25$ m/s has been subtracted from the flow, giving the flow field an inertial frame of reference.
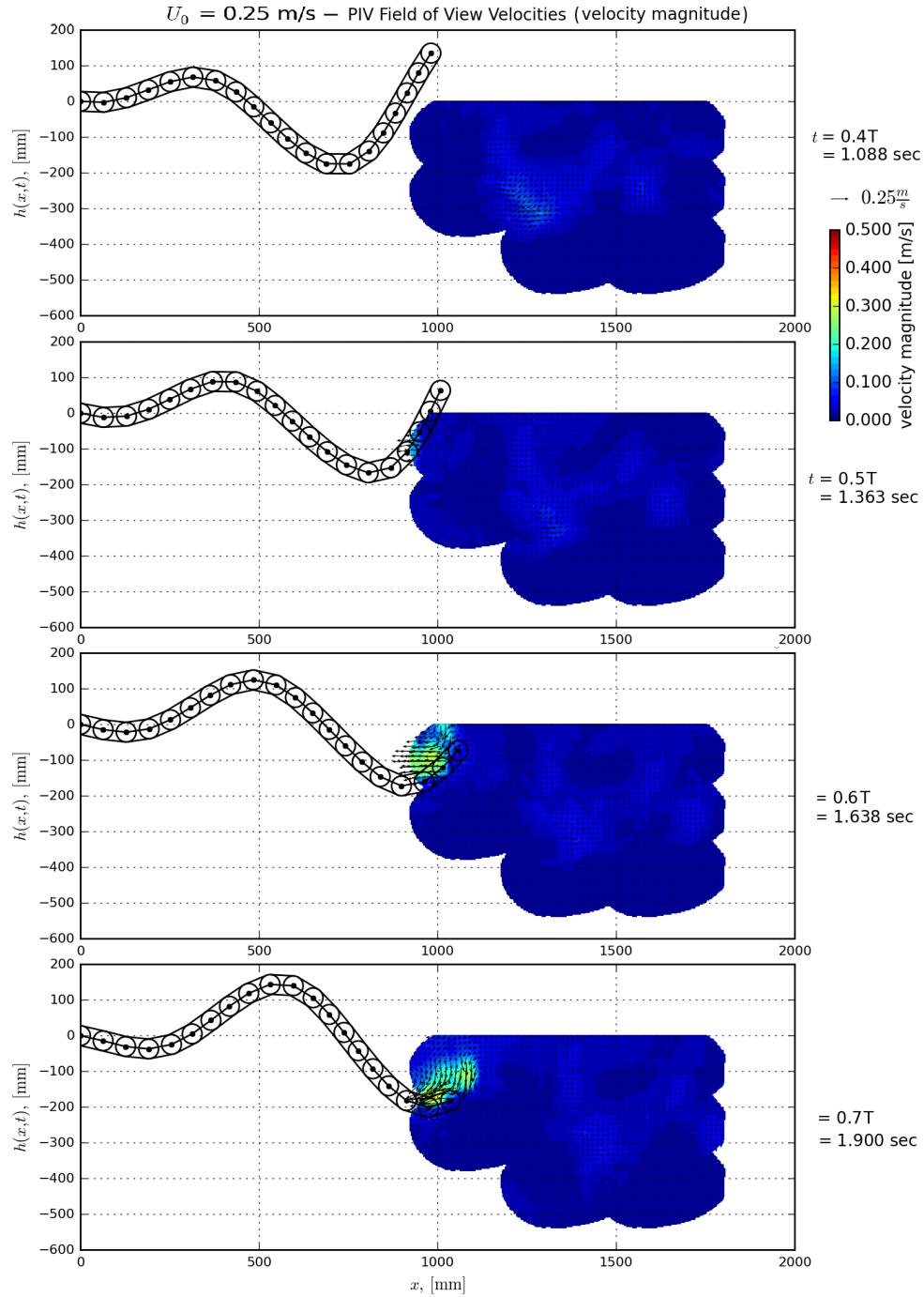
Figure 4.68:
Timesteps 0.4T, 0.5T, 0.6T, and 0.7T of filtered (f_{c} = 3.625 Hz) velocities at equal time steps over the robotic eel motion cycle for U_0 = 0.25 m/s. The uniform flow of u = 0.25 m/s has been subtracted from the flow, giving the flow field an inertial frame of reference.
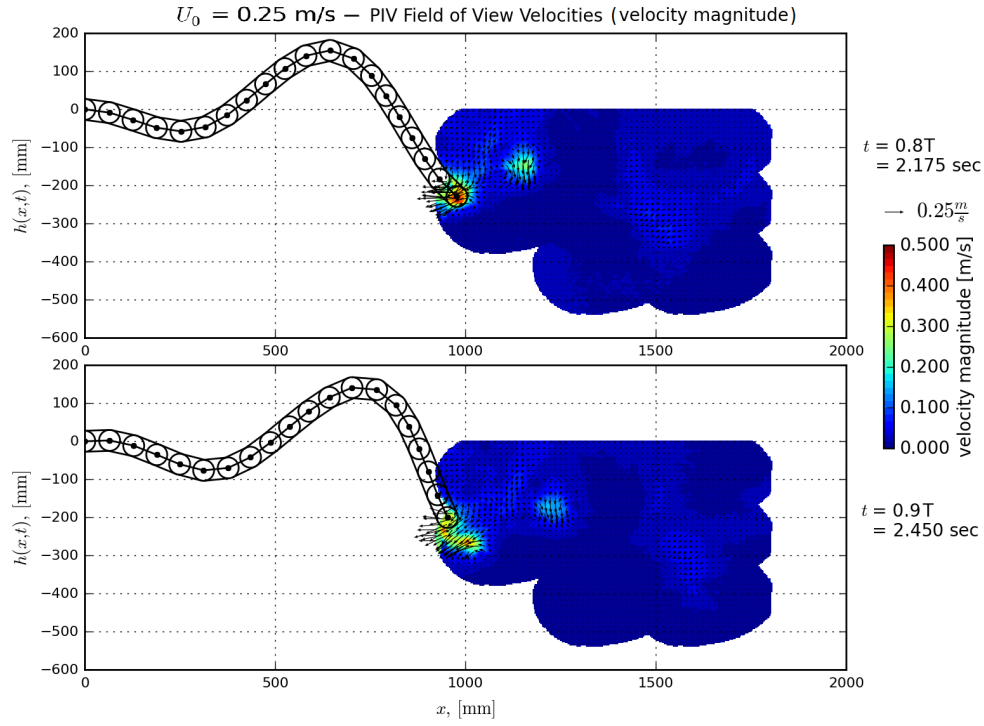
Figure 4.69: Timesteps 0.8T and 0.9T of filtered ($f_{\mathrm{c}} = 3.625$ Hz) velocities at equal time steps over the robotic eel motion cycle for $U_0 = 0.25$ m/s. The uniform flow of $u = 0.25$ m/s has been subtracted from the flow, giving the flow field an inertial frame of reference.
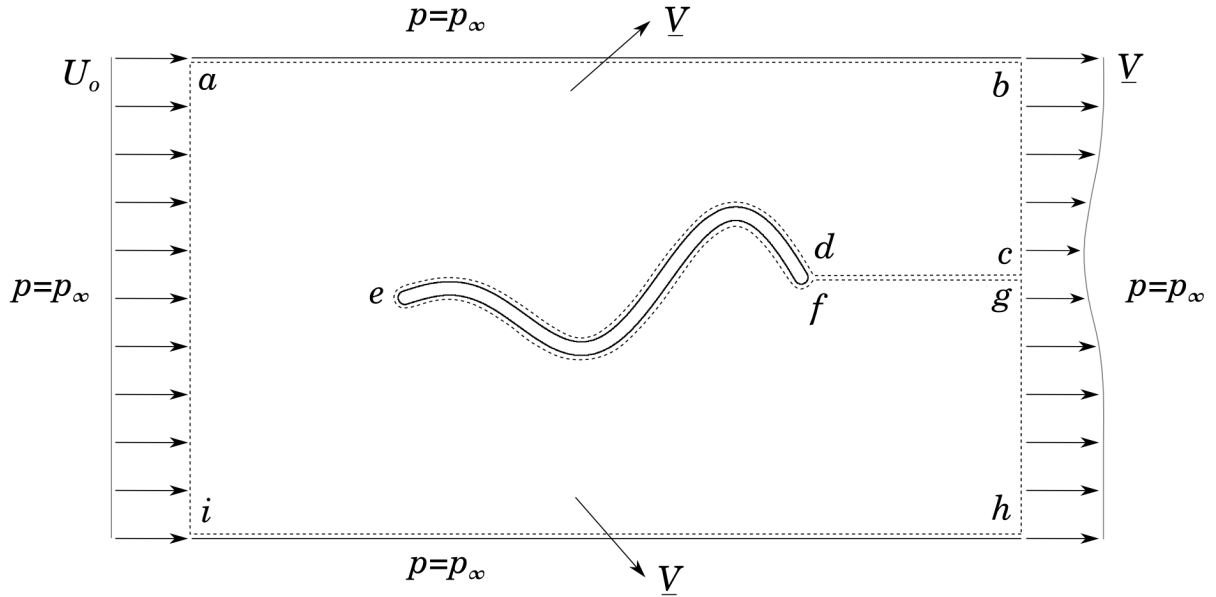
Figure 4.70: Control volume of momentum integral analysis of anguilliform eel.

175

The revised momentum integral equation is now

$$\frac{\partial}{\partial t} \iiint \rho \underline{V} d\mathcal{V} + \iint_{abhi} \rho \underline{V} (\underline{n} \cdot \underline{V}) dA = \iint_{def} -p\underline{n} dA + \underline{F}_{\text{viscous}} \qquad (4.34)$$

The two terms on the right hand side are the resultant forces acting on the body, modeling the thrust and drag of the anguilliform shape. Unfortunately, it is effectively impossible to separate the two with this type of analysis. Thus, the two terms are lumped into two terms, thrust, T, and drag, D.

$$\frac{\partial}{\partial t} \iiint \rho \underline{V} d\mathcal{V} + \iint_{abhi} \rho \underline{V} (\underline{n} \cdot \underline{V}) dA = \underline{T} - \underline{D} \qquad (4.35)$$

The two terms on the right hand side must sum to zero because this is the result of a momentumless wake. Momentumless flows are types of flows where it is difficult, if not impossible, to accurately separate the drag and thrust components of the flow in a control volume. It is most associated with self-propelled bodies, where the momentum deficit is cancelled out by a momentum excess.

This type of flow can be best explained for the scenario of a control volume analysis for a ship and its propeller. For a propeller on its own, it is relatively easy to compute the thrust it produces by calculating the momentum flux input and output of the streamtube the propeller is entrained in. For a ship hull on its own, the drag can be computed by a deficit in the wake speed at the outlet of the control volume. However, when both of these components are combined, it is impossible to determine the individual thrust of the propeller and the individual drag of the ship.

There are numerous researchers that have investigated momentumless wakes, going back several decades. Lin and Pao (1979) gives a summary of results from early self-propelled wake studies. de Stadler and Sarkar (2012) gives a much more updated summary in their introduction, and their research entails using direct numerical simulation (DNS) to simulate momentumless flows. Meunier and Spedding (2006) presents experimental results on the wake of a self-propelled bluff body at a constant speed. The authors state that momentumless flows are very peculiar and that unlike drag wakes, there is no single rescaling based only on wake momentum flux that will predict, in a more general way, wake dynamics. A similar consensus has been reached by Sirviente and Patel (2000), in that the scaling of momentumless wakes require two separate velocity and length scales to describe the flow, one each for the drag and thrust components. Having one scale to describe

176

the entire flow is insufficient. These are all thoughts to take into consideration when investigating the momentumless wake of the robotic anguilliform shape. In fact, as explained later, only the momentum flux at the outlet of the control volume will be investigated due to lack of data and momentumless flow aspects.

Since the PIV results are discrete values, the above equation will need to be discretized and placed in numerical form. The control volume has an inifinitesimal thickness in the vertical direction, so that dimension can be effectively eliminated, simplifying the equation and making the result be momentum flux per unit length. The first term can use a 2nd order central difference for the time derivative and a double summation for the control volume integral. The second term will simply be a summation over the boundary:

$$
\rho \sum_{i=0}^{N} \sum_{j=0}^{M} \frac{\underline{V}_{i,j,t+1} + 2\underline{V}_{i,j,t} + \underline{V}_{i,j,t-1}}{\Delta t^2} \Delta x \Delta y + \rho \sum_{i=0}^{N} \underline{V}_i (\underline{n} \cdot \underline{V}_i) \Delta x \Big|_{ab}
$$
$$
+ \rho \sum_{j=0}^{M} \underline{V}_j (\underline{n} \cdot \underline{V}_j) \Delta y \Big|_{bh} + \rho \sum_{i=0}^{N} \underline{V}_i (\underline{n} \cdot \underline{V}_i) \Delta x \Big|_{hi}
$$
$$
+ \rho \sum_{j=0}^{M} \underline{V}_j (\underline{n} \cdot \underline{V}_j) \Delta y \Big|_{ia} = \underline{T} - \underline{D} \quad (4.36)
$$

Unfortunately, the PIV testing of the current NEELBOT-1.1 could not practically gather vectors for the entire flow field. Only vectors immediately downstream of the robot and to one side (although these can be phase-shifted and assumed to be mirrored to the other side of the medial plane) were able to be acquired. This makes it impossible to perform a complete control volume analysis in the style of Figure 4.70. Thus, only certain terms of the conservation of momentum equation are used for comparison.

Only the momentum flux at the downstream edge of the control volume is being computed and compared to the theoretical results for a couple of practical reasons, in addition to the reasons stated above for lack of data and momentumless flows. Because of the moving control volume along the robot body's surface, it is fairly difficult to compute the change in momentum, which is the first term in the momentum integral. Also, this testing lacks the data on the sides of the control volume. This is the only feasible and practical analysis for the current research results that can be done. Thus, only the third term of equation 4.36 is computed and plotted in Figures 4.71 through

Cross-section of Flow Field Velocity

$t=0.0T$, frame: 51, $x=1.15L$, $\dot{M}_{\mathrm{cs,PIV}}=37.8$ N/m, $\dot{M}_{\mathrm{cs,theory}}=86.4$ N/m

Figure 4.71:

Component velocities of the flow field along a cross-section in the y-direction, comparing theoretical and experimental values for time $t = 0.0T$.

4.80 for equally spaced time steps over the robot cycle. This term is defined as

$$\underline{M}_{\mathrm{flux},bh} = \rho \sum_{j=0}^{M} \underline{V}_j (\underline{n} \cdot \underline{V}_j) \Delta y \Big|_{bh} \qquad (4.37)$$

Figures 4.71 through 4.80, for 10 equally spaced time steps, show plots of the theoretical and experimental velocity components in the downstream flow field for a slice in the y-direction (radial direction). These slices are located immediately downstream of the tail of the anguilliform shape, at $1.15L$. The x-axis, or rather the longitudinal direction, is pointing positively out of the paper towards the reader.

The theoretical velocities are centered on the $y = 0$ axis due to the constraint of the doublets being collapsed to the x-axis, whereas the maximum absolute value of the experimental velocities is located where the tip of the tail is in time. This location could have been centered at the $y = 0$ axis for a better comparison, but alteration of the data was kept at a minimum to confuse the reader as little as possible. Even taking this into account, the magnitudes and width of the fluid disturbance can be compared. The width of the overall fluid disturbance is determined by the points in the radial direction where the velocity magnitude of the disturbance is 0.95 times that of the nominal velocity magnitude. Disturbance widths for the velocity components are computed similarly.

The disturbance width for the experimental axial velocity components are generally half as wide

Figure 4.72: Component velocities of the flow field along a cross-section in the y-direction, comparing theoretical and experimental values for time $t = 0.1T$.

Figure 4.73: Component velocities of the flow field along a cross-section in the y-direction, comparing theoretical and experimental values for time $t = 0.2T$.

Figure 4.74: Component velocities of the flow field along a cross-section in the y-direction, comparing theoretical and experimental values for time $t = 0.3T$.
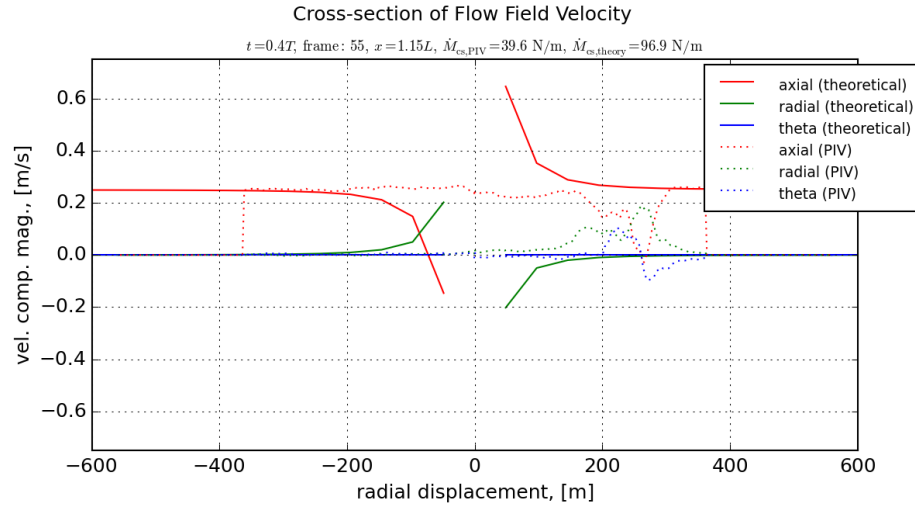
Figure 4.75: Component velocities of the flow field along a cross-section in the y-direction, comparing theoretical and experimental values for time $t = 0.4T$.
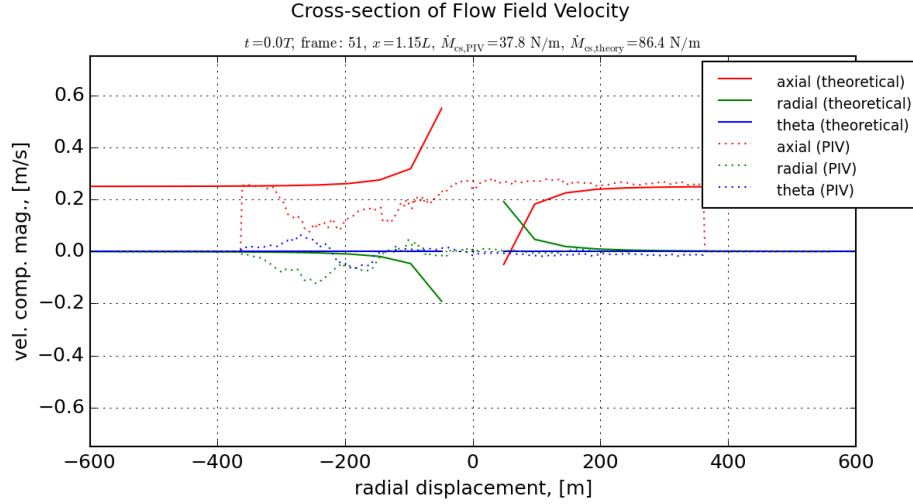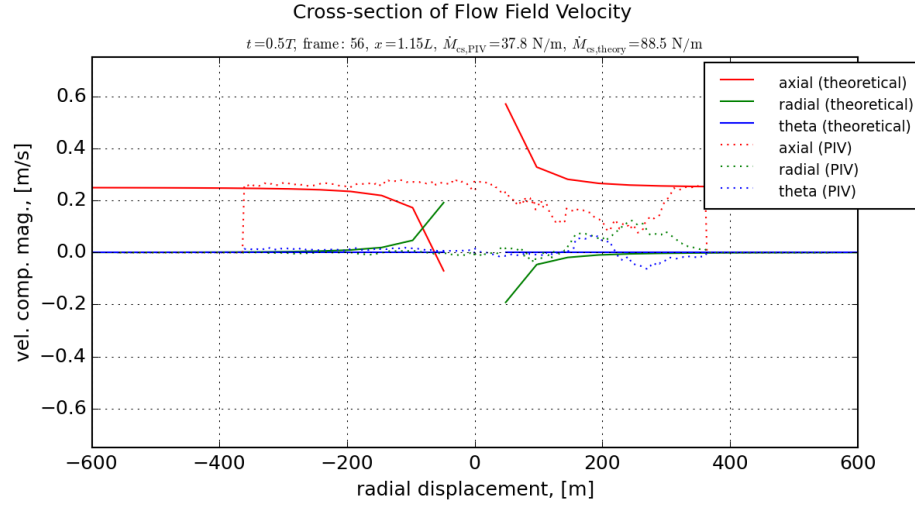
Figure 4.76: Component velocities of the flow field along a cross-section in the y-direction, comparing theoretical and experimental values for time $t = 0.5T$.
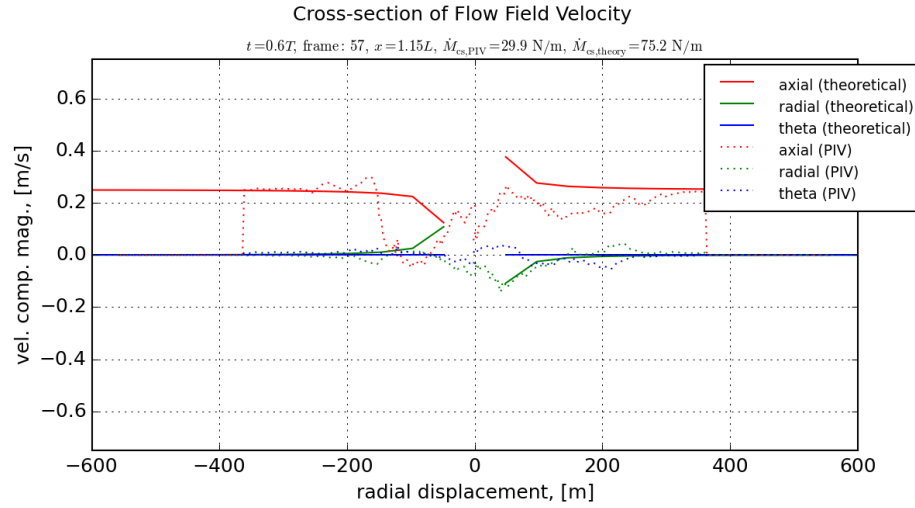
Figure 4.77: Component velocities of the flow field along a cross-section in the y-direction, comparing theoretical and experimental values for time $t = 0.6T$.
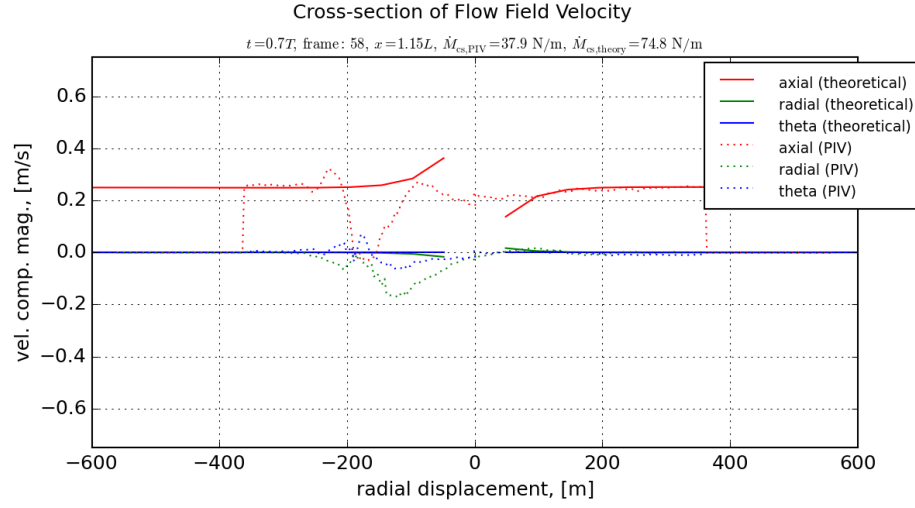
Figure 4.78: Component velocities of the flow field along a cross-section in the y-direction, comparing theoretical and experimental values for time $t = 0.7T$.
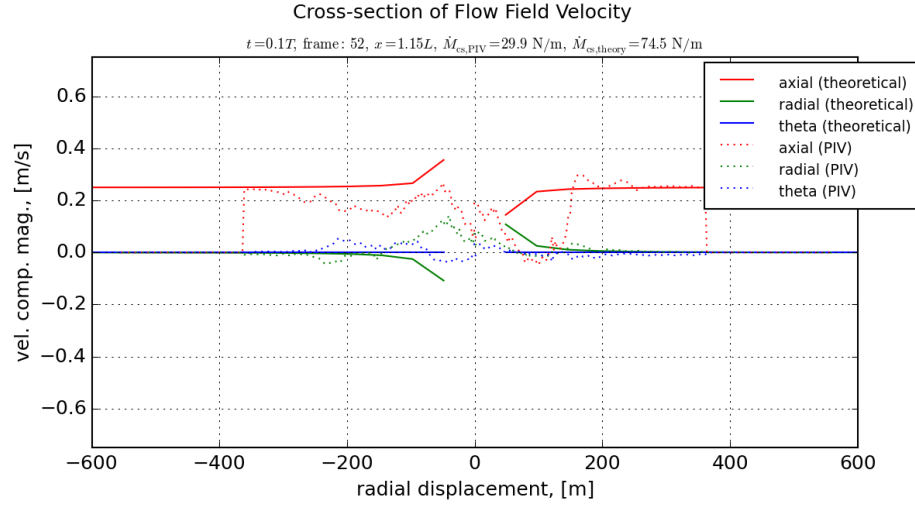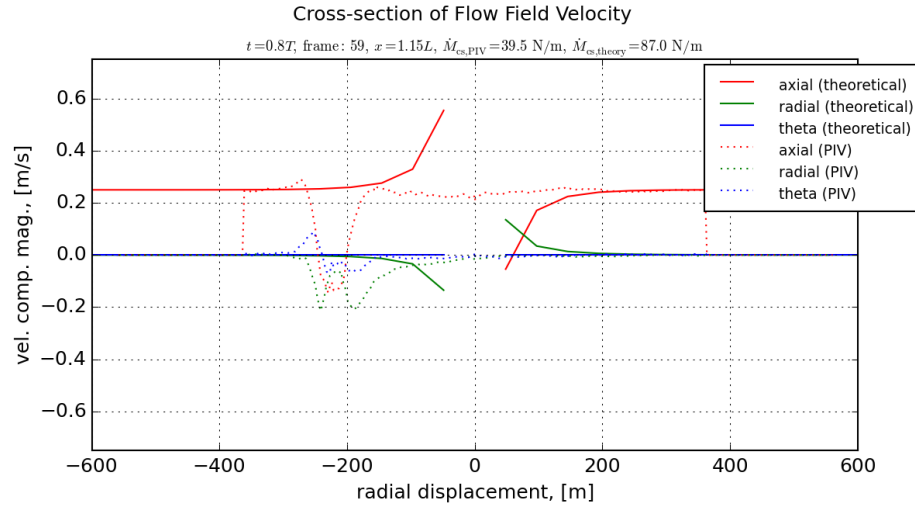

Figure 4.79: Component velocities of the flow field along a cross-section in the y-direction, comparing theoretical and experimental values for time $t = 0.8T$.
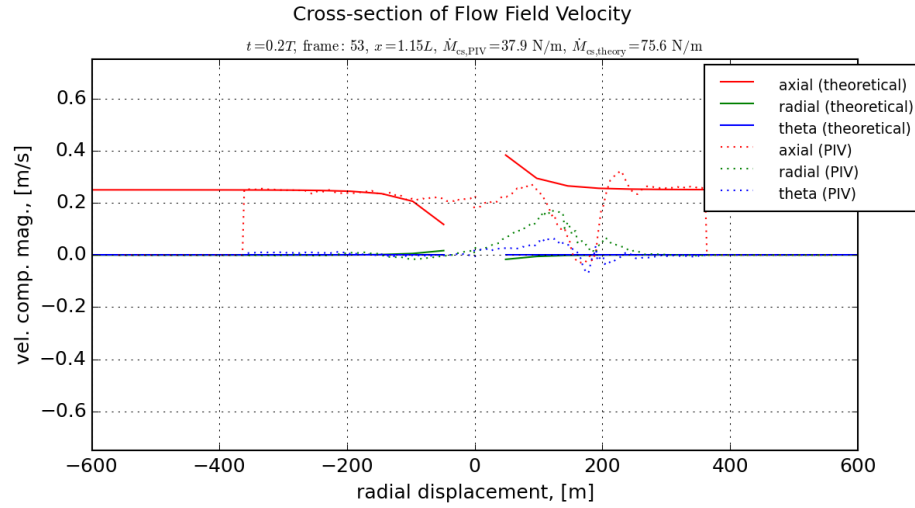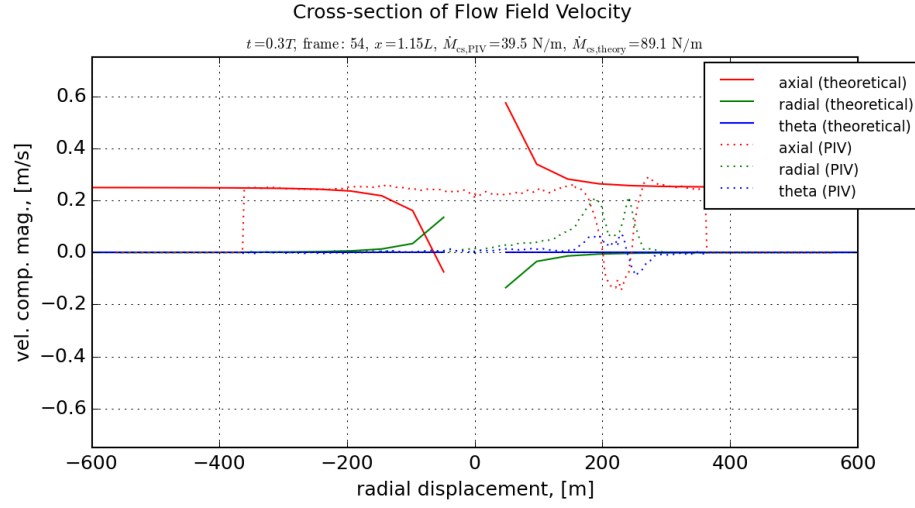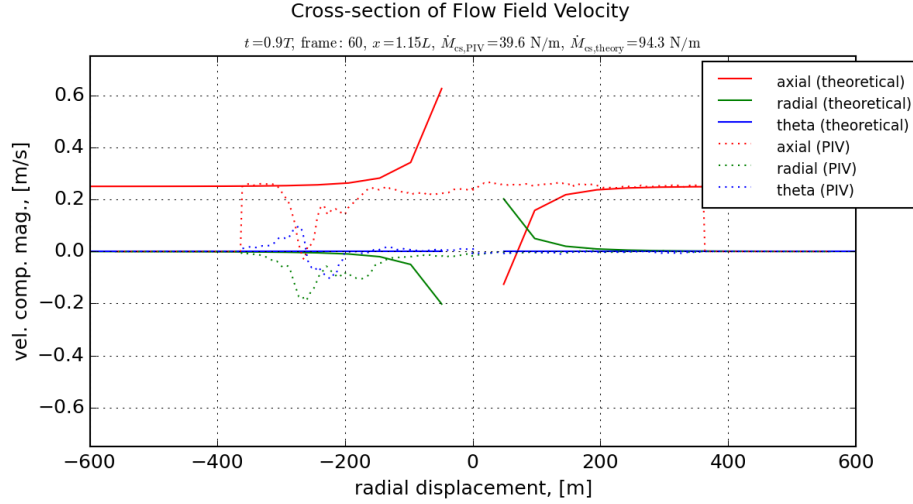
Figure 4.80: Component velocities of the flow field along a cross-section in the y-direction, comparing theoretical and experimental values for time $t = 0.9T$.

in the radial direction as that of the theoretical results. The width of the radial components match more exactly, but the theoretical has an odd-shape, whereas the experimental is even-shaped.

For each of the timesteps, each of the theoretical velocity components, except for the component in the circumferential direction (θ), are an odd function with respect to the $y = 0$ axis. Due to the assumptions of slender body theory, the circumferential component is eliminated. For the experimental results, this is not the case. The axial velocity components form an even function across the tail's centerline, and this position ranges from $-0.22L$ to $0.22L$. The circumferential velocity component shows an odd-shaped function across the tail centerline.

Figure 4.81 shows the momentum flux on the control volume outlet over time for one motion cycle, for both the theoretical and experimental cases. While the two cases do not agree in magnitude, they agree in qualitative shape, with both showing two cycles of flux over one cycle of the motion. This agrees with the propulsive thrust as predicted by Vorus (2005) having two cycles of thrust for each motion cycle.

For the theoretical cases, there is no data plotted between $-0.05L$ and $0.05L$ along the y-axis, or rather, the radial direction. This is because this area of the solution domain of the fluid velocities asymptotically approaches infinity because of the wake elements being modelled as a singularity.
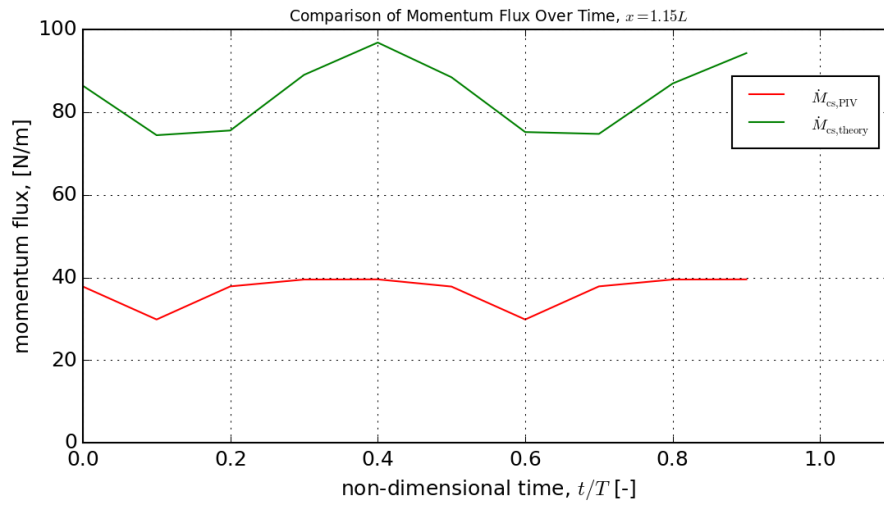
Figure 4.81: Comparison of momentum flux at y cross-section $x = 1.15$ versus time. The comparison is between the momentum flux calculated from the PIV and theoretical results.

4.4.2.3 Advance Speed: 0.16 m/s

Figure 4.82:
Timesteps 0.0T, 0.1T, 0.2T, and 0.3T of filtered ($f_c = 3.625$ Hz) velocities at equal time steps over the robotic eel motion cycle for $U_0 = 0.16$ m/s. The uniform flow of $u = 0.16$ m/s has been subtracted from the flow, giving the flow field an inertial frame of reference.

Figure 4.83:

Timesteps 0.4T, 0.5T, 0.6T, and 0.7T of filtered ($f_c = 3.625$ Hz) velocities at equal time steps over the robotic eel motion cycle for $U_0 = 0.16$ m/s. The uniform flow of $u = 0.16$ m/s has been subtracted from the flow, giving the flow field an inertial frame of reference.

Figure 4.84:
Timesteps 0.8T and 0.9T of filtered ($f_{\mathrm{c}} = 3.625$ Hz) velocities at equal time steps over the robotic eel motion cycle for $U_0 = 0.16$ m/s. The uniform flow of $u = 0.16$ m/s has been subtracted from the flow, giving the flow field an inertial frame of reference.

4.4.2.4 Advance Speed: 0.00 m/s

Figure 4.85: Timesteps 0.0T, 0.1T, 0.2T, and 0.3T of filtered ($f_\mathrm{c} = 3.625$ Hz) velocities at equal time steps over the robotic eel motion cycle for $U_0 = 0.0$ m/s.

Figure 4.86: Timesteps 0.4T, 0.5T, 0.6T, and 0.7T of filtered (f_c = 3.625 Hz) velocities at equal time steps over the robotic eel motion cycle for U_0 = 0.0 m/s.
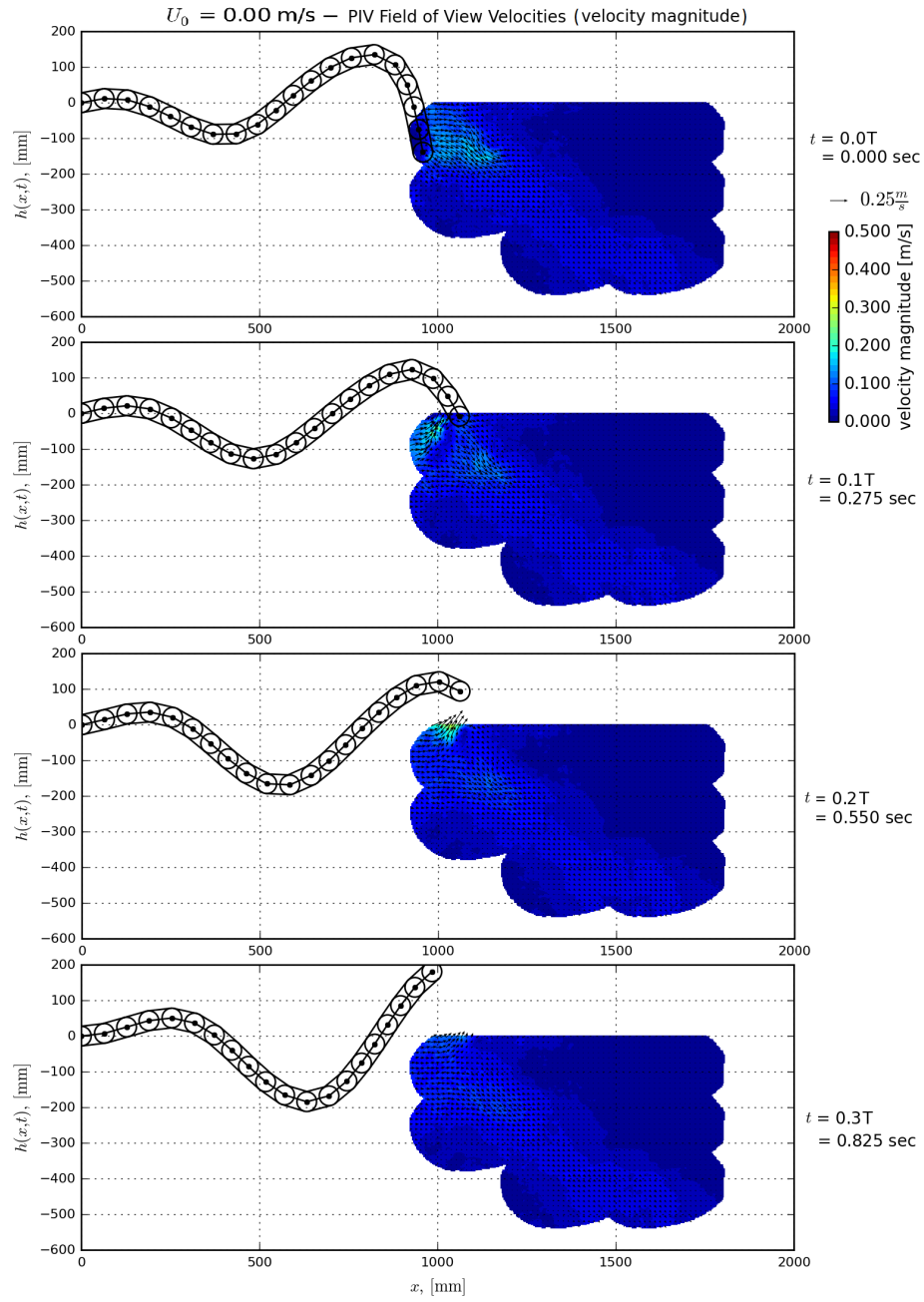
Figure 4.87: Timesteps 0.8T, and 0.9T of filtered (f_c = 3.625 Hz) velocities at equal time steps over the robotic eel motion cycle for U_0 = 0.0 m/s.

4.4.2.5 Advance Speed: 0.40 m/s

4.4.2.6 Visibly Distinct Phenomenon

There are a few distinct fluid phenomena occurring downstream of the robot in the SPIV results. For now, I will solely be referring to the 0.25 m/s (139 rpm) test case for the velocity magnitude plots created from the video.

There seems to be 2, maybe 3, distinct wake structures downstream of the robot and only on the port semi-plane (the wake structures on the starboard semi-plane would be equal and opposite and out of phase by half a cycle).

The 1st distinct structure consists of a general, residual-looking wake disturbance in the shape of a sinusoid-like track that is plotted out where the robot tail is and moves aft in time at the speed of advance. In other words, if the head of the robot was fixed, and the robot was articulating normally in place over a sheet of paper moving aft at the speed of advance. Tape a pen to the tail and have it write on the moving sheet of paper. The shape drawn out would resemble a sinusoid and is where there is a, as of yet unknown magnitude, definite disturbance downstream of the robot. It is unclear what this disturbance is, but what it is can be hypothesized.

This disturbance appears to be dissipating within 0.6 m downstream of the robot's tail, and it follows the shape of the sinusoidally waving tail. Because of this observation, this could be the boundary layer disturbance which is always there yet cancels out quickly. Some questions left to be answered:

- How quickly should it cancel/dissipate out?

- How does the foil and tether rod affect the fluid flow downstream? Preliminary results prove that this disturbance is minimal but plot the results to prove this statement.

The 2nd distinct wake structure is what appears to be a vortex pair (jet) being shed, starting at time 0.7T in the motion (See Figure **??**). Looking in the x-y plane with the positive x and y axes pointing right and up, respectively, this phenomenon is being shed when the robot tail is moving in a negative y-direction and beginning to move negative in x. The phenomenon is being shed in a positive-x, negative-y direction, relative to the head of the robot. It appears that this occurrence consists of two vortices in equal and opposite directions. Refer to the time sequence of illustrations
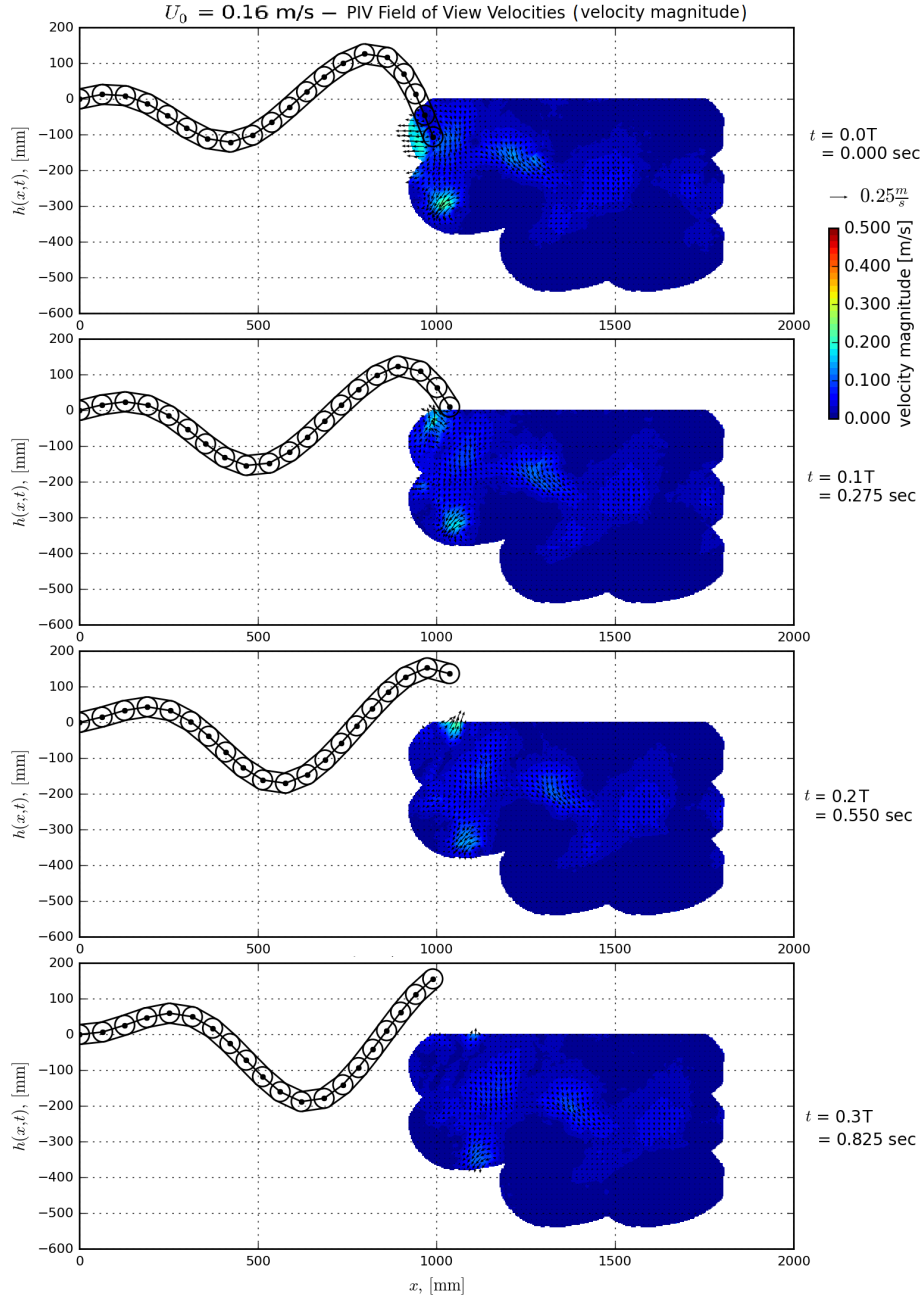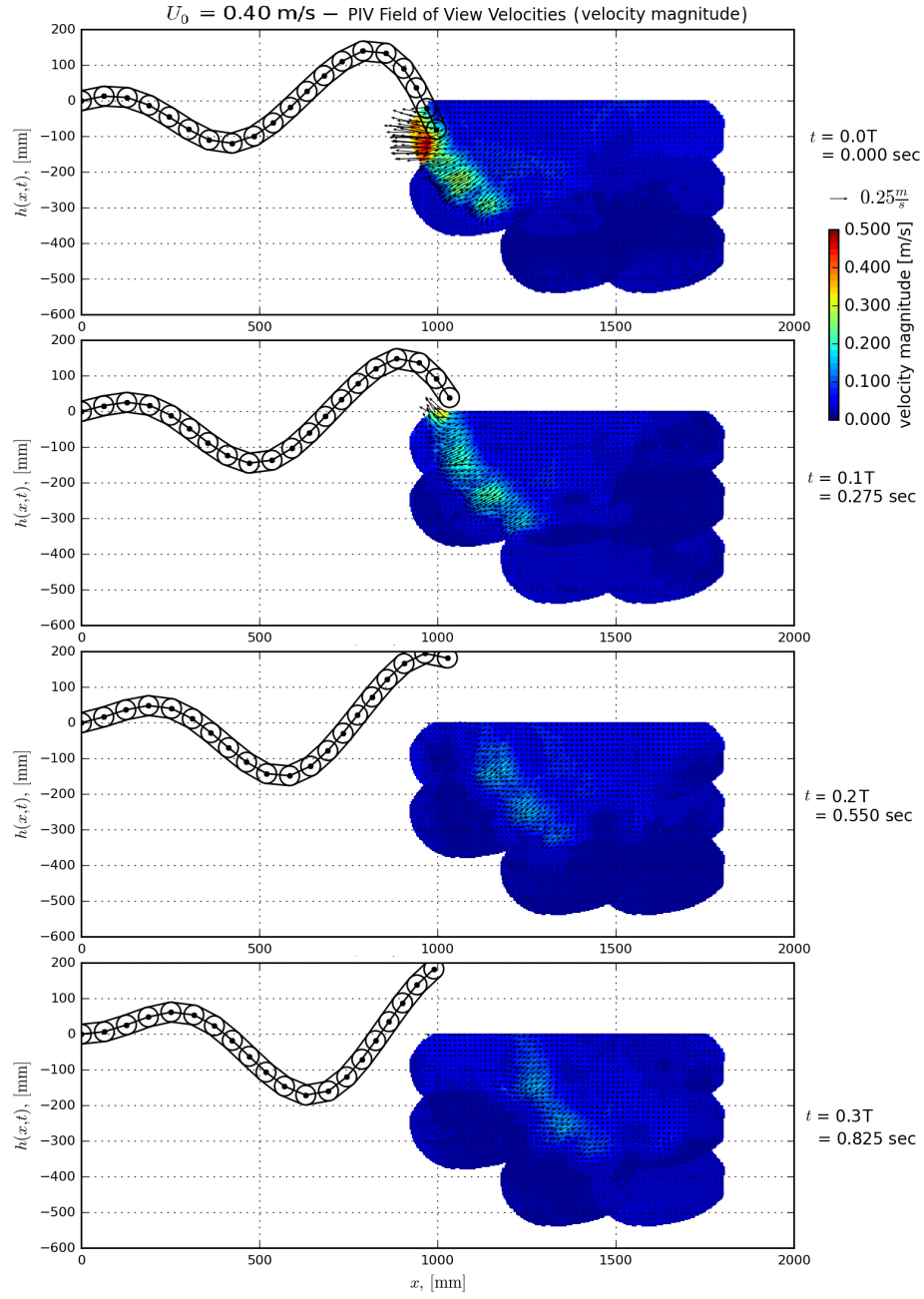
Figure 4.88: Timesteps 0.0T, 0.1T, 0.2T, and 0.3T of filtered ($f_c = 3.625$ Hz) velocities at equal time steps over the robotic eel motion cycle for $U_0 = 0.40$ m/s. The uniform flow of $u = 0.40$ m/s has been subtracted from the flow, giving the flow field an inertial frame of reference.

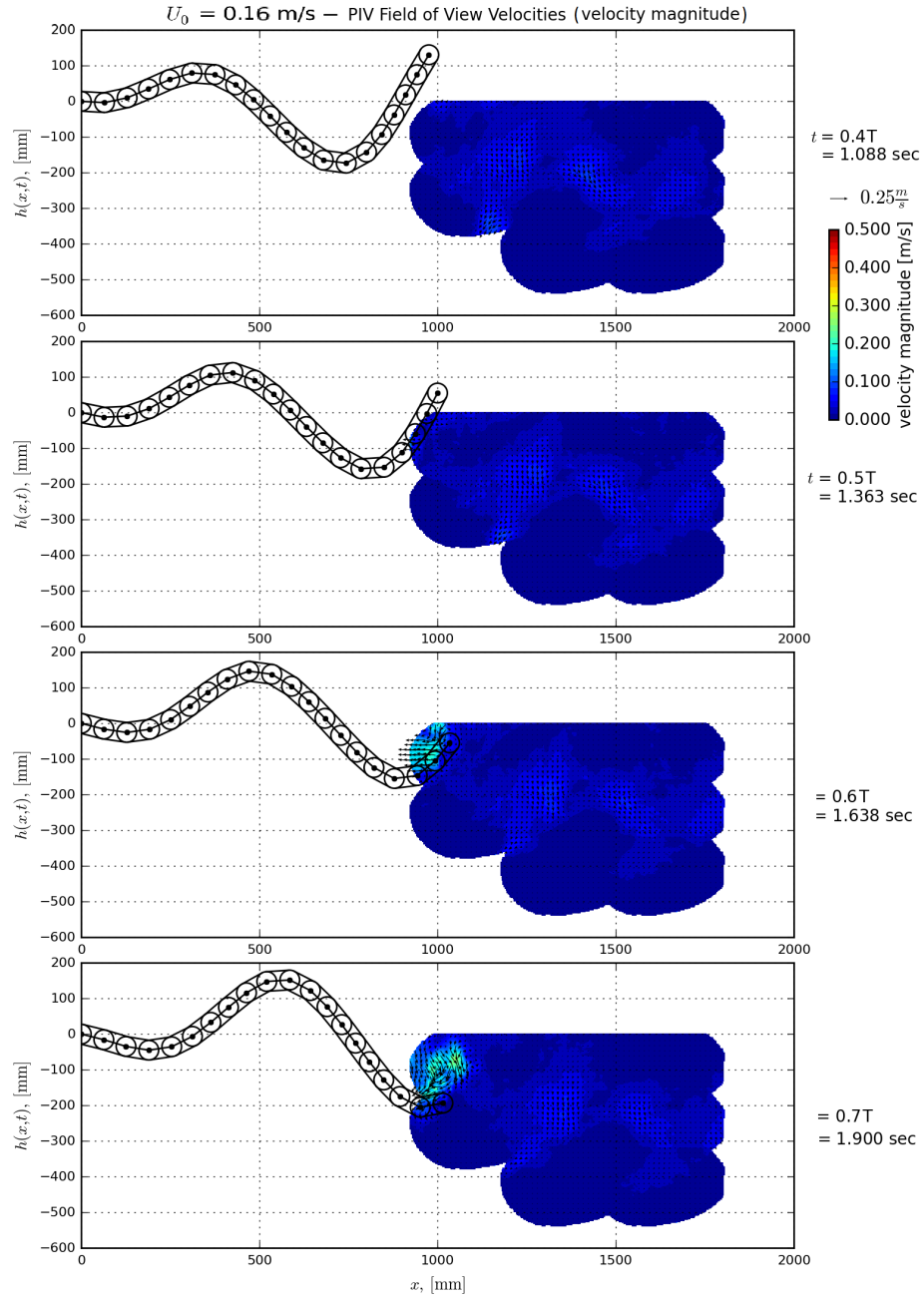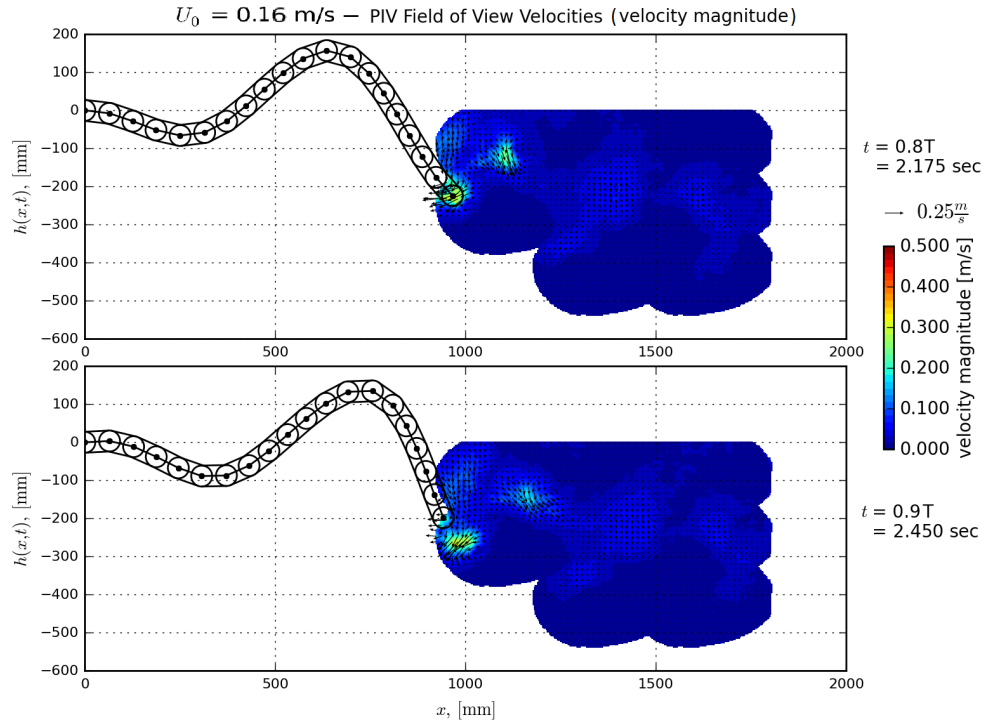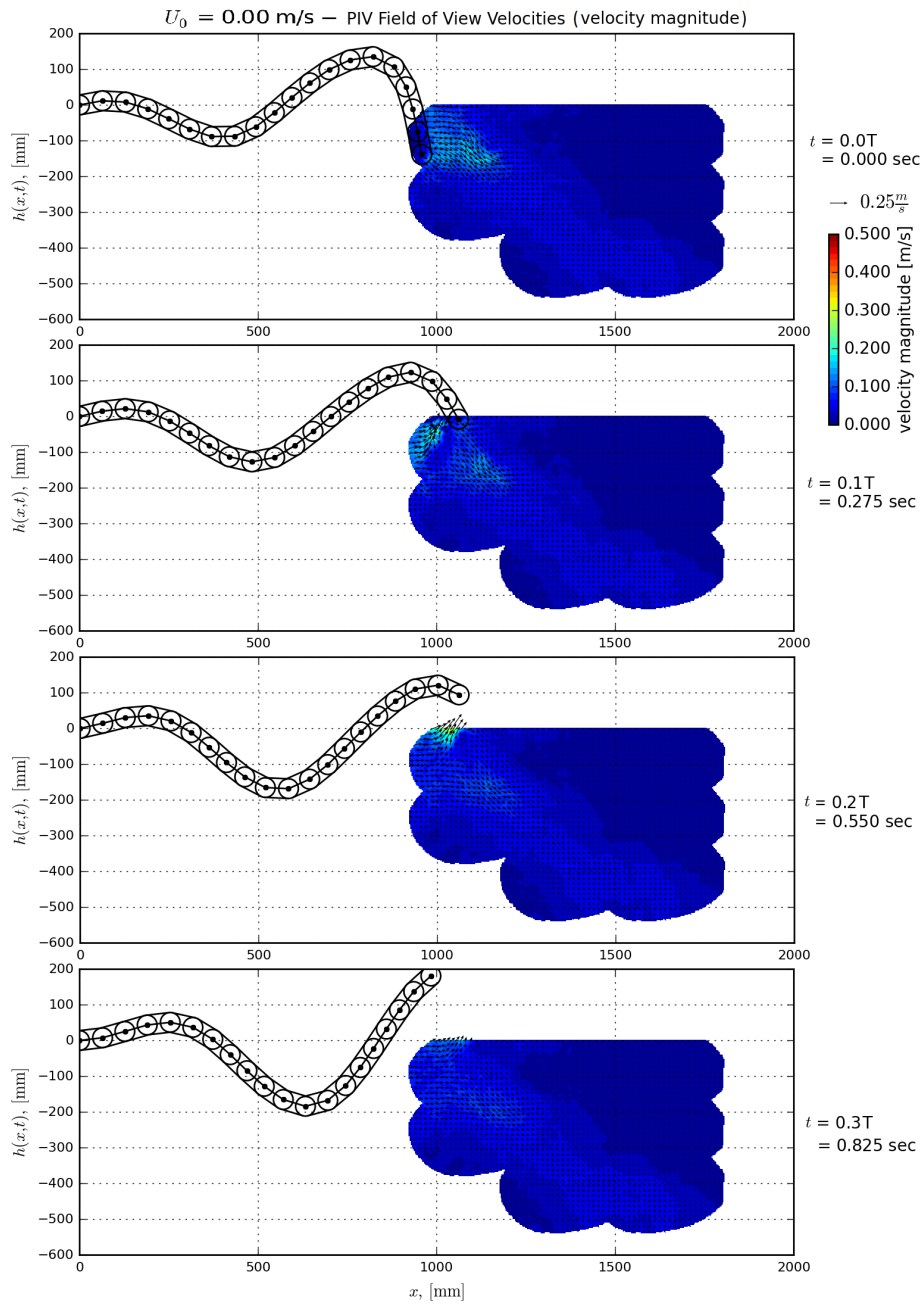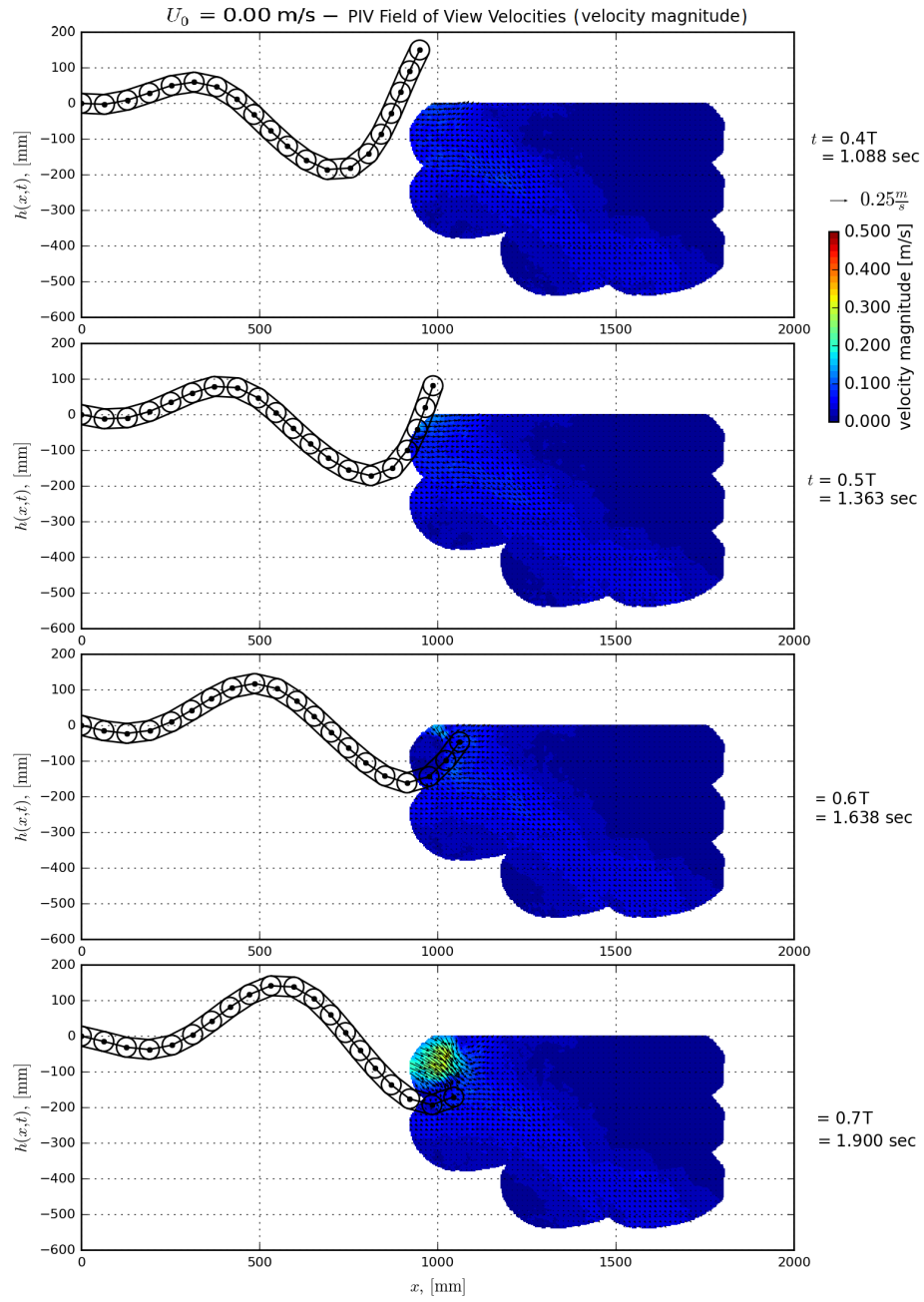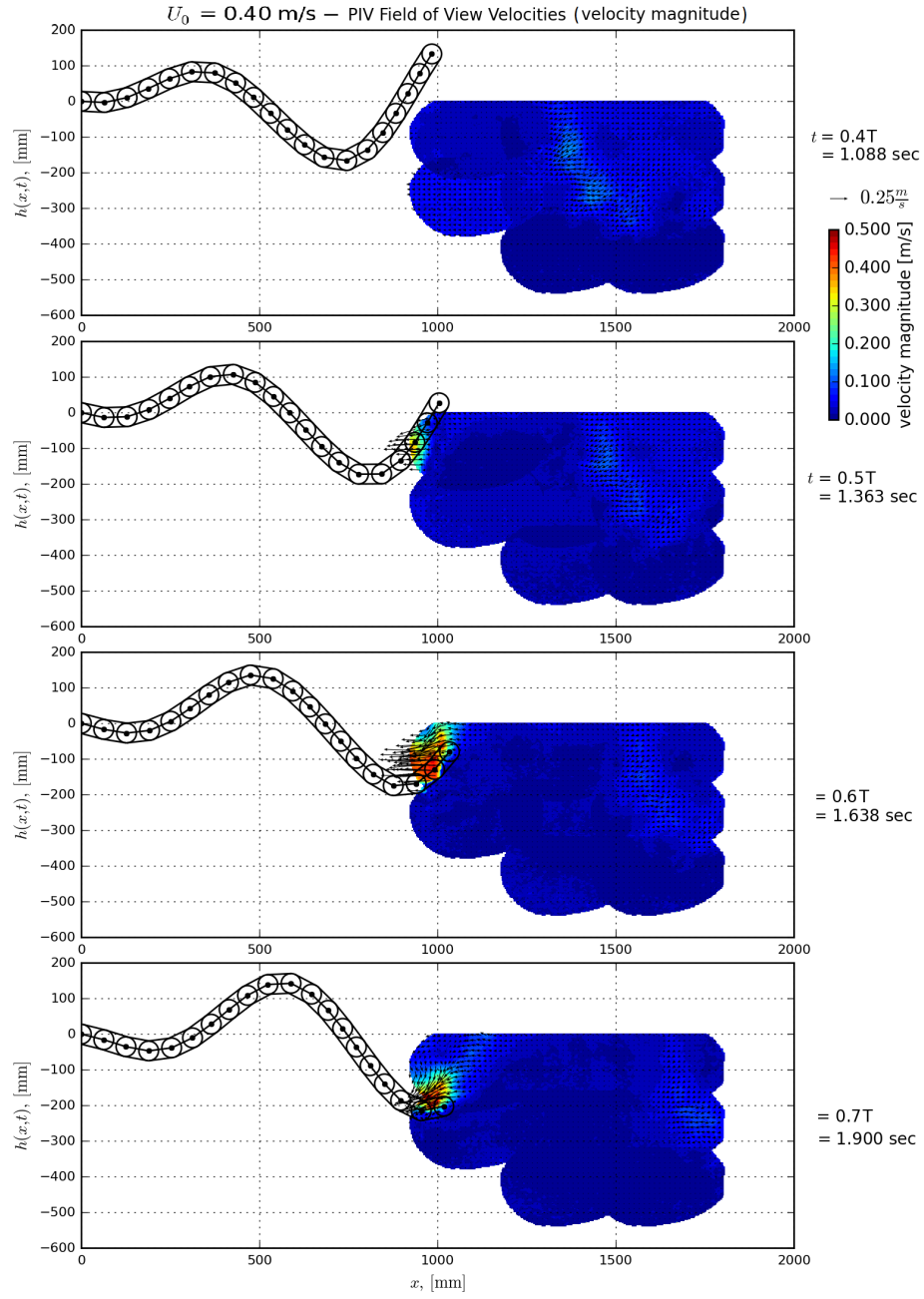Figure 4.89: Timesteps 0.4T, 0.5T, 0.6T, and 0.7T of filtered ($f_c = 3.625$ Hz) velocities at equal time steps over the robotic eel motion cycle for $U_0 = 0.40$ m/s. The uniform flow of $u = 0.40$ m/s has been subtracted from the flow, giving the flow field an inertial frame of reference.
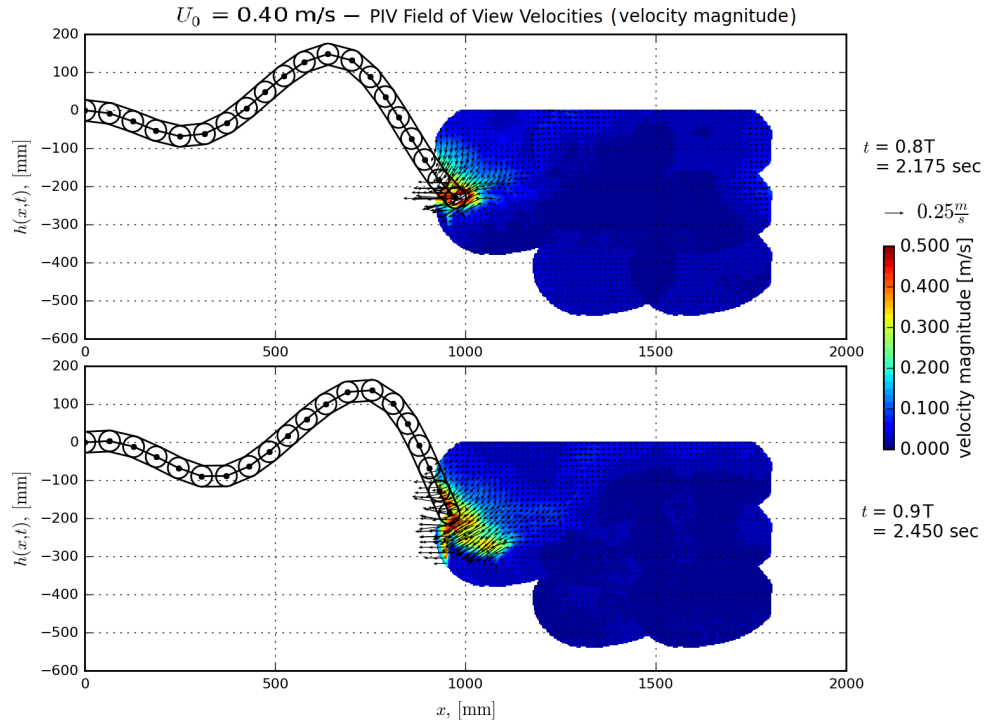
Figure 4.90:
Timesteps 0.8T and 0.9T of filtered ($f_c = 3.625$ Hz) velocities at equal time steps over the robotic eel motion cycle for $U_0 = 0.40$ m/s. The uniform flow of $u = 0.40$ m/s has been subtracted from the flow, giving the flow field an inertial frame of reference.
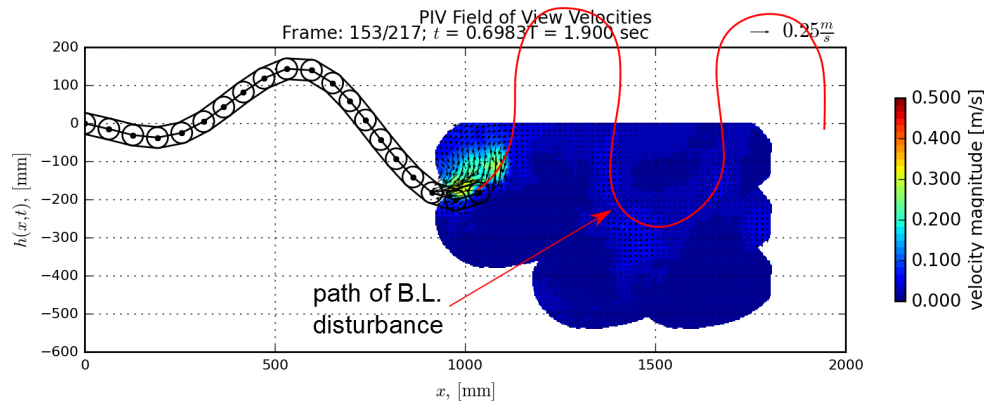
Figure 4.91:
Trace of the approximate path of the disturbance due to the boundary layer shedding for timestep 0.6T of the filtered ($f_c = 3.625$ Hz) velocities for $U_0 = 0.25$ m/s. The uniform flow of $u = 0.25$ m/s has been subtracted from the flow, giving the flow field an inertial frame of reference.
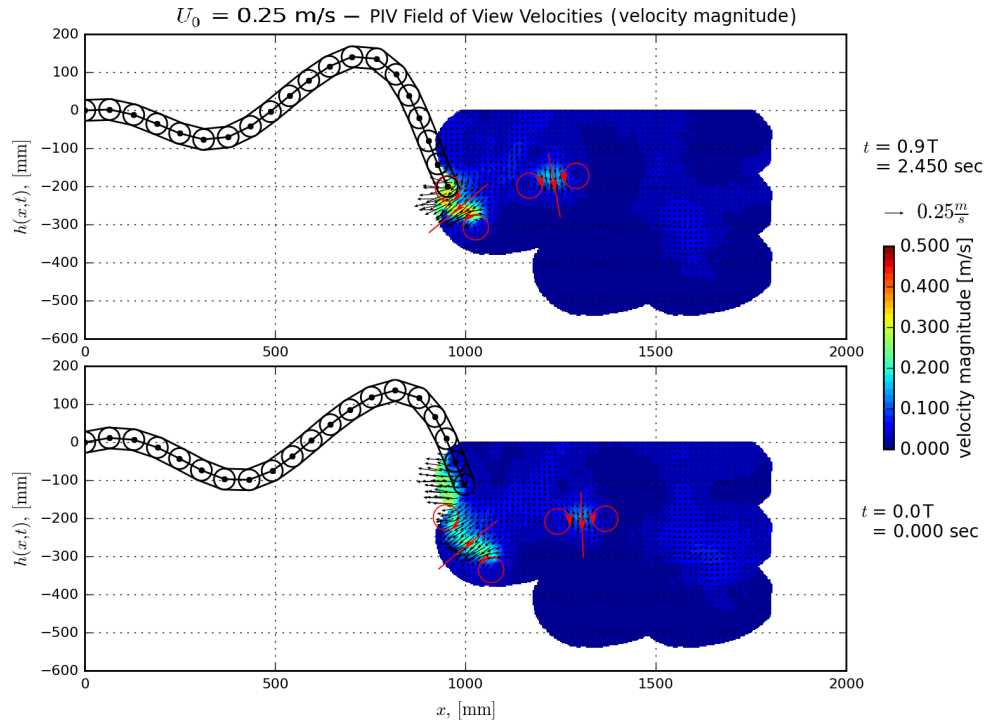
Figure 4.92: Approximate locations of vortices that are assumed to be part of three-dimensional vortex rings for timesteps 0.9T and 0.0T of the filtered ($f_c = 3.625$ Hz) velocities for $U_0 = 0.25$ m/s. The uniform flow of $u = 0.25$ m/s has been subtracted from the flow, giving the flow field an inertial frame of reference.

for a better explanation of what the structure is doing.
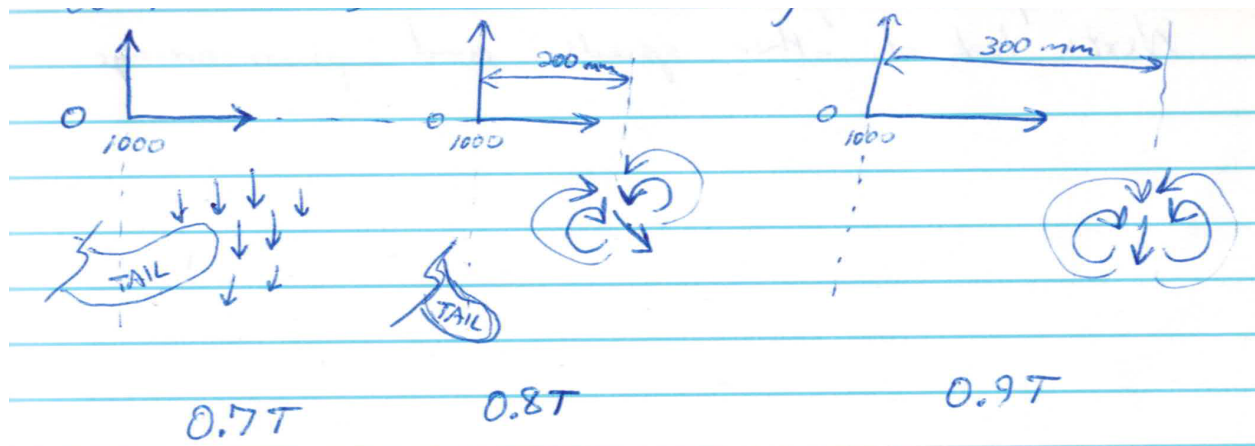
Figure 4.93: Time-sequence of 2nd distinct wake structure, a vortex pair being shed from the tail.

This vortex pair is moving aft at approximately 0.37 m/s from the tail. This corresponds to the robot's wave displacement speed of 0.357 m/s.

The 3rd possible distinct wake structure is a similar vortex pair being shed when the tail has ended its downstroke and has started moving back up in the frame of reference explained above. If it there, it is most noticeable after t=0.9T, and maybe more so at 1.0T. What I am seeing could be a phenomenon part of that explained in the 1st distinct wake structure. This is hard to distinguish at the moment and may be better explained once some phase-averaged plots have been generated. These phase-averaged plots will eliminate any noise in the fluid flow and focus on the more "solid" structures.

When and why these wake structures are being shed might be better explained when there timing is compared to the speed/acceleration of the joints.

CHAPTER V

Conclusions

The theoretical motion is theorized to produce "wakeless" swimming, which is described by Vorus and Taravella (2011) to be a reactive swimming technique that produces thrust by accelerations of the added mass in the vicinity of the vehicle, as opposed to carangiform swimmers which produce thrust by first-order lift of the rapidly accelerating tail fin. Due to the viscosity of the fluid, this swimming technique will inherently include relatively small-order boundary layer shedding that is expected to cancel out relatively quickly downstream from the anguilliform robot. Typical vortex shedding from an unsteady airfoil produces a net circulation in the wake equal and opposite in magnitude to the circulation about the object for each instant in time during acceleration. This net circulation is theoretically proven to be eliminated for this ideal swimming motion, as shown in the schematic of Figure 5.3.

Figures 5.1 through 5.3 show schematics for the three scenarios of unsteady propulsion at a steady swimming/forward speed. Figure 5.3 shows the ideal design motion explained above which produces forward thrust via reactive swimming forces of added mass. In an ideal fluid, this motion does not shed any vortices and thus does not have an induced drag. The plots in Figure **??** show that there is no disturbance in the flow field of velocity vectors downstream from the ideal anguilliform motion.

Unfortunately, NEELBOT-1.1 never consistently and accurately replicated the desired ideal motion, prohibiting an exact comparison of the experimental results with the theory of wakeless swimming. As explained in detail in Section 3.2.3, there were some physical limitations to obtaining the motion. The data upload and download rates between the servos themselves and the mainframe were too low to use a full-knowledge control scheme such as robust or adaptive control. Each
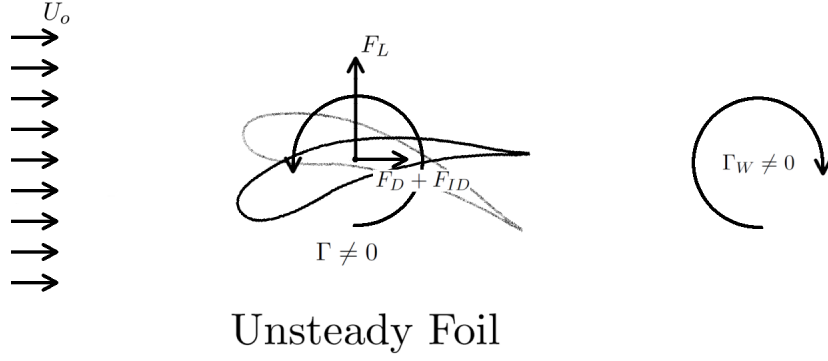
Unsteady Foil

Figure 5.1: Simplified schematic showing dynamics of unsteady foil in a free-stream fluid (the lighter-colored outline contrasted with the darker-colored one denote the unsteady motion of the foil).
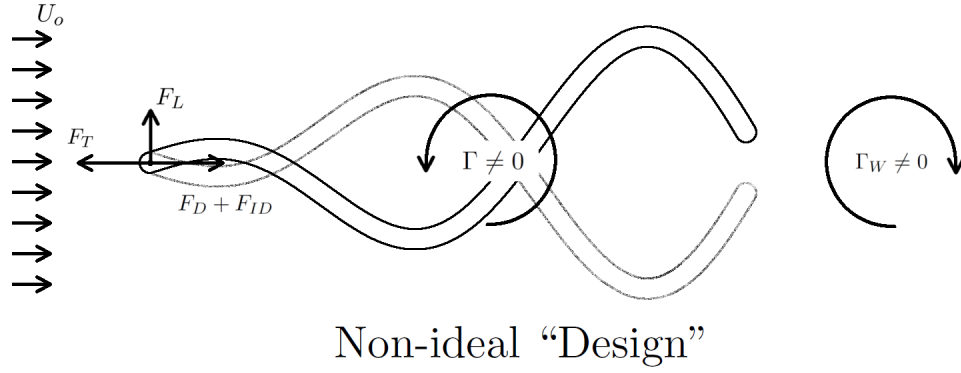
Non-ideal "Design"

Figure 5.2: Schematic showing dynamics of the non-ideal design of the anguilliform robot motion (the lighter-colored outline contrasted with the darker-colored one denote the unsteady motion of the anguilliform shape).
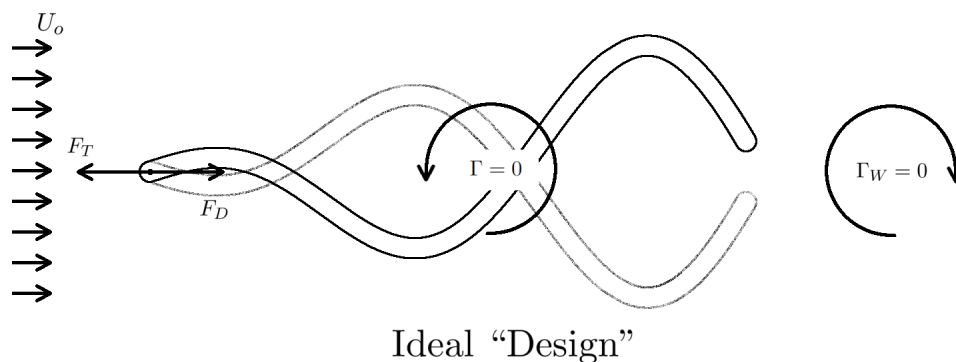
Ideal "Design"

Figure 5.3: Schematic showing dynamics of ideal design of the anguilliform robot motion (the lighter-colored outline contrasted with the darker-colored one denote the unsteady motion of the anguilliform shape).

joint's servo had to perform independent joint control, not knowing anything about the angles of the other joints. Additionally, the 19 degree-of-freedom system's dynamics proved to be very cumbersome to invert the inertia matrix describing the system within the time allotted and on the simple hardware provided. The highly non-linear and time-varying system made it difficult to run simulations to optimize the PID gains for each of the servos. Three methods were attempted to help with optimizing the gains: time-domain simulation, heuristic transfer function matrix/system identification modeling, and empirical Ziegler-Nichols tuning.

Deriving the Lagrangian equations of motion of the time-domain simulation proved to be extremely time consuming and was abandoned due to time constraints. Simultaneously, the heuristic transfer function matrix method was attempted and completed before the time-domain method got anywhere close to being finished. Time constraints forced the heuristic method to be used. Unfortunately, this method utilized several assumptions such as time invariance and linearization of the dynamics. This method also decomposed the system into several SISO systems, making it a coupled matrix of transfer functions, effectively a MIMO system. This method improved the motion obtained but it could not be repeated consistently (see Figure 3.28 for the motion obtained briefly). The Ziegler-Nichols approach did not improve the motion attainment substantially to be relied upon any more than the former approach. Mostly due to time constraints forcing the need to push forward with the research, the final obtained motions (Figures 3.24 through 3.30) had to

be used for the comparison with the theoretical results. However, the theoretical results are for the ideal and non-ideal motion.

Thus, changes were made to the research plans, and the slender body theory was applied to the new, actual motion, now referred to as "non-ideal design." Figure 5.2 shows a simplified schematic of what is happening dynamically with the non-ideal design. It shows an oscillating transverse lift force, a periodic forward thrust, induced drag, and shed circulation, or vortices, in the wake downstream from the motion.

Figure 5.1 shows a typical airfoil in a free stream rotating periodically about its centroid. For each instant in time, the foil is shedding a wake circulation, Γ_W, equal and opposite in magnitude to the circulation about the foil. The foil is always producing a lift force perpendicular to the free-stream velocity direction and an induced drag force in the direction of the free stream. It is not shown here, but the forward thrust propelling it through the fluid would come from some other device such as an engine and not the foil itself (but the foil can sometimes produce forward thrust depending on its orientation and rate of rotation; this exception is ignored for purposes of this simple comparison), unlike the anguilliform motion. (However, carangiform motion works under the principle of producing thrust via this first-order lifting process by changing shape rapidly and periodically.)

The forward thrust of the non-ideal design is being produced from both the reactive swimming motion of shifting the added mass and a first-order lifting method of circulation, typical of unsteady airfoils. Three different techniques were used to confirm this hypothesis of what is happening: the slender body theory applied to the actual robot motion (Sections 2.1.1 and 2.1.2), the measurement of thrust and drag produced by the swimming robot (Section 4.2), and the measurement of the downstream velocity vectors using PIV techniques (Section 4.4). The load cell results were used to confirm the thrust and drag forces of the hydrodynamic prediction, whereas the PIV results were used to confirm the predicted velocity vectors.

This forward thrust, or backwards drag, of the articulating robot under way was able to be measured with a 6-DOF load cell. The longitudinal and transverse forces (lift forces) recorded by the load cell compare favorably to the revised prediction method both qualitatively and quantitatively. Figures 4.10 through 4.41 show that both the theoretical and recorded data contain the same number of cycles per motion cycle of NEELBOT-1.1. For each of the speeds, design and off-design,

202
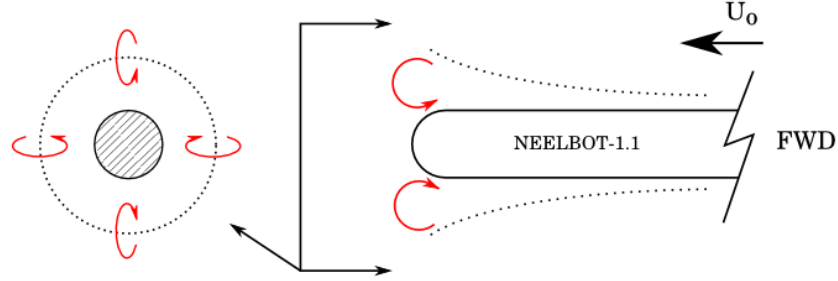
Figure 5.4: Illustration of shed boundary layer.

the newly predicted thrust and lift forces match the filtered, measured results within 30% over time. Due to the transverse loads being produced, which resemble lift forces for a typical thrust-producing vehicle, the robotic eel for this non-ideal motion is producing a typical first-order lift force. This is further proved by the vortex shedding illustrated in the PIV results, as explained later. The favorable comparison in magnitude and frequency of the loads to that of the predicted off-design case show that the slender-body theory is in fact relevant and works reasonably well for the off-design case, and one should expect it to be an adequate prediction method for the design shape, based on results of the load cell measurements. Thus, it is possible that the forces as a result of an ideal motion will be accurately predicted by the theoretical code.

With respect to the predicted downstream velocity vectors and the results of the PIV measurements, again the experiment compares very favorably to that of the theoretical with respect to velocity magnitudes, direction, and momentum flux. As stated earlier, there is always a local wake which for the robot case is a shed boundary layer disturbance. This shed boundary layer results in a vortex profile that is even across the longitudinal axis of the body. The illustration in Figure 5.4 shows what the flow would look like when looking at a cross-section of the robot near the end. The view of the cross-section is looking from the tail towards the head of the robot. Looking at the experimental PIV results, the velocity profile across the longitudinal axis of the shed boundary layer should be even. With the shedding of vortices in addition to the boundary layer shedding, it is rather difficult to differentiate the velocity vectors due to the boundary layer shedding. However, it can still be faintly seen in Figures 4.67 through **??**, where they form a sinusoidal-like path dependent on the location of the tail as it travels in space.
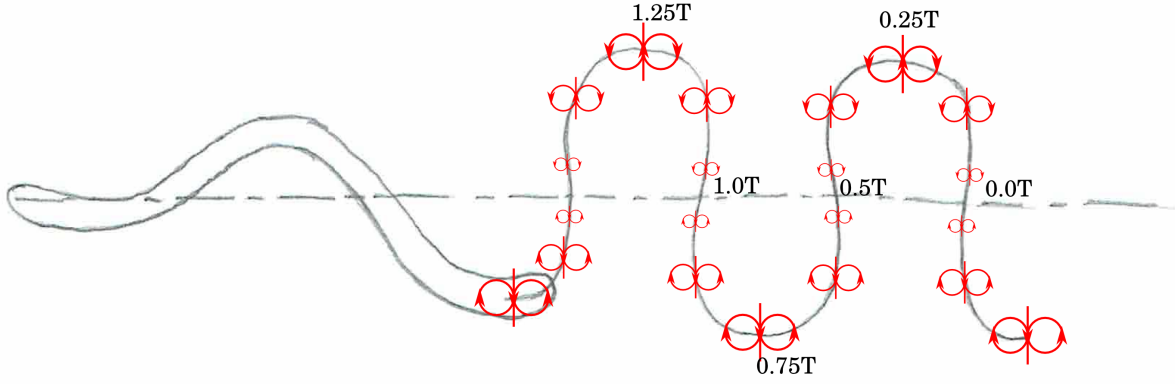
Figure 5.5: Proposed simplified model of the vortex shedding occurring for the non-ideal motion, as determined from the comparison of experimental and theoretical results.

The viscous drag of the robot traveling through the fluid is due to the shear stresses acting between the surface of the robot and the fluid.

This shedding of the boundary layer is due to the frictional drag created by the robot travelling through a viscous fluid. Specifying the frictional drag magnitude a priori is one of the key parameters that defines the motion shape definition, so getting this right is rather critical. The initial quasi-static method of predicting its value is explained in Vorus and Taravella (2011), in which it was determined by the Blasius flat plate drag prediction. Over the course of this research, it was determined that this prediction was insufficient due to the motion not producing the speed and thrust as predicted. Thus, a new method was formulated in order to determine a better frictional drag coefficient. Section 4.3 elaborates on determining what the magnitude of this frictional drag coefficient should be, and also shows some results of the off-design motion's effect on the efficiency. The viscous resistance was found to be 3-5 times greater than the quasi-static approach used in the second prediction using ITTC-57 line and "straight-line" test resistance.

The tail amplitude needed to overcome a viscous resistance at this magnitude for "ideal motion" swimming at 0.25 m/s is 23% of the length, which is XX% greater than the current nominal amplitude. This amplitude is not possible with the current robot design due to the physical limitations of the joints in terms of both angular displacement and rotational speed and torque provided by the servos. Figure XXX shows the motion needed to overcome this value of drag.

More important than the boundary layer shedding is the shedding of larger phenomenon, can be

204

modelled as vortices in 2-D or doublets in 3-D, due to the non-ideal motion, which is rather difficult to compare between the experimental and theoretical due to many assumptions of the theoretical. There are still many discrepancies between the theoretical and experimental results, but there is also some reconcilable agreement between the two. For the following discussion, the reader is referred to Figures **??** and **??**, which show the results of the theoretical code applied to the actual motion and the measurements of the PIV equipment. In addition, the shed doublet schematic of Figure 5.5 shows a simple model of the proposed doublet shedding occurring downstream of the robot, as determined from the comparison of the experimental and theoretical results. This schematic combines aspects of both the experimental and theoretical in order to get a better understanding of what is happening: the theory "collapses" all the doublets on to the centerline and adjusts the doublet strength dependent on the shed wake element's strength, but this is clearly not happening in real life, so the doublets are brought off the centerline and superimposed on to the path of the robot's tail as found from the PIV imagery.

Taking a look at the results and going forward in time, starting at time $0.5T$, the PIV experimental results show the robot tail beginning to cross centerline from $+y$ and $-y$. This position in time and space corresponds to the maximum transverse tail velocity with zero acceleration which corresponds with a local minimum of net circulation being shed. This point corresponds to the location marked $0.0T$ in the shed-doublet schematic of Figure 5.5, where it is shown that the vortex strength, denoted by the relative size of the sketched vortices, is relatively small compared to others in space and time. This smaller value correlates to the low velocity magnitude in the theoretical results of Figure **??**.

Increasing in time from $0.5T$, the vortex strength being shed from the tail slowly increases until a maximum is reached ($t \approx 0.75T$) at the tail's maximum lateral excursion, which also corresponds to the largest accelerations of the tail (push these time values slightly back because the phase is slightly behind from what I am stating). These unsteady movements cause circulation to be shed. This maximum acceleration corresponds to the time frame $t \approx 0.8T$ for the PIV results and the same for the theoretical plots. The theoretical plots show increased velocity magnitude that matches those of the experimental in order of magnitude at the tail at this point in time. These points in space and time correspond to the positive vortex at $t \approx 0.75T$ in the vortex schematic (again, I need to push some of these time back so that they all align correctly between the theory,

experiemnt, and schematic).

Final powerful statement(s) summing everything up: Even with all the assumptions, the theory still does a very good job of predicting the general, big picture physics of the anguilliform swimming robot.

5.1 Call to Future Work and Improvements

- CFD model of the robot using the velocities from the current research as an initial guess for the computations

- improvements to the actuators and the control algorithm to attain a more consistent, accurate replication of the desired motion

- better model of the "plant" with respect to control theory applications

- 2-DOF motion at each of the joints for a more practically-oriented product

- PIV testing in planes above and below the medial plane of the current testing

- more customized actuation and design of components, which will waste less space and improve the power density of the joints by providing more torque and speed

5.1.1 Possible Design Features of a Future Robotic Design

BIBLIOGRAPHY

BIBLIOGRAPHY

Anderson, E. J., McGillis, W. R., and Grosenbaugh, M. A. (2001). The boundary layer of swimming fish. *Journal of Experimental Biology*, 204(1):81 – 102.

Anderson, J. M. (1996). *Vorticity control for efficient propulsion.* PhD thesis, Massachusetts Institute of Technology.

Blasius, P. H. (1908). Grenzschichten in flussigkeiten mit kleiner reibung. *Z. Math. Physik*, 56:1–37.

Borazjani, I. and Sotiropoulos, F. (2008). Numerical investigation of the hydrodynamics of carangiform swimming in the transitional and inertial flow regimes. *Journal of Experimental Biology*, 211(10):1541–1558.

Borazjani, I. and Sotiropoulos, F. (2009). Numerical investigation of the hydrodynamics of anguilliform swimming in the transitional and inertial flow regimes. *Journal of Experimental Biology*, 212(4):576–592.

Bracewell, R. N. (2000). *The Fourier transform and its applications.* McGraw Hill, Boston, 3rd edition.

Buchholz, J. H. J. and Smits, A. J. (2006). On the evolution of the wake structure produced by a low-aspect-ratio pitching panel. *Journal of Fluid Mechanics*, 546:433–443.

Carling, J., Williams, T., and Bowtell, G. (1998). Self-propelled anguilliform swimming: Simultaneous solution of the two-dimensional navier-stokes equations and newton's laws of motion. *The Journal of Experimental Biology*, 201:3143–3166.

Cheng, J.-Y. and Chahine, G. L. (2001). Computational hydrodynamics of animal swimming: Boundary element method and three-dimensional vortex wake structure. *Comparative Biochemistry and Physiology Part A: Molecular & Integrative Physiology*, 131(1):51–60.

Corke, P. (2011). *Robotics, Vision and Control.* Springer-Verlag, 2nd edition.

Craig, J. J. (1988). *Adaptive control of mechanical manipulators.* Addison-Wesley Publishing Company, Inc.

Dabiri, J. O. (2005). On the estimation of swimming and flying forces from wake measurements. *Journal of Experimental Biology*, 208(18):3519–3532.

de Silva, C. W. (2007). *Sensors and actuators: control system instrumentation.* CRC Press.

de Stadler, M. B. and Sarkar, S. (2012). Simulation of a propelled wake with moderate excess momentum in a stratified fluid. *Journal of Fluid Mechanics*, 692:28–52.

Digi International (2009). *XBee®/Xbee-PRO® ZB RF Modules.* Digi International, Inc., Minnetonka, MN.

Dongbu Robotics (2012). *Herkulex DRS-0101/DRS-0201 User Manual.* South Korea, 1.1 edition. `http://www.robotshop.com/media/files/PDF/manual-drs-0101.pdf`.

Drucker, E. G. and Lauder, G. V. (1999). Locomotor forces on a swimming fish: Three-dimensional vortex wake dynamics quantified using digital particle image velocimetry. *Journal of Experimental Biology*, 202(18):2393 – 2412.

Falkner, V. M. and Skan, S. W. (1930). Some approximate solutions of the boundary layer equations. Technical Report 1314, Reports and Memoranda of the Aeronautical Research Council.

Gradshteyn, I. and Ryzhik, I. (1980). *Table of Integrals, Series, and Products, Corrected and Enlarged Edition.* Academic Press.

Gray, J. (1933a). Studies in animal locomotion. i. the movement of fish with special reference to the eel. *Journal of Experimental Biology*, 10(1):88–104.

Gray, J. (1933b). Studies in animal locomotion. ii. the relationship between waves of muscular contraction and the propulsive mechanism of the eel. *Journal of Experimental Biology*, 10(4):386–390.

Gray, J. (1936). Studies in animal locomotion: Vi. the propulsive powers of the dolphin. *Journal of Experimental Biology*, 13(2):192–199.

Hahn, W. (1967). *Theory and Application of Lyapunov's Direct Method.* Prentice Hall, Englewood Cliffs, NJ.

Hughes, G. (1954). Friction and form resistance in turbulent flow, and a proposed formulation for use in model and ship correlation. In *Transactions of the Royal Institution of Naval Architects*, volume 96, pages 314–376.

Hughes, G. (1966). An analysis of ship model resistance into viscous and wave components. In *Transactions of the Royal Institution of Naval Architects*, volume 108.

Hultmark, M., Leftwich, M. C., and Smits, A. J. (2007). Flowfield measurements in the wake of a robotic lamprey. *Experiments in Fluids*, 43(5):683–690.

ITTC (1957). *Eighth International Towing Tank Conference*, Canal de Experiencias Hidrodinamicas, El Pardo, Madrid.

ITTC (2011). Fresh water and seawater properties. 7.5-02-01-03.

Katz, J. and Plotkin, A. (2001). *Low Speed Aerodynamics.* Cambridge University Press.

Kern, S. and Koumoutsakos, P. (2006). Simulations of optimized anguilliform swimming. *The Journal of Experimental Biology*, 209:4841–4857.

Lasalle, P. and Lefschetz, S. (1961). *Stability by Lyapunov's Direct Method.* Academic Press, New York.

Leftwich, M. C. and Smits, A. J. (2011). Thrust production by a mechanical swimming lamprey. *Experiments in Fluids*, 50(5):1349–1355.

Lewis, F. L., Abdallah, C., and Dawson, D. (1993). *Control of robot manipulators.* Macmillan Publishing Company, New York, New York.

Lighthill, M. (1960). Note on the swimming of slender fish. *Journal of Fluid Mechanics*, 9(2):305–317.

Lighthill, M. (1964). *Fourier Analysis and Generalized Functions.* Cambridge University Press, Cambridge.

Lighthill, M. (1969). Hydromechanics of aquatic animal propulsion. *Annual Review of Fluid Mechanics*, 1(1):413–446.

Lighthill, M. (1970). Aquatic animal propulsion of high hydromechanical efficiency. *Journal of Fluid Mechanics*, 44(2):265–301.

Lighthill, M. (1971). Large-amplitude elongated-body theory of fish locomotion. *Proceedings of the Royal Society of London*, 179(1055):125–138.

Lin, J. T. and Pao, Y. H. (1979). Wakes in stratified fluids. *Annual Review of Fluid Mechanics*, 11:317–338.

Meunier, P. and Spedding, G. R. (2006). Stratified propelled wakes. *Journal of Fluid Mechanics*, 552:229–256.

Miloh, T. and Galper, A. (1993). Self-propulsion of general deformable shapes in a perfect fluid. *Proceedings: Mathematical and Physical Sciences*, 442(1915):273–299.

Müller, U. K., Smit, J., Stamhuis, E. J., and Videler, J. J. (2001). How the body contributes to the wake in undulatory fish swimming: Flow fields of a swimming eel (anguilla anguilla. *The Journal of Experimental Biology*, 204:2751–2762.

Müller, U. K., Van Den Heuvel, B. L. E., Stamhuis, E. J., and Videler, J. J. (1997). Fish foot prints: Morphology and energetics of the wake behind a continuously swimming mullet (chelon labrosus risso). *Journal of Experimental Biology*, 200(22):2893 – 2906.

Nauen, J. C. and Lauder, G. V. (2002). Hydrodynamics of caudal fin locomotion by chub mackerel, scomber japonicus (scombridae). *Journal of Experimental Biology*, 205(12):1709 – 1724.

Ogata, K. (2001). *Modern Control Engineering.* Prentice Hall, 4th edition.

Paul, R. P. (1981). *Robot manipulators.* The Massachusetts Institute of Technology.

Pedley, T. and Hill, S. (1999). Large-amplitude undulatory fish swimming: Fluid mechanics coupled to internal mechanics. *The Journal of Experimental Biology*, 202:3431–3438.

Potts, B., Taravella, B., and Thiel, R. (2013). Proof of concept development and motion verification of a swimming anguilliform robot (NEELBOT-1.0). In *Proceedings of the 2013 Grand Challenges on Modeling and Simulation Conference*, GCMS '13, pages 16:1–16:10, Vista, CA. Society for Modeling & Simulation International.

Prohaska, C. (1962). Trial trip analysis for six sister ships using a new method of analysis. In *Transactions of North East Coast Institution of Engineers and Shipbuilders*, volume 78.

Saffman, P. (1967). The self-propulsion of a deformable body in a perfect fluid. *Journal of Fluid Mechanics*, 28(2):385–389.

Schilling, R. J. (1990). *Fundamentals of robotics: analysis and control.* Prentice-Hall, Inc., Upper Saddle River, NJ.

Schultz, W. W. and Webb, P. W. (2002). Power requirements of swimming: Do new methods resolve old questions?. *Integrative and Comparative Biology*, 42(5):1018–1025.

Siciliano, B. and Khatib, O., editors (2008). *Springer Handbook of Robotics.* Springer.

Siciliano, B., Sciavicco, L., Villani, L., and Oriolo, G. (2010). *Robotics: modelling, planning and control.* Springer.

Sirviente, A. I. and Patel, V. C. (2000). Wake of a self-propelled body, part 1: Momentumless wake. *AIAA Journal*, 38(4):613–619.

Slotine, J.-J. E. and Li, W. (1991). *Applied Nonlinear Control.* Prentice Hall, Englewood Cliffs, NJ.

Sowerby, L. (1954). Secondary flow in a boundary layer. Technical Report 2512/16832, Aeronautical Research Council (Great Britain).

Spedding, G. R., Rayner, J. M., and Pennycuick, C. J. (1984). Momentum and energy in the wake of a pigeon (columba livia) in slow flight. *Journal of Experimental Biology*, 111:81–102.

Spong, M. W. (2006). *Robot modeling and control.* Wiley.

Stefanini, C., Orofino, S., L., M., Mintchev, S., Marrazza, S., Assaf, T., Capantini, L., Sinibaldi, E., Grillner, S., Wallen, P., and Dario, P. (2012). A compliant bioinspired swimming robot with neuro-inspired control and autonomous behavior. In *2012 IEEE International Conference on Robotics and Automation*, pages 5094–5098, RiverCentre, Saint Paul, Minnesota. IEEE.

Taylor, G. (1952). Analysis of the swimming of long and narrow animals. *Proceedings of the Royal Society*, 214(1117):158–183.

Thomson, W. T. and Dahleh, M. D. (1998). *Theory of vibration with applications.* Prentice-Hall, Inc., Upper Saddle River, New Jersey.

Tytell, E. D. (2004). The hydodynamics of eel swimming ii. effect of swimming speed. *The Journal of Experimental Biology*, 207:3265–3279.

Tytell, E. D. (2007). Do trout swimm better than eels? challenges for estimating performance based on the wake of self-propelled bodies. *Experiments in Fluids*, 43(5):701–712.

Tytell, E. D. and Lauder, G. V. (2004). The hydrodynamics of eel swimming i. wake structure. *The Journal of Experimental Biology*, 207:1825–1841.

Ulrich, K. T. and Eppinger, S. D. (2008). *Product Design and Development.* McGraw-Hill/Irwin, 4th edition.

USGS (2006). Gravity Base Station: New Orleans DA. `http://gis.utep.edu/subpages/states/documents/Louisiana/DESC.NEW_ORLEANS_DA.pdf`.

Verhulst, F. (1989). *Nonlinear Differential Equations and Dynamical Systems.* Springer-Verlag, Berlin.

Vidyasagar, M. (1978). *Nonlinear Systems Analysis.* Prentice Hall, Englewood Cliffs, NJ.

Vorus, W. S. (1995). The concept of a traveling-wave propulsor for high efficiency and low wake signature. In Johnson, P., editor, *24th American Towing Tank Conference*, volume 24, pages 179–184, Offshore Technology Research Center, Texas A & M University. ATTC.

Vorus, W. S. (2005). Swimming of the semi-infinite strip revisited. *Journal of Engineering Mathematics*, 51(1):35–55.

Vorus, W. S. (2013). Eel first order velocity field. Manuscript from email dated 2/13/13.

Vorus, W. S. and Taravella, B. M. (2011). Anguilliform fish propulsion of highest hydrodynamic efficiency. *Journal of Marine Science and Application*, 10(2):163–174.

Walker, M. W. and Orin, D. E. (1982). Efficient dynamic computer simulation of robotic mechanisms. *Journal of Dynamic Systems Measurement and Control*, 104(3):205–211.

Wikipedia (2015a). Refugio oil spill — wikipedia, the free encyclopedia. `https://en.wikipedia.org/w/index.php?title=Refugio_Oil_Spill&oldid=669190882`. [Online; accessed 16-July-2015].

Wikipedia (2015b). Search for malaysia airlines flight 370 — wikipedia, the free encyclopedia. `https://en.wikipedia.org/w/index.php?title=Search_for_Malaysia_Airlines_Flight_370&oldid=671622932`. [Online; accessed 16-July-2015].

Wilbur, C., Vorus, W., Cao, Y., and Currie, S. (2002). A lamprey-based undulatory vehicle. In Ayers, J., Davis, J. L., and Rudolph, A., editors, *Neurotechnology for Biomimetic Robots*, pages 285–296. Bradford Books, 1st edition.

Williamson, C. and Roshko, A. (1988). Vortex formation in the wake of an oscillating cylinder. *Journal of Fluids and Structures*, 2(4):355 – 381.

Wolfgang, M. J., Anderson, J. M., Grosenbaugh, M. A., Yue, D. K. P., and Triantafyllou, M. S. (1999). Near-body flow dynamics in swimming fish. *Journal of Experimental Biology*, 202(17):2303 – 2327.

Wu, T. Y. (1961). Swimming of a waving plate. *Journal of Fluid Mechanics*, 10(3):321–344.

Yamada, H., Chigisaki, S., Mori, M., Takita, K., Ogami, K., and Hirose, S. (2005). Development of amphibious snake-like robot acm-r5. In *The Proceedings of 36th International Symposium on Robotics*, Tokyo, Japan.

Young, W. C., Budynas, R. G., and Roark, R. J. (2011). *Roark's Formulas for Stress and Strain.* McGraw-Hill Education, New York, 8th edition.

VITA

Baker Potts was born and raised in New Orleans, LA, experiencing and growing a love for mechanical systems in his father's garage, which contained a mill and lathe, amongst other machinery. In the fall of 2005, he entered Tufts University to study Mechanical Engineering and compete on the varsity sailing team. In his junior and senior years, he lead the team as captain and competed nationally. Among the many courses of his curriculum, his favorite was the theory and applications of control engineering. He graduated "cum laude" in Spring 2009.

He immediately entered the University of New Orleans' graduate school for Naval Architecture and Marine Engineering and simultaneously worked part-time at various Naval Architecture firms. He focused on propeller boat refurbishment and testing 3-D printed propellers with open-water tests, graduating with a Master's in Science in Spring of 2012.

Before finishing his M.S., he joined Dr. Taravella to develop and build an anguilliform swimming robot. Over the next several years, he continued to develop and test the robot, comparing it to theoretical results, and receiving his Ph.D. in December, 2015. During his doctoral studies, he also kept a secondary focus on the analysis and design of floating and fixed offshore structures, which are of great interest to him.